



Assessment of extreme design loads for modern wind turbines using the probabilistic approach

Abdallah, Imad; Natarajan, Anand; Sørensen, John Dalsgaard

Publication date:
2015

Document Version
Publisher's PDF, also known as Version of record

[Link back to DTU Orbit](#)

Citation (APA):

Abdallah, I., Natarajan, A., & Sørensen, J. D. (2015). Assessment of extreme design loads for modern wind turbines using the probabilistic approach. DTU Wind Energy. (DTU Wind Energy PhD; No. 0048(EN)).

DTU Library

Technical Information Center of Denmark

General rights

Copyright and moral rights for the publications made accessible in the public portal are retained by the authors and/or other copyright owners and it is a condition of accessing publications that users recognise and abide by the legal requirements associated with these rights.

- Users may download and print one copy of any publication from the public portal for the purpose of private study or research.
- You may not further distribute the material or use it for any profit-making activity or commercial gain
- You may freely distribute the URL identifying the publication in the public portal

If you believe that this document breaches copyright please contact us providing details, and we will remove access to the work immediately and investigate your claim.

ASSESSMENT OF EXTREME DESIGN LOADS FOR MODERN WIND TURBINES USING THE PROBABILISTIC APPROACH

ASPECTS OF UNCERTAINTY QUANTIFICATIONS AND PROBABILISTIC METHODS

Department of
Wind Energy
PhD Report 2015

Imad Abdallah

DTU Wind Energy PhD-0048 (EN)

April 2015

DTU Wind Energy
Department of Wind Energy



Authors: Imad Abdallah

Title: Assessment of extreme design loads for modern wind turbines using the probabilistic approach

Department: Wind Energy

Summary:

This research aimed to contribute to the larger objective of reducing cost of energy through the implementation and application of uncertainty quantification and probabilistic methodologies on specific areas of design of wind turbines, namely: (a) aerofoil aerodynamic lift and drag, (b) load alleviation control features and (3) fusion of output from multi-fidelity aero-servo-elastic simulators.

The original contributions of this research were:

- A comprehensive list of sources of uncertainties affecting the prediction of extreme loads on a wind turbine.
- A stochastic model of aerofoil aerodynamic lift and drag coefficients, followed by a quantification of the effect of aerodynamic uncertainties on the extreme loads and an optimization of the load partial safety factors. An overall assessment of uncertainties in the aerodynamic static lift and drag coefficients showed a tangible reduction in the load partial safety factor for a blade and generally a larger impact on extreme loads during power production compared to stand-still. The stochastic model can also be used as a tool for a probabilistic design and risk mitigation in the early stages of the aerodynamic design of a wind turbine rotor.
- An in depth analysis of how various configurations of advanced load alleviation control features affect the structural reliability of a multi-megawatt wind turbine blade and tower when the extreme turbulence model is uncertain. The novelty is in the subsequent cost and reliability based optimization of the partial safety factors, turbine geometry, controller failure rate and structural reliability metrics when various configurations of the advanced load alleviation control features are used. A key take away is that the overall probability of failure of the structure-control system is by far dominated by the annual failure rate of the control system.
- A detailed implementation of several analytical methods for fusing the outputs from multiple aero-servo-elastic simulators. Designers increasingly use multiple commercial and research based aero-servo-elastic simulators to compare the predicted coupled dynamic loads and response of the system. The objective was to use these analytical methods to predict the most likely response and the corresponding model uncertainties when outputs from various multi-fidelity aero-servo-elastic simulators are available.

April 2015

Project Period:

2012.05.01 – 2015.04.30

Education:

PhD

Field:

Wind Energy

Supervisors:

Anand Natarajan
John Dalsgaard Sørensen

Project no.:

DTU Wind Energy PhD-0048 (EN)

Sponsorship:

MiTa-Teknik &
The Danish agency for Science
Technology and Innovation

ISBN:

978-87-93278-32-5

Technical University of Denmark

Department of Wind Energy
Frederiksborgvej 399
Building 118
4000 Roskilde
Denmark
Telephone 46 77 55 58

www.vindenergi.dtu.dk



Summary

There is a large drive to reduce the cost of energy of wind energy generators. Various tracks are being considered such as enhanced O&M strategies through condition monitoring, increased manufacturing efficiency through higher production volumes and increased automation, improved resource assessment through turbine-mounted real-time site assessment technologies, improved components reliability by increased laboratory testing, increased number of prototype test turbines before serial production, larger rotor and tower concepts for both onshore and offshore installations, advanced drive train designs, advanced load alleviation control systems, extensive industrialization and modularization of components, cost-out programs, increased components redundancies where possible, etc [Schwabe, P., Lensink, S., Hand, 2011] . Twenty five years ago an offshore wind turbine consisted of $\frac{2}{3}$ of the total capital cost (excluding foundations), today this value has dropped down to roughly 30 – 40% [IRENA, 2012, CleanEnergyPipeline, 2014]. Wind turbine manufacturers and researchers have indeed delivered on the promise of cost reduction, but the question remains: can we do more?

The research in this thesis aimed to contribute to the larger objective of reducing cost of energy through the implementation and application of uncertainty quantification and probabilistic methodologies on specific areas of design of wind turbines, namely: (a) aerofoil aerodynamic lift and drag, (b) load alleviation control features and (3) fusion of output from multi-fidelity aero-servo-elastic simulators. Why uncertainty quantification and probabilistic methodologies? Because such methodologies provide tools that makes it possible to design a wind turbine to a specific probability of failure, which means wind turbines are as strong as necessary, but no stronger [Veldkamp, 2006].

The original contributions of this research were:

- A comprehensive list of sources of uncertainties affecting the prediction of extreme loads on a wind turbine. Such a list is indeed subjective and subject to scrutiny and updating depending on a researcher's, scientist's and engineer's background, know-how and experiences.
- A fully encompassing stochastic model of aerofoil aerodynamic lift and drag coefficients, followed by a quantification of the effect of aerodynamic uncertainties on the extreme loads and an optimization of the partial safety factors.
- An in-depth analysis of how advanced load alleviation control features such as cyclic pitch, individual pitch, static thrust limiter, condition based thrust limiter and an active tower vibration damper affect the structural reliability of a multi-megawatt wind turbine blade and tower when the extreme turbulence model is uncertain. The novelty is in the subsequent cost and reliability based optimization of the load partial safety factor, turbine geometry, controller failure rate and structural reliability metrics of a large multi-megawatt wind turbine equipped with advanced load alleviation control features. The objective here

was to investigate how the load partial safety factors are affected by the performance of various configurations of advanced load alleviation control features to limit the excursion of extreme loads above a certain threshold.

- A review, implementation and demonstration of 5 analytical methods for fusing output from multi-fidelity aero-servo-elastic simulators with application to extreme loads on a wind turbine. Analysts and designers increasingly use multiple commercial and research-based aero-servo-elastic simulators such as FLEX, FAST, BLADED, HAWC2, Cp-Lambda, etc. to compare the predicted coupled dynamic loads and response of the system. This review attempts to demonstrate the potential to fuse (combine) the output of various multi-fidelity aero-servo-elastic simulators to predict the most likely response and the corresponding model uncertainty.
- A detailed implementation of a model fusion technique called co-Kriging to predict the extreme response in the presence of non-stationary noise in the output (i.e. the magnitude of noise varies as a function of the input variables) in the case when the low and high-fidelity aero-servo-elastic simulators of the same wind turbine are implemented by two independent engineers (i.e. human error and uncertainty in the modelling and input assumptions are implicitly included). We demonstrate the co-Kriging methodology to fuse the extreme blade root flapwise bending moment of a large multi-megawatt wind turbine by using two aero-servo-elastic simulators, FAST [Jonkman and Buhl, 2005] and BLADED ([Bossanyi, 2003b], [Bossanyi, 2003a]).

The main findings of the work and their implications were:

- The assessment of uncertainties in the aerodynamic lift and drag were done through a heuristic based stochastic model which replicates the uncertainties in airfoil characteristics by parameterizing the lift and drag coefficients polar curves. In the IEC61400-1 design standard for wind turbines, a value of 10% for the coefficient of variation (COV) on the uncertainty related to the assessment of the aerodynamic lift and drag coefficients is used. The findings in this research indicate that while this value is appropriate for certain structural components such as blade tip flapwise and main shaft tilt and yaw moments, it is conservative for components such as blade root flapwise, edgewise and tower. An overall assessment of uncertainties in the aerodynamic static lift and drag coefficients showed (a) a tangible reduction in the load partial safety factor for a blade and (b) generally a larger impact on extreme loads during power production compared to stand-still. Therefore, the way forward is for wind turbine manufactures to further update the stochastic model by integrating their own data to assess the impact of the aerodynamic uncertainty on their specific wind turbine. The stochastic model can also be used as a tool for a probabilistic design and risk mitigation in the early stages of the aerodynamic design of a wind turbine rotor.
- Large uncertainties in the extreme turbulence model can be significantly mitigated through the use of advanced load control features. The magnitude, scatter and shape of the annual maximum distribution of the loads is dependent on the performance of the load alleviation control features such as individual pitch control and condition based thrust limiter to limit the excursion of extreme loads above a certain threshold. The reduction in the mean of the annual maximum load distribution and the coefficient of variation due to the action of advanced load alleviation control features in turn translated into a higher structural reliability level in the face of uncertainties in the extreme turbulence model.

-
- The probabilistic cost and reliability based optimization methodology showed that a tangible reduction in the load partial safety factors can be achieved when advanced load alleviation control features are used while maximizing the benefits versus costs and while maintaining acceptable target probability of failure. However, some configurations of advanced load alleviation control features yield annual maximum load distribution with very low coefficient of variation (i.e. on the order of 2 – 3%); in this case the model and statistical sources of uncertainties dominate the reliability analysis resulting in higher load partial safety factors. It was shown that the benefits were maximized when the annual failure rate of advanced load alleviation control features is around 10^{-3} . A key finding is that the overall probability of failure of the structure-control system is by far dominated by the annual failure rate of the control system. This means that decreasing the annual failure rate of the control system would have a larger impact than improving the reliability of the structure.
 - Assuming that the output of the high-fidelity (BLADED) and low-fidelity (FAST) aero-servo-elastic simulators follow similar trends as a function of an independent variables (i.e. bending moment as a function of wind speed), the co-Kriging based methodology fused the "noisy" extreme flapwise bending moment at the blade root of a large wind turbine from a low fidelity and a high-fidelity aero-servo-elastic simulators; the co-Kriging predictions compared well with validation data. Therefore, the way forward is to fuse output from multiple aero-servo-elastic simulators in order to reduce model uncertainties and refine the probability of failure of the wind turbine structure.

Finally, the findings and contributions are presented in a series of publications including:

- Abdallah et al. [2015] Impact of uncertainty in airfoil characteristics on wind turbine extreme loads. / Abdallah, Imad; Natarajan, Anand; Sørensen, John Dalsgaard. Published In: *Renewable Energy*, Vol. 75, 2015, p. 283-300.
- Abdallah et al. [2015] Influence of the control system on wind turbine loads in power production in extreme turbulence: structural reliability. / Abdallah, Imad; Natarajan, Anand; Sørensen, John Dalsgaard. Submitted to: *Renewable Energy*, 2015.
- Abdallah et al. [2015] Influence of the control system on wind turbine loads in power production in extreme turbulence: Cost and reliability-based optimization of partial load factors. / Abdallah, Imad; Natarajan, Anand; Sørensen, John Dalsgaard. To be submitted to: *Renewable Energy*, 2015.
- Abdallah et al. [2015] Co-Kriging: fusing simulation results from multifidelity aero-servo-elastic simulators - Application to extreme loads on wind turbines. / Abdallah, Imad; Sudret, Bruno; Lataniotis, Christos; Sørensen, John Dalsgaard; Natarajan, Anand. Accepted for publication in: *ICASP12 - Proceedings of the 12th International Conference on Applications of Statistics and Probability in Civil Engineering*: Vancouver, Canada, July 12-15, 2015.

Resumé

Forskningen i denne Ph.d. afhandling har til formål at bidrage til det overordnede mål at reducere energi omkostningerne (Cost of Energy) ved at gennemføre og anvende usikkerhed kvantificering og probabilistiske metoder for specifikke områder ved design af vindmøller, nemlig: (a) aerofoil aerodynamisk løft og drag, (b) kontrol algoritmer til last reduktion og (3) fusion af output fra multi-fidelity aero-servo-elastiske simulatorer.

De originale forskningsbidrag er:

- En omfattende liste over kilder til usikkerhed der påvirker forudsigelse af ekstreme belastninger på en vindmølle.
- En stokastisk model af aerofoil aerodynamiske løft og drag koefficienter, efterfulgt af en kvantificering af effekten af aerodynamisk usikkerhed på den ekstreme belastning og optimering af last partialkoefficienter. En samlet vurdering af usikkerheder for de aerodynamiske statiske løft og drag koefficienter viste en mærkbar reduktion i last partialkoefficient for en vinge og generelt en større betydning på ekstreme belastninger under produktion af el i forhold til stand-still. Den stokastiske model kan også bruges som et redskab ved probabilistisk design og risiko reduktion i de tidlige faser af det aerodynamiske design for en vindmølle rotor.
- En grundig analyse af, hvordan forskellige konfigurationer af avancerede lastreduktions kontrol funktioner påvirker den strukturelle pålidelighed for en multi-megawatt vindmøllevinge og tårn når den ekstreme turbulens model er usikker. Nyskabelsen er i den tilhørende bestemmelse af optimale last partialkoefficienter ved hjælp af modeller for omkostninger og pålidelighed, turbine geometri, styresystem svigtrater og strukturel pålidelighed når der anvendes forskellige konfigurationer af avancerede last reduktions kontrolfunktioner. En central pointe er, at den samlede sandsynlighed for svigt af konstruktion-styresystem er domineret af den årlige svigtrate af styresystemet.
- En detaljeret implementering af flere analysemetoder til fusion af output fra flere aero-servo-elastisk simulatorer. Designere bruger i stigende grad flere kommercielle og forskningsbaserede aero-servo-elastiske simulatorer til at sammenligne de estimerede koblede dynamiske belastninger og respons af systemet. Formålet var således at anvende disse analysemetoder til at forudsige det mest sandsynlige respons og de tilsvarende model usikkerheder, når output fra forskellige multi-fidelity aero-servo-elastiske simulatorer er tilgængelige.



List Publications

Publications included in this thesis:

- Abdallah et al. [2015] Impact of uncertainty in airfoil characteristics on wind turbine extreme loads. / Abdallah, Imad; Natarajan, Anand; Sørensen, John Dalsgaard. Published In: *Renewable Energy*, Vol. 75, 2015, p. 283-300.
- Abdallah et al. [2015] Influence of the control system on wind turbine loads in power production in extreme turbulence: structural reliability. / Abdallah, Imad; Natarajan, Anand; Sørensen, John Dalsgaard. Submitted to: *Renewable Energy*, 2015.
- Abdallah et al. [2015] Influence of the control system on wind turbine loads in power production in extreme turbulence: Cost and reliability-based optimization of partial load factors. / Abdallah, Imad; Natarajan, Anand; Sørensen, John Dalsgaard. To be submitted to: *Renewable Energy*, 2015.
- Abdallah et al. [2015] Co-Kriging: fusing simulation results from multifidelity aero-servo-elastic simulators - Application to extreme loads on wind turbines. / Abdallah, Imad; Sudret, Bruno; Lataniotis, Christos; Sørensen, John Dalsgaard; Natarajan, Anand. Accepted for publication in: *ICASP12 - Proceedings of the 12th International Conference on Applications of Statistics and Probability in Civil Engineering*: Vancouver, Canada, July 12-15, 2015.

Publications not included in this thesis:

- Influence of the control system on wind turbine reliability in extreme turbulence. / Abdallah, Imad; Natarajan, Anand; Sørensen, J. D. Published In: *Journal of Physics: Conference Series (Online)*, Vol. 524, No. 1, 012069, 2014.
- Predicting extreme loads effects on wind turbines considering uncertainty in airfoil data. / Abdallah, Imad; Natarajan, Anand; Sørensen, John Dalsgaard. *Safety, Reliability, Risk and Life-Cycle Performance of Structures and Infrastructures -Proceedings of 11th International Conference on Structural Safety and Reliability*. Taylor & Francis, 2013. p. 215-222.



Acknowledgements

I would like to thank the Danish Ministry of Science, Innovation and Higher Education for their financial support of this industrial PhD. The work presented herein is also a part of the Danish Energy Technology Development and Demonstration (EUDP) project titled, “Demonstration of a basis for tall wind turbine design”, Project no 64011-0352. I appreciate their financial support.

I originally started this research at Vestas Wind Systems A/S and then WindNordic A/S. I would like to thank both companies for initiating and supporting this research.

I would like to acknowledge former Vestas colleagues and in particular Jakob Wedel-Heinen, John T. Olesen and Frank Ormel amongst others for taking part in the brain storming sessions to elucidate the sources of uncertainties affecting variations in the predicted wind turbine loads.

I would like to gratefully acknowledged the generous financial and technical support of MiTa-Teknik A/S and for providing the control systems for the FAST and BLADED aero-servo-elastic simulations. I would like to thank Lars Risager from MiTa Teknik for his thoughtful technical know-how and recommendations on the industrial side of this PhD research.

I would like to thank Dr. Henrik Stensgaard Toft from Aalborg University for sharing his thoughts and giving me feedback and input to some of the work herein presented.

I would like to use this opportunity to express my gratitude to Professor Dr. Brunot Sudret for giving me the opportunity to spend 5 months as a visiting PhD at the Chair of Risk, Safety and Uncertainty Quantification at ETH Zurich.

Last but not least I wish to express my sincere thanks and appreciation to my thesis supervisors Dr. Anand Natarajan and Professor Dr. John Dalsgaard Sørensen for their immense knowledge of the subject and their input, support and for continuously challenging my work.

Copenhagen, 30 April 2015

Imad.



Contents

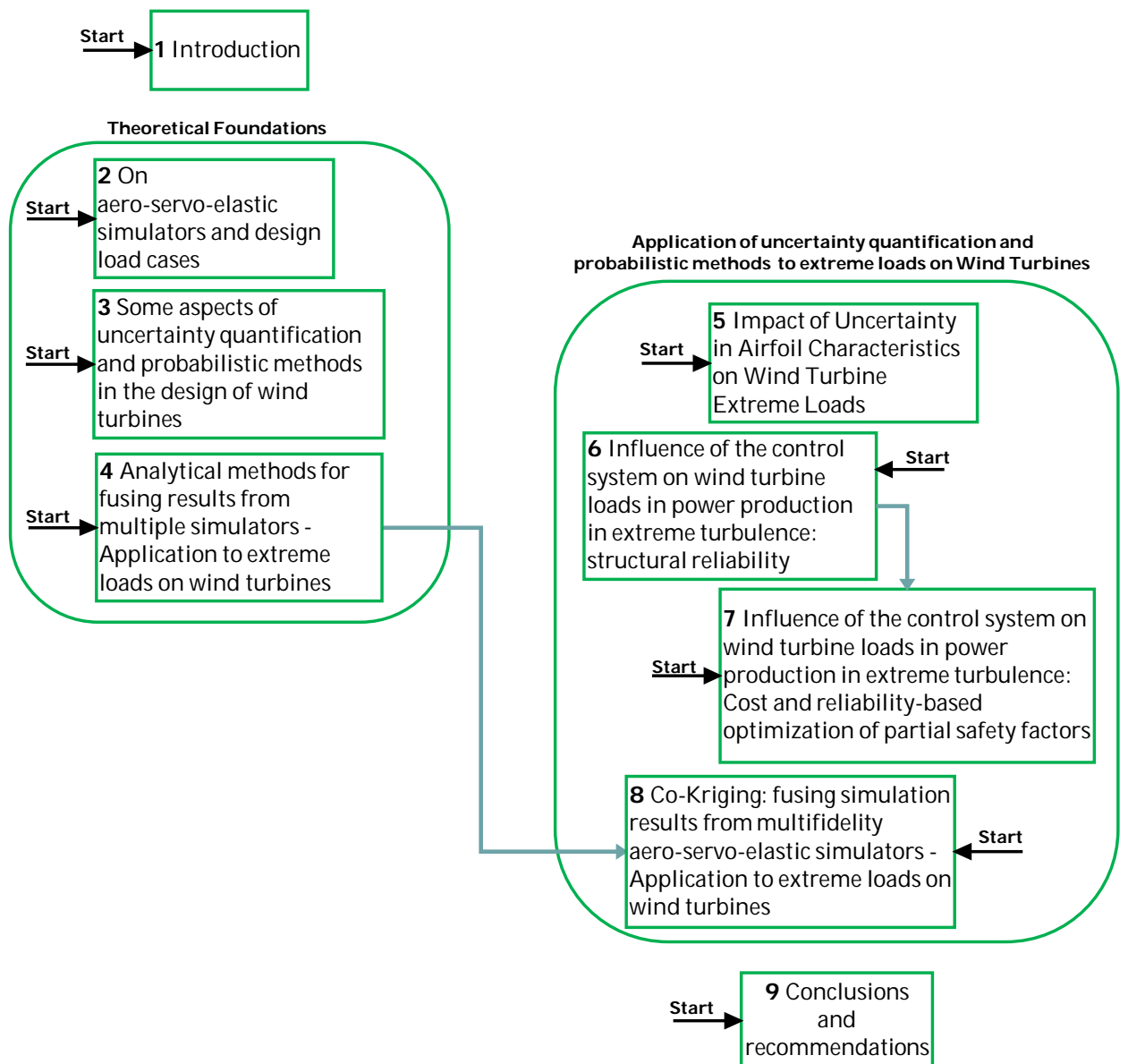
Summary	iii
Resumé	vii
Publications	ix
Acknowledgements	xi
Reading Path	xvii
1 Introduction	1
1.1 Relevance	1
1.2 Aims and motivations	2
1.3 Scope	5
1.4 Outline	5
2 Review: On aero-servo-elastic simulators and design load cases	7
2.1 Aero-servo-elastic simulators	7
2.2 Design load cases	8
3 Review: Some aspects of uncertainty quantification and probabilistic methods in the design of wind turbines	13
3.1 The uncertainty quantification framework	13
3.2 Methods for quantification of sources of uncertainty	14
3.2.1 Building probabilistic models of the inputs when data is available	15
3.2.2 Building probabilistic models of the inputs when limited or no data are available	15
3.3 Dependence structures amongst input random variables	18
3.3.1 Correlations: Pearson, Spearman and Kendall	18
3.3.2 Random vectors and joint distributions	18
3.3.3 Copulas	19
3.4 Sources of uncertainties in the prediction of a wind turbine's extreme loads	22
3.4.1 Types of uncertainties	22
3.4.2 Sources of uncertainties	23
3.5 Some structural reliability methods	30
3.5.1 The probability of failure	30
3.5.2 Simulation based methods: Monte Carlo	31
3.5.3 Optimization based method: The First Order Reliability Method	31

Contents

3.6	From uncertainty to safety factors	33
3.6.1	Cost and reliability-based optimization of safety factors	33
4	Review: Analytical methods for fusing results from multiple simulators - Application to extreme loads on wind turbines	37
4.1	Introduction	38
4.1.1	The current practice of comparing loads and response estimates from multiple aero-servo-elastic simulators	38
4.2	Model uncertainty in aero-servo-elastic simulators	39
4.2.1	Sources of model uncertainty	39
4.3	The case for data fusion	41
4.4	Analytical method 1: Co-Kriging	42
4.4.1	Problem setup	42
4.4.2	Kriging theory	42
4.4.3	Kriging for noisy data	44
4.4.4	Co-Kriging theory	44
4.4.5	Demonstration of Co-Kriging in UQLab	45
4.5	Analytical method 2: the multivariate normal aggregation approach	48
4.5.1	Theory of the the multivariate normal aggregation approach	48
4.5.2	Toy examples on the multivariate normal aggregation approach	49
4.6	Analytical method 3: Adjustment Factor Approach	51
4.6.1	Theory of the Adjustment Factor Approach	51
4.6.2	Demonstration of the Adjustment Factor Approach	53
4.7	Analytical method 4: copula models for aggregation of multi-model simulations	54
4.7.1	Theory of the Copula models for aggregation	54
4.7.2	Demonstration of the Copula Aggregation Method	55
4.8	Analytical method 5: Bayesian Model Averaging (BMA)	59
4.8.1	Theory of the Bayesian model averaging (BMA)	59
4.8.2	Demonstration of the Bayesian Model Averaging	63
5	Publication: Impact of Uncertainty in Airfoil Characteristics on Wind Turbine Extreme Loads	65
6	Publication: Influence of the control system on wind turbine loads in power production in extreme turbulence: structural reliability	85
7	Publication: Influence of the control system on wind turbine loads in power production in extreme turbulence: Cost and reliability-based optimization of partial safety factors	111
8	Publication: Co-Kriging: fusing simulation results from multifidelity aero-servo-elastic simulators - Application to extreme loads on wind turbines	127
9	Conclusions and Recommendations	137
9.1	Uncertainty in aerodynamic lift and drag	137
9.2	Effect of advanced load alleviation control features on structural reliability . . .	138
9.3	Fusing the output of multi-fidelity aero-servo-elastic simulators	139

9.4 Recommendations for further research	139
A Appendix - Iso-probabilistic transformations for FORM	141
B Truncating probability density functions	147
C FORM iterative scheme	149
D A simple example of load and resistance uncertainty	151
E Background of the partial load factors in the IEC61400-1 ed. 3 design standard	155
Bibliography	166
Curriculum Vitae	167

Reading path



1 Introduction

1.1 Relevance

Technical perspective The size of wind turbines is reaching dimensions which are starting to test the limits of the aero-servo-elastic simulators. Wind farms are reaching utility scale size, wind turbines are being installed in large clusters and in a variety of locations (offshore, onshore, flat terrain, near shore, complex terrain, forests, mountains, etc.) resulting in large variations of climates and inflow conditions experienced by wind turbines. Furthermore, advanced load alleviation control features are being deployed on modern large wind turbines resulting in significant load reductions. All the above makes it difficult to establish and abide by a relevant deterministic standard for the design of wind turbines. In order to improve the competitiveness of wind energy, researchers and industrialists shall systematically quantify each and every source of uncertainty in the design of wind turbines and assess its impact. Equation 1.1 depicts the ultimate load L_{ULT} and the various uncertainties associated with the prediction of L_{ULT} :

$$LOAD = L_{ULT} X_{dyn} X_{st} X_{ext} X_{sim} X_{exp} X_{aero} X_{str} \quad (1.1)$$

The uncertainties (stochastic) variables are defined as multiplicative factors to L_{ULT} to take into account the model and statistical sources of uncertainties. X_{dyn} accounts for model uncertainty due to the modelling of the wind turbine dynamic response. X_{st} accounts for the statistical uncertainty of wind climate assessment. X_{ext} is associated with the uncertainty in the extrapolated load model. X_{sim} accounts for statistical uncertainties caused by the limited number of loads simulations. X_{exp} accounts for the model uncertainties related to modelling the terrain and roughness. X_{aero} accounts for the model uncertainties related to the assessment of aerodynamic

Chapter 1. Introduction

lift and drag coefficients. Finally the uncertainties related to the computation of the stresses on components from the loads are considered through X_{str} .

Economic perspective Offshore wind energy has just started to become competitive against various sources of energy. The offshore wind market, however, relies heavily on massive governmental subsidies of various sorts. Several tracks for reducing the cost of wind energy have been suggested [Schwabe, P., Lensink, S., Hand, 2011] such as enhanced O&M strategies through condition monitoring, increased manufacturing efficiency through higher production volumes and increased automation, improved resource assessment through turbine-mounted real-time site assessment technologies, improved components reliability by increased laboratory testing, increased number of prototype test turbines before serial production is launched, larger rotor and tower concepts for both onshore and offshore installations, advanced drive train designs, advanced load alleviation control systems, extensive industrialization and modularization of components, cost-out programs, increased components redundancies where possible, etc [Schwabe, P., Lensink, S., Hand, 2011].

This thesis takes a stab at reducing the levelized cost of energy from a slightly different perspective; by assessing and quantifying specific uncertainties in the aero-servo-elastic simulations and prediction of extreme loads. Uncertainty quantification is a largely ignored field in the context of reducing the levelized cost of energy of wind turbines. Why uncertainties matter? as of today, the single largest cost component for offshore wind farms is still the wind turbine, accounting for 30% – 40% of the total capital cost [IRENA, 2012]. So, any savings due to uncertainty analyses in the turbine design translate, possibly, into not so insignificant capital cost savings.

1.2 Aims and motivations

The idea of using uncertainty quantification approaches and probabilistic methods in the design and analysis of aero-elastic predictions of wind turbine loads is nothing new. The approaches, however, have always been generalistic, the conclusions generally wide, and the rationale behind how the sources of uncertainty are modelled has always been ambiguous. What is different here? we take a deep dive into very specific sources of uncertainty and assess their impact on the extreme loads. All analysis are done on multi-megawatt wind turbines with industrial grade control systems. There are an extensive number of uncertainties, three of which have been chosen in this thesis:

Uncertainty in aerodynamic lift and drag: The aim is to quantify the uncertainty in airfoil static lift and drag coefficients based on field and wind tunnel data, aero-servoelastic calculations and engineering judgement. Subsequently assess the effect of the uncertainty in airfoil static lift and drag coefficients on the prediction of extreme loads, structural reliability and optimization of the load partial safety factor of large wind turbines. *Motivation:* *Various studies have tackled several aspects of airfoil aerodynamic uncertainty. Results are presented in the form of examples usually too theoretical in nature with limited applicability in a wind turbine design practice. In this thesis we establish a stochastic model for the static lift and drag coefficients by tapping into a wealth of publicly available aerodynamic tests, measurements and simulations on various aspects*

of aerodynamic uncertainties. The motivation for this research is based on the following scenario: when an airfoil section is placed in four different wind tunnels, the result is four different lift coefficient curves as a function of angle of attack. In a deterministic context, a wind turbine blade designer will have to choose one of the lift curves (or a blend of said lift curves) and base his/her blade design on that choice (see Figures 1.1a and 1.1b).

Research questions

What are the sources of uncertainties that contribute to the variation in the static lift and drag coefficients of an airfoil section? and what is the effect of this uncertainty on structural reliability and the load partial safety factor in extreme operating conditions?

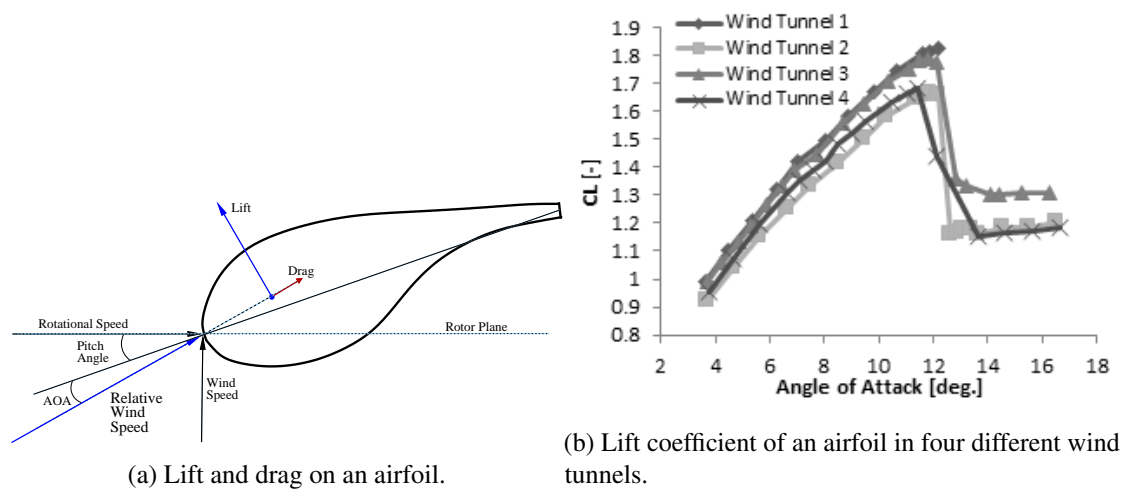


Figure 1.1: Large variation in the lift coefficient when the same airfoil section is measured in four different wind tunnels.

Effect of advanced load alleviation control features on structural reliability: The aim is to show that despite large uncertainty in the inflow and turbulence models, advanced load alleviation control systems yield both a reduction in magnitude and scatter of the extreme load which in turn translates in a change in the shape of the annual maximum load distribution function resulting in improved structural reliability. This is followed by a cost and reliability-based optimization of the load partial safety factor for a large multi-megawatt wind turbine in power production in extreme turbulence when various configurations of advanced load alleviation control features of varying performance are used. **Motivation:** *Sophisticated load alleviation control systems are increasingly being designed, implemented and deployed on large wind turbines to specifically reduce the adverse effects of extreme load events resulting in a lighter structural design. The load alleviation control features, which are an integral part of the design of large wind turbines, not only affect the magnitude of the extreme load level but also the scatter and the shape of the probability distribution function of the extreme loads (see Figures 1.2a and 1.2b). Consequently, it is not clear how the control features affect the overall structural reliability and safety factors in the presence of uncertainty in the extreme inflow such as turbulence. It is also not clear how the failure rate of the control features affects the overall structural reliability of the wind turbine.*

Research questions

How does the structural reliability of the wind turbine change if the extreme turbulence model is uncertain? In the presence of such uncertainty how does the structural reliability change with/without advanced load alleviation control features or various load alleviation control strategies? Can wind turbine designers leverage the load limiting effects of the advanced load alleviation control features to optimize the load partial safety factor (and how)?

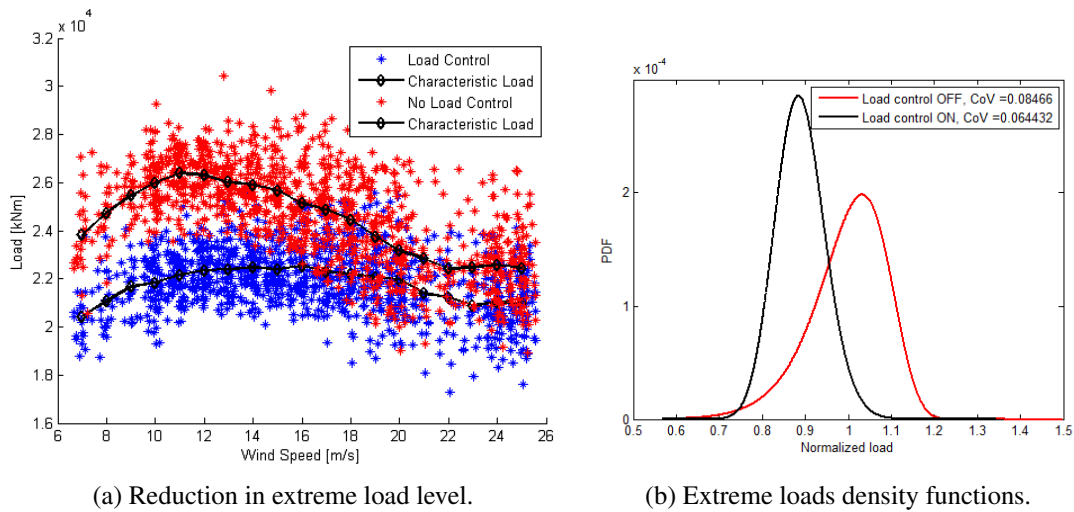


Figure 1.2: When turned on, advanced load alleviation control features not only reduce the extreme load level but also modify the extreme load distribution and its tail.

Fusing the output of multi-fidelity aero-servo-elastic simulators: The aim is to fuse the extreme response from multiple aero-servo-elastic simulators of various fidelity and complexity to predict "the most likely" extreme response of a wind turbine. **Motivation:** Analysts and designers increasingly use multiple commercial and research-based aero-servo-elastic simulators to compare the prediction of wind turbines' structural response. The aero-servo-elastic simulators are of varying fidelity and have different underlying assumptions. As a result, the aeroservo-elastic response may vary amongst simulators even if the external inflow condition is the same. The sub-models with the largest impact on the aero-servo-elastic response variability are aerodynamic, structural, control systems and wind inflow. The aero-servo-elastic simulators are validated using test measurements from prototype wind turbines. The current practice is to cover the discrepancy amongst the simulators by imposing safety factors resulting in a safe design. It is reasonable to assume that model uncertainty is of the epistemic type and can be estimated at the design stage with (usually) decreasing uncertainty when more simulations from multiple sources are available. As a result of model uncertainty, discrepancy amongst models predictions can easily be up to 20%. The current practice is to select the peak response from one particular simulator and impose a "large enough" safety factor resulting in a "safe" and "conservative" design peak response (see Figure 1.3). This practice, however, may prove to be overly conservative.

Research questions

Does it make any sense to fuse the output from various multi-fidelity aero-servo-elastic simulators \mathcal{M}_i ? What analytical methods can be used to predict the most likely response when output from various multifidelity aero-servo-elastic simulators are available? What is the uncertainty associated with the aggregated (fused) response?

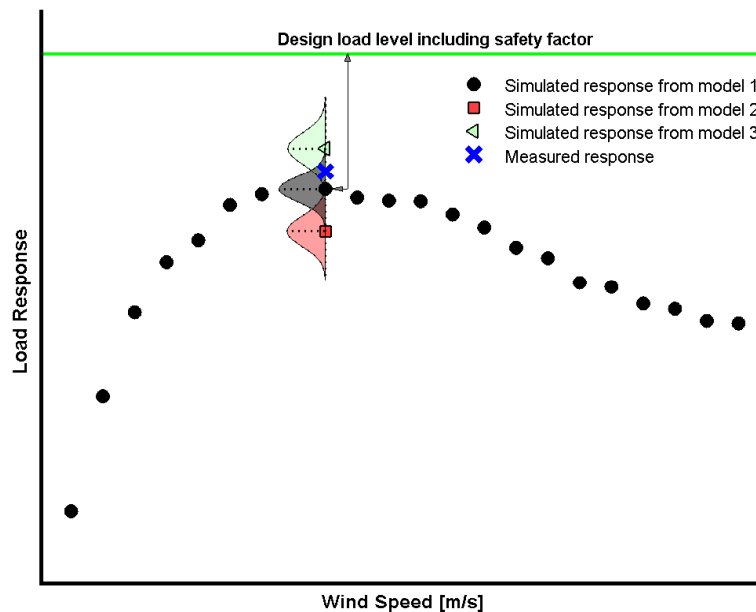


Figure 1.3: Peak load response and their corresponding variations from three different simulation models. The measured response is also shown.

1.3 Scope

- This work focuses on extreme loads only.
- Only variable speed pitch controlled wind turbines are considered.
- Only large multi-megawatt wind turbines are considered. Two turbines are used; in one instance a large commercial multi-megawatt offshore wind turbine is considered with nominal power $> 5MW$ and rotor diameter $> 130m$. In other cases the turbine considered has a nominal power $2MW$ and $110m$ in rotor diameter.
- Industrial grade control systems with various load alleviation features are used.
- In order to keep the loads evaluations simple, DLC1.1NTM (power production in normal turbulence model) and DLC1.3ETM (power production in extreme turbulence model) are used to evaluate the aero-servo-elastic extreme loads simulations.
- The optimization of the safety factors is solely limited to the load partial safety factor.

1.4 Outline

In chapter 2 we give an overview of the concept of aero-servo-elastic simulations and a definition of loads and design load cases.

Chapter 1. Introduction

In Chapter 3 we present an overview of the sources of uncertainty affecting the prediction of the extreme loads on a wind turbine. We discuss some probabilistic methods most commonly used in structural reliability. Then we detail the steps necessary to derive a cost and reliability-based safety factors and we illustrate that with a simple example. We finish Chapter 3 by describing how the safety factors in the IEC61400-1 ed.3 design standard are derived. We get an outlook of possible developments in future editions of the IEC61400-1 design standard. Chapter 3 can be considered as the theoretical supporting material for the research done in the subsequent publications.

In Chapter 4 we review 5 analytical methods for fusing (aggregating) the output from multi-fidelity simulators with application to extreme loads on wind turbines. Chapter 4 should be consider as a theoretical foundation for the understanding of the research in Chapter 8.

In Chapter 5 we look at the impact of uncertainty in aerofoil lift and drag on wind turbine extreme loads, structural reliability and load partial safety factors. We derive a stochastic model for the static lift and drag coefficients by tapping into publicly available aerodynamic tests, measurements and simulations on various aspects of aerodynamic uncertainties.

In Chapter 6 we look at the influence of various configurations of load alleviation control features on a wind turbine structural reliability in power production when the extreme turbulence model is uncertain. In Chapter 7 we expand on the previous chapter's work to optimize the load partial safety factor and other structural, control and reliability metrics when various configurations of load alleviation control features are used.

In Chapter 8 we present and demonstrate the co-Kriging technique to predict the extreme response in the presence of non-stationary noise in the output (i.e. the magnitude of noise varies as a function of the input variables) in the case when the low and high-fidelity aero-servo-elastic simulators of the same wind turbine are implemented by two independent engineers (i.e. human error and uncertainty in the modelling and input assumptions are implicitly included).

Final conclusions and recommendations are found in Chapter 9.

2 Review: On aero-servo-elastic simulators and design load cases

The first aim in this chapter is to give a brief description of the concept of aero-servo-elastic loads in the context of wind turbines design. The second aim is to introduce some of the design load cases which are used as input to the aero-servo-elastic simulators. Both topics are discussed at length in the IEC61400-1 ed.3 design standard , [Hansen, 2000], [DNV/Risø, 2002], [Hau and von Renouard, 2005], and [Manwell et al., 2010].

2.1 Aero-servo-elastic simulators

The design of a modern wind turbine involves solving the differential equation of motion

$$\mathbf{M}\ddot{\mathbf{y}} + \mathbf{D}\dot{\mathbf{y}} + \mathbf{K}\mathbf{y} = \mathbf{F}_{ext} \quad (2.1)$$

by means of a computer simulator based on an aero-servo-elastic calculation procedure. Aero-servo-elastic is a term that refers to the coupling of aerodynamics, structural dynamics and controls under the stochastic external forcing of the turbulent wind field including wakes in the time domain [Rasmussen et al., 2003]. For offshore wind turbines, additional external hydrodynamic forcing is included to model the effects of waves, currents and ice on the support structure and tower (aero-hydro-servo-elastic). The main modules of an aero-hydro-servo-elastic simulator are shown in Fig. 2.1 and an illustration is made in Fig. 2.2. The computational models are categorized into modules representing external conditions, modules representing the loads and modules representing the wind turbine structure and controls. An example of time series output of an aero-servo-elastic simulation is shown in Fig. 2.3.

A list of industry and research based aero-servo-elastic simulators includes FLEX5, FAST, HAWC2, Bladed, Cp-Lambda, BHawC. On most (if not all) simulators, the aerodynamics are generally assumed to be based on the Blade Element Momentum method (modified, corrected and calibrated with engineering models). The structural dynamic methods found in these simulators can be generally classified into three approaches: multibody dynamics, finite element methods, and the assumed-modes approach. Most of these codes, however, are being modified to accommodate large and flexible wind turbines in order to include the torsional degrees of freedom, aeroelastic stability, large blade deflections, prediction of aerodynamic modal damping, inclusion of 3D computational aerodynamics and fluid dynamics, wake effects, floating offshore installations, hydrodynamics, etc.

2.2 Design load cases

Wind turbines are designed to operate and produce power for a period of upto 30 years. Over its lifetime a wind turbine is subjected to various operating conditions and failure modes. As a result, a wind turbine must be analysed for all possible design load cases. Load cases are constructed by combining wind turbine operating conditions (or failure modes) with external conditions.

A wind turbine operating conditions and operating modes can be generally grouped into the following categories:

- Normal operation and power production
- Start (cut-in) and stop (cut-out)
- Idling and stand-still
- Transportation
- Installation and assembly
- Testing and commissioning
- Maintenance and repair
- Faults such as control faults, sensor faults or grid faults
- Large yaw error during power production or stand-still or idling or start/stop

The external conditions could include (but not constrained to):

- Normal wind profile and normal turbulence
- Extreme wind profile (i.e. extreme shear)
- Extreme turbulence
- Coherent gust and direction change
- Extreme operating gust
- Extreme wind

Indeed, a designer can choose to combine any operating condition, failure mode and external condition and analyse the ensuing loads, their effect on the structural integrity and stability of a wind turbine. However, a designer shall always keep in mind the return period of the combined events; one can always find a design load case which will result in the failure of a wind turbine. Constructing such a wind turbine, however, would be very expensive.

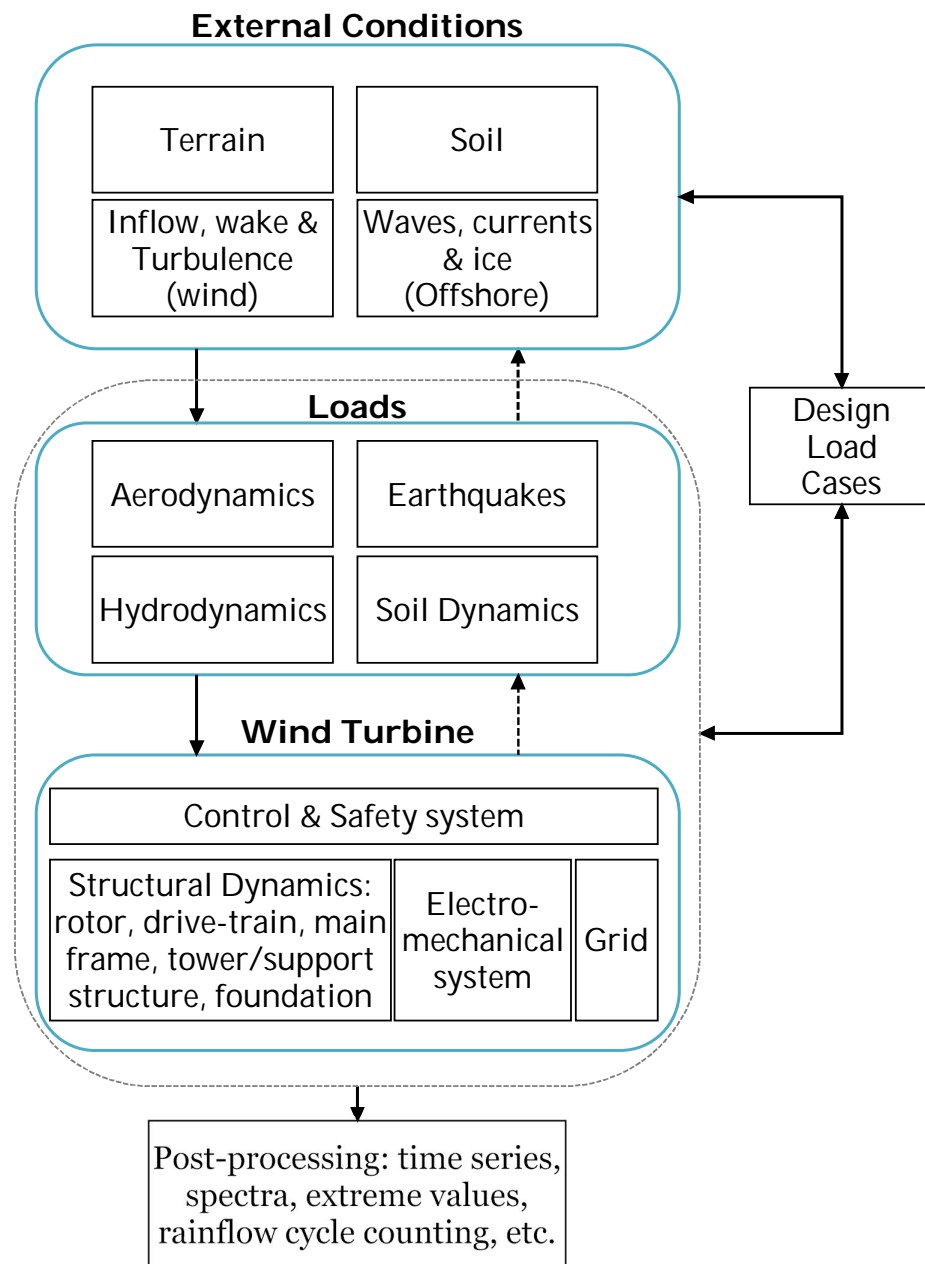


Figure 2.1: The major modules of a wind turbine aero-servo-elastic simulator.

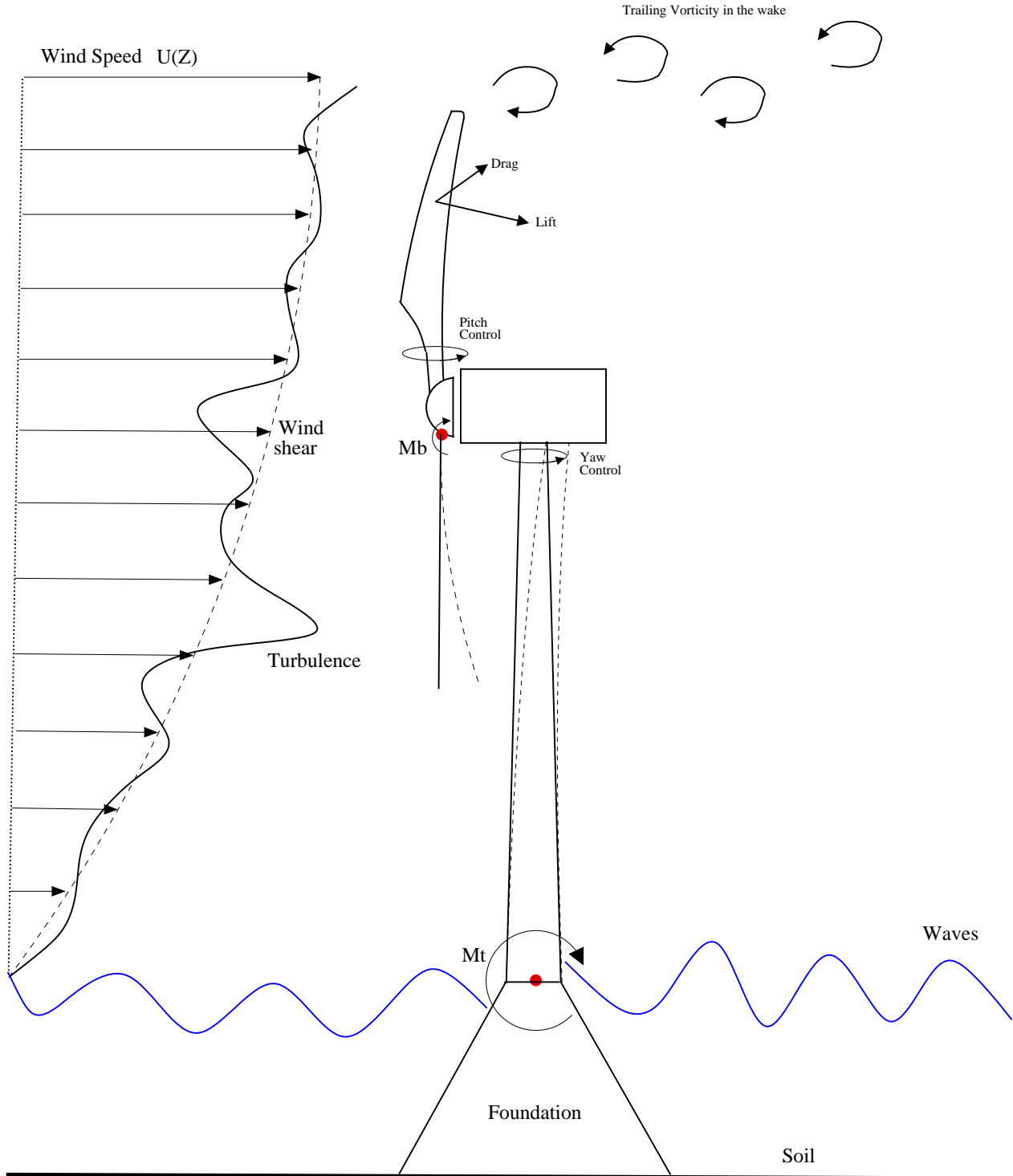


Figure 2.2: A wind turbine. M_b is the flapwise bending moment at the blade root. $U(Z)$ is the mean wind speed at height Z . Vertical wind shear (dotted grey line) and turbulence (thick black line).

2.2. Design load cases

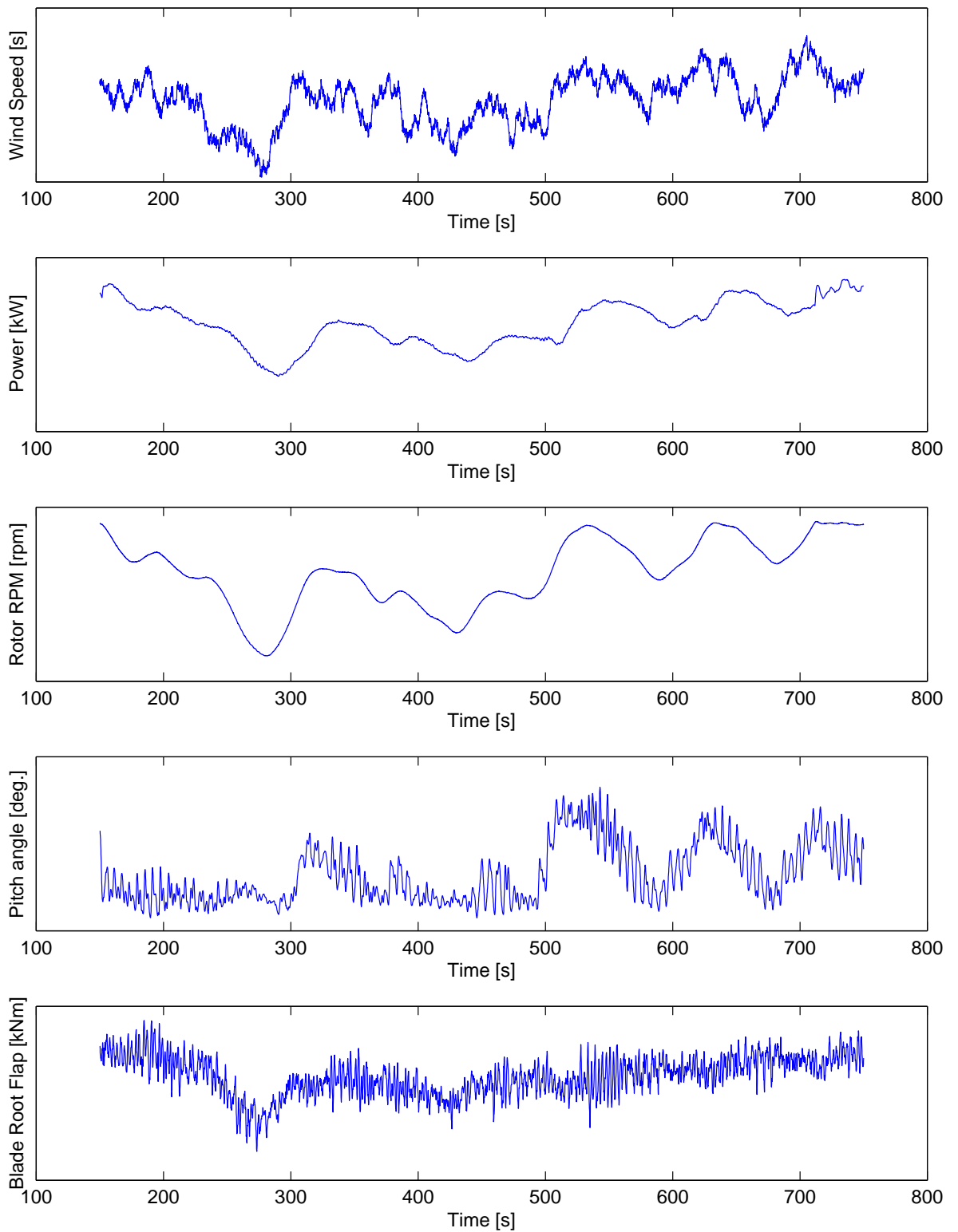


Figure 2.3: An example of time series output of an aero-servo-elastic simulation in FAST.

3 *Review:* Some aspects of uncertainty quantification and probabilistic methods in the design of wind turbines

The first aim in this chapter is to propose a list containing the sources of uncertainties related to variations in the prediction of extreme design loads. The second aim is to expose the reader to multiple probabilistic methods (far from exhaustive) that could be employed in the design of wind turbines. Where necessary illustrative examples are provided. The probabilistic methods described herein are invariably used at various stages of this research. Finally we treat a small example showing how to optimize safety factors given reduced uncertainties.

3.1 The uncertainty quantification framework

Three essential parts that are required in order to quantify uncertainties and assess their impact are:

- A computational model or meta-model that describes the physics of the problem and computes some quantities of interest.
- Sources of uncertainty in the inputs and parameters with possible time- and/or space variability, and their dependence structure.
- The output (quantity of interest) can be described by statistical quantities such as mean, standard deviation, distribution, quantiles and probability of failure.

A generalized framework for uncertainty quantification can thus be represented as in Fig. 3.1 [Sudret, 2007b]:

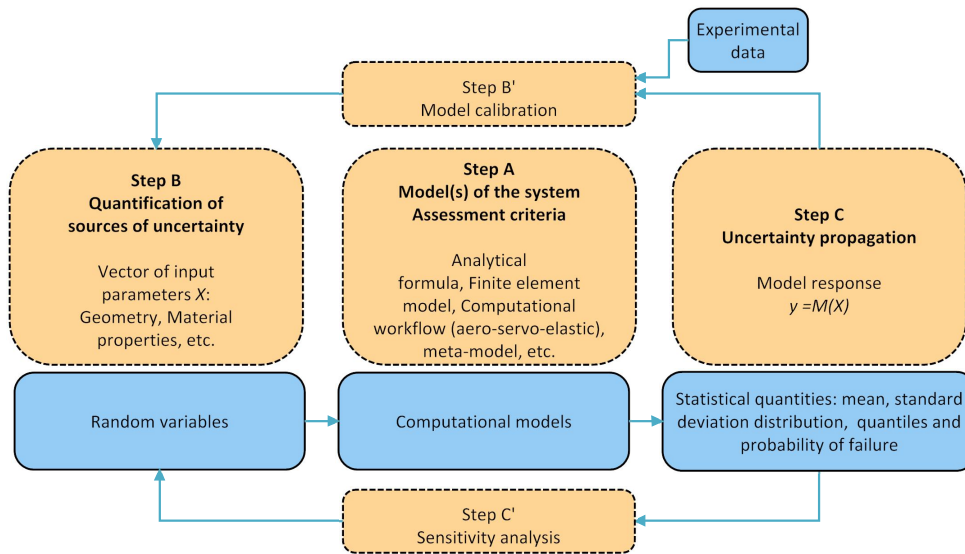


Figure 3.1: A generalized framework for uncertainty quantification [Sudret, 2007b].

Step A consists in defining the computational model \mathcal{M} of the physical system; in the context of design and simulations of wind turbines the computational model could be the so-called aero-servo-elastic model coupling the aerodynamic to the elastic response of the wind turbine under the influence of a control system. Furthermore, the computational model could be a finite element of a blade or a multi-body dynamics model of a gearbox.

Step B consists in defining the inputs \mathbf{X} in a probabilistic context and identifying any dependency structure amongst the inputs. It could be that the inputs display possible time- and/or space variability which then requires the introduction of random fields and random processes.

Step C consists in propagating the uncertain inputs (random vector \mathbf{X}) through the computational model \mathcal{M} and characterizing the probabilistic content of the random response $\mathbf{Y} = \mathcal{M}(\mathbf{X})$. The probabilistic content can be described through second moment methods or maximum likelihood to infer parameters of the underlying distribution of the response such as the mean and variance, through Monte Carlo method or structural reliability methods (FORM/SORM [Ditlevsen and Madsen, 2007]) to compute the probability of failure, and through Monte Carlo or spectral methods to describe the full probability density function of the response [Sudret, 2007b].

3.2 Methods for quantification of sources of uncertainty

In the context of uncertainty quantification and probabilistic engineering, one might devise accurate and precise computational models and simulators of physical systems/events (aero-servo-elastic simulator of a wind turbine, or a finite element model of a blade or a meta-model of some response, etc.), but if the probabilistic model of the uncertain inputs are not properly specified then the probabilistic assessment of those uncertain inputs on the system response will be flawed and any conclusions based on such analysis will be erroneous. There are two cases which can be envisaged; (1) building probabilistic models of the inputs when data is available and (2) building probabilistic models of the inputs when very limited or no data is available. When large amount of data is available, the tools of statistical inference may be used in order to setup a probabilistic

model of the inputs, but when limited amount of data are available one can resort to Bayesian inference. Alternatively, gathering data about a variable may prove difficult and/or expensive and/or impossible.

3.2.1 Building probabilistic models of the inputs when data is available

Given a unidimensional data set of input parameter $\mathcal{X} = \{x_1, x_2, \dots, x_n\}$ which is a set of independent random realizations of random variable $X \sim f_X(x; \boldsymbol{\theta})$, where f_X is a density function with hyperparameters $\boldsymbol{\theta}$. The first step is to look at descriptive statistics such as the *ordered set* $x_1 \leq x_2 \dots \leq x_n$, *range*, *median*, *sample mean*, *variance*, *coefficient of variation*, *skewness and kurtosis*, *quantiles*, *rank*, *box plots*, *scatter plots*, *histograms*, and *empirical CDF*. The second step is to look at statistical inference, i.e. infer the marginal distribution $f_X(x; \boldsymbol{\theta})$ of random variable X . The hyperparameters of parametric distributions can be estimated from a sample set of observations $\mathcal{X} = \{x_1, x_2, \dots, x_n\}$ using the method of moments or the maximum likelihood estimation. In the context of extreme loads on wind turbines, parametric distributions of interest could include Lognormal, Weibul (2 and 3 parameters), and Gumbel. Alternatively a non-parametric distribution can be fitted such a kernel density estimation. The third step is to look at goodness-of-fit criteria when several density functions are possible candidates to fit a sample set of observations $\mathcal{X} = \{x_1, x_2, \dots, x_n\}$. One can employ the Akaike Information Criterion [Akaike, 1974], the Bayesian Information Criterion [Raftery, 1995], the Kullback-Leibler index, the Kolmogorov-Smirnov test or the Chi-squared test to test for goodness of fit of the density functions [Noh et al., 2009, Evren and Tuna, 2012]. One can also visualize the goodness-of-fit qualitatively through QQ-plots for instance. In case where the available sample set of observations $\mathcal{X} = \{x_1, x_2, \dots, x_n\}$ is small/limited, we can use a Bayesian inference approach where a prior distribution $f'_{\Theta}(\boldsymbol{\theta})$ is assigned to the vector of hyperparameters. The Bayes theorem states that a posterior distribution $f''_{\Theta}(\boldsymbol{\theta})$ of hyperparameters Θ can be defined as:

$$f''_{\Theta}(\boldsymbol{\theta}) = \frac{f'_{\Theta}(\boldsymbol{\theta}) \mathbf{L}(\boldsymbol{\theta} | x_1, x_2, \dots, x_n)}{\int_{\mathcal{D}_{\Theta}} f'_{\Theta}(\boldsymbol{\theta}) \mathbf{L}(\boldsymbol{\theta} | x_1, x_2, \dots, x_n) d\boldsymbol{\theta}} \quad (3.1)$$

where \mathbf{L} is the likelihood function. The predictive distribution of random variable X becomes:

$$f''_X(x) = \int_{\mathcal{D}_{\Theta}} f_X(x | \boldsymbol{\theta}) f''_{\Theta}(\boldsymbol{\theta}) d\boldsymbol{\theta} \quad (3.2)$$

3.2.2 Building probabilistic models of the inputs when limited or no data are available

When very limited or no data are available to characterize the inputs, one may resort to expert judgement based on general knowledge on similar inputs or expert knowledge on bounds and most probable values (such as mode or mean). Furthermore, we can find recommendations for probabilistic models in the literature or through recommendations of committees such as the Joint Committee on Structural Safety (JCSS). Alternatively we can use the principle of maximum entropy. Some literature related to the practical application of the principle of maximum entropy can be found here: von Collani et al. [2008], Ahooyi et al. [2014], Li et al. [2012], Carta et al. [2009], Akpinar and Akpinar [2007], Ramirez and Carta [2006], Win [2015]. The principle of maximum entropy, stated most briefly: "when we make inference on random variables based on

Chapter 3. Review: Some aspects of uncertainty quantification and probabilistic methods in the design of wind turbines

incomplete information (data), we should draw them from that probability distribution that has the maximum entropy permitted by the information we have" [Jaynes, 1982]. The principle states that the most unbiased estimate of a probability distribution is that which maximizes the entropy subject to constraints supplied by the available information, e.g., moments of a random variable. The maximum entropy method of estimating $f_X(x)$ is expressed as [Pandey and Ariaratnam, 1996]:

$$\begin{aligned} & \text{maximize} \quad H[f_X] \stackrel{\text{def}}{=} - \int_R f_X(x) \ln(f_X(x)) dx \\ & \text{subject to} \quad \int_R f_X(x) dx = 1 \\ & \quad \int_R g^{(i)}(X) f_X(x) dx = \mu_X^{(i)} \end{aligned} \quad (3.3)$$

where H is the entropy of density function f_X , $\mu_X^{(i)}$ is the i^{th} moment of the random variable X and $g^{(i)}(X) = (X - \mu_x)^i$. The first constraint simply sums the probabilities to 1, and the second constraint sets a value for a higher order moment of the distribution. Hence, the predicted $f_X(x)$ should have the highest level of uncertainty amongst all possible density functions satisfying the constraints. In other words, this method does not impose any prior assumptions beyond the available constraints and as a result the selected $f_X(x)$ has the minimum bias possible. Constraints could be the mean value of the random variable; for instance, following one wind tunnel test the measured value of the lift coefficient C_L of the clean aerofoil section can be set to the expected value of the distribution describing the variations of the lift coefficients under various operating conditions. One classical way to solve the optimization problem in Equation 3.3 is by introducing Lagrange multipliers such as:

$$L(f, \lambda_j) = \int_R f_X(x) \ln(f_X(x)) dx + \sum_{i=0}^m \lambda_i \left(\int_R g^{(i)}(X) f_X(x) dx - \mu_X^{(i)} \right) \quad (3.4)$$

where λ_i are the Lagrange multipliers. The problem is thus transformed to find the extrema of the function $L(f, \lambda_j)$:

$$\begin{aligned} \frac{\partial L}{\partial f} &= 0 \\ &= \int_R \left[\ln(f_X(x)) + 1 + \sum_{i=0}^m \lambda_i g^{(i)}(X) \right] dx \end{aligned} \quad (3.5)$$

therefore,

$$\ln(f_X(x)) + 1 + \sum_{i=0}^m \lambda_i g^{(i)}(X) = 0 \quad (3.6)$$

which leads to the closed form solution for $f_X(x)$:

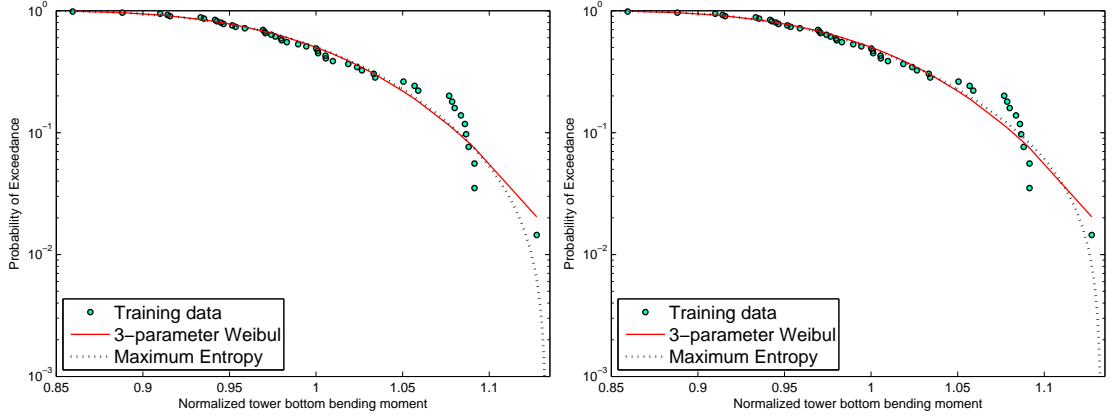
$$f_X(x) = \exp \left[-1 - \lambda_0 - \sum_{i=1}^m \lambda_i g^{(i)}(X) \right] \quad (3.7)$$

3.2. Methods for quantification of sources of uncertainty

The coefficients λ_i are then determined as solutions of the system of equations with respect to the constraints:

$$G(\lambda) = \int_R g^{(i)}(X) \exp \left[-1 - \lambda_0 - \sum_{i=1}^m \lambda_i g^{(i)}(X) \right] dx = \mu_X^{(i)} \quad (3.8)$$

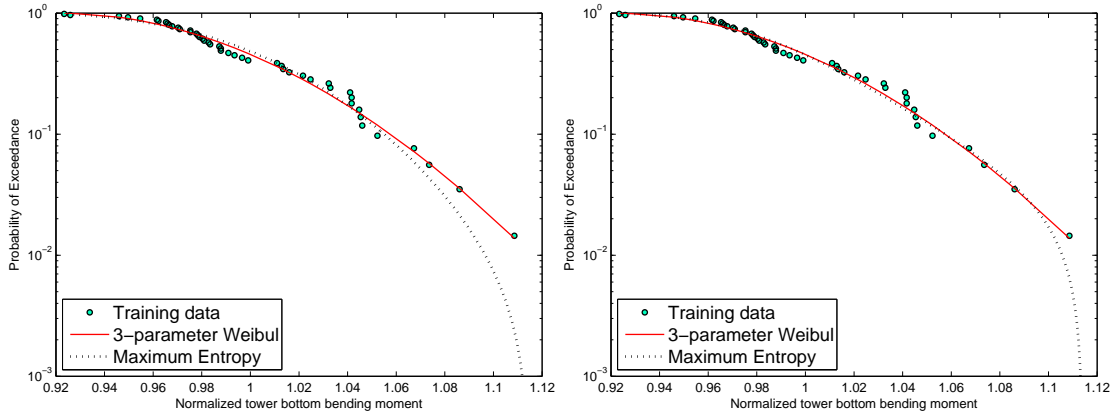
An application of the maximum entropy distribution of the extreme tower bottom bending moment is shown in Fig. 3.2 and 3.3. In Fig. 3.2 the extreme tower bottom bending moments are simulated in aero-servo-elastic simulator FAST using 48 seeds with mean wind speed of $4m/s$ and the turbulence standard deviation equals to $1m/s$. In Fig. 3.3 the extreme tower bottom bending moments are simulated in aero-servo-elastic simulator FAST using 48 seeds with mean wind speed of $10m/s$ and the turbulence standard deviation equals to $3m/s$. The loads are first fitted to a 3-parameter Weibull distribution and then compared to the maximum entropy distribution with only the first 2 moments and the first 3 moments. The moments of the 3-parameter Weibull distribution are derived using the maximum likelihood method.



(a) Max entropy distribution with 2 moments.

(b) Max entropy distribution with 3 moments.

Figure 3.2: The extreme tower bottom bending moments are simulated in aero-servo-elastic simulator FAST using 48 seeds with mean wind speed of $4m/s$ and the turbulence $1m/s$.



(a) Max entropy distribution with 2 moments.

(b) Max entropy distribution with 3 moments.

Figure 3.3: The extreme tower bottom bending moments are simulated in aero-servo-elastic simulator FAST using 48 seeds with mean wind speed of $10m/s$ and the turbulence $3m/s$.

Such an approach is of relevance when considering the stochastic model of lift and drag coefficients (Chapter 5) and in deriving the loads annual maximum distributions through probabilistic loads extrapolations (Chapters 6 and 7).

3.3 Dependence structures amongst input random variables

Once the marginal probabilistic models of the random variables have been defined as described above, we turn our attention to the dependence structure and correlations amongst the random variables. Correlations and dependence structures are of relevance when considering the parameters of the stochastic model of lift and drag coefficients (Chapter 5) and in the topic of fusing the output from multiple aero-servo-elastic simulators as discussed in Chapter 4 (i.e. how to describe the correlation amongst the output from multiple aero-servo-elastic simulators?).

3.3.1 Correlations: Pearson, Spearman and Kendall

The correlation between a two dimensional sample set $\mathcal{Z} = \{(x_i, y_i), i = 1, \dots, n\}$ can be expressed through the sample Pearson correlation coefficient as:

$$\begin{aligned} \rho_P &= \frac{\sum_{i=1}^n (x_i - \bar{x})(y_i - \bar{y})}{\sqrt{\sum_{i=1}^n (x_i - \bar{x})^2} \sqrt{\sum_{i=1}^n (y_i - \bar{y})^2}} \\ &= \frac{1}{n-1} \frac{\sum_{i=1}^n (x_i - \bar{x})(y_i - \bar{y})}{\sigma_x \sigma_y} \end{aligned} \quad (3.9)$$

The Pearson correlation coefficient characterizes the linear dependence between two random variables. On the other hand, the Spearman rank correlation coefficient describes the dependence between two variables through a monotonic function which is not necessarily linear. Given a sample set $\mathcal{X} = \{x_1, x_2, \dots, x_n\}$ the rank $r_{\mathcal{X}}$ of each point is defined as the ordinal number of that point in the ordered sample set (i.e. if $\mathcal{X} = \{10, 3, 2, 45, 21, 30\}$ then the rank $r_{\mathcal{X}} = \{3, 2, 1, 6, 4, 5\}$). The Spearman correlation coefficient can be practically computed as [Lebrun and Dutfoy, 2009a]

$$\rho_S = 1 - \frac{6 \sum_{i=1}^n (r_{\mathcal{X},i} - r_{\mathcal{Y},i})^2}{n^2 - 1} \quad (3.10)$$

Another approach is to use the Kendall τ rank correlation coefficient. Consider a two dimensional sample set $\mathcal{Z} = \{(x_i, y_i), i = 1, \dots, n\}$ and pairs $\{(x_i, y_i), (x_j, y_j)\}, 0 \leq i, j \leq 1\}$. A pair is concordant if $x_i < x_j$ **and** $y_i < y_j$ (resp. $x_i > x_j$ **and** $y_i > y_j$). The number of concordant pairs is assigned N_c . A pair is discordant if $x_i < x_j$ **and** $y_i > y_j$ (resp. $x_i > x_j$ **and** $y_i < y_j$). The number of discordant pairs is assigned N_d . The the Kendall τ coefficient is then given by:

$$\tau = \frac{N_c - N_d}{n(n-1)/2} \quad (3.11)$$

3.3.2 Random vectors and joint distributions

For multi-dimensional data sets of size n and dimension d , the dependence can be represented by a sample correlation matrix (symmetrical squared $d \times d$ matrix) containing the Pearson, or Spearman or Kendall coefficients. Random vectors are used to model multi-dimensional data sets, especially in the presence of dependence amongst the components. Random vector may be defined by their joint probability density function. If random vectors X and Y are independent, then the joint distribution can simply be defined as the product of the marginals:

$$f_{X,Y}(x, y) = f_X(x) \cdot f_Y(y) \quad (3.12)$$

3.3. Dependence structures amongst input random variables

If the occurrence of event $Y = y$ affects the probability of X , then the random variables are dependent and the joint density function can be expressed as:

$$f_{X,Y}(x, y) = f_{X|Y}(x | Y = y) \cdot f_Y(y) \quad (3.13)$$

where $f_{X|Y}(x | Y = y)$ is the conditional distribution of X given $Y = y$. So, modelling the dependence amongst random vectors, in the most general case, is the determination of the joint distribution of these random vectors. However, in most practical applications the marginal distributions are derived first, and then the dependence structure amongst the input random variables is investigated. If the marginals are given by normal distributions and the dependence structure is only described in terms of the correlation coefficient or correlation matrix, then there is only one possible multivariate distribution that fits with this information, that is the multivariate normal distribution [Embrechts et al., 1999].

In Fig. 3.6 we show two different joint probability model for a set of 1000 (X_1, X_2) data points. In both models, X_1 follows a Weibull distribution $X_1 \sim WBL(a = 11.28, k = 2.0)$ and X_2 follows a Lognormal distribution $X_2 \sim LN(\mu = 0.451, \sigma = 0.127)$ and with a linear correlation coefficient between them $\rho = 0.8$. It is clear from Fig. 3.6 that the dependence between X_1 and X_2 is quite different even though they are governed by the same correlation coefficient. In particular, the correlation does not inform about the dependence in the tail of the underlying joint distribution; note how extreme values of X_1 and X_2 occur together/simultaneously resulting in a pronounced tail dependence in the Gumbel distribution (Copula). Tail dependence is rather weak in the Gaussian distribution; extreme values of X_1 and X_2 do not necessarily occur simultaneously. This tail dependence is especially relevant in the context of extreme loading on wind turbines. Another issue which is often overlooked when describing correlations: [Embrechts et al., 1999] and [Lebrun and Dutfoy, 2009a] show - following the *Frechet-Hoeffding* theorem - that for specific choices of marginal distributions, there exist correlation values in the range $[-1, 1]$ that cannot be reached whatever the Copula we choose: these values are simply not compatible with the chosen marginal distributions. Furthermore, several studies of probability uncertainty treatment propose sensitivity studies which consist of considering a set of different marginal distributions without changing the linear correlation coefficients, and without verifying the constraints expressed by *Frechet-Hoeffding* theorem.

3.3.3 Copulas

The term "Copula" was introduced in the previous section. As discussed above, the correlation does not necessarily inform about the dependence in the tail of the underlying joint distribution. This is where the Copula theory [Nelsen, 2010] becomes very handy. The Copula theory allows one to represent a random vector $\mathbf{X} = \{X_1, X_2, \dots, X_n\}$ as a set of marginals and a function (the Copula) that "couples" them to form a joint probability density function. We start with the Sklar theorem [Sklar, 1959] which states that given an n-dimensional joint distribution function F with marginals $F_{X_1}, F_{X_2}, \dots, F_{X_n}$, then there exists a unique function C which we will call *Copula*, which satisfies:

$$F(X_1, X_2, \dots, X_n) = C[F_{X_1}(x_1), F_{X_2}(x_2), \dots, F_{X_n}(x_n)] \quad (3.14)$$

Chapter 3. Review: Some aspects of uncertainty quantification and probabilistic methods in the design of wind turbines

In the case of continuous marginal distributions and a known joint distribution F , the Copula C is unique and reads:

$$\begin{aligned} C(u_1, u_2, \dots, u_n) &= P[F_{\mathcal{X}_1}(x_1) \leq u_1, F_{\mathcal{X}_2}(x_2) \leq u_2, \dots, F_{\mathcal{X}_n}(x_n) \leq u_n] \\ &= P[x_1 \leq F_{\mathcal{X}_1}^{-1}(u_1), x_2 \leq F_{\mathcal{X}_2}^{-1}(u_2), \dots, x_n \leq F_{\mathcal{X}_n}^{-1}(u_n)] \\ &= \mathbf{F}[F_{\mathcal{X}_1}^{-1}(u_1), F_{\mathcal{X}_2}^{-1}(u_2), \dots, F_{\mathcal{X}_n}^{-1}(u_n)] \end{aligned} \quad (3.15)$$

By differentiating the joint cumulative distribution function F in Equation 3.14 we get the joint density function f (using the chain rule):

$$\begin{aligned} f &= \frac{\partial^n F}{\partial x_1 \partial x_2 \dots \partial x_n} \\ &= \frac{\partial^n C}{\partial u_1 \partial u_2 \dots \partial u_n} \cdot \frac{dF_{\mathcal{X}_1}(x_1)}{dx_1} \cdot \frac{dF_{\mathcal{X}_2}(x_2)}{dx_2} \dots \frac{dF_{\mathcal{X}_n}(x_n)}{dx_n} \\ &= c[F_{\mathcal{X}_1}(x_1), F_{\mathcal{X}_2}(x_2), \dots, F_{\mathcal{X}_n}(x_n)] \prod_{i=1}^n f_{\mathcal{X}_i}(x_i) \end{aligned} \quad (3.16)$$

where the joint PDF f is the product of the marginals $f_{\mathcal{X}_i}$ and the Copula density function c . In other words, the value taken by a joint probability density function is the value taken by a Copula, once the effect of the marginal density functions has been taken into account [Lebrun and Duffoy, 2009a]. There are several classes of bi-variate Copulas including the Archimedean Copulas such as the Frank, Clayton and Gumbel Copulas. The class of Elliptical Copulas such as the Gaussian and student-t Copulas. From here, there are two paths for practical engineering applications of the Copula formalism: (1) given a set of marginal distributions $F_{\mathcal{X}_i}$, simulate a joint distribution via a Copula OR (2) identify the joint distribution of a random vector \mathbf{X} from a data sample \mathcal{X} .

Given a set of marginal distributions $F_{\mathcal{X}_i}$, simulate a joint distribution via a Copula

- Step 1: Simulate a sample \mathcal{U} with Copula C and uniform margins on $[0, 1]$
- Step 2: Transform the sample \mathcal{U} to \mathcal{X} by applying the marginals such as $x_i^{(k)} = F_{\mathcal{X}_i}^{-1}(u_i^{(k)})$, $i = 1, \dots, n$ and $k = 1, \dots, N$ where N is the sample size (number of data points in \mathcal{X}).

The data in Fig. 3.6 have been generated with a Gaussian and a Gumbel Copula.

Identify the joint distribution of a random vector \mathbf{X} from a data sample \mathcal{X}_i

- Step 1: Identify the marginal distributions for each of the components \mathcal{X}_i
- Step 2: Identify the Copula structure (dependence structure amongst the \mathcal{X}_i)

The identification of the marginals is described in Section 3.2.1. Identification of the Copula structure consists in erasing the effect of the marginals so that only the Copula is preserved. This is done by normalizing the rank $r_{x_i^{(k)}}$ of the data in each \mathcal{X}_i by N . In Fig. 3.4 we show how the bivariate distribution of (X_1, X_2) corresponding to the Gumbel Copula are transformed into their corresponding normalized ranks. We can then use the Kendall plots to identify the most appropriate Copula structure that fits the normalized ranks in the *dependogram* in Fig. 3.5. The Kendall plots compare the empirical quantiles calculated from the data:

$$H_{i,obs} = \frac{1}{N-1} N_Q \quad (3.17)$$

to the theoretical quantiles of a selected Copula. $N_Q = \# \left\{ k \neq j, X_1^k \leq X_1^j, X_2^k \leq X_2^j \right\}$. In Fig. 3.5 we compare the empirical quantiles to both a theoretical Calyton and Gumbel Copula

3.3. Dependence structures amongst input random variables

quantiles. The Kendall plot indeed indicates that the Gumbel Copula fits best the observed data.

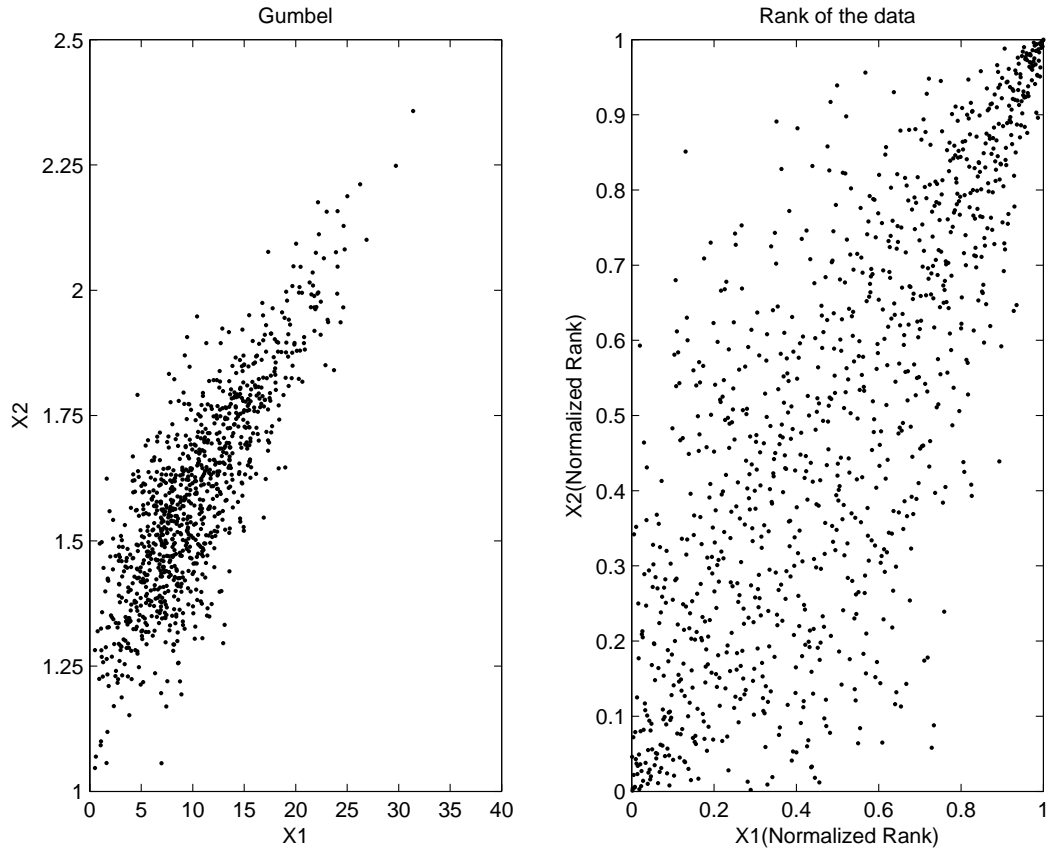


Figure 3.4: the bivariate distribution of (X_1, X_2) corresponds to the Gumbel Copula are transformed into their corresponding normalized ranks.

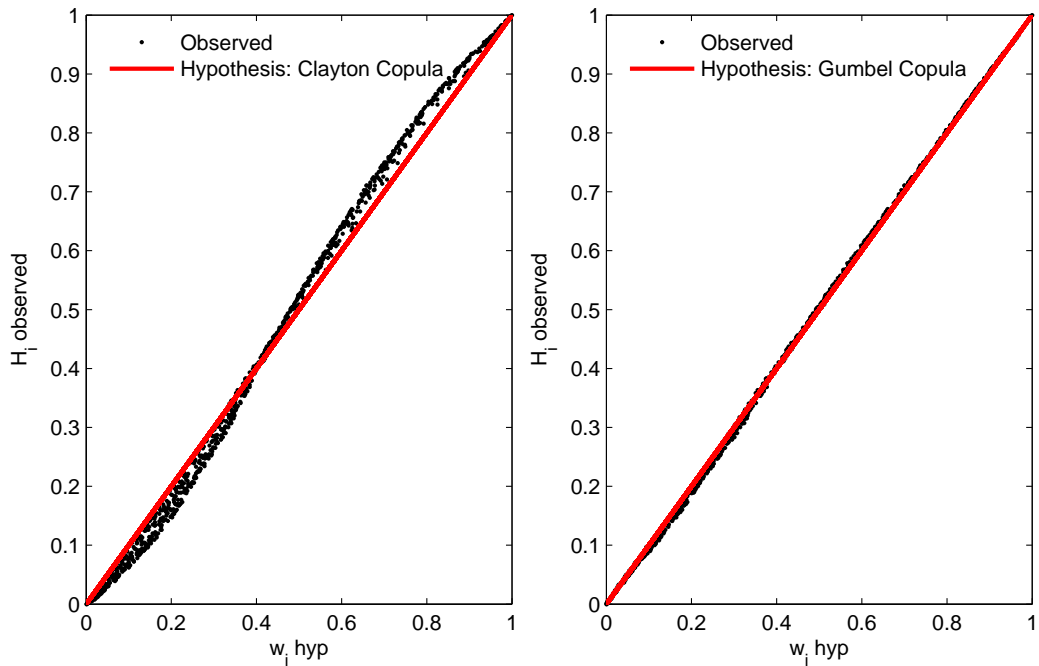


Figure 3.5: Kendall plots comparing the empirical (observed) quantiles to both a theoretical Calyton and Gumbel Copula quantiles.

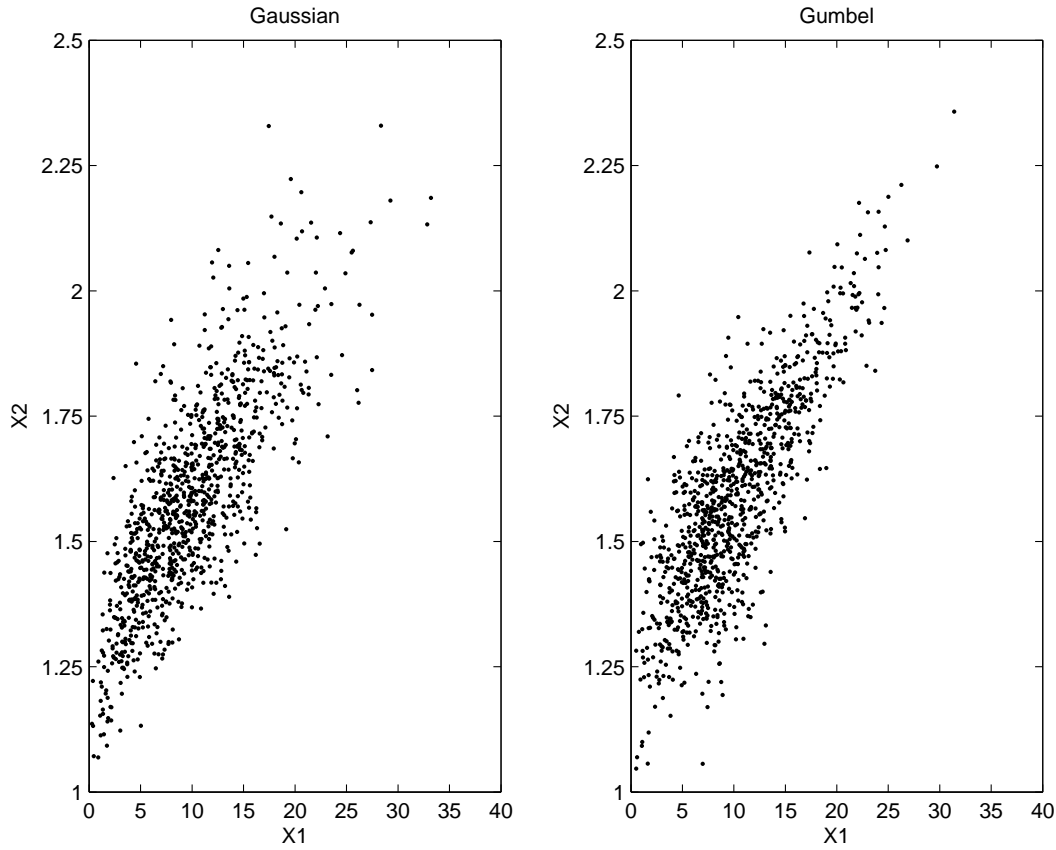


Figure 3.6: 1000 data points generated for two multivariate distributions with identical marginals $X_1 \sim WBL(a = 11.28, k = 2.0)$ and $X_2 \sim LN(\mu = 0.451, \sigma = 0.127)$ and identical correlation $\rho = 0.8$, but different dependence structures. The dependence between X_1 and X_2 in the two models cannot be distinguished on the basis of correlation alone.

3.4 Sources of uncertainties in the prediction of a wind turbine’s extreme loads

The aim in this section is to collect all possible sources of uncertainty influencing the variation of extreme design loads on wind turbines.

3.4.1 Types of uncertainties

Uncertainties can be classified as either Aleatoric and Epistemic. **Aleatoric** or physical uncertainties are unknowns that differ each time the same experiment is ran. Aleatoric uncertainties can not be suppressed by more accurate measurements. They are irreducible. An example of aleatoric uncertainties include wind speed, materials data, wave and wind loading. **Epistemic** or systematic uncertainties are due to lack of knowledge of a system and its environment. Epistemic uncertainties are reducible if better models and data are available. This may be because a quantity has not been measured sufficiently, or because a numerical model neglects certain effects. In engineering applications, both kinds of uncertainties are often present. The distinction between aleatory and epistemic uncertainties is determined by our modeling choices [Kiureghian and Ditlevsen, 2009]. Uncertainties are divided into the following groups: **(a) Physical uncertainties**

3.4. Sources of uncertainties in the prediction of a wind turbine's extreme loads

are related to the natural randomness of a quantity such as the uncertainty in the yield stress due to production variability. Physical uncertainties are of the aleatoric type. **(b) Model uncertainties** such as imperfections and assumptions made in the aero-structural representation of a wind turbine versus real life. Model uncertainties are of the epistemic type. **(c) Statistical uncertainties** such as scatter in materials test data, limited number of measurements, limited number of simulations for loads extrapolations, etc. Statistical uncertainties are of the epistemic type. **(d) Measurement uncertainties** such as sensor calibration, sensor noise, etc. Measurement uncertainties are of the epistemic type. **(e) Gross errors** such as human errors.

3.4.2 Sources of uncertainties

This is an exposé of uncertainties affecting the variations in the extreme design loads through aero-servo-elastic simulations of wind turbines. An overview of the uncertainties categories are presented in Fig. 3.7; the process begins with the specifications describing the technical details of the wind turbine, which are interpreted by the engineer and converted into a set of model inputs (e.g. airofoil lift and drag coefficients, blade stiffness distribution, tower geometry, control system DLL, etc.). The engineering inputs are then used to run various design load cases in a time domain aero-servo-elastic simulator. The output time series are post-processed to extract statistical information such as maximum/minimum loads, rainflow counting to compute equivalent fatigue loads and power spectral densities of the time series to verify modal frequencies and stability. The final two steps—before the final extreme design loads are certified—include the aero-servo-elastic load model verification through test measurements on a wind turbine prototype, followed by measurements on a number of "zero-series" prototypes where site specific loads admission is also performed. Certain external factors may introduce additional uncertainties such as human error or out-of-control production processes. Fig. 3.8-3.13 show the details of the sources of uncertainties for each of the categories listed in Fig. 3.7.

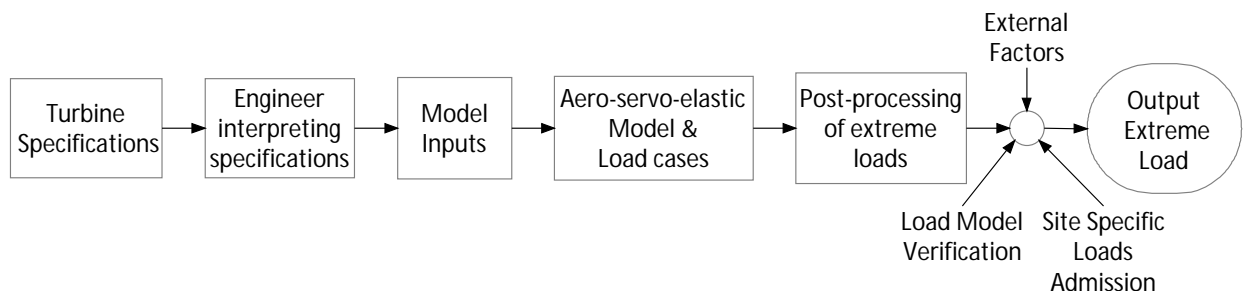


Figure 3.7: Overview of the sources of uncertainties in the process of determining the extreme design loads of a wind turbine.

Chapter 3. Review: Some aspects of uncertainty quantification and probabilistic methods in the design of wind turbines

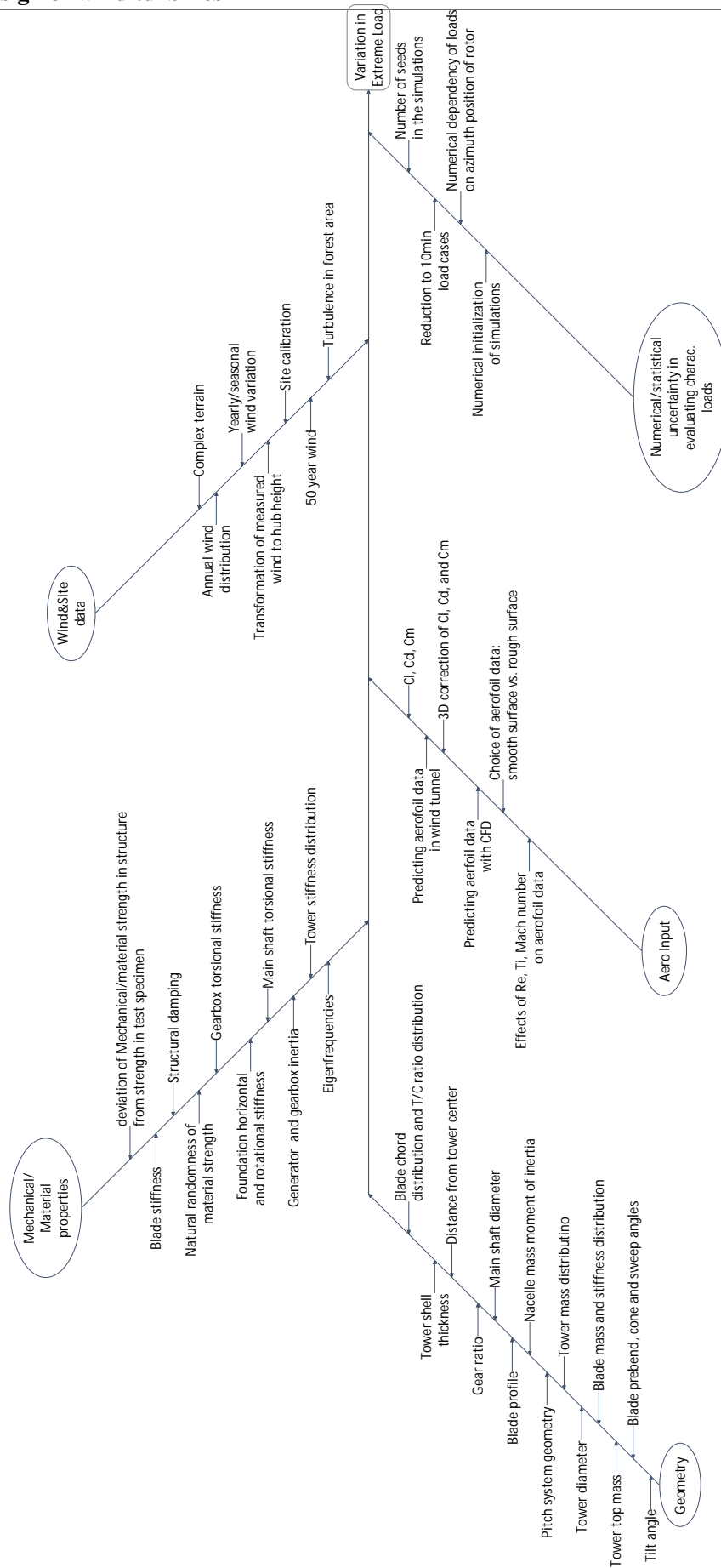


Figure 3.8: Fishbone of uncertainties in the **inputs** of the aero-servo-elastic models leading to variations in extreme loads.

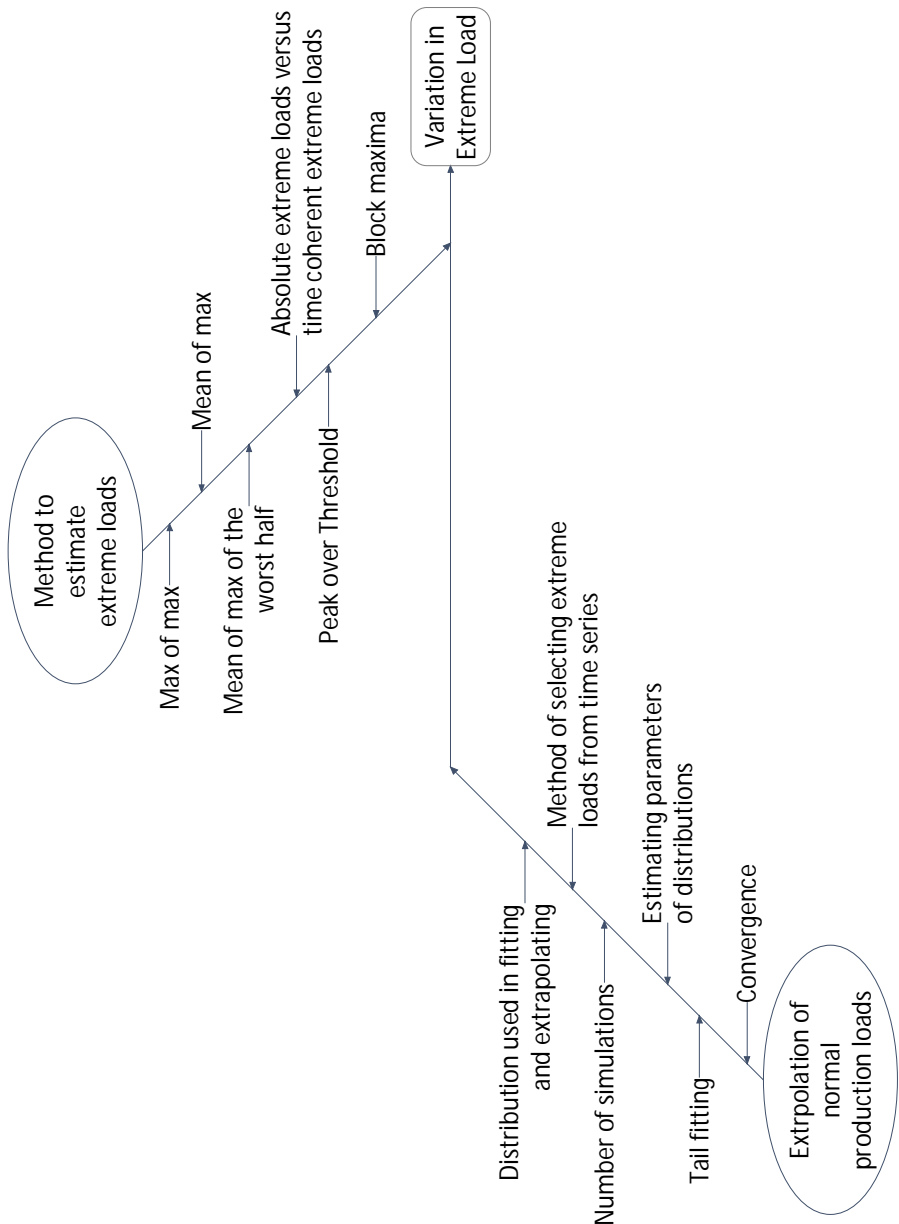


Figure 3.10: Fishbone of uncertainties in the **post-processing** of aero-servo-elastic outputs leading to variations in extreme loads.

3.4. Sources of uncertainties in the prediction of a wind turbine's extreme loads

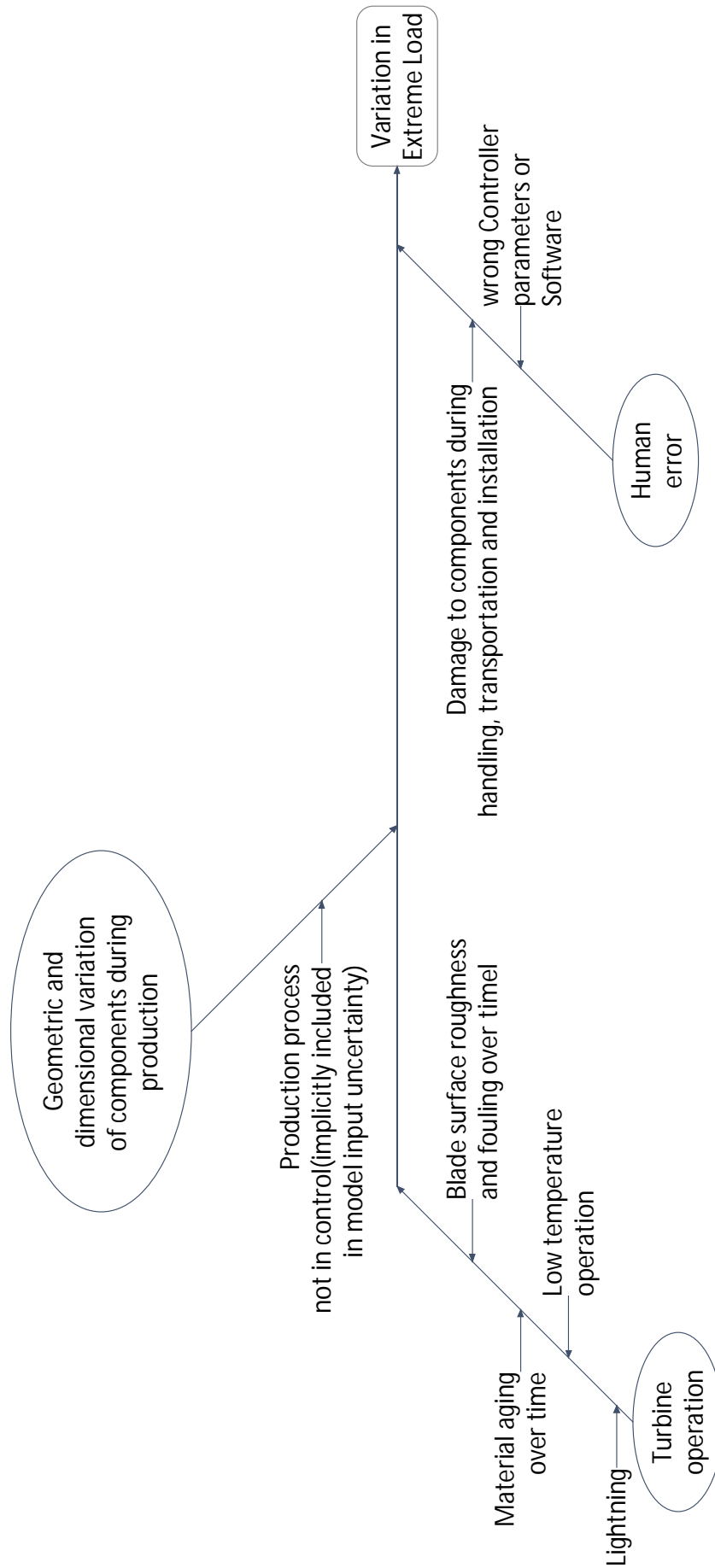


Figure 3.11: Fishbone of uncertainties in the **external factors** leading to variations in extreme loads.

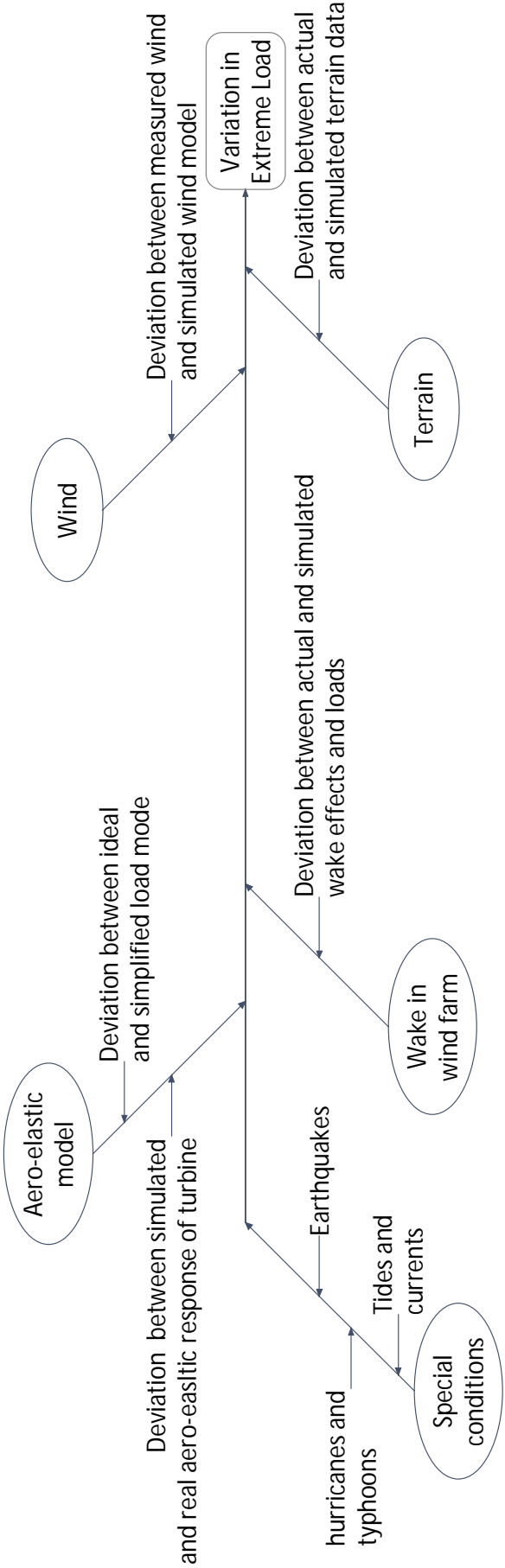


Figure 3.12: Fishbone of uncertainties in the site specific loads admission leading to variations in extreme loads.

3.4. Sources of uncertainties in the prediction of a wind turbine's extreme loads

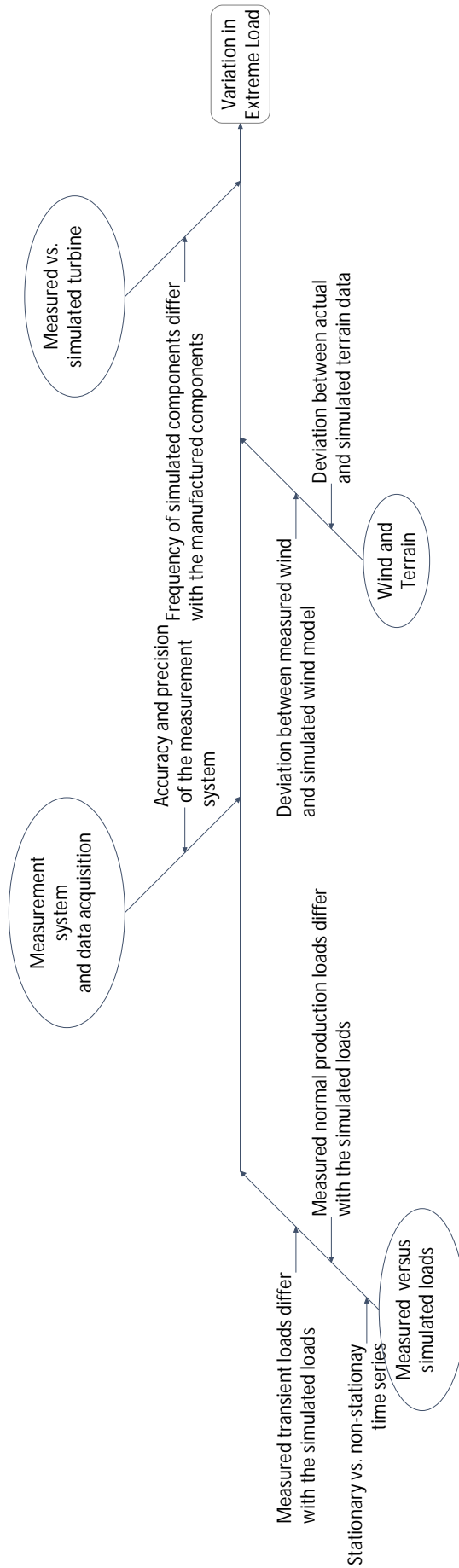


Figure 3.13: Fishbone of uncertainties in the load aero-servo-elastic **model verification** leading to variations in extreme loads.

3.5 Some structural reliability methods

Here we explore some concepts of probabilistic methods in structural reliability that link steps A-C in the uncertainty quantification framework presented in Fig. 3.1. In Chapter 5 the uncertainty of the lift and drag coefficients is propagated through the aero-servo-elastic simulations using the Monte Carlo technique. In Chapters 5, 6, and 7 the probability of failure and structural reliability is assessed using the First Order Reliability Method.

3.5.1 The probability of failure

The probability of failure p_f of any designed structure can be interpreted as the integral of the joint distribution of all its random variables over the failure domain D_f delimited by a limit state function (LSF) $g(\mathbf{x}) = R - L$. R is the resistance of the structure and L the loading.

$$p_f = \int_{D_f} f_{\mathbf{X}}(\mathbf{x}) d\mathbf{x} \quad (3.18)$$

$$D_f = \{\mathbf{x} \in \mathcal{D}_{\mathbf{X}} : g(\mathbf{x}) \leq 0\}$$

where $f_{\mathbf{X}}(\mathbf{x})$ is the joint probability density function of the random vector \mathbf{X} . A simple illustrative interpretation is shown in Fig. 3.14a. X_1 and X_2 are normally distributed with means $\{1, 1\}$ and covariance matrix $\Sigma = \begin{bmatrix} 0.25 & 0.33 \\ 0.33 & 0.9 \end{bmatrix}$. The p_f is evaluated as the volume of the joint probability density function on the failure domain. The failure domain is delimited by the dashed line corresponding to the limit state function $g(X_1, X_2) = 0$. The resulting probability of failure (Equation 3.18) is in fact a multidimensional integral over the failure domain whose dimension is equal to the number of basic input variables. The main difficulty lies in the fact that the failure domain is implicitly defined by $\{\mathbf{x} \in \mathcal{D}_{\mathbf{X}} : g(\mathbf{x}) \leq 0\}$. Evaluating this integral is a problem when the random variables are not normal and dependent or the limit state function is not linear, which is often the case. There are simulation based methods and optimization based methods that can be employed to solve the above integral.

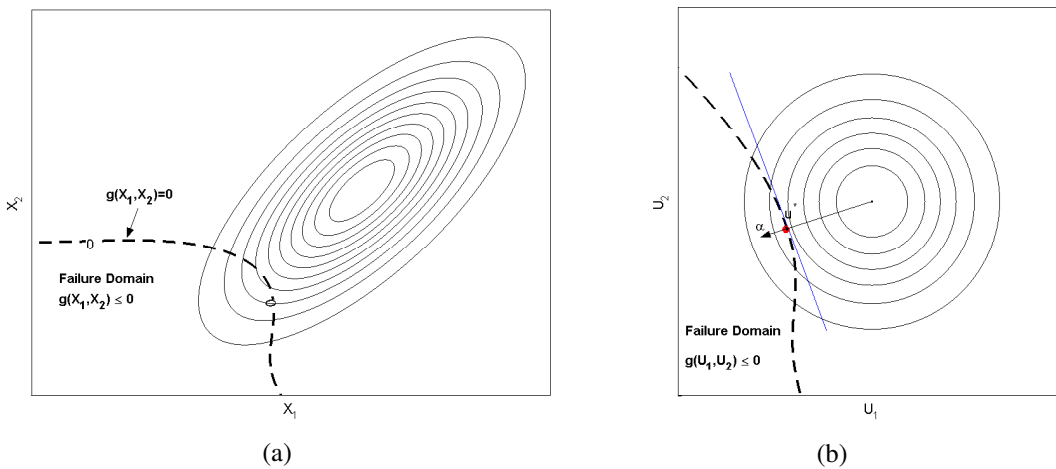


Figure 3.14: (3.14a) Illustration of the contour lines of the joint probability density function of random variables X_1 and X_2 , and the limit state function $g(X_1, X_2)$ which delimits the failure domain in the physical space. (3.14b) illustrates the equivalent joint probability density function and limit state function transformed in the standard normal space (i.e. u-space).

3.5.2 Simulation based methods: Monte Carlo

One way to approximate the probability of failure (Equation 3.18) is through simulation based methods. Simulation based methods to assess the probability of failure involves a large number of evaluations of the limit state function $g(\mathbf{x})$. Such methods include crude Monte Carlo sampling [Metropolis and Ulam, 1949]

$$\begin{aligned} p_f &= \int_{D_f} \mathbb{1}_{D_f}(\mathbf{x}) f_{\mathbf{X}}(\mathbf{x}) d\mathbf{x} = \mathbb{E} [\mathbb{1}_{D_f}(\mathbf{x})] \\ &= \frac{1}{N} \sum \mathbb{1}_{D_f}(\mathbf{x}^{(j)}) = \frac{n_{fail}}{N} \end{aligned} \quad (3.19)$$

where N is the total number of simulated samples $\{\mathbf{x}^{(1)}, \dots, \mathbf{x}^{(N)}\}$ from the random vector \mathbf{X} . For each sample, the limit state function $g(\mathbf{x}^{(j)})$ is then evaluated; $\mathbb{1}_{D_f}(\mathbf{x}^{(j)})$ take value 1 if $g(\mathbf{x}^{(j)}) \leq 0$ and 0 if $g(\mathbf{x}^{(j)}) > 0$. n_{fail} is the number of $g(\mathbf{x}^{(j)})$ samples in the failure domain. [Sudret, 2007b] shows how for a target probability of failure $p_f = 10^{-k}$ and a coefficient of variation of 5% on the estimation of p_f , the total number of samples N should be $N > 4 \cdot 10^{k+2}$. Such number of samples (and the corresponding evaluations of $g(\mathbf{x}^{(j)})$) becomes infeasible when p_f is small (say $\sim 10^{-4}$) and $g(\mathbf{x}^{(j)})$ is expensive to evaluate. Additional Monte Carlo based methods include: Latin HyperCube sampling, Sobol series sampling, importance sampling, asymptotic sampling, directional sampling, stratified Monte Carlo sampling (splitting of the integration space into k regions), adaptive Monte Carlo methods and hierarchical Monte Carlo methods [Helton and Davis, 2003, Bucher, 2009, Naess et al., 2009, Sichani et al., 2011]. All the listed methods have the common feature that the sampling density is modified in order to obtain more failure outcomes per number of trials. Those and various classical methods can be found in the textbooks by [Ditlevsen and Madsen, 2007, Melchers, 1999, Lemaire et al., 2009]. An alternative could be found in metamodelling where an expensive to evaluate computational model is replaced by a simple surrogate model (metamodel). The metamodel is determined through a small number of support points ($n \ll N$) defined by a design of experiments. The metamodel is thus fast to evaluate and may be used in place of the original model to evaluate the probability of failure. Two of the more popular metamodelling techniques include Polynomial Chaos Expansions (PCE) and Kriging (Gaussian Processes) or a combination thereof [Sudret, 2007a, 2012, Schöbi and Sudret, 2014].

3.5.3 Optimization based method: The First Order Reliability Method

The First Order Reliability Method (FORM) is an optimization based method, where $g(\mathbf{x}^{(j)})$ are nonetheless still required, albeit a much lower number of evaluations of the limit state function compared to Monte Carlo simulations. The first step when using FORM is to transform the original random variables $\mathbf{X} = \{x_1, x_2, \dots, x_n\}$ to the independent standard normal variables $\mathbf{U} = \{u_1, u_2, \dots, u_n\}$ by using the well-known Nataf or Rosenblatt transformations (see Appendix A), which we denote by \mathcal{T} , i.e. $\mathbf{X} \rightarrow \mathbf{U} = \mathcal{T}(\mathbf{X})$. The probability of failure in Equation 3.18 becomes after the transformation:

$$p_f = \int_{D_f} f_{\mathbf{X}}(\mathbf{x}) d\mathbf{x} = \int_{g(\mathcal{T}^{-1}(\mathbf{u}) \leq 0)} \phi_{\mathbf{U}}(\mathbf{u}) d\mathbf{u} \quad (3.20)$$

Chapter 3. Review: Some aspects of uncertainty quantification and probabilistic methods in the design of wind turbines

where ϕ is the standard multinormal probability density function, centered at the origin. In standard normal space, Equation 3.20 is recast into an optimization problem to search for the shortest distance from the origin to the failure hyperplane $g(\mathcal{T}^{-1}(\mathbf{u})) = 0$:

$$\begin{aligned} & \text{minimize} \quad \|\mathbf{u}\| \\ & \text{subject to} \quad g(\mathcal{T}^{-1}(\mathbf{u})) = 0 \end{aligned} \quad (3.21)$$

The second step is thus to solve the optimization problem. The optimum point \mathbf{u}^* derived from the optimization scheme above is called the design point or the most probable point. One way to approach this optimization problem is to introduce Lagrange multipliers, which would then cast Equation 3.21 as:

$$L(\mathbf{u}) = \frac{1}{2}\|\mathbf{u}\|^2 + \lambda g(\mathbf{u}) \quad (3.22)$$

where λ is the Lagrange multiplier, and $1/2$ is added for convenience of latter expressions. Optimality is found by setting the gradient of the Lagrange function L to zero:

$$\nabla L(\mathbf{u}) = \|\mathbf{u}\| + \lambda \nabla g(\mathbf{u}) = 0 \quad (3.23)$$

A possible solution is found as:

$$\lambda = \frac{\|\mathbf{u}\|}{\|\nabla g(\mathbf{u})\|} \quad (3.24)$$

Substituting in Equation 3.23 we get:

$$\frac{\mathbf{u}}{\|\mathbf{u}\|} + \frac{\nabla g(\mathbf{u})}{\|\nabla g(\mathbf{u})\|} = 0 \quad (3.25)$$

which is indeed satisfied if vector \mathbf{u} is parallel to the gradient at the trial point on the limit state function and of opposite direction. We can then deduce that the shortest distance from the origin to the limit state function can be depicted by vector \mathbf{u}^* that fulfils the following relation:

$$\mathbf{u}^* = \Delta \frac{\nabla g(\mathbf{u}^*)}{\|\nabla g(\mathbf{u}^*)\|} \quad (3.26)$$

where Δ is the length of the vector \mathbf{u}^* . For a point \mathbf{u}_0 on the limit state function, we first consider the first approximation of $g(\mathbf{u})$ in \mathbf{u}_0 using a Taylor expansion:

$$g(\mathbf{u}^*) \approx g(\mathbf{u}_0) + \nabla g(\mathbf{u}_0)^T \cdot (\mathbf{u}^* - \mathbf{u}_0) \quad (3.27)$$

Or, \mathbf{u}_0 is a point very close to \mathbf{u}^* :

$$\mathbf{u} = \mathbf{u}_0 + \Delta \mathbf{u} \quad (3.28)$$

replacing Equation 3.26 and 3.28 into 3.27 we get:

$$\begin{aligned} g(\mathbf{u}^*) & \approx g(\mathbf{u}_0) + \nabla g(\mathbf{u}_0)^T \cdot (\mathbf{u}^* - \mathbf{u}_0) \\ & \approx g(\mathbf{u}_0) + \nabla g(\mathbf{u}_0)^T \cdot \left(\Delta \frac{\nabla g(\mathbf{u}^*)}{\|\nabla g(\mathbf{u}^*)\|} - \mathbf{u}_0 \right) \end{aligned} \quad (3.29)$$

Since \mathbf{u}^* is a point on the limit state hyperplane, then $g(\mathbf{u}^*) = 0$:

$$g(\mathbf{u}_0) + \nabla g(\mathbf{u}_0)^T \cdot \left(\Delta \frac{\nabla g(\mathbf{u}^*)}{\|\nabla g(\mathbf{u}^*)\|} - \mathbf{u}_0 \right) = 0 \quad (3.30)$$

from which we determine Δ as:

$$\frac{\Delta}{\|\nabla g(\mathbf{u}_0)\|} = \frac{\nabla g(\mathbf{u}_0)^T \mathbf{u}_0 - g(\mathbf{u}_0)}{\nabla g(\mathbf{u}_0)^T \nabla g(\mathbf{u}_0)} \quad (3.31)$$

An iterative scheme to solve the FORM optimization problem is presented in Appendix C.

3.6 From uncertainty to safety factors

So far we have explored methodologies to build probabilistic methods of the random variables based on available data. We have also reviewed some correlation and dependence structures to link the random variables. In the previous section we have seen how to compute the probability of failure. In this section we illustrate how uncertainties in random variables translate in terms of safety factors. The First Order Reliability Method is employed as the main driver for the derivation of the safety factors satisfying a target reliability level.

3.6.1 Cost and reliability-based optimization of safety factors

This is a general account on how to determine and optimize safety factors (not calibration).

$$g = R(z) - L \quad (3.32)$$

The design equation corresponding to the limit state function (Equation 3.32) is:

$$G = \frac{R_c}{\gamma_m} - L_c \gamma_l \quad (3.33)$$

where z is some design variable such as diameter, thickness, surface area, etc. R is the resistance of the structure and L is the loading. R_c and L_c correspond to the characteristic values of the resistance and load, usually set to the 5th and 98th percentile, respectively. γ_m and γ_l are the material and load safety factors. Analysis by FORM leads to determination of z in order to meet a target structural reliability level β corresponding to a probability of failure p_f . At the limit state surface, the design equation can be set to zero:

$$\frac{R_c}{\gamma_m} - L_c \gamma_l = 0 \Rightarrow R_c - L_c \gamma_l \gamma_m = 0 \quad (3.34)$$

Given a value for z , the safety factors read:

$$\gamma_m \cdot \gamma_l = \frac{R_c(z)}{L_c} \quad (3.35)$$

$\gamma_m \cdot \gamma_l$ satisfy the target probability of failure. Now, given one random variable for resistance, one random variable for load and one failure mode for the structure (i.e. one LSF), then the safety factors can be directly derived in FORM as:

$$\gamma_m = \frac{R_c}{R^*}, \quad \gamma_l = \frac{L^*}{L_c} \quad (3.36)$$

where L^* and R^* are the design points of the load and resistance respectively as computed in FORM. However, in case of multiple design variables, multiple load and resistance random variables for the structure, then the process is more involved and iterative:

Chapter 3. Review: Some aspects of uncertainty quantification and probabilistic methods in the design of wind turbines

- a. Initial guess of γ_l and γ_m
- b. Solve for the design variable \mathbf{z} s.t. $G(\mathbf{X}_c, \mathbf{z}, \gamma) = 0$
- c. $\mathbf{z} \rightarrow$ FORM/SORM/Monte Carlo
 - Compute reliability index β
- d. Is $\beta \geq \beta^*$?
 - if yes, then exit
- e. Make new guess of $\gamma_l \gamma_m$
- f. Repeat steps b – e

In case of multiple failure modes and/or multiple structures, the above optimization process is repeated for every structure and failure mode. In order to ensure a more or less uniform reliability index across all sets of structures considered in the design; the deviation of the reliability index for each of the structures and the overall desired (target) reliability index is minimized such that $err = \sum_{i=1}^N \omega_i (\beta_i - \beta^*)^2$, where β^* is the target reliability index, ω_i are weighting factors indicating the relative importance of the various structures and failure modes. The difference between the reliability index for each of the structures β_i and the desired (target) reliability index β^* reaches an error threshold err . Hence the chosen safety factors result in a more or less uniform reliability across all N structures and failure modes. The above procedure can be further augmented as described in the JCSS procedure [Fris Hansen and Sørensen, 2002, Vrouwenvelder, 2002] to take into account in addition the cost of the designed structure:

- a. Initial guess of γ_l and γ_m
- b. Solve for the design variable \mathbf{z} as follows:

$$\begin{aligned} & \underset{\mathbf{z}}{\text{maximize}} && W(\mathbf{z}, \gamma) = \mathbf{B} - \mathbf{C} - \mathbf{D} \\ & \text{s.t.} && G(\mathbf{X}_c, \mathbf{z}, \gamma) = 0 \\ & && \mathbf{z}^l \leq \mathbf{z} \leq \mathbf{z}^u \end{aligned}$$
- c. $\mathbf{z} \rightarrow$ FORM/SORM/Monte Carlo
 - Compute reliability index β
- d. Is $\beta \geq \beta^*$?
 - if yes, then exit
- e. Make new guess of $\gamma_l \gamma_m$
- f. Repeat steps b – f

In the above, B are the benefits such as the annual energy production of a wind turbine, C are the costs of research, development, manufacturing and installation, and D are the costs of failure and replacement. A wind turbine, unlike civil engineering structures, is active under the influence of a control system. Hence, the design variable \mathbf{z} can include control variables in addition to structural/geometric/mechanical properties. Advanced load alleviation control features reduce the mean and variation of the annual maximum distribution of the load. We will show in the following simple example how a reduction in the mean and variance affect the safety

factors. This example is inspired from [Sørensen, 2004], page 141. The Limit State Function $g = zR - G - Q$, where z is a design variable, R is a resistance, G is the gravitational load and Q is the variable load such as the annual maximum wind load. The random variables are described in Table 3.1, where COV is the coefficient of variation. The characteristic values of the random variables are chosen as in Table 3.2, where R^* , G^* , Q^* are the design points (most likely failure points) where the limit state is reached (i.e. where failure occurs). These points are computed in FORM. Fig. 3.15 shows the PDF of the resistance and the load. The following tables present the calculated safety factors for various scenarios where the mean and COV of the load Q is reduced simulating the load limiting effects of the load alleviation control features. First the safety factors are computed when the coefficient of variation of the variable load Q is varied from 0.4 to 0.2. From the results in Table 3.3 we observe that reducing the scatter of the loads (COV) reduces the load safety factor from 1.61 to 1.28 while maintaining a reliability level of $\beta = 3.8$. That is also accompanied by a reduction in the design variable z from 15.6 to 11.3 indicating a lighter design of the structure. The safety factors are then computed when the coefficient of variation of the variable load Q is kept constant at 0.4 while varying the mean from 3 to 2.2. From the results in Table 3.4 we observe that reducing the mean of the loads results in a marginal reduction of the load safety factor from 1.61 to 1.58 while maintaining a reliability level of $\beta = 3.8$. However, the design variable z drops from 15.6 to 12.2 indicating a lighter design of the structure. Finally the safety factors are computed when the coefficient of variation and the mean of the variable load Q are varied. From the results in Table 3.5 we observe a reduction of the load safety factor from 1.61 to 1.24 while maintaining a reliability level of $\beta = 3.8$. The design variable z exhibits a significant drop from 15.6 to 9.1 in this case. The main conclusions can be stipulated as follows: (1) reducing the scatter of the loads has a significant impact on the reduction of the safety factors while maintaining an acceptable reliability level, and (2) reducing the mean of the load has a marginal impact on the safety factor while resulting in a lighter design structure at an acceptable reliability level. For a mean of 3 and $COV = 0.3$, the safety factor drops from 1.61 to 1.47, a reduction of $\sim 10\%$ while the design becomes $\sim 16\%$ lighter. Now, when the mean also drops from 3 to 2.8, the design variable further drops by another $\sim 5\%$ while the safety factor remains unchanged. This is an interesting result for the design and performance evaluation of load alleviation control features. The wind energy industry almost exclusively uses the latter potential of the load alleviation features and rarely the former, i.e. leverage the reduction in scatter to optimize the safety factors.

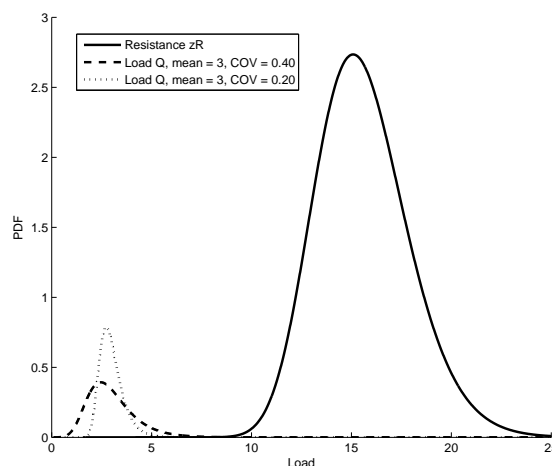


Figure 3.15: the probability density functions of the resistance and the load.

Chapter 3. Review: Some aspects of uncertainty quantification and probabilistic methods in the design of wind turbines

Table 3.1: Parameters of the stochastic model.

Random Variable	Distribution	Expected Value	COV
R	Lognormal	1	0.15
G	Normal	2	0.10
Q	Gumbel	3	0.40

Table 3.2: Parameters of the stochastic model.

Random Variable	Quantile	Characteristic value	Safety factor
R	5% quantile	$R_c = 0.77$	$\gamma_R = R_c/R^*$
G	50% quantile	$G_c = 2$	$\gamma_G = G^*/G_c$
Q	98% quantile	$Q_c = 6.11$	$\gamma_Q = Q^*/Q_c$

Table 3.3: Safety factors as a function of the coefficient of variation of the load Q . The mean of the load Q is kept constant.

mean Q	COV Q	γ_R	γ_G	γ_Q	z	β
3	0.4	1.02	1.02	1.61	15.6	3.8
3	0.3	1.05	1.03	1.47	13.4	3.8
3	0.2	1.10	1.04	1.28	11.3	3.8

Table 3.4: Safety factors as a function of the mean of the load Q . The COV is kept constant.

mean Q	COV Q	γ_R	γ_G	γ_Q	z	β
3	0.4	1.02	1.02	1.61	15.6	3.8
2.8	0.4	1.02	1.02	1.60	14.7	3.8
2.6	0.4	1.02	1.02	1.59	13.9	3.8
2.2	0.4	1.03	1.03	1.58	12.2	3.8

Table 3.5: Safety factors as a function of the mean of the load Q . Both the mean and COV are varied.

mean Q	COV Q	γ_R	γ_G	γ_Q	z	β
3	0.4	1.02	1.02	1.61	15.6	3.8
2.8	0.3	1.05	1.03	1.46	12.7	3.8
2.6	0.3	1.05	1.03	1.46	11.98	3.8
2.6	0.2	1.11	1.04	1.27	10.2	3.8
2.2	0.2	1.12	1.05	1.24	9.1	3.8

4 *Review: Analytical methods for fusing results from multiple simulators - Application to extreme loads on wind turbines*

The first aim in this chapter is to expose the reader to the fundamental thesis of information fusion from multiple sources, and lay out the main uncertainties in aero-servo-elastic simulators (model uncertainties). The second aim is to review 5 analytical methods for fusing (aggregating) output results from multi-fidelity simulators with application to extreme loads on wind turbines. Simple numerical examples are given to demonstrate each of the analytical methods.

This chapter attempts to address the following design scenarios:

- A designer computes the loads for the same wind turbine geometry and technical specifications in 3 aero-servo-elastic simulators (FLEX5, Bladed, HAWC2). The designer then derives the annual maximum distribution of the loads from the 3 simulators, and observes some discrepancies in the mean and coefficient of variation of the distributions. The designer would like to know what is the most likely load level to design the wind turbine structure for.
- A designer has conducted a long term (≥ 1 year) loads test and measurement campaign on 5 wind turbines (same mark, same geometry, and same technical specifications) located on various sites. Given the scatter and discrepancy of the turbines' loads measurements from the various sites, the designer is interested in knowing how to combine all these measurements from the 5 test sites in order to compare to the simulated loads.

4.1 Introduction

4.1.1 The current practice of comparing loads and response estimates from multiple aero-servo-elastic simulators

Multiple commercial and research based aero-servo-elastic simulators are available to compute the coupled dynamic loads and response of the wind turbine (e.g. Flex, FAST, GH Bladed, HAWC2, CP-Lambda, etc.). As depicted in Fig. 4.1 analysts and designers compute and compare the output from multiple simulators [Buhl et al., 2000, 2001, Simms et al., 2001, Schepers et al., 2002, Buhl and Manjock, 2006, Jonkman et al., 2008, Jonkman and Musial, 2010]. Differences in predictions are reported and possible root causes are described. No attempts are usually made to combine the results from multiple simulators. The models uncertainty are assumed to be covered by safety factors as shown in Fig. 4.2.

Traditionally, wind turbine designers would validate and verify a model using the prototype verification data. The model is more or less validated and verified (and calibrated) for every new wind turbine design. The model is then assumed to be capable of predicting "correct" aero-servo-elastic responses of current and future turbines. Given the very low number of structural failures in the field, it is fair to assume that the aero-servo-elastic models are biased to be on the "conservative side". Other reasons include the benign climatic conditions in which the wind turbine operates compared to the design climatic conditions or overly conservative safety factors (hidden safety). There are issues with this approach, such as:

- Once the prototype stage has been reached, all main components of the wind turbine have already been designed and built, and very little room is available for major changes (unless done at a significant cost).
- A large jump in wind turbine dimensions is being undertaken at the moment with increasing uncertainty in the suitability of calibrated aero-servo-elastic simulators to predict the correct design loads and dynamic responses, as very little experience is available with large offshore wind turbines.
- Sometimes large variations in the predicted responses are exhibited amongst the simulators; it is not clear if these variations are fully covered by the loads partial safety factor.
- The model verification, validation and calibration is done through prototype tests under "controlled" conditions in very well studied sites. Future turbines in the field, however, operate in widely varying conditions such as climate and terrain conditions.

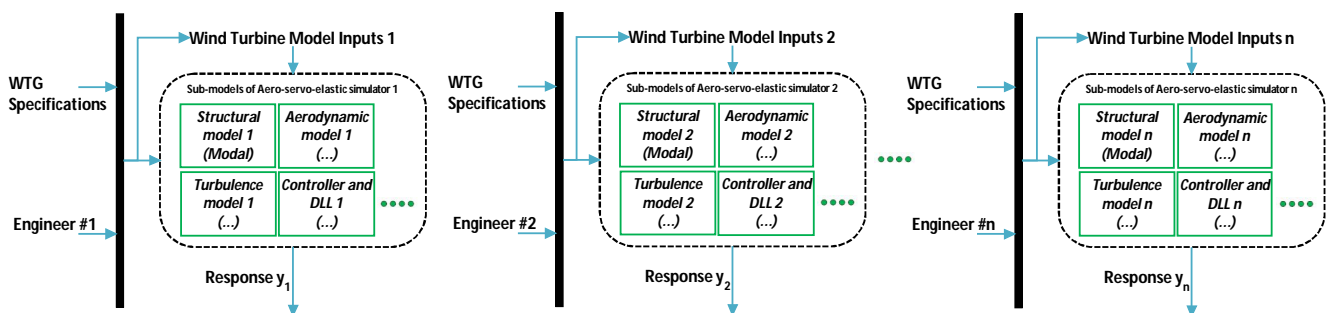


Figure 4.1: A depiction of how multiple aero-servo-elastic simulators are used to compute the response of a wind turbine.

4.2. Model uncertainty in aero-servo-elastic simulators

As a result of model uncertainty, discrepancy amongst models predictions can easily be up to 20%. The current practice is to select the peak response from one particular simulator and impose a "large enough" safety factor resulting in a "safe" and "conservative" design peak response as shown in Fig. 4.2. This practice, however, may prove to be overly conservative.

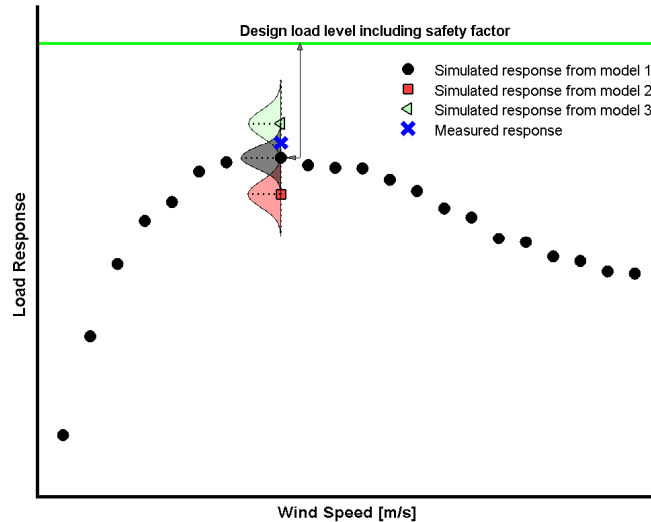


Figure 4.2: Peak load response and their corresponding variations from three different simulation models. The measured response is also shown.

4.2 Model uncertainty in aero-servo-elastic simulators

4.2.1 Sources of model uncertainty

Mathematical models of reality implemented in computer codes contain many different sources of uncertainty. Among these are parameter uncertainty, residual variability, parametric variability, observation error, code uncertainty, and model discrepancy [Kennedy and O'Hagan, 2001]. Following [Kennedy and O'Hagan, 2001], parameter uncertainty relates to uncertainty associated with the values of model inputs; residual variability relates to the variation of a particular process outcome even when the conditions of that process are fully specified, parametric variability results when certain inputs require more detail than is desired (or possible) and are thus left unspecified in the model; observation error involves the use of actual observations in a model calibration process; code uncertainty results when a code is so complex or computationally involved that it may not be possible to execute the code at every possible input configuration of interest, thus there is some additional uncertainty related to regions of the input space that have not been interrogated; and model discrepancy relates to the fact that no model is perfect, and thus some aspects of reality may have been omitted, improperly modeled, or contain unrealistic assumptions [Allaire and Willcox, 2014]. The choices made in the physics and implementation of the submodels drive the model uncertainty. Another aspect, generally overlooked, is the validation (calibration) process of the parameters of such simulators. The validation is generally based on few test data from turbines of varying size. The validation process from simulator to simulator may have not necessarily employed the same data, which creates some scatter amongst the simulators. The sources of model uncertainty listed in Figure 4.3 are based on [Allaire and Willcox, 2014] and [Alvin et al., 1998].

Chapter 4. Review: Analytical methods for fusing results from multiple simulators - Application to extreme loads on wind turbines

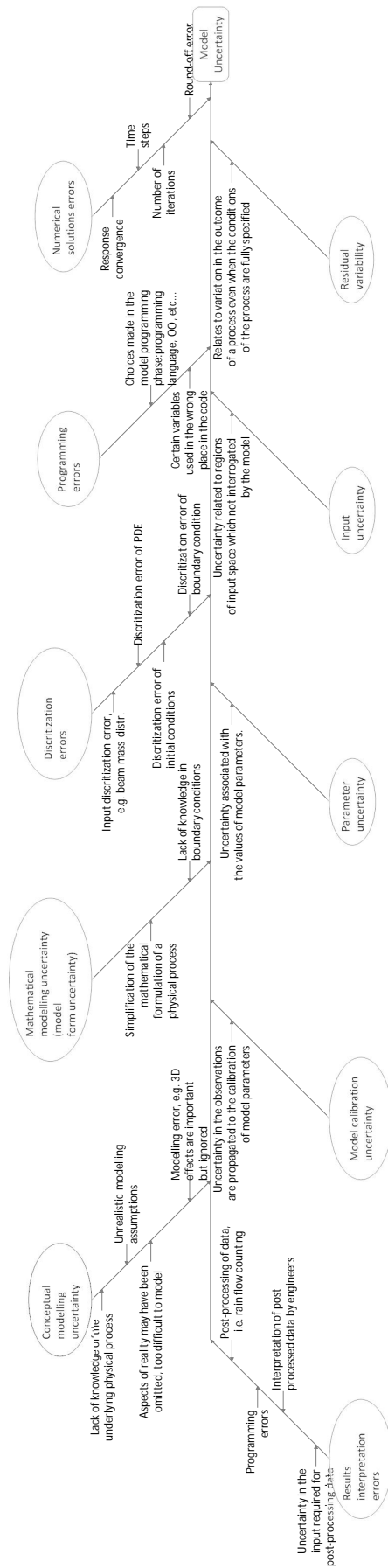


Figure 4.3: Fishbone depicting an overview of sources of model uncertainties in generic computational models/simulators of physical phenomena.

4.3 The case for data fusion

The simulators are considered as individual (and maybe correlated) information sources. We are thus able to maintain the output response from each aero-servo-elastic model and fuse these estimates rather than discard information from lower fidelity models [Allaire et al., 2010]. Fusing simulations predictions in the early stages of the conceptual design of a wind turbine results in risk mitigation and reduction in model uncertainty.

Wind turbine aero-servo-elastic simulators of varying fidelities exhibit similarities and dependence in terms of the input variables and the underlying physical models (aerodynamic, structural, control systems and wind inflow). The dependence amongst various simulators may not be quantified by a single scalar number; it may well be that the dependence varies as a function of the design and input space [Christensen, 2012].

Thus, we ask the fundamental question: Does it make any sense to fuse information from multifidelity aero-servo-elastic simulators \mathcal{M}_i ?

- To a great extent, simulators $\{\mathcal{M}_i, i=1, \dots, n\}$ share similar (type and structure) often identical inputs and describe similar (often identical) underlying modelling and physics assumptions.
- The output of the various aero-servo-elastic simulators is generally smooth with respect to small variations in the inputs.
- The various simulators may have been calibrated using the same test measurements.
- The higher fidelity simulators may simply be an expansion of the lower fidelity simulation model by inclusion of additional physics. The sub-models can differ from simulator to simulator either fully different (such as modal versus FEM) or partially different (such as simplified FEM formulation with some assumptions).
- Let us assume that for a given set of inputs $\mathcal{X} = [\mathbf{x}^{(1)}, \dots, \mathbf{x}^{(N)}]$, simulators \mathcal{M}_i predict responses $\mathcal{Y} = [\mathcal{M}_1(\mathbf{x}^{(1)}), \dots, \mathcal{M}_N(\mathbf{x}^{(N)})]^T$. For instance, given the same wind turbine specifications, various engineers can interpret, build and use the same aero-servo-elastic simulators while predicting different response $\{y_i, i = 1 \dots N\}$. Then, \mathcal{Y}_i generally share the same trend and do not differ significantly from each other. In addition, the simulators \mathcal{M}_i do not exhibit clear bias in the predicted response \mathcal{Y}_i .
- The various aero-servo-elastic simulators may have been coded by the same or cooperating engineers, scientists and research institutes, and the same experts may have given their inputs/reviews/recommendations during the development and validation of the various simulators \mathcal{M}_i resulting in similar assumptions, biases and even possibly gross errors being used.
- The various simulators \mathcal{M}_i are certified by accredited institutes for use in the industry to design wind turbines. The certification process involves a lengthy validation and verification against measurements. Hence, no particular simulator \mathcal{M}_i is deemed better than the other.

The implication of the argumentation above is that rather than treating the aero-servo-elastic numerical simulators as parts of a hierarchy, they are considered as individual (but correlated) information sources. Furthermore, the simulators are assumed to be black boxes and we focus on the output quantity of interest (response) \mathcal{Y}_i .

4.4 Analytical method 1: Co-Kriging

4.4.1 Problem setup

Several high fidelity wind turbine aero-servo-elastic numerical simulators are complex and expensive to run especially when multi-dimensional Design of Experiments (DoE) are required for uncertainty quantification, feasibility studies, optimizations, etc. Surrogate modelling (response surface) is one approach to address computationally expensive problems. In particular, variable-fidelity (also known as multi-fidelity) surrogate modelling techniques have proven to improve building a surrogate model for the output of a computer code; the strategy entails combining approximate but cheap simulations with sophisticated but expensive simulations for improving the precision of surrogate models without significantly impacting computational time.

Kriging is one such surrogate modelling technique. The mathematical fundamentals of Kriging and Co-Kriging are expanded below.

4.4.2 Kriging theory

Kriging is a method of interpolation for which the interpolated values are modeled by a Gaussian process. In this section we present a brief theoretical description of Kriging and Co-Kriging based on work by Sacks et al. [1989], Kennedy and O'Hagan [2000], Jones [2001], Forrester et al. [2007], Dubourg [2011], Han et al. [2012], Picheny et al. [2012], Sudret [2012] and Schöbi and Sudret [2014].

The main assumption behind Kriging is that the system response (model output) is a realization of a (unknown) Gaussian process. The Gaussian process is described by an autocorrelation function whose parameters are fitted from the experimental design [Schöbi and Sudret, 2014]. The Kriging surrogate modelling is a stochastic interpolation technique which assumes that the "true" model output (response) \mathcal{Y} is a realization of a Gaussian process:

$$Y(x) = \mu(x) + Z(x) \quad (4.1)$$

where $\mu(x)$ is the mean value of the Gaussian process (trend) and $Z(x)$ is a zero-mean stationary Gaussian process with variance σ_Y^2 and a Covariance of the form:

$$C(\mathbf{x}, \mathbf{x}') = \sigma_Y^2 R(\mathbf{x} - \mathbf{x}' \mid \boldsymbol{\theta}) \quad (4.2)$$

where $\boldsymbol{\theta}$ gathers the hyperparameters of the autocorrelation function R . From a design of experiments \mathcal{X} , one can build the correlation matrix with terms $\mathbf{R}_{ij} = R(\mathbf{x}^{(i)}, \mathbf{x}^{(j)} \mid \boldsymbol{\theta})$ representing the correlation between the sampled (observed) points. In the case of simple Kriging $\mu(x)$ is assumed to be a known constant. In the case of ordinary Kriging $\mu(x)$ is assumed to be an unknown constant. In the case of universal Kriging $\mu(x)$ is cast as $\sum_{j=1}^m \beta_j f_j(x)$, i.e. a linear combination of unknown (to be determined) linear regression coefficients $\beta_j, j = 1, \dots, m$ and a set of preselected basis functions $f_j(x), j = 1, \dots, m$ (usually predefined polynomial functions). The autocorrelation function R may be a generalized exponential kernel:

$$R(\mathbf{x}, \mathbf{x}') = \exp\left(-\sum_{i=1}^M \theta_i (\mathbf{x}_i - \mathbf{x}'_i)^{p_i}\right), \theta_i \geq 0, p_i \in (0, 2] \quad (4.3)$$

where M is the number of dimensions of the input space and θ_i and p_i are unknown parameters to be determined. Other choices for R is a Gaussian kernel, or a Matérn kernel, etc. In order to establish a Kriging surrogate model, a design of experiments is formed $\mathcal{X} = [\mathbf{x}^{(1)}, \dots, \mathbf{x}^{(N)}]$ and a corresponding set of computer simulations are performed. The output is gathered in a vector $\mathcal{Y} = [\mathcal{M}(\mathbf{x}^{(1)}), \dots, \mathcal{M}(\mathbf{x}^{(N)})]^T$. The Kriging estimator (predicted response given the design of experiments) at a new point $\mathbf{x}^* \in \mathcal{D}_X$ is a Gaussian variable $\hat{Y}(\mathbf{x}^*)$ with mean $\mu_{\hat{Y}}$ and variance $\sigma_{\hat{Y}}^2$ defined as (Best Linear Unbiased Estimator):

$$\begin{aligned} \mu_{\hat{Y}}(\mathbf{x}^*) &= \mathbb{E} \left[\hat{Y}(\mathbf{x}^*) \mid \mathcal{M}(\mathbf{x}^{(i)}) \right] \\ &= \mathbf{f}^T \hat{\boldsymbol{\beta}} + \mathbf{r}^T \mathbf{R}^{-1} (\mathcal{Y} - \mathbf{F} \hat{\boldsymbol{\beta}}) \end{aligned} \quad (4.4)$$

$$\begin{aligned} \sigma_{\hat{Y}}^2(\mathbf{x}^*) &= \text{Var} \left[\hat{Y}(\mathbf{x}^*) \mid \mathcal{M}(\mathbf{x}^{(i)}) \right] \\ &= \hat{\sigma}_Y^2 \left[\mathbf{1} - \mathbf{r}^T \mathbf{R}^{-1} \mathbf{r} + \mathbf{u}^T (\mathbf{F}^T \mathbf{R}^{-1} \mathbf{F})^{-1} \mathbf{u} \right] \end{aligned} \quad (4.5)$$

where the optimal Kriging variance $\hat{\sigma}_Y^2$ and optimal Kriging trend coefficients $\hat{\boldsymbol{\beta}}(\boldsymbol{\theta})$ are given by:

$$\hat{\sigma}_Y^2 = \frac{(\mathcal{Y} - \mathbf{F} \hat{\boldsymbol{\beta}})^T \mathbf{R}^{-1} (\mathcal{Y} - \mathbf{F} \hat{\boldsymbol{\beta}})}{N} \quad (4.6)$$

$$\hat{\boldsymbol{\beta}} = (\mathbf{F}^T \mathbf{R}^{-1} \mathbf{F})^{-1} \mathbf{F}^T \mathbf{R}^{-1} \mathcal{Y} \quad (4.7)$$

and \mathbf{u} , \mathbf{r} and \mathbf{F} are given by:

$$\mathbf{u} = \mathbf{F}^T \mathbf{R}^{-1} \mathbf{r} - \mathbf{f} \quad (4.8)$$

$$\mathbf{r} = \begin{bmatrix} R(\mathbf{x}^* - \mathbf{x}^{(1)}; \hat{\boldsymbol{\theta}}) \\ \vdots \\ R(\mathbf{x}^* - \mathbf{x}^{(N)}; \hat{\boldsymbol{\theta}}) \end{bmatrix} \quad (4.9)$$

$$\mathbf{F} = \left[f_j(\mathbf{x}^{(i)}) \right] = \begin{bmatrix} f_0(\mathbf{x}^{(1)}) & \dots & f_m(\mathbf{x}^{(1)}) \\ \vdots & & \vdots \\ f_0(\mathbf{x}^{(N)}) & \dots & f_m(\mathbf{x}^{(N)}) \end{bmatrix} \quad (4.10)$$

Note that \mathbf{r} is the correlation matrix between the sampled points and the point where a prediction is to be made. In the general case of a-priori unknown correlation parameters $\hat{\boldsymbol{\theta}}$, the optimal values can either be estimated through Bayesian inference, maximum likelihood estimate [Dubourg et al., 2011] or a leave-one-out cross-validation estimate (CV) [Bachoc, 2013]. Figure 4.4 shows an example of simulated blade root flapwise bending moment as a function of wind speed and the corresponding Kriging interpolation model. The Kriging is performed in the Matlab tool UQLab[Marelli and Sudret, 2014].

4.4.3 Kriging for noisy data

In case the outputs of the computer experiments contain "noise", the Kriging model should regress the data in order to generate a smooth trend. The Kriging thus amounts to conditioning $\hat{Y}(\mathbf{x}^*)$ on noisy observations $\mathcal{M}(\mathbf{x}^{(i)}) + \epsilon_i$. The Kriging estimator mean $\mu_{\hat{Y}}(\mathbf{x}^*)$ and variance $\sigma_{\hat{Y}}^2(\mathbf{x}^*)$ are given by Equations 4.4 and 4.5, respectively by replacing the correlation matrix \mathbf{R} with $\mathbf{R} + \lambda^2 \mathbf{I}$, where λ^2 is the estimated variance of the noise term ϵ_i . Figure 4.5 shows an example of simulated blade root flapwise bending moment as a function of wind speed and the corresponding Kriging model in noisy data. The Kriging is performed in the Matlab tool UQLab[Marelli and Sudret, 2014].

4.4.4 Co-Kriging theory

We now consider how to build a surrogate model of a highly complex and expensive to run aero-servo-elastic response that is enhanced by data from cheaper and approximate analyses of the response. Variations to the traditional Co-Kriging Kennedy and O'Hagan [2000] have been proposed under various names such as: "Hierarchical Kriging", "multifidelity surrogate modelling", "variable fidelity surrogate modelling", "data fusion", "multistage surrogate modelling" "Recursive Co-Kriging", etc. We present a brief theoretical definition of Co-Kriging based on work by Han [2012]: We consider l sets of response data obtained by running l aero-servo-elastic numerical simulators of varying fidelity and computational expense. We denote by level s the response data of the highest level of fidelity. For any given level $1 \leq l \leq s$, co-Kriging can be written as:

$$\mu_{\hat{Y}}^{(l)} = \hat{\beta} \mu_{\hat{Y}}^{(l-1)} + \mathbf{r}^T \mathbf{R}^{-1} (\mathcal{Y} - \mathbf{F} \hat{\beta}) \quad (4.11)$$

where $\hat{\beta}$ is a scaling factor with a similar expression as in Equation 4.7, indicating how much the low- and high-fidelity responses are correlated to each other. $\mu_{\hat{Y}}^{(l-1)}$ is the trend in the Kriging of the data at level l and the expression $\mathbf{R}^{-1} (\mathcal{Y} - \mathbf{F} \hat{\beta})$ depends only on the sampled data at level l . An appealing feature of the above formulation is that it entails very little modifications to an existing Kriging code if the latter is sufficiently modular. Figure 4.6 shows an example of simulated blade root flapwise bending moment as a function of wind speed in a high fidelity simulator and the corresponding Co-Kriging mode. The trend is based on the low fidelity Kriging model shown in Figure 4.4. The Co-Kriging is performed in the Matlab tool UQLab[Marelli and Sudret, 2014]. We see that based on only three high fidelity observations, the Co-Kriging model shows an improved prediction capability compared to the Kriging model.

One may argue that few additional high fidelity data points would result in a superior Kriging predictions (i.e. Kriging and Co-Kriging would yield the similar prediction errors) without the need to run multiple additional low fidelity simulations. This is probably a valid argument if the purpose is to only get a surrogate model for the high fidelity response; in such a case the analyst is better off with directly performing HF simulations at the appropriately sampled space. However, this argument is valid for a low dimensional problem, it becomes far more difficult in high dimensional problems. In this research both the high fidelity and low fidelity responses are needed to perform model uncertainty quantification; hence, the low fidelity response is being simulated anyway so might as well make use of this additional data to built the high fidelity

surrogate model at, presumably, a lower cost. Another point worth making is that the Kriging and Co-Kriging surrogate models shown above would differ had the high fidelity observations (green circles) been sampled differently. The high fidelity observations were chosen such that they correspond to the wind turbine cut-in wind speed, cut-out wind speed and rated wind speed where the peak load occurs.

4.4.5 Demonstration of Co-Kriging in UQLab

UQLab [Marelli and Sudret, 2014] is a software framework for uncertainty quantification (UQ) written in Matlab, based on the global theoretical framework developed by [Sudret, 2007a].

Example 1: Co-Kriging of one dimensional analytical functions: The analytical function of the low fidelity simulations is given by (Forrester 2007 and Le Gratiet 2013):

$$y_1(x) = 0.5(6x - 2)^2 \sin(12x - 4) + 10(x - 0.5) - 5 \quad (4.12)$$

The analytical function of the high fidelity simulations is given by:

$$y_2(x) = 2y_1(x) - 20x + 20 \quad (4.13)$$

The experimental design set of the low fidelity simulations is $D_1 = \{0 : 0.1 : 1\}$, and the experimental design set of the high fidelity simulations is $D_2 = \{0, 0.4, 0.6, 1\}$. Figure 4.7 shows a comparison between the ordinary Kriging using only the high fidelity data and the co-Kriging using high and low fidelity data. The Kriging in both Figure 4.7(a) and (b) are done using ordinary Kriging with a *Gaussian* autocorrelation function type.

Example 2: Co-Kriging of one dimensional analytical functions: The analytical function of the low fidelity simulations is given by (Le Gratiet 2013 and Forrester 2007):

$$y_1(x) = 0.5(6x - 2)^2 \sin(12x - 4) + 10(x - 0.5) - 5 \quad (4.14)$$

The analytical function of the high fidelity simulations is given by:

$$y_2(x) = 2y_1(x) - 20x + 20 + \sin(10 \cos(5x)) \quad (4.15)$$

The experimental design set of the low fidelity simulations is $D_1 = \{0 : 0.1 : 1\}$, and the experimental design set of the high fidelity simulations is $D_2 = \{0, 0.4, 0.6, 1\}$. Through the term $\sin(10 \cos(5x))$, the high fidelity simulations have high frequency content which are not captured by the low fidelity simulations. Figure 4.8 shows a comparison between the ordinary Kriging using only the high fidelity data and the co-Kriging using high and low fidelity data. The high frequency content are not predicted since they are not captured by the low fidelity simulations nor is the size of the experimental design sufficient enough to detect them either. The Kriging in both Figure 4.8(a) and (b) are done using ordinary Kriging with a *Gaussian* autocorrelation function type.

Chapter 4. Review: Analytical methods for fusing results from multiple simulators - Application to extreme loads on wind turbines

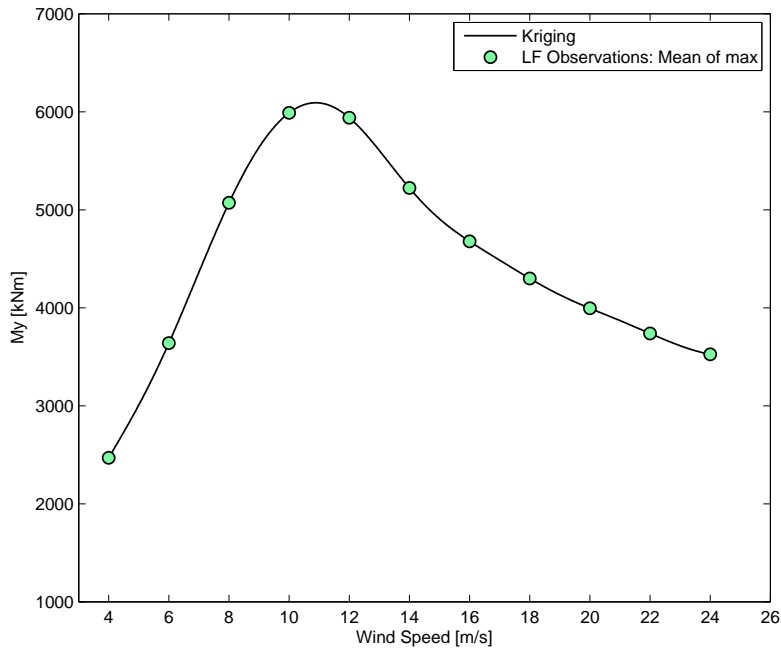


Figure 4.4: Kriging model of simulated (observations) blade root flapwise bending moment as a function of wind speed. A Universal Kriging model is fitted to the response using a Gaussian correlation function R and a 3^{rd} -order polynomial basis.

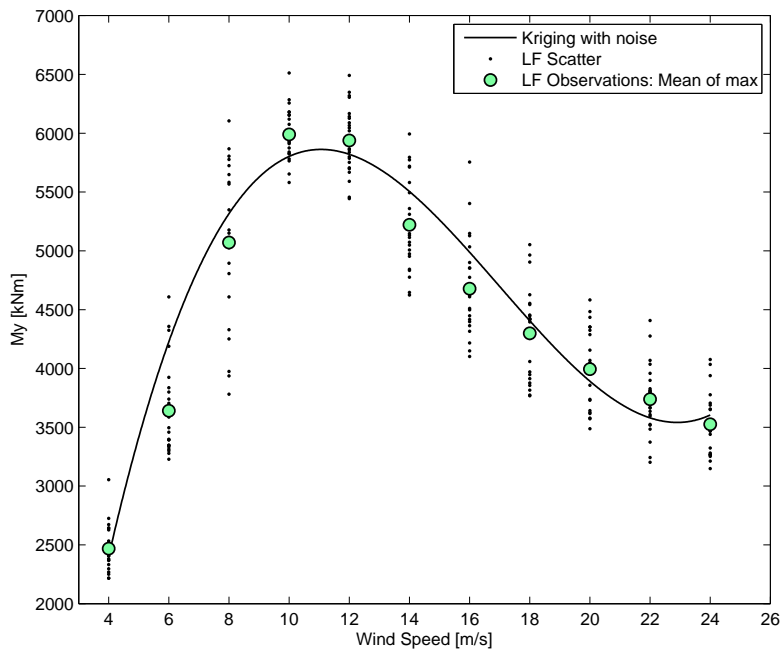


Figure 4.5: Kriging model of simulated (observations) blade root flapwise bending moment as a function of wind speed with noisy data. The mean of the 24 samples is calculated and represented by the black dots (mean of max). The mean of max in this figure are the same as in Figure 4.4. A Universal Kriging model with a nugget (noise) is fitted to the response using a Gaussian correlation function R and a 3^{rd} -order polynomial basis. The noise is represented by the variance of the response scatter at each wind speed.

4.4. Analytical method 1: Co-Kriging

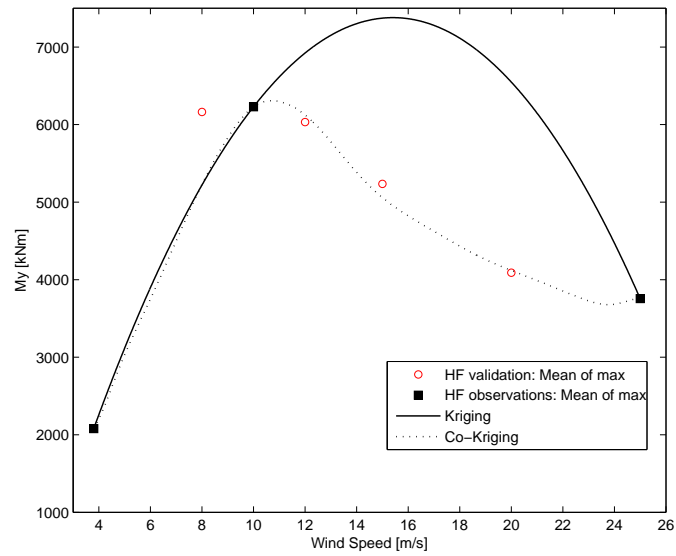


Figure 4.6: Response of the high-fidelity simulator at 3 wind speeds (black squares). The Kriging model is the dashed green line. The Co-Kriging model is the dotted red line. The trend of the Co-Kriging model is based on the low fidelity Kriging model shown in Figure 4.4.

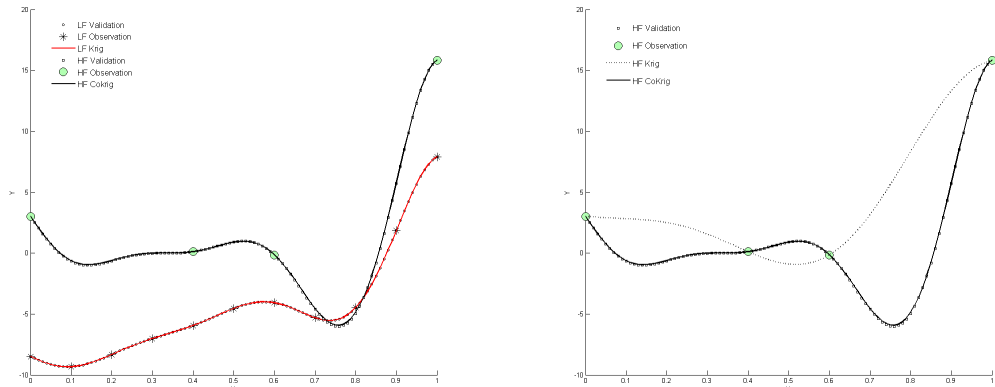


Figure 4.7: plots of the Kriging and Co-Kriging surrogate models. The Co-Kriging model represents well the high fidelity validation data compared to ordinary Kriging.

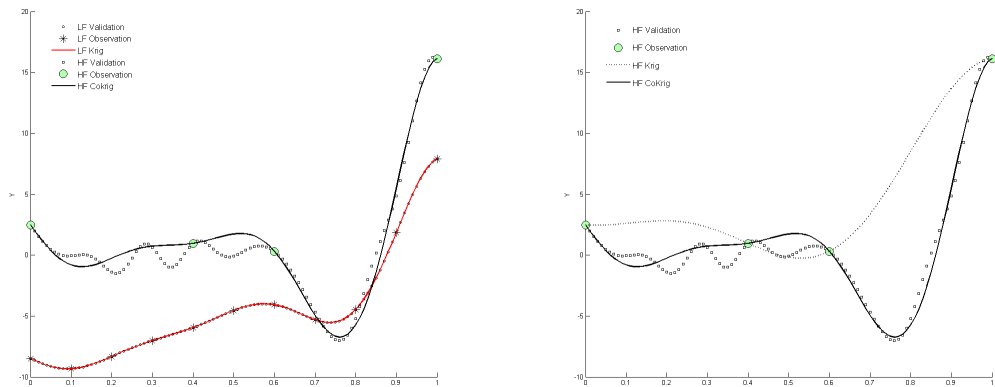


Figure 4.8: The Co-Kriging model represents better the high fidelity validation data. The Co-Kriging surrogate model is unable to capture the high frequency content in the high fidelity simulations.

4.5 Analytical method 2: the multivariate normal aggregation approach

Here we present a theoretical description of the multivariate normal aggregation approach based on [Winkler, 1981, Clemen and Winkler, 1999, Allaire et al., 2010, Allaire and Willcox, 2014].

4.5.1 Theory of the the multivariate normal aggregation approach

The objective of this method is to combine the output from various numerical simulators while taking into account any correlation (dependence) amongst the numerical simulators. The multivariate normal aggregation approach is based on a Bayesian formulation. This approach was first proposed by [Winkler, 1981]. Suppose that the fused/combined quantity of interest is denoted by random variable \mathcal{Y}^* . Numerical simulation model \mathcal{M}_i predicts a mean and variance value of \mathcal{Y}^* given by μ_i and σ_i^2 , respectively. We define a vector of errors (discrepancies) between the true value of \mathcal{Y}^* and its model estimates $\epsilon = (\mu_1 - \mathcal{Y}^*, \mu_2 - \mathcal{Y}^*, \dots, \mu_N - \mathcal{Y}^*)$. ϵ is thus multivariate normal such that ϵ follows a multivariate Normal distribution $\epsilon \sim MVN(0, \Sigma)$ where Σ is the covariance matrix. We note that ϵ can vary throughout the input space. Using a Bayesian formulation, we write:

$$P(\mathcal{Y}^* | \mu_i) \propto P(\mathcal{Y}^*) P(\mu_1 - \mathcal{Y}^*, \mu_2 - \mathcal{Y}^*, \dots, \mu_N - \mathcal{Y}^*) \quad (4.16)$$

where $P(\mu_1 - \mathcal{Y}^*, \mu_2 - \mathcal{Y}^*, \dots, \mu_N - \mathcal{Y}^*)$ is the likelihood function. Assuming an improper and noninformative flat prior $P(\mathcal{Y}^*)$ then:

$$P(\mathcal{Y}^* | \mu_i) \propto P(\mu_1 - \mathcal{Y}^*, \mu_2 - \mathcal{Y}^*, \dots, \mu_N - \mathcal{Y}^*) \quad (4.17)$$

Given the noninformative prior and a multivariate normal distribution for $\epsilon \sim MVN(0, \Sigma)$, then the posterior density for \mathcal{Y}^* is:

$$P(\mathcal{Y}^* | \mu_i) = \frac{1}{\sqrt{2\pi Var[\mathcal{Y}^*]}} \exp\left(-\frac{(\mathcal{Y}^* - E[\mathcal{Y}^*])^2}{2Var[\mathcal{Y}^*]}\right) \quad (4.18)$$

where

$$E[\mathcal{Y}^*] = \frac{e' \Sigma^{-1} \mu}{e' \Sigma^{-1} e} \quad (4.19)$$

$$Var[\mathcal{Y}^*] = \frac{1}{e' \Sigma^{-1} e}$$

where e is a vector of 1, $e = [1 \dots 1]$. The covariance matrix Σ is written as a function of the individual model predictions variances σ_i^2 and the correlation between models \mathcal{M}_i and \mathcal{M}_j :

$$\Sigma = \begin{pmatrix} \sigma_1^2 & \rho_{12}\sigma_1\sigma_2 & \dots & \rho_{1N}\sigma_1\sigma_N \\ \rho_{21}\sigma_2\sigma_1 & \sigma_2^2 & \dots & \rho_{1N}\sigma_1\sigma_N \\ \cdot & \cdot & \dots & \cdot \\ \cdot & \cdot & \dots & \cdot \\ \rho_{N1}\sigma_N\sigma_1 & \rho_{N2}\sigma_N\sigma_2 & \dots & \sigma_N^2 \end{pmatrix} \quad (4.20)$$

For example, if two numerical simulation models are used to predict the fused/combined quantity

4.5. Analytical method 2: the multivariate normal aggregation approach

of interest \mathcal{Y}^* , then the expected value and variance of \mathcal{Y}^* become:

$$\begin{aligned} E[\mathcal{Y}^*] &= \frac{(\sigma_2^2 - \rho_{12}\sigma_1\sigma_2)\mu_1 + (\sigma_1^2 - \rho_{12}\sigma_1\sigma_2)\mu_2}{\sigma_1^2 + \sigma_2^2 - 2\rho_{12}\sigma_1\sigma_2} \\ Var[\mathcal{Y}^*] &= \frac{(1 - \rho_{12}^2)\sigma_1^2\sigma_2^2}{\sigma_1^2 + \sigma_2^2 - 2\rho_{12}\sigma_1\sigma_2} \end{aligned} \quad (4.21)$$

A main assumption is to consider the quantity \mathcal{Y}^* as normally distributed, which is not necessarily the case.

4.5.2 Toy examples on the multivariate normal aggregation approach

Figure 4.9 shows how this method is used to aggregate predictions from three numerical models. The plots in (a_1 , a_2 and a_3) demonstrate how aggregation is performed when the predictions of the numerical simulation models are similar to each other in terms of mean and variance. The output mean and variance of the three simulators are:

$$\mu = \{21500 \quad 22100 \quad 23500\} \quad \sigma^2 = \{110000 \quad 75000 \quad 140000\} \quad (4.22)$$

The outputs are assumed to be normally distributed. In a_1 the output of the simulators are assumed independent with correlation matrix \mathbf{R}_1 . As a result, the aggregated prediction has a mean which is the average of the three numerical simulation models and a variance smaller than the three numerical simulation models ($\sigma_{agg}^2 = 3.34 \cdot 10^4$). In the absence of correlation there is no overlapping of information from the various simulators, resulting in low aggregated model variance. In a_2 the output of the simulators are assumed dependent with correlation¹ matrix \mathbf{R}_2 . In this case the variance of the aggregated prediction increases to ($\sigma_{agg}^2 = 6.45 \cdot 10^4$) and pushes the aggregated prediction mean towards the model with the lowest variance. In a_3 the output of the simulators are assumed highly correlated with correlation matrix Σ_3 . In this case the variance of the aggregated prediction increases to ($\sigma_{agg}^2 = 6.45 \cdot 10^4$). As the correlation amongst the models increases, the aggregated model becomes more spread, intuitively this means that less information is available when dependence amongst simulators is higher. In addition, as the correlation increases considerably (a_3), the aggregated prediction tends to the left of all three models. This is explained by the fact that highly correlated model predictions will tend to be on the same side of the "true" model prediction. Note that in all cases presented above, the variance of the aggregated prediction is still lower than the output variance of any of the three simulators.

$$\mathbf{R}_1 = \begin{pmatrix} 1 & 0 & 0 \\ 0 & 1 & 0 \\ 0 & 0 & 1 \end{pmatrix}, \quad \mathbf{R}_2 = \begin{pmatrix} 1 & 0.6 & 0.5 \\ 0.6 & 1 & 0.4 \\ 0.5 & 0.4 & 1 \end{pmatrix}, \quad \mathbf{R}_3 = \begin{pmatrix} 1 & 0.9 & 0.9 \\ 0.9 & 1 & 0.9 \\ 0.9 & 0.9 & 1 \end{pmatrix} \quad (4.23)$$

The plots b_1 , b_2 and b_3 in Figure 4.9 demonstrate how aggregation is performed when the output of the numerical simulators are dissimilar to each other in terms of variance; the variance of the output of simulator 2 is considerably smaller compared to the variance of the output of simulators 1 and 3. This could be the case if for instance simulator 2 is of high fidelity while simulators 1 and 3 and of lower fidelity:

$$\mu = \{21500 \quad 22100 \quad 23500\} \quad \sigma^2 = \{250000 \quad 75000 \quad 1000000\} \quad (4.24)$$

¹The covariance $\Sigma = \mathbf{DRD}$, where \mathbf{D} is a diagonal matrix containing the standard deviations and \mathbf{R} is the correlation matrix.

Chapter 4. Review: Analytical methods for fusing results from multiple simulators - Application to extreme loads on wind turbines

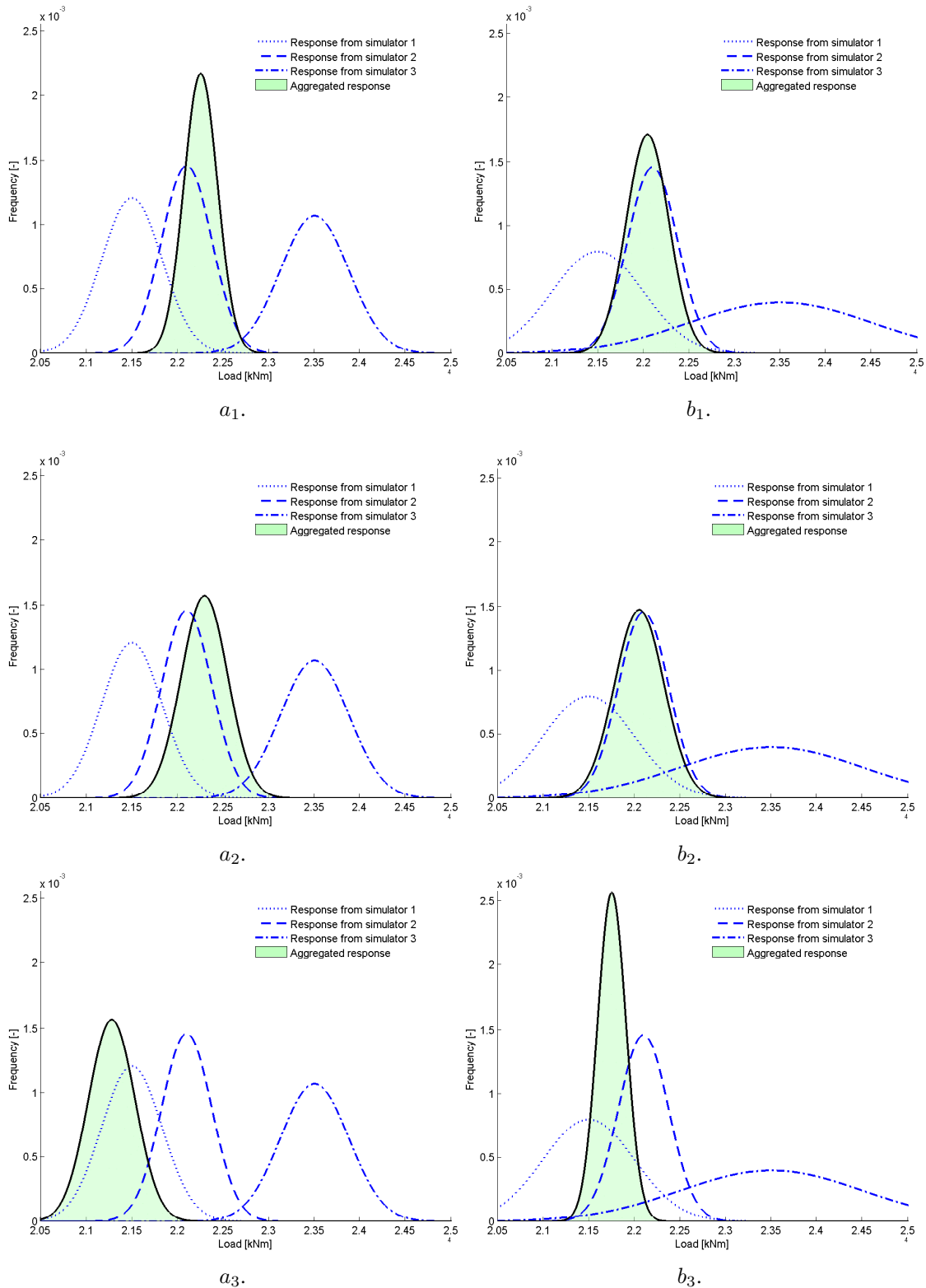


Figure 4.9: Plots depicting an application to the multivariate normal aggregation approach. a_1 , a_2 , and a_3 demonstrate the aggregation of three outputs from three simulators with close variances. In a_1 the three simulators outputs are independent while in a_3 the outputs are highly correlated. b_1 , b_2 , and b_3 demonstrate the aggregation of three outputs from three simulators with one of the variances significantly larger than the other two. In b_1 the three simulators outputs are independent while in b_3 the outputs are highly correlated.

4.6. Analytical method 3: Adjustment Factor Approach

In b_1 the output of the simulators are assumed uncorrelated, and as we move to the plot in b_3 the correlation amongst the output of the simulators are assumed to increase considerably. In b_1 , b_2 and b_3 , the aggregated model prediction will tend to be close to the output of the simulator with the lowest variance (discrepancy). The aggregated prediction will also tend to have a smaller variance compared to the three simulators output. Unlike in plot a_3 , as the model correlation increases considerably in (b_3), the aggregated prediction variance decreases considerably to ($\sigma_{agg}^2 = 2.40 \cdot 10^4$), which is explained by the fact that a diffuse model (output of simulator 3) and low variance model (output of high fidelity simulator 2) are highly correlated which suggests that the high variance model contribution is under-estimated, i.e. the high variance simulator is providing us with more valuable information than its high variance (low fidelity) leads us to believe, since it is highly correlated to a high fidelity simulator [Allaire et al., 2010].

4.6 Analytical method 3: Adjustment Factor Approach

4.6.1 Theory of the Adjustment Factor Approach

In the absence of any empirical experimental data of the system at the design stage, we must resort to alternative methods in order to quantify the model uncertainty of the quantities of interest ([Mosleh and Apostolakis, 1986], [Zio and Apostolakis, 1996], [Riley, 2007], [Park et al., 2010], and [Riley and Grandhi, 2011]). The Adjustment Factor Approach makes use of an adjustment factor that is added (or multiplied) to the best model amongst all models considered. The best model is assigned a probability by expert opinion. The adjustment factor may represent aleatory or epistemic uncertainties.

Let $P(\mathcal{M}_i)$ be the probability of simulator $\{\mathcal{M}_i, i = 1 \dots N\}$:

$$\sum_{i=1}^N P(\mathcal{M}_i) = 1 \quad (4.25)$$

It should be noted that the simulator probabilities $P(\mathcal{M}_i)$ are assigned by expert judgement based on the merit and accuracy of each individual simulator. The probabilities reflect a degree of belief that a simulator is the best approximating model among a set of models. The expert judgement however could be biased or correlated; expert talk to each other, probably share the same information, etc. Let \mathcal{Y}^* be the output (quantity of interest) of the simulator with the highest probability assigned by expert opinion. The simulator output \mathcal{Y} can be expressed as a function of \mathcal{Y}^* and an adjustment factor:

$$\mathcal{Y} = \mathcal{Y}^* + \epsilon_a^* \quad (4.26)$$

where ϵ_a^* is the so called "additive adjustment factor". ϵ_a^* is assumed to be normally distributed with an expected value and variance:

$$\begin{aligned} E[\epsilon_a^*] &= \sum_{i=1}^N P(\mathcal{M}_i)(\mathcal{Y}_i - \mathcal{Y}^*) \\ Var[\epsilon_a^*] &= \sum_{i=1}^N P(\mathcal{M}_i)(\mathcal{Y}_i - E[\mathcal{Y}])^2 \end{aligned} \quad (4.27)$$

where \mathcal{Y}_i is the prediction of the quantity of interest from model \mathcal{M}_i and $P(\mathcal{M}_i)$ represents the

Chapter 4. Review: Analytical methods for fusing results from multiple simulators - Application to extreme loads on wind turbines

model probability of model \mathcal{M}_i .

The expected value and variance of a simulator's output can now be written as:

$$\begin{aligned} E[\mathcal{Y}] &= \mathcal{Y}^* + E[\epsilon_a^*] \\ Var[\mathcal{Y}] &= Var[\epsilon_a^*] \end{aligned} \quad (4.28)$$

Alternative, instead of the additive adjustment factor, a multiplicative adjustment factor can be proposed:

$$\mathcal{Y} = \mathcal{Y}^* \cdot \epsilon_m^* \quad (4.29)$$

where ϵ_m^* is the so called multiplicative adjustment factor. If we assumed ϵ_m^* to be lognormally distributed with first and second moments:

$$\begin{aligned} E[\epsilon_m^*] &= \sum_{i=1}^N P(\mathcal{M}_i)(LN(\mathcal{Y}_i) - LN(\mathcal{Y}^*)) \\ Var[\epsilon_m^*] &= \sum_{i=1}^N P(\mathcal{M}_i)(LN(\mathcal{Y}_i) - E[LN(\mathcal{Y})])^2 \end{aligned} \quad (4.30)$$

Similarly, the expected value and variance of a simulator's output become:

$$E[\mathcal{Y}] = LN(\mathcal{Y}^*) + E[LN(\epsilon_a^*)] \quad (4.31)$$

$$Var[\mathcal{Y}] = Var[LN(\epsilon_a^*)] \quad (4.32)$$

The above derivation of the adjustment factor approach assumes \mathcal{Y} and \mathcal{Y}^* to be deterministic. However, the responses could be stochastic in nature (i.e. due to input parameters uncertainty):

$$f_{\mathcal{Y}_i} \sim \mathcal{N}(\mu_i, \sigma_i) \forall i = 1 \dots N \quad (4.33)$$

The model response can then be written as:

$$\mathcal{Y} = E[\mathcal{Y}^*] + \epsilon_a^* \quad (4.34)$$

where \mathcal{Y}^* is stochastic and hence the use of the expectation $E[\cdot]$. The first and second moments of the additive adjustment factor become:

$$\begin{aligned} E[\epsilon_a^*] &= \sum_{i=1}^N P(\mathcal{M}_i)(E[\mathcal{Y}_i] - E[\mathcal{Y}^*]) \\ Var[\epsilon_a^*] &= \sum_{i=1}^N P(\mathcal{M}_i)(E[\mathcal{Y}_i] - E[\mathcal{Y}])^2 \end{aligned} \quad (4.35)$$

Finally, the expected value and variance of model predictions become:

$$\begin{aligned} E[\mathcal{Y}] &= E[\mathcal{Y}^*] + E[\epsilon_a^*] \\ Var[\mathcal{Y}] &= \underbrace{Var[\epsilon_a^*]}_{\text{Within model variance}} + \underbrace{\sum_{i=1}^N P(\mathcal{M}_i)(Var[\mathcal{Y}_i])^2}_{\text{Between model variance}} \end{aligned} \quad (4.36)$$

The above probabilistic adjustment factor approach can similarly be written in terms of the

4.6. Analytical method 3: Adjustment Factor Approach

multiplicative adjustment factor. The probabilistic adjustment factor approach can also be written if f_{y_i} follows a Beta distribution or a lognormal distribution for instance.

Deriving the adjustment factor approach relies on $P(\mathcal{M}_i)$ which are mostly based on expert opinion at the design phase of the system. So far $P(\mathcal{M}_i)$ is assigned a deterministic value. It is interesting to check the sensitivity of the model response \mathcal{Y} on the uncertainty due to $P(\mathcal{M}_i)$. As such, $P(\mathcal{M}_i)$ becomes a random variable:

$$P(\mathcal{M}_i) \sim \mathcal{N}(P(\mathcal{M}_i)_{exp}, \sigma_i) \forall i = 1 \dots N \quad (4.37)$$

where $\sigma_i = \min[0.05, 0.25 \cdot P(\mathcal{M}_i)_{exp}]$. The N probability distributions are then independently sampled m times using Monte Carlo sampling resulting in a set of modified adjusted models $\{\mathcal{Y}_{adj}^{(j)}, j = 1 \dots m\}$. The individual adjusted models are then sampled k times. Using the k samples from the m adjusted models, a new aggregate adjusted model \mathcal{Y}_{mafa} can then be constructed by fitting a distribution to the samples.

4.6.2 Demonstration of the Adjustment Factor Approach

Three aeroelastic simulators are used to predict an extreme bending moment response for the same wind turbine geometry and structure, terrain, inflow conditions and turbulence. The simulators' output and the probabilities assigned by expert judgement are shown in Table 4.1.

In table 4.1 we see up to 10% variation in the prediction of the extreme bending moment. Since all three aeroelastic simulators are based on sound physics it is difficult for an analyst to decide which extreme load level is "most correct". Thus, all three values are used to quantify the model uncertainty while predicting the most likely extreme load level at the design stage. Using the values in Table 4.1 and using the adjustment factor approach and the modified adjustment factor approach, the expected value and standard deviation of the bending moment are shown in Table 4.2. The additive adjustment factor and modified adjustment factor yield a normal uncertainty distribution around the expected value of the load level as shown in Figure 4.10. Both methods yield similar results indicating that in this case the uncertainty model is not sensitive to the models probabilities assigned by the expert judgement.

Table 4.1: Simulators predictions of bending moments and Model probabilities.

Simulator	Load [kNm]	$P(\mathcal{M}_i)_{exp}$
Aeroelastic Simulator 1	21500	0.45
Aeroelastic Simulator 2	23500	0.20
Aeroelastic Simulator 3	22100	0.35

Table 4.2: Distribution parameters of the adjustment factor approach.

Method	Mean [kNm]	STD [kNm]
Additive Adjustment Factor	22110	744
Modified Adjustment Factor	22099	693

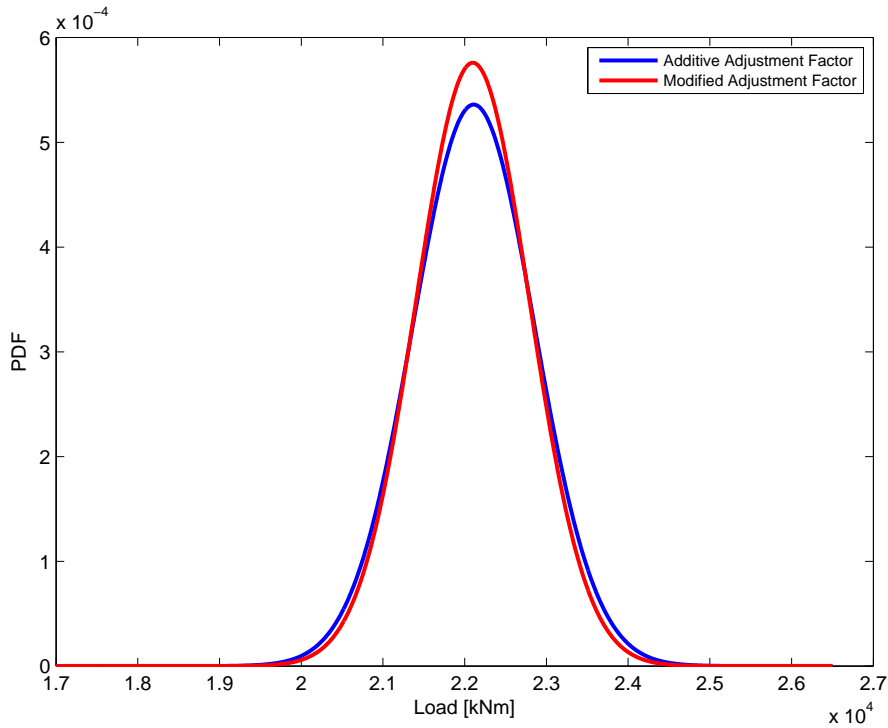


Figure 4.10: Load level prediction by the adjustment factor approach.

4.7 Analytical method 4: copula models for aggregation of multi-model simulations

Dependence amongst the numerical simulation models in the multivariate normal aggregation approach is introduced through the covariance matrix. A natural extension to the previous method is to use the Copula formalism to capture the dependence amongst the simulators. A Copula is a function that links/"glues" the marginals of the quantity of interest (output of the simulator). The quantity of interest is described by its marginal distributions (one marginal distribution per simulator), and dependence among the marginals is embedded into the Copula function, which joins the marginal distributions into a single multivariate distribution. The structure and type of the Copula can be either be derived through expert opinion or through fitting to the output of simulators.

4.7.1 Theory of the Copula models for aggregation

The theory originally proposed by [Jouini and Clemen, 1995] uses Copulas as the basis for modelling dependence among the experts' opinions; here the experts' opinions are substituted for the output of n simulators $\{s_i, \forall i = 1 \dots n\}$. Suppose that the quantity of interest is denoted by random variable Y and simulators s_i provide their estimate of Y . The objective is to determine the posterior distribution of Y given the estimates made by s_i , formally this can be written in Bayesian format as:

$$p(\mathcal{Y} \mid s_1, s_2, \dots, s_n) \propto \underbrace{p(\mathcal{Y})}_{\text{prior}} \underbrace{l(s_1, s_2, \dots, s_n \mid \mathcal{Y})}_{\text{likelihood}} \quad (4.38)$$

4.7. Analytical method 4: copula models for aggregation of multi-model simulations

The prior density function can be interpreted as the prior belief of an analyst about \mathcal{Y} ; in the context of wind turbine loads this could for instance represent former measurements on similar turbines or estimation of the loads based on some scaling rules. The likelihood function assesses the probability of \mathcal{Y} arising from simulators s_i , it can also be interpreted as the analyst's belief about the quality/ability of simulators s_i to estimate and predict \mathcal{Y} and dependence amongst them. If the analyst believes that numerical simulation model s_i is very accurate, then the estimates of s_i will be expected to fall near \mathcal{Y} . On the other hand, if the numerical simulation model is thought to be inaccurate or biased, then the estimates of s_i will be expected to fall substantially above or below \mathcal{Y} . In addition, the likelihood density function l is also expected to capture aspects of dependence amongst the numerical simulation models.

The conditional likelihood can thus be given by the conditional version of the Sklar's Theorem; thus an expression equivalent to Equation 3.14 is given by [Jouini and Clemen, 1995, Smith, 2011]:

$$L(s_1, s_2, \dots, s_n | \mathcal{Y}) = C_n \left[L_1(s_1 | \mathcal{Y}), L_2(s_2 | \mathcal{Y}), \dots, L_n(s_n | \mathcal{Y}) \right] \quad (4.39)$$

The conditional likelihood L is constructed as an n -dimensional joint CDF in terms of n marginal distributions and a copula that captures the dependence among the individual random variables². C_n is a unique n -dimensional Copula. Taking the n^{th} mixed derivative of L with respect to s_1, s_2, \dots, s_n generates the likelihood function l such as:

$$\begin{aligned} l &= \frac{\partial^n L}{\partial s_1 \dots \partial s_n} \\ &= \frac{\partial^n C}{\partial u_1 \dots \partial u_n} \cdot \frac{dL_1}{ds_1} \cdot \frac{dL_2}{ds_2} \dots \cdot \frac{dL_n}{ds_n} \\ &= C_n \left[L_1(s_1 | \mathcal{Y}), L_2(s_2 | \mathcal{Y}), \dots, L_n(s_n | \mathcal{Y}) \right] \cdot l_1 \cdot l_2 \dots \cdot l_n \end{aligned} \quad (4.40)$$

where $l_1 \dots l_n$ are the marginals given by $l_1 = l_1(s_1 | \mathcal{Y}), \dots, l_n = l_n(s_n | \mathcal{Y})$. Finally, the posterior distribution of the quantity of interest Y becomes:

$$p(\mathcal{Y} | s_1, \dots, s_n) \propto p(\mathcal{Y}) \cdot C_n \left[L_1(s_1 | \mathcal{Y}), L_2(s_2 | \mathcal{Y}), \dots, L_n(s_n | \mathcal{Y}) \right] \cdot l_1 \cdot l_2 \dots \cdot l_n \quad (4.41)$$

When more than two simulators are involved ($s_i, i > 2$), then multi-dimensional Copulas are required. Recent research in the copula literature has focused on building copulas in $i > 2$ dimensions, including 'Vines' [Clemen and Winkler, 1993, Joe, 1996, 1997, Bedford and Cooke, 2002], [Brechmann et al., 2013], 'Pair-Copulas' [Schirmacher and Schirmacher, 2008] and [Aas et al., 2009] and 'Hierarchical Archimedean Copulae' [Ristig, 2014]. Recent overviews are given by [Hobæk et al., 2010] and [Czado, 2010]. It can be easily shown that the Copula aggregation approach is equivalent to the multivariate normal aggregation approach when the marginals are normal and the Copula is Gaussian.

4.7.2 Demonstration of the Copula Aggregation Method

Say that the marginals are defined as $s_1 \sim \mathcal{LN}(\mu = 21500kNm, \sigma^2 = 110000kNm)$ and $s_2 \sim \mathcal{LN}(\mu = 23500kNm, \sigma^2 = 1000000kNm)$, and say we establish that the dependence

²An alternative is given by [Clemen and Winkler, 1993].

Chapter 4. Review: Analytical methods for fusing results from multiple simulators - Application to extreme loads on wind turbines

structure between the output of simulator s_1 and the output of simulator s_2 fit a Gumbel Copula with a Kendall's $\tau = 0.5$, then the joint (multivariate) likelihood density function is derived as shown in Figure 4.11.

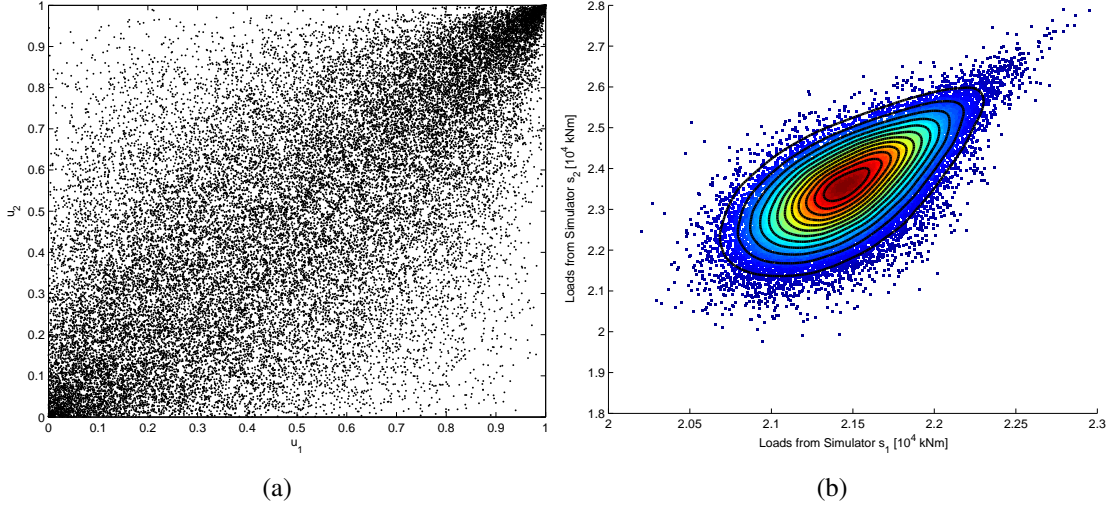


Figure 4.11: (4.11a) Samples from a Gumbel copula and (4.11b) joint pdf of loads from numerical simulation models s_1 and s_2 . $s_1 \sim \mathcal{LN}(\mu = 21500kNm, \sigma^2 = 110000kNm)$ and $s_2 \sim \mathcal{LN}(\mu = 23500kNm, \sigma^2 = 140000kNm)$.

Having derived the joint (multivariate) likelihood density function $l(s_1, s_2 | \mathcal{Y})$, the next step is to determine the posterior distribution $p(\mathcal{Y} | s_1, s_2)$ of the quantity of interest (as in Equation 4.41), namely the load as shown in Figure 4.12, 4.13 and 4.14.

In Figure 4.12 the aggregation of the Lognormal distributions is done through a Gumbel Copula with Kendall's $\tau = 0.5$. In Figure 4.13 the aggregation of the Lognormal distributions is done through a Frank Copula with Kendall's $\tau = 0.5$. In Figure 4.14 the aggregation of the Lognormal distributions is done through a Gaussian Copula with Kendall's $\tau = 0.5$. For each case, we also show how the aggregated posterior distribution of the load output varies as a function of the Kendall's τ values. We see that with increasing correlation amongst the simulators (larger Kendall's τ) the aggregated posterior distribution moves closer and to the left of simulator 1 which has a lowest variance. In addition, with increasing correlation amongst the simulators (larger Kendall's τ) the variance of the aggregated posterior distribution decreases (less spread). Furthermore, whether the dependence structure is described by a Gaussian, Gumbel or Frank Copula, we see that the aggregated models are not significantly different. This indicates that predicting the most likely load level might not be affected by the choice of the dependence structure amongst the simulators. The reason for this is the large difference in the predictive spread (variance) of the output between simulator 1 and simulator 2, as a result of which the aggregated model does not differ significantly from the output of simulator 1. Contrast that with the results in Figures 4.15 to 4.17 where the variance of the output of the three simulators are similar. Here the distributions are: $s_1 \sim \mathcal{LN}(\mu = 21500kNm, \sigma^2 = 110000kNm)$, $s_2 \sim \mathcal{LN}(\mu = 22100kNm, \sigma^2 = 75000kNm)$, and $s_3 \sim \mathcal{LN}(\mu = 23500kNm, \sigma^2 = 140000kNm)$.

4.7. Analytical method 4: copula models for aggregation of multi-model simulations

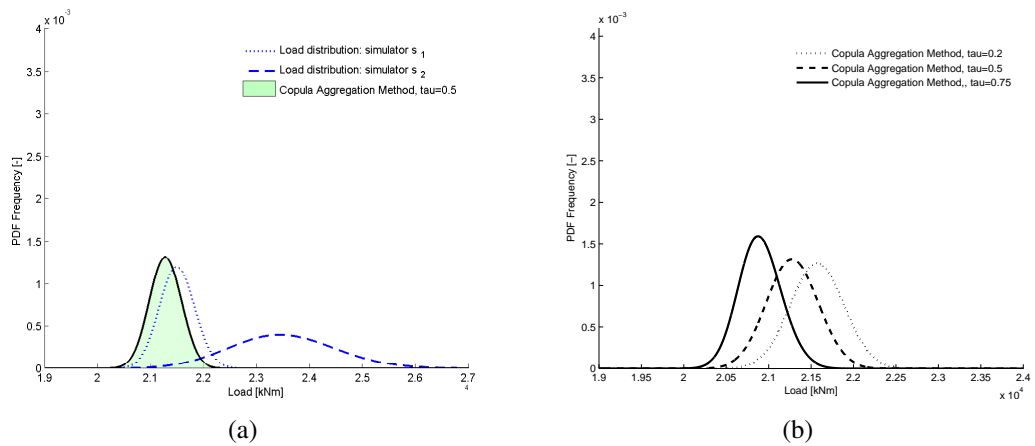


Figure 4.12: (4.12a) Aggregation with the Gumbel copula of loads outputs from 2 simulators and (4.12b) shows how the aggregated distribution changes with various Kendall τ values.

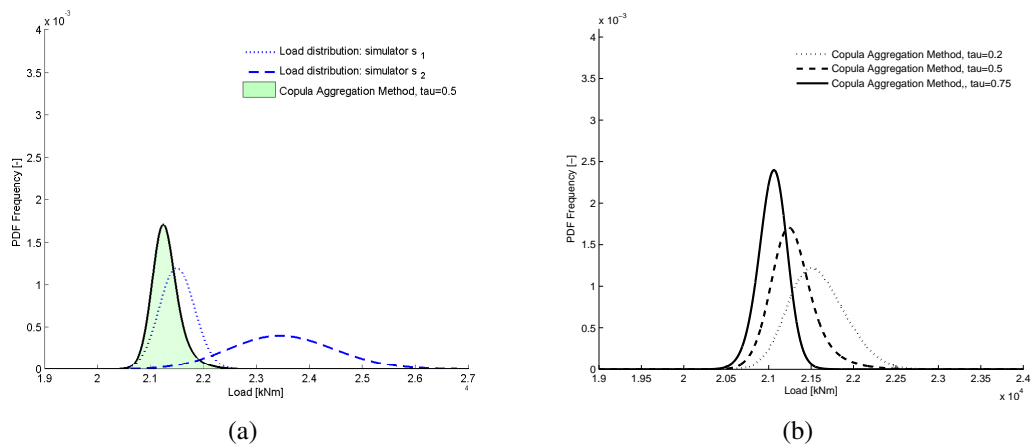


Figure 4.13: (4.13a) Aggregation with the Frank copula of loads outputs from 2 simulators and (4.13b) shows how the aggregated distribution changes with various Kendall τ values.

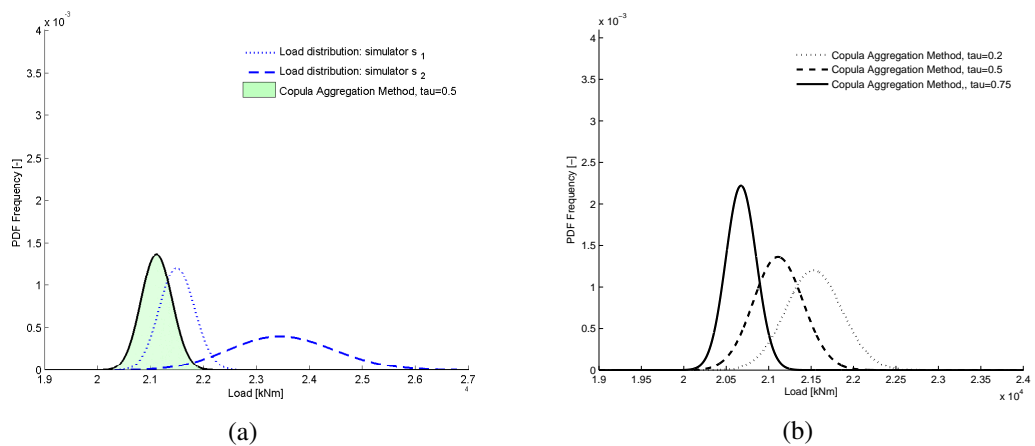


Figure 4.14: (4.14a) Aggregation with the Gaussian copula of loads outputs from 2 simulators and (4.14b) shows how the aggregated distribution changes with various Kendall τ values.

Chapter 4. Review: Analytical methods for fusing results from multiple simulators - Application to extreme loads on wind turbines

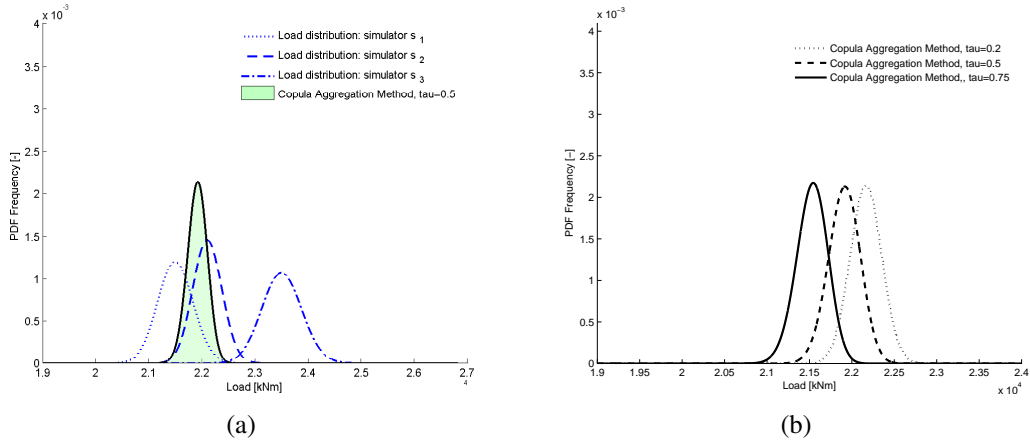


Figure 4.15: (4.15a) Aggregation with the Gumbel copula of loads outputs from 3 simulators and (4.15b) shows how the aggregated distribution changes with various Kendall τ values.

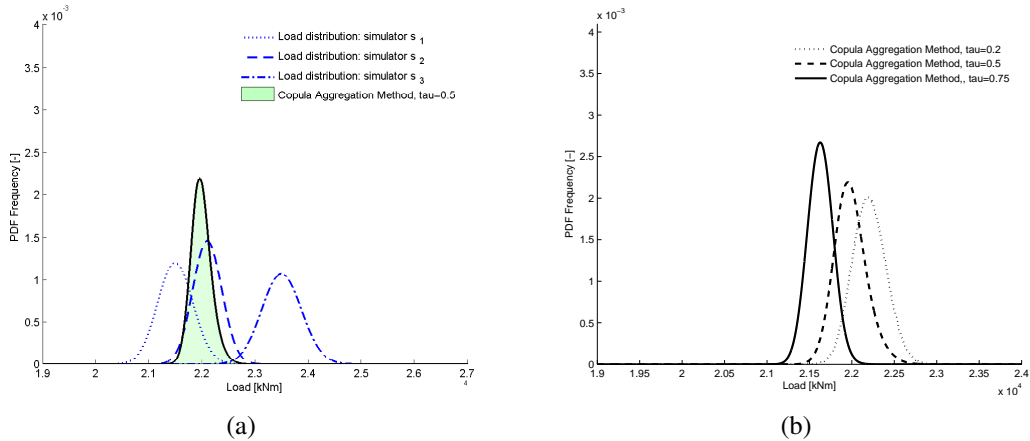


Figure 4.16: (4.16a) Aggregation with the Frank copula of loads outputs from 3 simulators and (4.16b) shows how the aggregated distribution changes with various Kendall τ values.

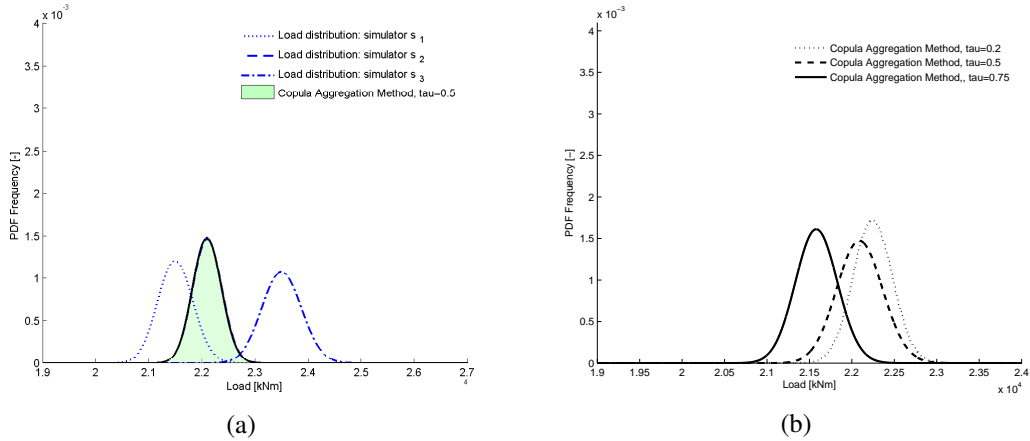


Figure 4.17: (4.17a) Aggregation with the Gaussian copula of loads outputs from 3 simulators and (4.17b) shows how the aggregated distribution changes with various Kendall τ values.

4.8 Analytical method 5: Bayesian Model Averaging (BMA)

The above methods are useful in the absence of any empirical test data. However, in the presence of empirical test data the Bayesian Model Averaging technique can be used to (1) update the individual model predictions to include the predictive uncertainty associated with each models prediction of the points included in the empirical data set \mathcal{D} (let \mathcal{D} denote data from available measurements on the system) and (2) update the model probabilities $P(\mathcal{M}_j)$ by means of the model likelihoods evaluated given the data set \mathcal{D} using Bayes Theorem. An appealing feature of BMA approach is that it permits the assessment of mathematical model uncertainty, as distinct from parameter uncertainty [Alvin et al., 1998].

4.8.1 Theory of the Bayesian model averaging (BMA)

The basic idea of BMA is to combine the predictions from several models (simulators) through a model averaging procedure [Gibbons et al., 2008]. The final predictions are a weighted average of the set of model predictions. The weights (or probabilities) can be purely subjective (e.g. equal weights) or may begin with assumed subjective probabilities (e.g. expert judgement) which are then updated quantitatively using relevant existing data [Alvin et al., 1998]. Note that the models under consideration are supported by expert knowledge, and available experimental data and differ in their implementation and predictive capability. [Madigan and Raftery, 1994] show that averaging over all the models provides better average predictive ability than using any single model, empirical evidence now exists to support this claim [Hoeting et al., 1999]. The weighting factors for averaging are essentially related to the model performance (according to an expert opinion or diagnostic data); in a Bayesian framework the weighting factors become *Posterior Model Probabilities* (PMP) as described below. Several approximations are available to calculate the posterior model probabilities, among which are AIC, BIC, DIC, Laplace, Bayes Factors, and Markov Chain Monte Carlo (MCMC) method (Metropolis - Hastings) [Raftery, 1993, Hoeting et al., 1999]. Say \mathcal{Y} is a quantity of interest (i.e. a simulator output), then the posterior distribution of \mathcal{Y} given observed data \mathcal{D} is

$$P(\mathcal{Y} | \mathcal{D}) = \sum_{j=1}^J \underbrace{P(\mathcal{Y} | \mathcal{M}_j, \mathcal{D})}_{\text{Predictive dist.}} \underbrace{P(\mathcal{M}_j | \mathcal{D})}_{\text{PMP}} \quad (4.42)$$

The BMA PDF is a weighted average of the conditional PDFs given each of the individual models, weighted by their posterior model probabilities. This is an average of the posterior predictive distribution for \mathcal{Y} under each of the simulators \mathcal{M}_j considered, weighted by the corresponding posterior model probability given observed data \mathcal{D} . Equation 4.42 has its own computational difficulties. The predictive distribution $P(\mathcal{Y} | \mathcal{M}_j, \mathcal{D})$ requires integrating out the model parameters (in case they are stochastic). The posterior model probabilities $P(\mathcal{M}_j | \mathcal{D})$ similarly involves the calculation of a likelihood function [Volinsky et al., 1997]. The posterior model probability (PMP) can be given by pure subjective (qualitative) knowledge [Alvin et al., 1998]:

$$P(\mathcal{M}_j | \mathcal{D}) = P(\mathcal{M}_j) \quad (4.43)$$

**Chapter 4. Review: Analytical methods for fusing results from multiple simulators -
Application to extreme loads on wind turbines**

with the constraint:

$$\sum_{j=1}^J P(\mathcal{M}_j) = 1 \quad (4.44)$$

Another approach is to use observational data to assess the posterior model probability such as:

$$P(\mathcal{M}_j | \mathcal{D}) = P(\mathcal{M}_j) \frac{P(\mathcal{D} | \mathcal{M}_j)}{\sum_{j=1}^J P(\mathcal{M}_j) P(\mathcal{D} | \mathcal{M}_j)} \quad (4.45)$$

The posterior predictive distribution for \mathcal{Y} under each of the models \mathcal{M}_j reads (assuming model \mathcal{M}_j is stochastic):

$$P(\mathcal{Y} | \mathcal{M}_j, \mathcal{D}) = \int P(\mathcal{Y} | \theta_j, \mathcal{M}_j, \mathcal{D}) P(\theta_j | \mathcal{M}_j, \mathcal{D}) \quad (4.46)$$

The posterior predictive distribution determines the prediction statistics for model output \mathcal{Y} given uncertainty in the parameters of the model θ_j , conditional on the data \mathcal{D} and a particular model structure \mathcal{M}_j . The BMA then extends this to the space of models \mathcal{M} using the probability weights $P(\mathcal{M}_j | \mathcal{D})$ [Alvin et al., 1998]. Finally the posterior mean and variance of the quantity of interest \mathcal{Y} are as follows [Draper, 1995, Hoeting et al., 1999, Duan et al., 2007]:

$$\begin{aligned} E[\mathcal{Y} | \mathcal{D}] &= \int \mathcal{Y} P(\mathcal{Y} | \mathcal{D}) d\mathcal{Y} = \int \mathcal{Y} \sum_{j=1}^J P(\mathcal{Y} | \mathcal{M}_j, \mathcal{D}) P(\mathcal{M}_j | \mathcal{D}) d\mathcal{Y} \\ &= \sum_{j=1}^J \int \mathcal{Y} P(\mathcal{Y} | \mathcal{M}_j, \mathcal{D}) d\mathcal{Y} P(\mathcal{M}_j | \mathcal{D}) \\ &= \sum_{j=1}^J \hat{\mathcal{Y}}_j P(\mathcal{M}_j | \mathcal{D}) \end{aligned} \quad (4.47)$$

4.8. Analytical method 5: Bayesian Model Averaging (BMA)

where $\hat{\mathcal{Y}}_j = E[\mathcal{Y} | \mathcal{D}, \mathcal{M}_j]$.

$$\begin{aligned}
 Var[\mathcal{Y} | \mathcal{D}] &= \int (\mathcal{Y} - E[\mathcal{Y} | \mathcal{D}])^2 P(\mathcal{Y} | \mathcal{D}) d\mathcal{Y} \\
 &= \int (\mathcal{Y}^2 - 2\mathcal{Y}E[\mathcal{Y} | \mathcal{D}] + E[\mathcal{Y} | \mathcal{D}]^2) P(\mathcal{Y} | \mathcal{D}) d\mathcal{Y} \\
 &= \int \mathcal{Y}^2 P(\mathcal{Y} | \mathcal{D}) d\mathcal{Y} + \int E[\mathcal{Y} | \mathcal{D}]^2 P(\mathcal{Y} | \mathcal{D}) d\mathcal{Y} - \int 2\mathcal{Y}E[\mathcal{Y} | \mathcal{D}] P(\mathcal{Y} | \mathcal{D}) d\mathcal{Y} \\
 &= \int \mathcal{Y}^2 P(\mathcal{Y} | \mathcal{D}) d\mathcal{Y} + E[\mathcal{Y} | \mathcal{D}]^2 \underbrace{\int P(\mathcal{Y} | \mathcal{D}) d\mathcal{Y}}_{=1} - 2E[\mathcal{Y} | \mathcal{D}] \underbrace{\int \mathcal{Y} P(\mathcal{Y} | \mathcal{D}) d\mathcal{Y}}_{E[\mathcal{Y} | \mathcal{D}]} \\
 &= \int \mathcal{Y}^2 \sum_{j=1}^J P(\mathcal{Y} | \mathcal{M}_j, \mathcal{D}) P(\mathcal{M}_j | \mathcal{D}) d\mathcal{Y} - E[\mathcal{Y} | \mathcal{D}]^2 \\
 &= \sum_{j=1}^J \underbrace{\left(\int \mathcal{Y}^2 P(\mathcal{Y} | \mathcal{M}_j, \mathcal{D}) \right)}_{E[\mathcal{Y}^2 | \mathcal{M}_j, \mathcal{D}]} P(\mathcal{M}_j | \mathcal{D}) d\mathcal{Y} - E[\mathcal{Y} | \mathcal{D}]^2 \\
 &= \sum_{j=1}^J \left(Var[\mathcal{Y} | \mathcal{M}_j, \mathcal{D}] + E[\mathcal{Y} | \mathcal{M}_j, \mathcal{D}]^2 \right) P(\mathcal{M}_j | \mathcal{D}) - E[\mathcal{Y} | \mathcal{D}]^2 \\
 &= \sum_{j=1}^J \left(Var[\mathcal{Y} | \mathcal{M}_j, \mathcal{D}] + \hat{\mathcal{Y}}_j^2 \right) P(\mathcal{M}_j | \mathcal{D}) - E[\mathcal{Y} | \mathcal{D}]^2
 \end{aligned} \tag{4.48}$$

Let us next look a bit more in detail at the derivation of the Posterior Model Probability given experimental dataset \mathcal{D} , $P(\mathcal{M}_j | \mathcal{D})$, and the Posterior Predictive Distribution of the quantity of interest given simulator \mathcal{M}_j and experimental dataset \mathcal{D} , $P(\mathcal{Y} | \mathcal{M}_j, \mathcal{D})$.

Solving the posterior model probability distribution $P(\mathcal{M}_j | \mathcal{D})$

The posterior model probability distribution reads:

$$P(\mathcal{M}_j | \mathcal{D}) = P(\mathcal{M}_j) \frac{P(\mathcal{D} | \mathcal{M}_j)}{\sum_{j=1}^J P(\mathcal{M}_j) P(\mathcal{D} | \mathcal{M}_j)} \tag{4.49}$$

where, $p(\mathcal{M}_j)$ is the prior model distribution before observing data \mathcal{D} , $P(\mathcal{D} | \mathcal{M}_j)$ represents the likelihood of observed data \mathcal{D} given the model \mathcal{M}_j and $\sum_{j=1}^J P(\mathcal{M}_j) P(\mathcal{D} | \mathcal{M}_j)$ is a normalizing factor. Given that the normalizing factor is a constant, one can write:

$$P(\mathcal{M}_j | \mathcal{D}) \propto P(\mathcal{M}_j) P(\mathcal{D} | \mathcal{M}_j) \tag{4.50}$$

Chapter 4. Review: Analytical methods for fusing results from multiple simulators - Application to extreme loads on wind turbines

where $\mathcal{D} = \{d_k, \forall k = 1, \dots, m\}$. The question is, how to solve the likelihood distribution $P(\mathcal{D} | \mathcal{M}_j)$? we may use a simple formulation as follows: assume that the model response \mathcal{Y}_j can be expressed as a combination of a deterministic prediction term f_j and ϵ_j :

$$\mathcal{Y}_j = f_j + \epsilon_j \quad (4.51)$$

where f_j can be thought of as the mean value of output simulator \mathcal{M}_j , and ϵ_j is an i.i.d normal random variable with zero mean $\sim \mathcal{N}(0, \sigma_j)$. Consequently $\mathcal{Y}_j \sim \mathcal{N}(f_j, \sigma_j)$. The likelihood function then becomes (assuming data d_k are independent):

$$P(\mathcal{D} | \mathcal{M}_j) = P(d_1, \dots, d_m | f_j, \sigma_j) = \prod_{k=1}^m P(d_k | f_j, \sigma_j) \quad (4.52)$$

But since $\mathcal{Y}_j \sim \mathcal{N}(f_j, \sigma_j)$, then $P(d_k | f_j, \sigma_j)$ can be expressed as:

$$P(d_k | f_j, \sigma_j) = \frac{1}{\sigma_j \sqrt{2\pi}} \exp\left(-\frac{(d_k - f_j)^2}{2\sigma_j^2}\right) \quad (4.53)$$

Substituting the expression for $P(d_k | f_j, \sigma_j)$ shown in Equation 4.53 into Equation 4.52 yields:

$$P(\mathcal{D} | \mathcal{M}_j) = \prod_{k=1}^m P(d_k | f_j, \sigma_j) = \left(\frac{1}{\sigma_j^2 2\pi}\right)^{m/2} \exp\left(-\frac{\sum_{k=1}^m (d_k - f_j)^2}{2\sigma_j^2}\right) \quad (4.54)$$

d_k is the empirical test data and f_j takes the value of model prediction. All is left is to estimate σ_j using the Maximum Likelihood Estimation (MLE) approach. In this context, it simply means differentiating the logarithm of Equation 4.54 with respect to σ_j and setting it equal to 0, which yields:

$$\sigma_j^2 = \frac{\sum_{k=1}^m (d_k - f_j)^2}{m} \quad (4.55)$$

Thus the likelihood function $P(\mathcal{D} | \mathcal{M}_j)$ is fully defined and the posterior model probability of model \mathcal{M}_j given the empirical data \mathcal{D} can now be computed. However, if the normality and independence assumptions stated above are not valid and if model \mathcal{M}_j is stochastic, then $P(\mathcal{D} | \mathcal{M}_j)$ reads:

$$P(\mathcal{D} | \mathcal{M}_j) = \int P(\mathcal{D} | \theta_j, \mathcal{M}_j, \mathcal{D}) P(\theta_j | \mathcal{M}_j) d\theta_j \quad (4.56)$$

which could be intractable to solve. Other solutions should be pursued, namely Markov Chain Monte Carlo (MCMC) method (Metropolis - Hastings) to solve the integrals.

Solving the posterior predictive distribution $p(\mathcal{Y} | \mathcal{M}_j, \mathcal{D})$

Assuming model \mathcal{M}_j yields a deterministic model predictions f_j , then as stated above $\mathcal{Y}_j \sim \mathcal{N}(f_j, \sigma_j)$. This then leads to the predictive distribution for \mathcal{Y} :

$$P(\mathcal{Y} | \mathcal{M}_j, \mathcal{D}) \sim \mathcal{N}(f_j, \sigma_j) \quad (4.57)$$

4.8. Analytical method 5: Bayesian Model Averaging (BMA)

on the other hand, if model \mathcal{M}_j is stochastic, then the predictive distribution for \mathcal{Y} reads:

$$P(\mathcal{Y} | \mathcal{M}_j, \mathcal{D}) = \int P(\mathcal{Y} | \theta_j, \mathcal{M}_j, \mathcal{D}) P(\theta_j | \mathcal{M}_j, \mathcal{D}) d\theta_j \quad (4.58)$$

which does not have a closed form and shall be computed using MCMC. According to (Volinsky 1996) an excellent approximation can be written as:

$$P(\mathcal{Y} | \mathcal{M}_j, \mathcal{D}) = P(\mathcal{Y} | \mathcal{M}_j, \hat{\theta}_j, \mathcal{D}) \quad (4.59)$$

where $\hat{\theta}_j$ are the maximum likelihood estimates of the model parameters. Bayesian techniques and BMA is a vast topic, and what we present here is nothing but a taste of how BMA can be used to predict the most likely load output from various aero-servo-elastic simulators.

4.8.2 Demonstration of the Bayesian Model Averaging

Say that empirical test data of a blade's bending moment in normal production are extrapolated to a value of $\mathcal{D} = \{23100\}$ kNm (verifying observation). Using this experimental data point and Bayesian Model Averaging, the model probabilities are first updated as shown in Table 4.3 and second the BMA predictive distribution is computed. Figure 4.18 shows the BMA predictive PDF. This PDF (shown as the thick curve) is a weighted sum of three normal PDFs [Raftery et al., 2005]. The predictive BMA distribution is bimodal, reflecting the fact that there are two groups of forecasts that disagree with one another. The right mode is centred around the cluster of one higher forecast (23500kNm), while the left mode is centred around the cluster of two lower forecasts. In Figure 4.18 the BMA distribution which fuses the output load distributions from three simulators have in this case a larger variance than the estimates from the individual models. However, if further observational data are available $\mathcal{D} = \{23100 \ 23300 \ 23150 \ 23200\}$ from three additional test wind turbines say located in three different sites, the predictive BMA distribution becomes as shown in Figure 4.19, with less spread compared to the BMA distribution in Figure 4.18.

Table 4.3: Predicted load level by simulator \mathcal{M}_j and the Posterior Model Probability $P(\mathcal{M}_j | \mathcal{D})$. The empirical test data of a blade's bending moment (verifying observation) is 23100 kNm.

Simulator	Load prediction from simulator	$P(\mathcal{M}_j)_{prior}$	$P(\mathcal{M}_j \mathcal{D})_{posterior}$
\mathcal{M}_1	21500kNm	1/3	0.1515
\mathcal{M}_2	22100kNm	1/3	0.2424
\mathcal{M}_3	23500kNm	1/3	0.6061

Chapter 4. Review: Analytical methods for fusing results from multiple simulators - Application to extreme loads on wind turbines

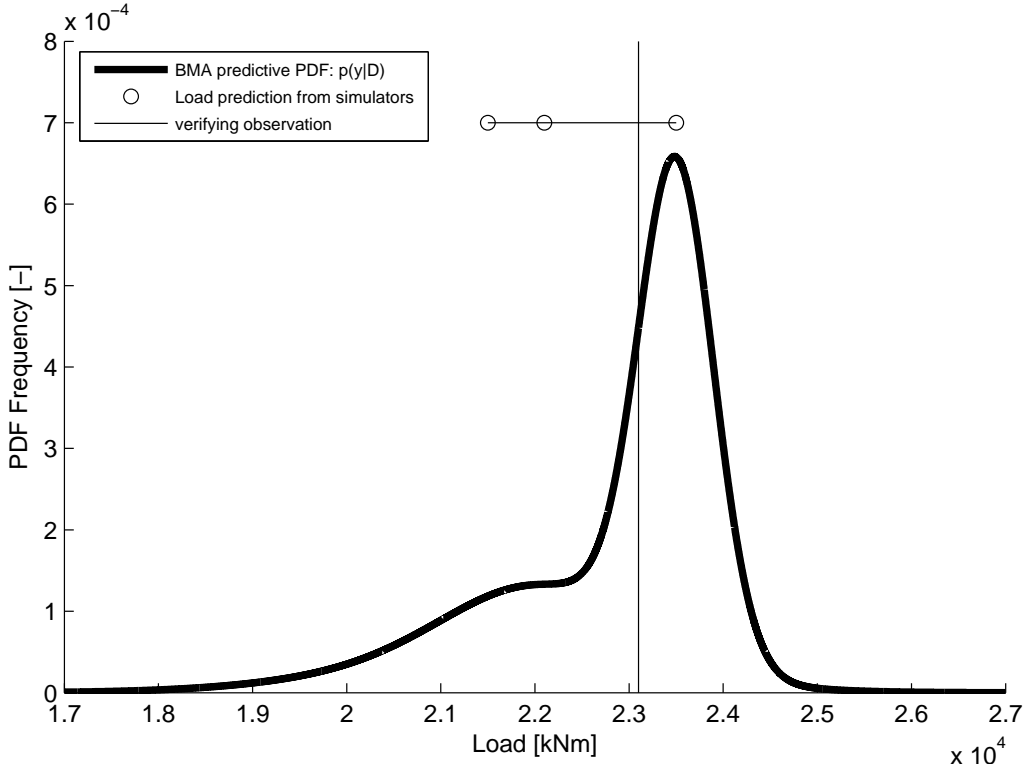


Figure 4.18: BMA predictive PDF (thick curve) for the blade root bending moment. Also shown are the load prediction from three simulators (solid horizontal line and bullets) and the one experimental verifying observation (solid vertical line).

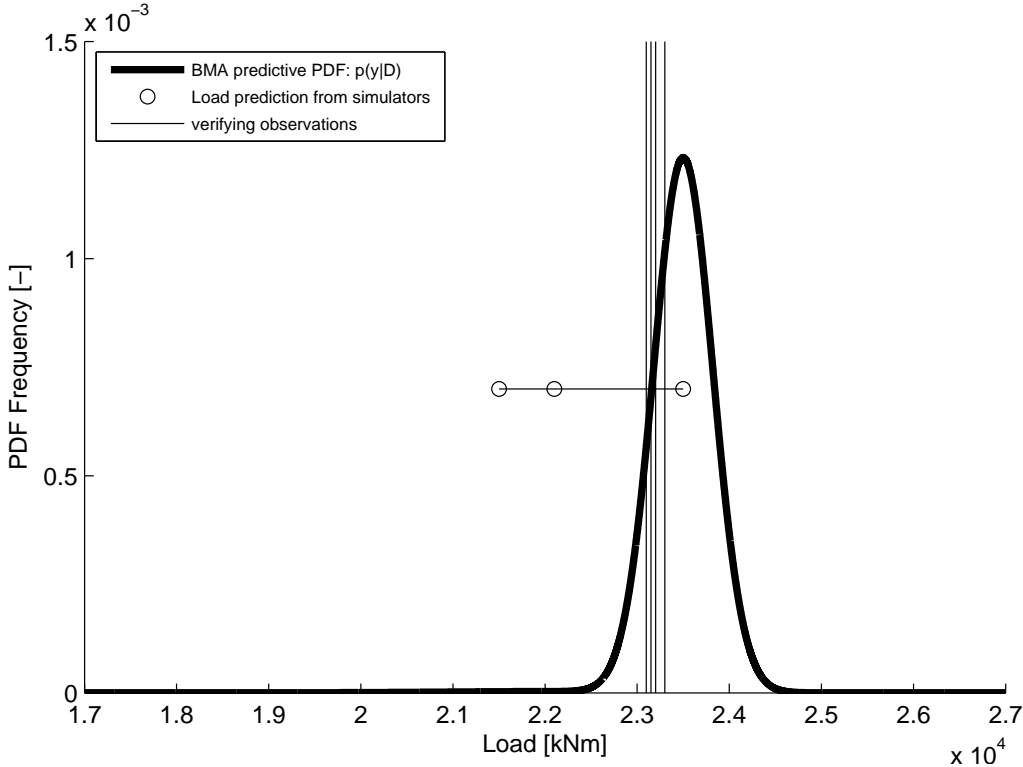
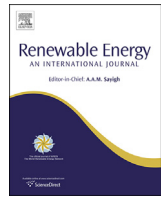


Figure 4.19: BMA predictive PDF (thick curve) for the blade root bending moment. Also shown are the load prediction from three simulators (solid horizontal line and bullets) and four experimental verifying observations (solid vertical line).

5 *Publication:* Impact of Uncertainty
in Airfoil Characteristics on Wind
Turbine Extreme Loads



Review

Impact of uncertainty in airfoil characteristics on wind turbine extreme loads

I. Abdallah^{a,*}, A. Natarajan^a, J.D. Sørensen^b^a Technical University of Denmark, Department of Wind Energy, Risø Campus, DK-4000 Roskilde, Denmark^b Aalborg University, Department of Civil Engineering, Sohngårdsholmsvej 57, DK-9000 Aalborg, Denmark

ARTICLE INFO

Article history:

Received 8 January 2014

Accepted 2 October 2014

Available online

Keywords:

Wind turbines

Airfoil aerodynamics uncertainty

Extreme wind loads

Probabilistic modeling

Aerodynamic stochastic model

Structural reliability

ABSTRACT

Wind tunnel test measurements to characterize the static lift and drag coefficients of airfoils used in wind turbine blades are shown to possess large uncertainties, which leads to uncertainties in the aerodynamic loads on the rotor. In this paper a rational stochastic model is proposed to quantify the uncertainty in airfoil static lift and drag coefficients based on field and wind tunnel data, aero-servo-elastic calculations and engineering judgment. The stochastic model is subsequently used to assess the effect of the uncertainty in airfoil static lift and drag coefficients on the prediction of extreme loads and structural reliability of large wind turbines. It is shown that the uncertainty in the static airfoil data has a significant impact on the prediction of extreme loads effects and structural reliability depending on the component, operating conditions (stand-still versus power production) and the correlations of aerodynamic variables along the span of the blades.

© 2014 Elsevier Ltd. All rights reserved.

1. Introduction

Considerable effort and capital is invested in predicting the static aerodynamic lift and drag coefficients of airfoils as accurately as possible. The lift and drag coefficients are then used by the wind turbine designers as input to aero-servo-elastic simulations to predict extreme and fatigue loads in addition to stability margins in normal and extreme operating and stand still conditions. An airfoil's static aerodynamic data are almost exclusively derived from measurements acquired in wind tunnel tests. However, an airfoil section on the wind turbine rotor operates in 3-dimensional, unsteady and turbulent inflow under the guidance of a control system, none of which are accounted for in static wind tunnel tests. Some aspects of uncertainty in airfoil data (surface roughness, 3D corrections, effect of Re numbers, wind tunnel measurements or geometric distortions) have been studied in Refs. [1–7]. The general consensus is that uncertainties in airfoil data do affect a wind turbine's performance and structural loading. Aerodynamic uncertainties are widely acknowledged in the industry; this is demonstrated by cross validating wind tunnel measurements with

CFD or cross validating wind tunnel measurements with full scale test data or performing wind tunnel measurements under various inflow conditions. Manufacturers also try to mitigate aerodynamic uncertainties by ensuring tight controls on the tolerances of blade geometry during manufacturing and handling. In addition, a widely performed practice is to tune the static airfoil data used in the aero-servo-elastic simulations using measurements from a prototype wind turbine. The tuning of aerodynamic data is usually done indirectly through performance metrics such as power production or structural loading. In wind turbine structural reliability analysis [8], an overall value of 10% is used as the coefficient of variation (COV) for airfoil uncertainty as affecting the structural loads. With the advent of advanced wind tunnel testing, computational fluid dynamics and full scale testing it is deemed necessary to review this value. In this paper we establish a stochastic model for the static lift and drag coefficients by tapping into publicly available aerodynamic tests, measurements and simulations on various aspects of aerodynamic uncertainties. The stochastic model is developed by (1) replicating the physical variations in airfoil characteristics by parameterizing the lift and drag coefficients curves, (2) allowing selected points on the lift and drag curves to be distributed randomly around the measured values and (3) simulating their impact on extreme loads using a Monte Carlo scheme with varying degree of correlation among the aerodynamic properties along the span of the blade. The proposed stochastic analysis

* Corresponding author. Tel.: +45 22833005.

E-mail address: imad.abdallah.81@gmail.com (I. Abdallah).

Nomenclature			
2D	two-dimensional	COV	coefficient of variation
3D	three-dimensional	Re	reynolds number
CL,max	max lift coefficient	t/c	thickness to chord ratio
AoAmax	angle of attack where CL,max occurs	RootMyb1	blade root flap bending moment
CL,TES	lift coefficient where trailing edge separation starts	Spn4MLyb1	blade ¼ span flap moment
AoATES	angle of attack corresponding to CL,TES	RootMxb1	blade root edge bending moment
CL,SR	lift coefficient where stall recovery starts	Spn4MLxb1	blade ¼ span edge moment
AoASR	angle of attack where stall recovery starts	OoPDefl1	blade out of plane deflection
CL,90	lift coefficient at 90° angle of attack	LSSTipMzs	low speed shaft yaw moment
CD,90	drag coefficient at 90° angle of attack	LSSTipMys	low speed shaft tilt moment
TES	trailing edge separation	LSShftMxa	low speed shaft driving moment (torque)
		TwrBsMyt	for-aft tower bottom bending moment
		TwHt4MLyt	for-aft ¾ height bending moment

quantifies the model, statistical and measurement uncertainties of blade aerodynamics and its effects on the extreme structural loads. The stochastic model is first used in structural reliability optimization against extreme loading of a wind turbine tower in stand-still in a 50-year storm, then for evaluating the structural reliability index and optimization of the partial load safety factors of a blade in power production. A commercial multi-megawatt offshore wind turbine is considered in the calculations of the extreme loads effects (nominal power >5 MW and rotor diameter >130 m).

2. Airfoils database

A database of airfoils lift and drag polars measurements is collected for this study and is presented herein. The database is largely built upon publicly available wind tunnel tests and 3D full scale measurements.

2.1. Wind tunnels

Table 1 lists the wind tunnels that have historically been widely used for testing airfoils for the wind turbine and aerospace industries. Publicly available data from these wind tunnels are

Table 1
List of wind tunnels and their characteristics.

Wind tunnel	Characteristics
Delft wind tunnel (Netherlands)	Max speed 120 m/s, max Re 3.5 million, $Ti < 0.02\%$, test section 1.25×1.80 m
Velux wind tunnel (Denmark)	Max speed 40 m/s, max Re 1.6 million, $Ti \sim 1\%$, open jet test section 7.5×7.5 m
LM wind power wind tunnel (Denmark)	Max speed 105 m/s, max Re 6.0 million, $Ti \sim 0.1\%$, test section 1.35×2.70 m
Stuttgart wind tunnel LWK (Germany)	Max speed 90 m/s, max Re 5.0 million, $0.0002\% < Ti < 0.0005\%$, test section 2.73×0.73 m
NASA Langley LTPT wind tunnel (USA)	Max speed 130 m/s, Max Re 6 million at Mach 0.3, Ti is N/A, test section 0.91×2.29 m,
Large scale low speed wind tunnel facility (LLF) of the German Dutch wind tunnel organization (Germany)	Max speed 80 m/s, open jet test section 9.5×9.5 m Max speed 152 m/s, closed wall test section 6.0×6.0 m Max Re 6 million at Mach 0.45, $Ti < 0.4\%$,
The NASA-AMES wind tunnel (USA)	Max speed 50 m/s, $Ti < 0.4\%$, test section 24.4×36.6 m

collected and used as a basis for the stochastic model of the airfoils static lift and drag coefficients.

2.2. Full scale measurements

Table 2 presents a list of 3D wind turbine rotor measurement campaigns that are widely reported in the literature. Publicly available data from these tests are also collected and used as basis for the stochastic model.

2.3. Airfoil families

Table 3 shows an exhaustive list of airfoils used in this study as a basis for the stochastic model. The airfoils lift and drag curves for the airfoils listed in Table 3 are collected and categorized with regards to their fundamental sources of uncertainty studied in the referenced literature.

3. Airfoil aerodynamics

The rate of change of the lift coefficient with angle of attack, $dC_L/d\alpha$, can be inferred from thin airfoil theory to be 2π per radian change of angle of attack and slightly lower when taking the effects of airfoil thickness and fluid viscosity into account. Deviation from the linear slope is the start of the progressive movement of the turbulent flow separation point from the trailing edge (TE) towards

Table 2
List of 3D full scale wind turbine measurements campaigns.

Test	Description	Reference literature
DANAERO project	NM80 variable speed pitch regulated wind turbine (80 m rotor diameter)	[9]
NREL unsteady aerodynamics experiment phase VI	NASA/AMES wind tunnel test of an experimental two blades rotor with 10 m rotor diameter stall regulated	[2]
MEXICO project	Wind tunnel test of a three bladed rotor of 4.5 m diameter including a speed controller and pitch actuator.	[10]

Table 3
Airfoil families included in the study.

Sources of uncertainty	
Variations in wind tunnels measurements	3D rotational correction
Reference literature	[5,11–15]
Airfoil family	LM38.8 sections 32.5%, 47.5%, 75%, 92.5% S809
	NACA63418
	Risø B1-18
	NACA63018
	NACA63421
	NACA63418
	NACA0012
	NACA6212
	DU97-W300
Surface roughness	[5,11,14,18–21]
	NACA63418
	NACA63615
	Risø B1-18,
	Risø P1-15
	Risø-1
	DU97-W300
	Risø-A1-18
	Risø-A1-21
	Risø-A1-24
	NACA23012
	LS(1)-0417
Geometric distortions of the blade sections during manufacturing and handling	[22], Appendix A
	Risø B1-15
	NACA63418
	Cottingen387
	NACA0021
	NACA100
Effect of Reynolds number	[5,12–14,23,24]
	NACA63018
	NACA63418
	NACA63618
	Risø B1-18
	Risø B1-15
	Risø P1-15
	NACA8318
	NACA0012
	DU 91-W2-250
	NACA63018
	DU 97-W-300
	NACA 23012
Geometric distortions of the blade under loading	[3]
	NACA0012
	NACA5412
Extending airfoil data to post-stall	[25–29]
	S809
	NACA4415
Validation of airfoil data by full scale wind turbine measurements in the field or wind tunnel	[2,9,10]
	LM38.8 blade sections 32.5%, 47.5%, 75%, 92.5% S809
	DU 91-W2-250
	RISØ A1-21
	NACA 64-418

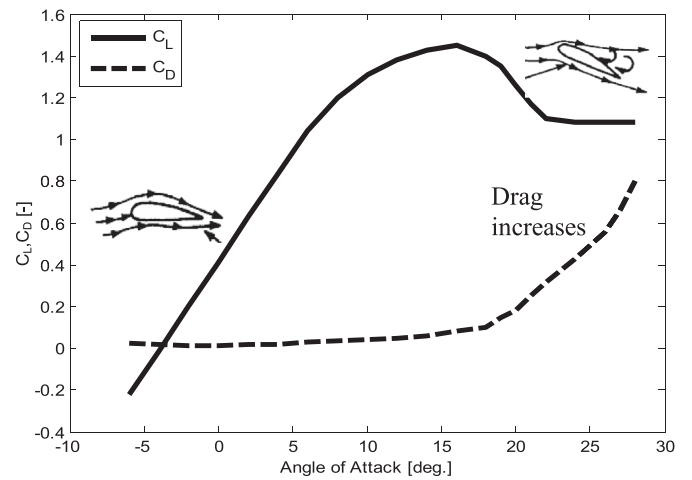


Fig. 1. Lift and drag coefficients.

the leading edge. As the separation point begins to move upstream along the suction side, the lift coefficient (C_L) reaches the point of maximum lift ($C_{L,max}$) as depicted in Fig. 1. The angle of attack at maximum lift is termed the static stall angle of attack (AoA). The drag coefficient is constant or slightly increasing. Beyond the stall angle of attack, the lift coefficient starts to decrease; the stalled region on the suction side of the airfoil continues to grow as the separation point continues its progression upstream to the airfoil leading edge. When leading edge separation (also called deep stall) is reached, increasing the angle of attack further often results in a neutral or even slightly increasing lift (stall recovery) while the drag is steadily increasing at a much faster rate until a 90° angle of attack.

4. Sources of uncertainty in the static airfoil lift and drag polars

The static airfoil data utilized as an input to the aero-servo-elastic simulations are not unique and exhibit variations which are driven by physical uncertainty (aleatory) or simply driven by lack of evidence (model, measurement and statistical uncertainty) as shown in Table 4.

4.1. Variations among wind tunnel measurements

Many factors contribute to the uncertainty in the measurement of airfoils static lift and drag polar curves in wind tunnels ([5,15]). The focus herein will be on the results obtained when measuring the same airfoil geometry in various wind tunnels. The lift curves shown in Fig. 2 depict the lift coefficients of the same airfoil section measured in four different wind tunnels at $Re = 3$ million. One can easily notice the variation in the maximum lift coefficient, the offset in the linear part of the lift coefficient curve and the post stall characteristics as measured in the various wind tunnels. Based on this example and the references in Table 3 it can be shown that wind tunnel measurement uncertainty can result in a COV of the order of 6–9% on the maximum lift coefficient, 3–9% on the angle of attack corresponding to the maximum lift coefficient, 3–9% on the lift coefficient where stall recovery starts, 3–10% on the angle of attack corresponding to where stall recovery starts, 5–12% on the lift coefficient where trailing edge separation starts and 4–10% on the angle of attack corresponding to where trailing edge separation starts. These values may depend on the type of airfoil. For a given airfoil geometry and Re and Mach numbers, the factors that explain the scatter amongst wind tunnel measurements either in the

Table 4
Sources of uncertainties included in this study.

	Type of uncertainty			
	Inherent or physical	Model ^{a,b}	Measurement	Statistical
Variations in wind tunnels measurements			x	
3D rotational correction		x		
Surface roughness	x			
Geometric distortions of the blade sections during manufacturing and handling	x			
Effect of reynolds number		x		x
Geometric distortions of the blade under loading	x			
Extending airfoil data to post stall		x		x
Validation of airfoil data by full scale wind turbine measurements in the field or wind tunnel	x		x	

^a Not included in this study are the uncertainties in the numerical model of the loads simulations such as aero-servo-elastic models, or Extreme Turbulence Model or Extreme Wind Model, or dynamic stall and dynamic wake models, etc.

^b A widely performed practice is to tune the airfoil data used in the aero-servo-elastic simulations at the design stage using test data from a full scale prototype wind turbine. The tuning of aerodynamic data is usually done indirectly through performance metrics such as power production or structural loading. The same numerical models used at the design stage are used again at the tuning stage (using the measured inflow times series); This way the effect of uncertainty in airfoil data can be distinguished from the uncertainty in the numerical model such as dynamic wake, dynamic stall, BEM, etc.

attached flow region or the separated flow region of the lift coefficient curve can be explained by (but not confined to):

- Difference in the airfoil model geometry when constructed by the wind tunnel operator.

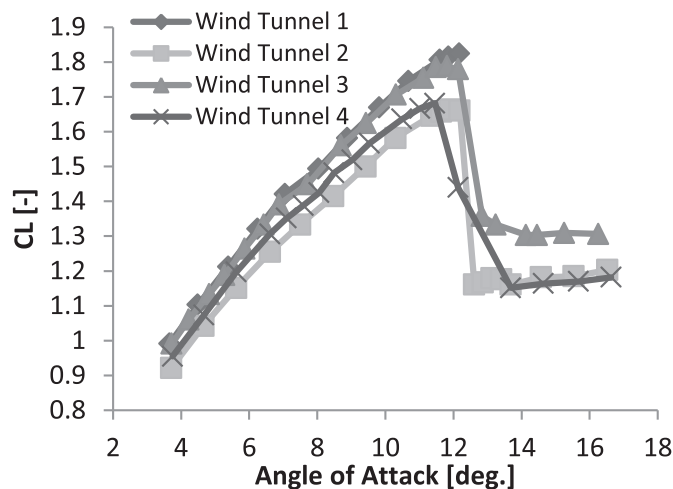


Fig. 2. Static lift coefficient curve for the same airfoil in 4 wind tunnels. Airfoil name and wind tunnels are not specified for proprietary reasons.

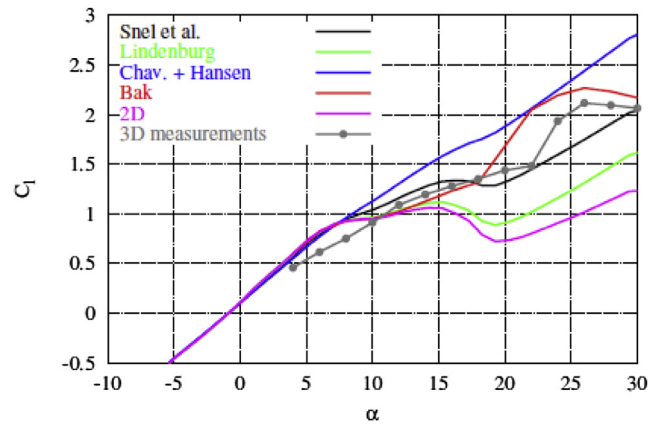


Fig. 3. Three dimensional corrected lift coefficient compared to measurements at a section corresponding to 30% of the blade length.[16].

- Differences in the surface roughness of the airfoil model when constructed by the wind tunnel operator.
- Wall effect corrections could differ from one wind tunnel operator to another.
- Difference in the turbulence level from wind tunnel to wind tunnel affects the transition from laminar to turbulent boundary layer.
- Difference in the measurement method from wind tunnel to wind tunnel, i.e. wall pressure taps versus airfoil pressure taps versus force balance.
- Tunnel blockage affects the wind tunnel walls boundary and how they interact with the flow over the airfoil section.

4.2. 3D rotational correction

Several empirical models exist to correct 2D wind tunnel measurements of the lift coefficient to include 3D rotational effects and in some instances also correct the drag coefficient. Models are developed by Bak et al., Snel et al., Du and Selig, Chaviaropoulos and Hansen, and Lindenburg ([16] and [30]). Fig. 3 displays the variation in C_L on the NREL/NASA AEMS rotor at a section corresponding to 30% of the blade length. The designer's choice of the 3D correction model can result in large variations in the lift coefficient [16]. In the

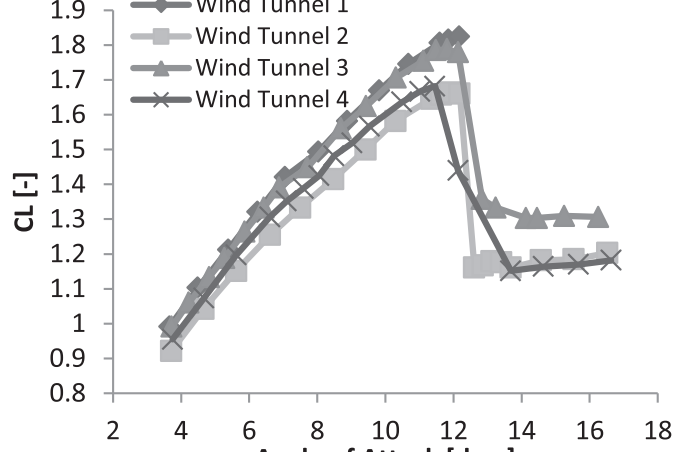


Fig. 4. CL of an airfoil with three roughness conditions. Zig-zag tape is used to simulate the roughness in the wind tunnel. Airfoil name and wind tunnel are not specified for proprietary reasons.

outer part of the blade, the choice of the 3D correction model can result in 6% COV for the maximum lift coefficient, which can go up to 14% close to the root of the blade. These values may depend on the type of airfoil.

4.3. Surface roughness

The blades' surface conditions vary over a wind turbine's life-time. The surface roughness variation is due to paint condition, surface finish, dust accretion, insects sticking to the surface and by surface erosion. Leading edge roughness is simulated in wind tunnel tests. For any given section along the span of the blade a designer can choose to use clean, rough or moderate roughness airfoil characteristics. As shown in Fig. 4, each has its own lift coefficient curve characteristics: a clean airfoil exhibits an abrupt stall and a higher maximum lift compared to a rough airfoil. Loads could be calculated with a clean airfoil while the turbine operates in rough conditions in the field or vice-versa. Consequently, it is estimated that roughness can result in a COV of the order of 4–12% on the maximum lift coefficient depending on how the roughness is simulated, 4–12% on the angle of attack corresponding to the maximum lift coefficient, 4–12% on the lift coefficient where stall recovery starts, 6–10% on the angle of attack corresponding to where stall recovery starts, 5–10% on the lift coefficient where trailing edge separation starts and 4–10% on the angle of attack corresponding to where trailing edge separation starts. These values may depend on the type of airfoil.

4.4. Geometric distortions of the blade during manufacturing and handling

The static lift and drag coefficients used by the blade designer are based on predefined geometry of the airfoils sections. However, manufacturing, handling, transportation and installation introduce geometric distortions to the blade sections, resulting in discrepancies between the design C_L and C_D and the “real” C_L and C_D [31]. Appendix A shows some of the distortions observed during manufacturing and handling. A combination of these distortions can occur anywhere along the span of the blade. The impact of geometric distortions on $C_{L,max}$ are quantified in a Monte Carlo simulations whereby the C_L and C_D of synthetically distorted NACA 63418 and Risø B15 airfoils are computed in XFOIL [32] up to the maximum lift coefficient and show a COV of the order of 3% on the maximum lift coefficient and less than 1% on the slope of the lift coefficient curve. In the Monte Carlo simulations all geometric distortions are assigned specific distributions and are assumed to be fully uncorrelated (see Appendix A for more details).

4.5. Effect of reynolds number (Re)

The Re number varies along the span of the blade but the wind tunnel measurements are usually performed at a limited range of Re numbers; the static airfoil lift and drag coefficients are then corrected to the actual Re number for each section along the span of the blade [23]. Fig. 5 depicts the variation of lift as a function of the angle of attack at two different Re numbers [24]. With increasing rotor diameters, the operating Re numbers are expected to rise above 20 million and few wind tunnels exist to perform measurement at such high values. Consequently, increased reliance on numeric Re number corrections is expected. Based on this and other such measurements (the references in Table 3) it can be shown that the Re number effects can result in a COV up to 10% on the maximum lift coefficient, up to 9% on the angle of attack corresponding to the maximum lift coefficient, up to 11% on the lift coefficient where stall recovery starts, up to 15% on the angle of attack

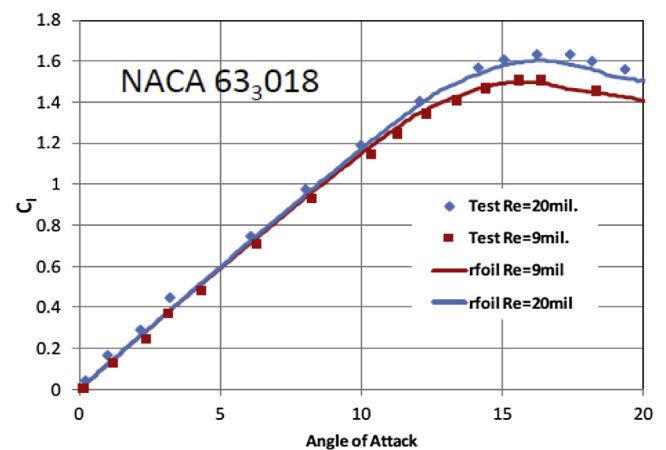


Fig. 5. Variation of lift with Re number in both wind tunnel test and numerical simulations.[24].

corresponding to where stall recovery starts, up to 13% on the lift coefficient where trailing edge separation starts and up to 8% on the angle of attack corresponding to where trailing edge separation starts. These values may depend on the type of airfoil, roughness conditions and Mach number.

4.6. Geometric distortions of the blade under loading

The blade deforms due to aerodynamic and inertial loading, centrifugal stiffening, and gravitational effects, resulting in discrepancy between the static C_L and C_D in the aero-servo-elastic model and the “real” C_L and C_D of the deformed blade. In Ref. [3] airfoil geometry distortion due to blade deflection is treated as a combination of uncertainty in max camber, camber position and thickness to chord ratio. This approach assumes that these three parameters are sufficient to model geometric distortions of airfoils sections when the blade deflects under loading. The uncertain

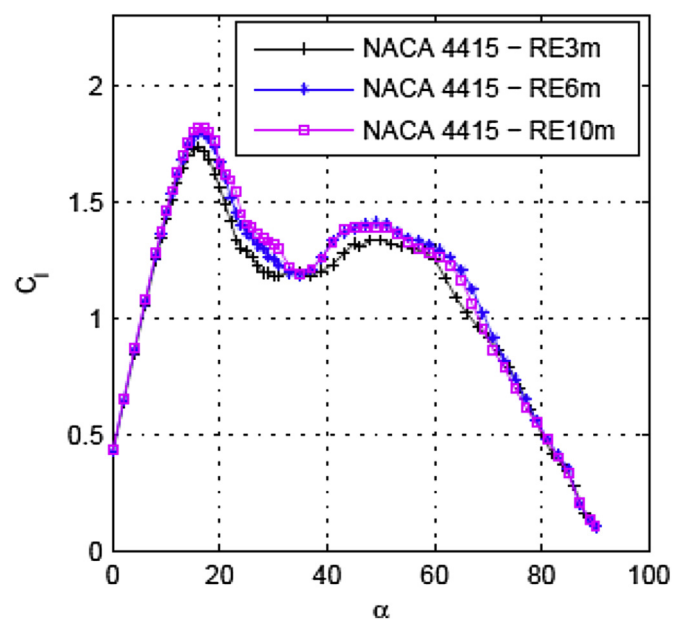


Fig. 6. Effect of Re number on post stall behavior on a NACA4415 airfoil (CFD simulations).[28].

camber, camber position and thickness to chord ratio are assigned truncated normal distributions with a COV = 10%. The result is a 4–6% COV on the maximum lift coefficient.

4.7. Extending airfoil data to post stall

The angles of attack on a wind turbine blade vary greatly depending on the operating conditions and external inflow. Wind tunnel measurements are however available for a limited range of angles of attack. Empirical models such as the Viterna method [33] or Montgomerie method [29] have been suggested to extend the airfoil data to post stall. Results presented by Tangler et al. [25] indicate that the Viterna method in post stall and deep stall is highly sensitive to the available wind tunnel measurement of C_L and C_D . A change of 10% in C_L and C_D results in 5% change in power at 25 m/s (thrust follows a similar trend). Another aspect is the effect of the Re on the post stall characteristics as shown in the CFD simulation in Fig. 6. Another aspect is the effect of airfoil/blade geometry on post stall, namely the TE geometry (sharp versus blunt) as shown in Fig. 7 or blade sweep in Fig. 8. Other aspects affecting the prediction of the post stall lift and drag coefficients include the blade rotation, aspect ratio of the blade and the thickness to chord ratio of the airfoil sections [26].

4.8. Validation of airfoil data by full scale measurements

Within the wind industry it is common to validate the static wind tunnel C_L and C_D data used in the aero-servo-elastic model by comparing the computed power curve to a measured power curve on a select number of wind turbine prototypes. The C_L and C_D are “adjusted” such that the simulated power curve fits the measured power curve (similarly for other metrics). The “adjusted” C_L and C_D are then utilized in the design of future rotors. It is evident that this process is only valid for a specific wind turbine and site conditions. It is difficult to assess how much uncertainty this process introduces on the airfoil characteristics in the absence of full scale measurements from multiple sites on the same turbine type. Hence this factor is neglected here.

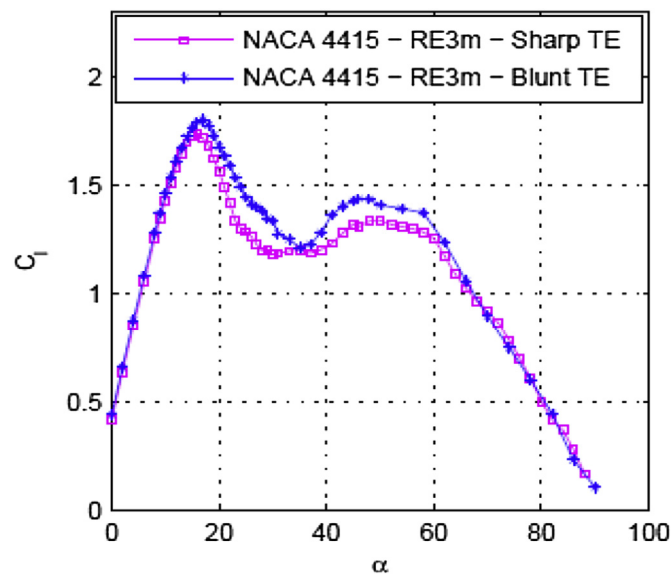


Fig. 7. Effect of TE geometry on post stall behavior on a NACA4415 airfoil (CFD simulations).[28].

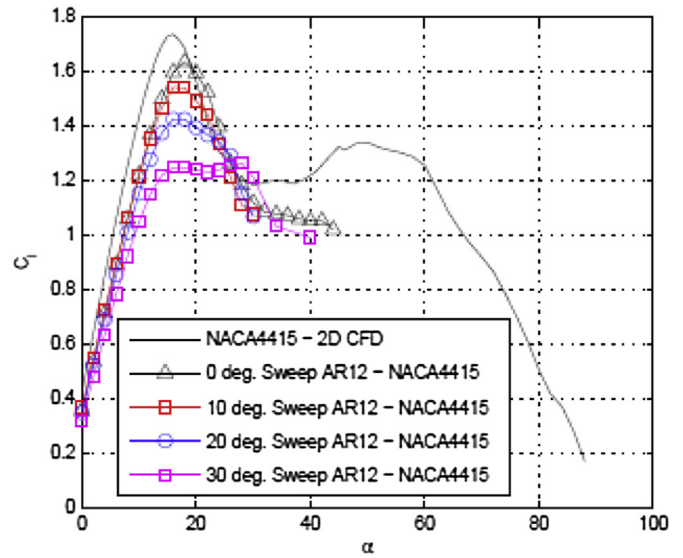


Fig. 8. Effect of blade sweep on post stall behavior on a NACA4415 airfoil (CFD simulations).[28].

5. Stochastic model of static airfoil lift and drag polar curves

5.1. Parameterization of the lift and drag coefficient curves

The sources of uncertainties depicted in Tables 3 and 4 result in variations of the lift and drag forces, as experienced by the rotor blades during different operating conditions over the life time of the wind turbine. It is therefore beneficial to reproduce these physical variations already at the design stage in order to take their effect on the extreme structural design loads (and in principle for fatigue loads as well). These variations may be quantified by parameterizing the lift and drag polar curves. The lift coefficient is parameterized by the slope in the linear range $dC_L/d\alpha$ (Fig. 9), the point indicating the start of TE separation (T_{ES}), the point of max lift (C_{Lmax}) and the point where stall recovery is initiated (S_R). The rate of change of the lift coefficient with angle of attack ($dC_L/d\alpha$) can be inferred from thin airfoil theory. On any given airfoil section and C_L curve, $dC_L/d\alpha$ is parameterized as $dC_L/d\alpha \pm 10\%$ (with $2\pi/rad$ as the upper limit). T_{ES} is selected when $dC_L/d\alpha$ drops strictly below 2π -

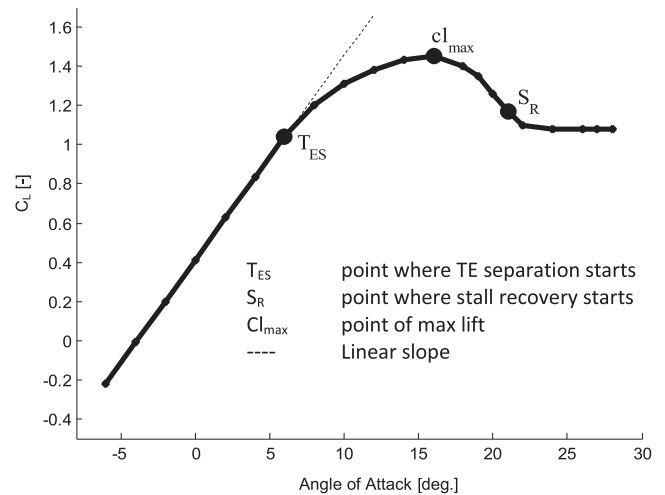


Fig. 9. C_L parameters for low angles of attack.

Table 5
Parameters of the static lift and drag stochastic model.

Parameter	Description
$C_{L,max}$	Max lift coefficient
AoA_{max}	Angle of attack corresponding to max lift
$C_{L,TES}$	Lift coefficient where trailing edge separation starts
AoA_{TES}	Angle of attack where trailing edge separation starts
$C_{L,SR}$	Lift coefficient where stall recovery starts
AoA_{SR}	Angle of attack where stall recovery starts
$dC_L/d\alpha$	Linear slope of the lift coefficient curve
$C_{D,90}$	Drag coefficient at 90° angle of attack

10% indicating a shift from attached flow in the linear region of the lift curve and the start of trailing edge separation. $C_{L,max}$ is chosen where the lift reaches a maximum value after the start of TE separation ($dC_L/d\alpha = 0$). Beyond $C_{L,max}$, the lift coefficient starts to decrease. Deep stall (S_R) is obtained when the separated flow reaches the leading edge; Mathematically S_R is chosen when the $d^2C_L/d\alpha^2$ reaches an inflection point after $C_{L,max}$. For high angles of attack the parameterization is performed as follows: at 90deg. AoA, an airfoil resembles a flat plat and exhibits C_L values approaching zero (depending on camber, thickness and LE radius). The parameterization is thus done by linearly reducing the C_L between S_R and $C_{L,90}$. Similarly, the C_L between 90 and 150°. AoA is linearly increased. The drag coefficient is several orders of magnitude smaller than the lift coefficient for small angles of attack (below stall) and thus its impact on extreme loads is limited. Upto 30°. AoA, the C_D displays minor change regardless of the airfoil type, geometry, or thickness to chord ratio [12]. Consequently, the drag coefficient is only parameterized by the point where max drag coefficient occurs at $\pm 90^\circ$. AoA where it exhibits the largest variations. In summary, the parameters of the stochastic model are listed in Table 5.

5.2. Stochastic model

In this section we will assign probabilistic distributions, expected values, COV and correlation coefficients to the parameters described in the previous section. Ideally an airfoil's stochastic characteristics could be expressed as: $C_L X_{wt} X_{3D} X_{sr} X_{gd} X_{ld} X_{re} X_{ps} X_{fv}$ (and a similar expression for drag) where C_L is the static lift coefficients measured in a wind tunnel (or CFD), X_{wt} accounts for the

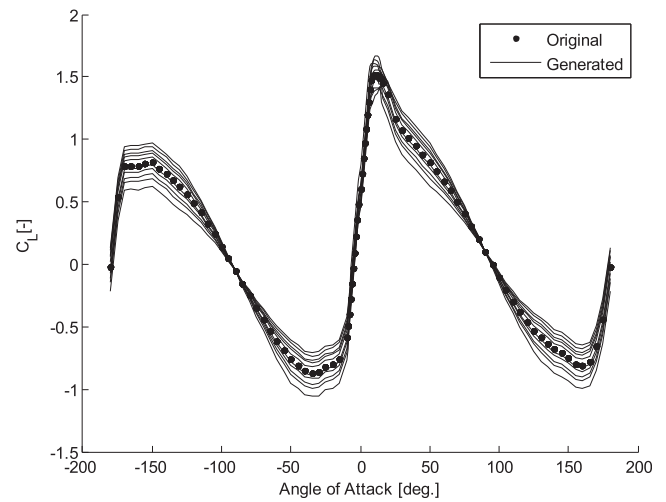


Fig. 10. Generated synthetic lift coefficient curves.

uncertainties associated with assessment of airfoil characteristics in wind tunnels, X_{3D} accounts for the uncertainties due to 3D flow correction, X_{sr} accounts for the uncertainties stemming from surface roughness, X_{gd} accounts for uncertainties related to the blade geometric distortions in manufacturing and handling, X_{ld} accounts for uncertainties related to the blade geometric distortions when deflected, X_{re} accounts for the uncertainties due to the effects of Reynolds number, X_{ps} accounts for uncertainties associated with extending airfoil aerodynamic characteristics to post stall, and finally X_{fv} accounts for uncertainties stemming from the validation of airfoil data by field full scale prototype test. It is not possible to quantify the joint distribution of X 's for each of the model parameters (Table 5) and as a result a more simplified approach is chosen such that $C_L X_{CL}$ where X_{CL} corresponds to the largest COV of the available $X_{wt}, X_{3D}, X_{sr}, X_{gd}, X_{ld}, X_{re}, X_{ps}, X_{fv}$. Indeed this is a fair (albeit conservative) simplification when assuming truncated distributions. The stochastic variables are defined in Table 6 by their distribution, expected value, the coefficient of variation and correlation coefficients. The COV in Table 6 are chosen as follows:

For each source of uncertainty in Table 3
 For each airfoil family in Table 3
 - Collect all available experimental and simulation data of lift and drag polars
 - Compute the COV for each of the variables listed in Table 6
 End
 End
 Assign the largest COV across all sources of uncertainty and all airfoil families for each variable in Table 6

Table 6
Stochastic variables and correlation matrix.

Variable	Distribution	Expected value	COV	Correlation matrix					
$X_{dCl/d\alpha}$	N (truncated)	1	0.033	$X_{CL,max}$	$X_{CL,SR}$	$X_{CL,TES}$	X_{AoAmax}	X_{AoASR}	X_{AoATES}
$X_{CD,90}$	N (truncated)	1	0.10						
$X_{CL,max}$	N (truncated)	1	0.12	1.0					
$X_{CL,SR}$	N (truncated)	1	0.08	0.9	1.0				
$X_{CL,TES}$	N (truncated)	1	0.13	0.9	0.9	1.0			
X_{AoAmax}	N (truncated)	1	0.08	0.6	0.5	0.6	1.0		
X_{AoASR}	N (truncated)	1	0.15	0.4	0.4	0.5	0.6	1.0	
X_{AoATES}	N (truncated)	1	0.10	0.5	0.5	0.6	0.5	0.8	1.00

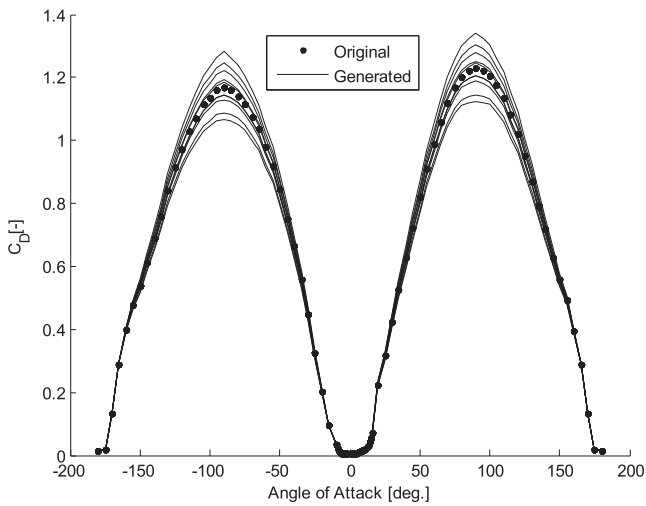


Fig. 11. Generated synthetic drag coefficient curves.

This approach is considered to be conservative as some airfoil families are less sensitive than others to the sources of uncertainty. The correlation matrix is computed by simply collecting all static lift polars available in the database (Table 3) and computing the Pearson correlation coefficients for the variables in Table 6. For each instance of the stochastic variables in Table 6, a lift and drag curve is synthetically generated by spline fitting a curve through the parameters points.

5.3. Results of parameterization

Figs. 10–12 represent a sample reproduction of synthetic C_L , C_D and C_L/C_D curves based on the parameterization and the stochastic model presented above. A brief verification guideline is used to ensure that the synthetic lift and drag coefficient curves are physical [12]:

- $C_L/C_D \sim 0$ at $\text{AoA} = 90^\circ$ and $C_L/C_D \sim 1$ at $\text{AoA} = 45^\circ$
- Comparable C_L/C_D from $\alpha = 30^\circ$ to $\alpha = 90^\circ$

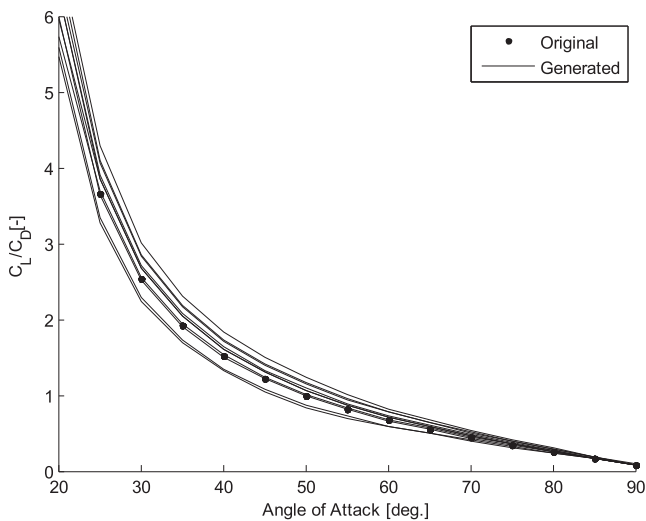


Fig. 12. Generated synthetic lift to drag ratio.

Table 7
Load cases simulations from IEC61400-1 (2005).

Load case	Simulated mean wind speed [m/s]	Yaw error [deg.]	Stochastic realizations per wind speed	Monte Carlo generated airfoil data	Total number of simulations
DLC 1.3 ETM	$V_{\text{rat}}^a = 11$	0	24	26	624
DLC 6.2EWIM	$V_{\text{ref}}^b = 50$	+30	24	26	624

^a V_{rat} is the rated mean wind speed.

^b V_{ref} is the reference wind speed averaged over 10 min (50 m/s for class IEC1).

Table 8
Simulated load output sensors.

Component	Load causing failure	Location
Blade	Flap and edge bending moments Out of plane tip deflection	Blade root and ¼ span Blade tip
Machine frame	Driving, tilt and yaw moments	Main bearing
Tower	Fore-aft bending moment	Tower base and ¼ hub height

6. Extreme loads effects on wind turbines

In this chapter we quantify the effect of the uncertainty in the static lift and drag coefficients on extreme loads on wind turbines. The extreme loads are evaluated using aero-servo-elastic calculations.

6.1. The aero-servo-elastic simulations

The aero-servo-elastic calculations are performed using the software FAST [34] with a custom PID controller for the turbine. This version of FAST models the turbine using 24 Degrees of Freedom (DOFs). These DOFs include two blade-flap modes and one blade-edge mode per blade. It also has two fore-aft and two side-to-side tower bending modes in addition to nacelle yaw. The other DOFs are for the generator azimuth angle, and the compliance in the drivetrain between the generator and hub/rotor. A limited number of design governing extreme load cases are used in this study which are DLC1.3 Extreme Turbulence Model and DLC6.2 Extreme Wind Model (IEC61400-1 2005 [35]). The load cases are only run at mean wind speeds where the load is known to reach peak values as shown in Table 7. Other IEC61400-1 load cases such as extreme coherent gusts and shear gusts, wind direction changes combined with control faults are also critical design driving load cases for large offshore wind turbines but are not considered here. Twenty four simulations (600s stochastic realizations) are carried out at V_{rat} (11 m/s) for DLC1.3ETM and V_{ref} for DLC6.2EWM at +30° yaw error which is usually a critical wind direction for loads effects for long and slender rotor blades. One thousand sets of synthetic static airfoil data are generated in a Monte Carlo scheme based on the parameterization method described in the previous chapter.

Table 9
COV for extreme load effects in DLC1.3ETM and DLC 6.2EWM.

Component	Sensor	Location	COV DLC1.3	COV DLC6.2
Blade	Edgewise bending moment (RootMxb1)	Root	1.7%	6.0%
	Edgewise bending moment (Spn4MLxb1)	¼ span	3.5%	8.5%
	Flapwise bending moment (RootMyb1)	Root	4.2%	3.8%
	Flapwise bending moment (Spn4MLyb1)	¼ span	6.0%	4.5%
	Out of plane tip deflection (OoPDefl1)	Tip	5.4%	5.8%
Machine frame	Driving moment (LSShftMxa)	Main bearing	0.9%	4.7%
	Tilt moment (LSSTipMys)		7.0%	9.9%
	Yaw moment (LSSTipMzs)		5.6%	2.9%
Tower	Fore-aft bending moment (TwrBsMyt)	Base	4.0%	1.8%
	Fore-aft bending moment (TwrHt4MLyt)	¼ H	4.6%	2.0%

From these, twenty six are randomly selected to estimate the extreme loads effects. Table 7 shows the total number of simulations per design load case. For each 600s simulation the global extreme load effect is extracted; in total 24x26 extreme values are extracted for each design load case. The extreme loads effects are estimated for the ‘sensors’ shown in Table 8. The notation ‘sensors’ is used because these loads effects are measured by strain gages on wind turbines.

6.2. Quantifying the effect of aerodynamic uncertainty on extreme loads

For each of the 24 600s time series simulations the global extreme load is extracted. A density function is then estimated from the 24 data points corresponding to one airfoil data set. Fig. 13 displays an example of ten probability density functions of the blade root extreme flap bending moment for DLC1.3ETM and DLC6.2EWM. Observing the modes of the density functions one can clearly confirm that variations in the static airfoil data have a direct net effect on extreme loads. Below are the steps explaining the process of computing the COV of the extreme loads effects:

- Step 1: Use the stochastic model to generate 1000 airfoil data, 26 of which are chosen at random.

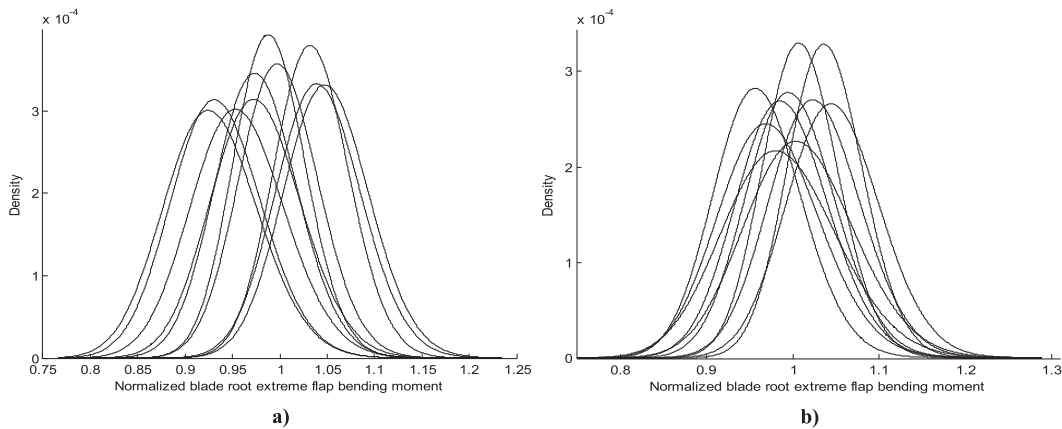


Fig. 13. Ten airfoil data are generated and the corresponding density functions of the normalized blade root extreme flap bending moment for a) DLC1.3ETM and b) DLC6.2EWM are displayed.

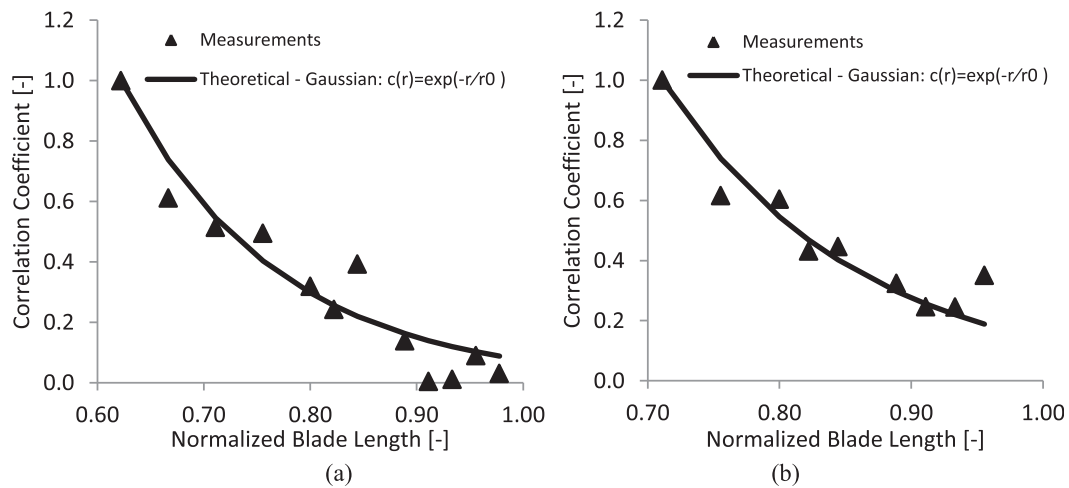


Fig. 14. A comparison between measured and theoretical correlation coefficients of (a) variation of blade chord length and (b) thickness along the span of the blade. The theoretical exponential correlation function has a correlation length corresponding to 15% of the blade length.

- Step 2: Generate 24 ETM turbulence seeds at 11 m/s mean wind speed (The IEC61400-1 standard recommends using 6 seeds [35]).
- Step 3: Select 1 out of 26 airfoil data.
 - Step 3.1: run the 24 seeds of DLC1.3ETM.
 - Step 3.2: extract absolute max load level from each of the 24 time series simulations.
 - Step 3.3: fit a distribution to the 24 extremes and record the mode of the distribution.
- Step 4: Repeat step 3 until all 26 stochastic airfoil data have been used.
- Step 5: Calculate the COV of the extreme load effect using the 26 modes of the loads distributions.

The same process is used to compute the COV of the extreme loads effects for DLC6.2EWM. The COV on the extreme load effect is calculated in Table 9.

General observations:

- The COV is lower than 10% [8] for all structural components in both operating extreme (DLC1.3ETM [35]) and stand-still (DLC6.2EWM [35]) conditions.
- In extreme operating conditions (DLC1.3ETM [35]), the driving torque loads on the main shaft and edgewise loads are the least affected by the static lift and drag coefficients uncertainty. Thrust driven components (i.e. flapwise loads, out-of-plane deflection, tilt and yaw loads) exhibit the largest sensitivity to aerodynamic uncertainty. The outer part of the blade is more affected by aerodynamic uncertainty compared to the root section.
- In extreme stand-still conditions (DLC6.2EWM [35]), the edgewise loads and tilt loads exhibit the largest sensitivity to aerodynamic uncertainty. This may be due to large unstable vibrations often observed in DLC6.2EWM simulations for long and slender blades.

6.3. Correlation of the airfoil aerodynamic characteristics along the span of the blade

In the results presented above it has been tacitly assumed that the adjacent aerodynamic sections along the blade are

independent. This is not a reasonable assumption as adjacent locations may well be aerodynamically correlated in aeroelastic simulations. The correlation of airfoil data along the span of the blade is now considered and thus a “correlation length” needs to be derived, which is not straightforward but is examined as per the following arguments based on engineering judgments:

- For long and slender blades as the one used in this study, radial flow in the root has reaching effects up to 20–30% of the blade length from the root.¹
- Depending on the blade geometry and operating rotor speed, the Re number is constant (within $\pm 5\%$) between 30% and 60% of the blade length. Near the root and the tip of the blade the Re exhibits steep change.
- On most large blades, the outer 20–30% of the blade is covered by the same airfoil family of similar thickness to chord ratio and the flow can be considered 2-dimensional.
- Fig. 14 shows the correlation coefficients of (a) blades' chord length and (b) absolute thickness along the span of the blade; the chord length measurements are performed on 144 blades in a wind turbines manufacturer's blade factory and the thickness measurements are performed on 32 blades. The plots compare the empirical correlation coefficients to a theoretical exponential correlation function with a correlation length corresponding to 15% of the blade length. The plots show a very good agreement, indicating that a correlation length of 15% of the blade length is a good estimate.
- In Fig. 15 uncertainties in the static airfoil lift and drag coefficients was introduced at the blade tip region and the effect on induction was studied. The variation in the induction seen here is model based (i.e. how the uncertainties are propagated in the aero-servo-elastic code itself including airfoil distribution along the span of the blade, blade discretization, airfoil data interpolation, etc.). The perturbation in induction is seen to span up to 15% of the blade length from the blade tip. It must be noted however that the magnitude and extent of the perturbation in induction near the tip region will be largely impacted by the tip loss correction models used in the BEM code [36].

¹ Rotational effects depend, amongst other metrics, on the chord to radius ratio. For small blades rotational effects could be as high as 50% of the blade length or more. The blade used in this research is long and slender.

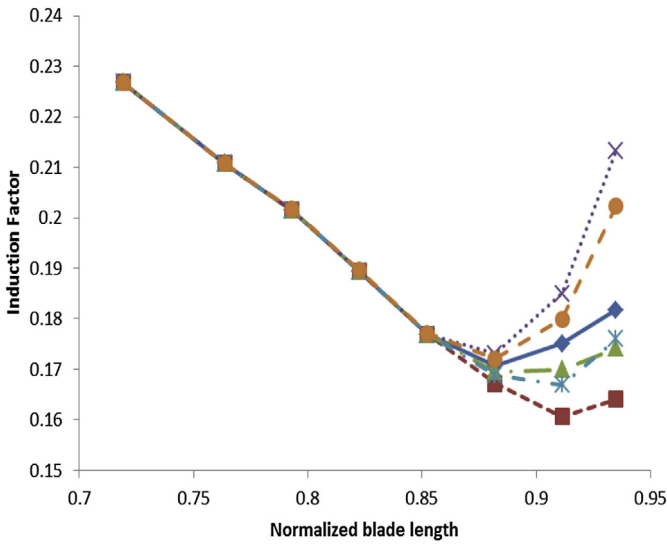


Fig. 15. Six random perturbations of the static airfoil data are introduced in the tip section of the blade and the induction factor is calculated along the span of the blade. The affected length is of the order of 15% of the blade length from the tip.

Given the above arguments it can be concluded that a reasonable correlation length for the aerodynamic stochastic variables is of the order of 15%–20% of the blade length. The blade sections are thus assumed correlated using an exponential correlation function with a correlation length equivalent to 20% of the blade length:

$$c(r) = \exp(-r/r_0) \tag{1}$$

where r is a radial location along the span of the blade ranging from 0 to R where R is the blade length and r_0 is the correlation length ($r_0 = 20\%$ of the blade length). The fully correlated airfoil stochastic parameters along the span of the blade are generated as:

$$\mathbf{X} = \boldsymbol{\mu} + \boldsymbol{\sigma}\mathbf{T}\mathbf{U} \tag{2}$$

where \mathbf{U} is a vector of standard normal stochastic variables, \mathbf{T} is a lower triangular matrix of the Cholesky decomposition of the correlation matrix, $\boldsymbol{\mu}$ is a vector of the mean values and $\boldsymbol{\sigma}$ is a diagonal matrix containing the standard deviations of the stochastic parameters. The diagonal blocks of the correlation matrix are the

correlations amongst the stochastic variables in one blade section; the off-diagonal elements are the cross-correlation coefficients from one section to another along the span of the blade generated by Equation (1).

The aeroelastic simulations described in the previous section are hereby repeated for correlated static airfoil data. Fig. 16 compares the COV of the extreme loads effects for both correlated and uncorrelated static airfoil data. The results reveal several interesting trends:

- There is a clear trend indicating an increase in the COV of the extreme load effects in both DLC1.3ETM and 6.2EWM when the static airfoil data are correlated along the span of the blade.
- The extreme tilt bending moment in both DLC1.3ETM and DLC6.2EWM exhibits the largest COV indicating that asymmetric loads are the most sensitive to uncertainty in the static airfoil data. A control system targeting asymmetric loads can potentially reduce this effect.
- The main shaft torque is the least affected by the uncertainty in airfoil data in operating conditions in DLC1.3ETM.
- In both extreme operating and stand still conditions, the flapwise and edgewise extreme bending moments near the blade tip exhibit larger sensitivity towards uncertainty in the static airfoil data compared to the blade root.
- Except for the extreme edgewise bending moment, tilt moment and driving torque on the main shaft, the effect of aerodynamic uncertainty is larger in extreme operating conditions (DLC1.3ETM) compared to extreme stand still conditions (DLC6.2EWM).
- In extreme stand still condition (DLC6.2EWM [35]), the edgewise loads and tilt loads exhibit significantly larger COV compared to the extreme operating conditions (DLC1.3ETM [35]). This is believed to be due to unstable vibrations often observed in DLC6.2EWM simulations of long and slender blades, and is not believed to be a direct effect of aerodynamic uncertainty.
- The COV of the extreme edgewise bending moments in DLC6.2EWM is significantly larger when the airfoil data in adjacent blade stations are correlated. This is an important observation indicating that a decoupling of blade sections aerodynamically can potentially reduce edgewise loads (instabilities/vibrations) in stand-still which is a significant problem for large and slender blades, due to large blade oscillations seen in stand-still in simulations. The same can be concluded for the extreme tilt moment

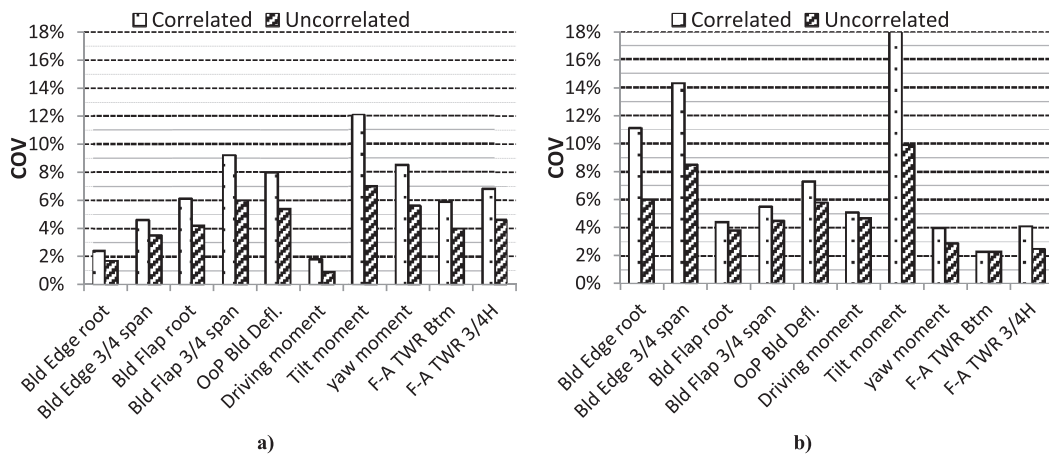


Fig. 16. COV for extreme load effects in (a) DLC1.3ETM and (b) DLC6.2EWM when the static airfoil data correlation along the span of the blade is included.

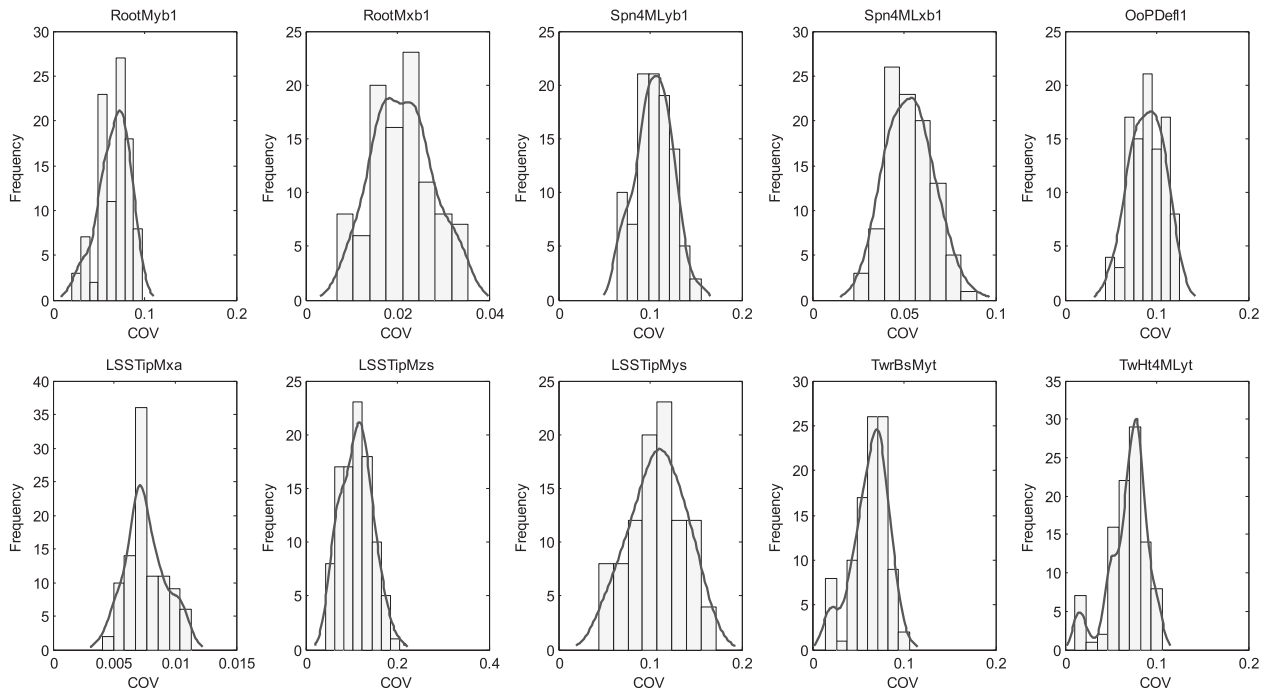


Fig. 17. Variation of COV when the airfoil data and wind seeds are bootstrapped. This is done on correlated airfoil data in DLC1.3ETM at 11 m/s wind speed IECIA.

7. Statistical uncertainty of the coefficients of variation in extreme turbulence operation

Following the observations and argumentation given above, it can be stated that the effect of aerodynamic uncertainty is more pronounced in extreme operating conditions compared to extreme stand still conditions (mainly because of larger angles of attack in operating conditions compared to stand-still conditions). As a result, this section is solely dedicated to the statistical uncertainty in determining the COV in extreme operating conditions (DLC1.3ETM). The COV presented in Fig. 16 are based on a set of 26 airfoil data and a set of 24 wind seeds. It is expected that the COV to vary if another set of airfoil data and wind turbulence seeds are chosen. The statistical uncertainty surrounding the estimation of

the COV is hereby assessed using the bootstrapping technique. The bootstrapping methodology is implemented as follows:

- Step 1: Generate 10,000 correlated stochastic airfoil data.
- Step 2: Generate 100 extreme turbulence seeds at 11 m/s mean wind speed.
- Step 3:
 - Step 3.1: Select 16 out of 10,000 airfoil data.
 - Step 3.2: Select 24 out of 100ETM seeds.
 - Step 3.2.1: for each one of the 16 airfoil data, run the 24 seeds of DLC1.3ETM.
 - Step 3.2.2: extract absolute max load level from each of the 24 time series simulations.
 - Step 3.2.3: fit a distribution to the 24 extremes and record the mode of the distribution.
 - Step 3.2.4: From 16 modes calculate the COV.
- Step 4: Repeat step 3 70 times.
- Step 5: fit a distribution to the 70 COV. This distribution describes the statistical uncertainty in the COV.

Table 10

Most likely COV of uncertainty related to airfoil data for various load components. The COV correspond to correlated airfoil data in DLC1.3ETM at 11 m/s mean wind speed.

Component	Sensor	Location	Most likely COV
Blade	Edgewise bending moment (RootMxb1)	Root	2%
	Edgewise bending moment (Spn4MLxb1)	¼ span	5%
	Flapwise bending moment (RootMyb1)	Root	7%
	Flapwise bending moment (Spn4MLyb1)	¼ span	11%
	Out of plane tip deflection (OoPDefl1)	Tip	10%
Machine frame	Driving moment (LSShtMxa)	Main bearing	1%
	Tilt moment (LSShtMys)		11%
	Yaw moment (LSShtMzs)		12%
Tower	Fore-aft bending moment (TwrBsMyt)	Base	7%
	Fore-aft bending moment (TwHt4MLyt)	¼ H	8%

The results are shown in Fig. 17 and Table 10.

Arguably, rated mean wind speed and cut out mean wind speed are the most critical for extreme loads and least favorable operating conditions in extreme turbulence. Comparing the most likely COV from Tables 9 and 10 to the 10% value used in Refs. [8], the following observations can be made:

Table 11

Optimal design of a tower in stand-still loading with a target probability of failure of 5×10^{-4} as a function of the COV of airfoil aerodynamic uncertainty.

Target P_F	COV X_{aero}	D [m]	T [mm]
5×10^{-4}	20%	5.65	15.9
5×10^{-4}	10%	5.40	15.1
5×10^{-4}	4%	5.33	14.9
5×10^{-4}	2%	5.33	14.9

7.1. Tower

The least favorable load cases for towers in IECIA/B sites are arguably DLC1.3ETM and DLC6.2EWM. In extreme turbulence the tower loads tend to peak around rated mean wind speed. As shown in Table 10 the most likely COV is of the order of 7% at the tower bottom to 8% at the tower top. This indicates that the value of 10% for X_{aero} in Ref. [8] is on the conservative side.

7.2. Blades

Two of the least favorable load cases for blades in IECIA/B sites are arguably DLC1.3ETM and DLC6.2EWM. In extreme turbulence the blade flapwise loads tend to peak around rated wind speed, while the blade edgewise loads tend to peak around cut-out wind speed. As shown in Table 10 the most likely COV for flapwise bending moment is of the order of 7% at the root to 11% close to the tip of the blade. This indicates that the value of 10% for X_{aero} in Ref. [8] is appropriate for the blade tip but on the conservative side for the blade root. The edgewise loads are largely driven by gravitational and inertial effects and to a lesser extent by aerodynamic effects. Consequently, any uncertainty in airfoil aerodynamics translates into negligible variations in extreme loads, and hence the COV is of the order of 2–5%.

7.3. Main frame

One of the least favorable load cases for the main frame in IECIA/B sites is arguably DLC1.3ETM. In extreme turbulence the main frame tilt and yaw moments tend to peak around rated mean wind speed or cut-out mean wind speed (depending on the performance of the control system). As shown in Table 10 the most likely COV for tilt and yaw is on the order of 11–12%. Therefore the value of 10% for X_{aero} in Ref. [8] is less conservative when the least favorable condition occurs at rated wind speed.

It must be noted that the values in Table 10 are derived based on the wind turbine operating with advanced load alleviation control features not engaged; hence the values are judged to be on the conservative side.

8. Applications in structural reliability

The impact of the uncertainty of static airfoil data on structural reliability is hereby investigated. The first application deals with the structural reliability optimization of a wind turbine tower bottom section, and the second application deals with the determination of the partial load factor of a wind turbine blade root bending moment.

8.1. Application 1: reliability based structural optimization

The reliability optimization framework is based on a cost-benefit model proposed by Rackwitz [37]. Put simply, the idea is to find the value of the design variables (i.e. tower diameter) that maximizes the benefits of a wind turbine (i.e. annual energy production) for the lowest cost possible. The reliability optimization problem is formulated as follows when systematic rebuilding is performed in case of failure:

$$\max_z W(\mathbf{z}) = \underbrace{\frac{b}{rC_0}}_{\text{Benefits}} - \underbrace{\left[\frac{C_I(\mathbf{z})}{C_0} + \left(\frac{C_I(\mathbf{z})}{C_0} + \frac{C_F}{C_0} \right) \frac{\lambda P_F(\mathbf{z})}{r + \lambda P_F(\mathbf{z})} \right]}_{\text{Costs}} \quad (3)$$

$$\text{s.t. } z_i^l \leq z_i \leq z_i^u \\ P_F(\mathbf{z}) \leq P_F^{\max}$$

where:

- \mathbf{z} Design variables $\mathbf{z} = (z_1, z_2, \dots, z_N)$, such as diameter and thickness of the tower bottom.
- $P_F(\mathbf{z})$ Probability of failure given the design variables \mathbf{z} with a reference period of 1 year.
- λ Failure rate assuming the failure events follow a Poisson process.
- $C_I(\mathbf{z})$ Initial building costs given the design variables \mathbf{z} .
- C_F Cost of failure.
- C_0 Reference cost.
- r Real rate of interest.
- b Yearly benefits (such as annual energy production).

The probability of failure is estimated based on a failure mode defined by a limit state function $g(X_1, X_n, \dots, X_n, \mathbf{z})$ and a stochastic model for the stochastic variables X_1, X_n, \dots, X_n . The Ultimate limit state function chosen here is of a tower in buckling in stand-still [37]. The Limit State Function for tower buckling:

$$g = M_{cr} - Qh \quad (4)$$

Resistance – tower bottom bending moment (stress x section modulus):

Table 12 Stochastic variables.

Variable	Description of variable	Distribution	Expected value	COV
P	Annual maximum mean wind pressure	G	538 Pa	0.23
I	Turbulence intensity in stand still	LN	0.11	0.05
$C_r A$	Thrust coefficient × rotor area	–	340 m ² at 25 m/s	–
K_p	Peak factor	–	3.3	–
X _{dyn}	Structural dynamics	LN	1	0.05
X _{aero}	Airfoil data uncertainty	G	1	0.10
X _{exp}	Exposure (terrain)	LN	1	0.10
X _{ext}	Extrapolation and operation simulation	LN	1	0.05
X _{st}	Climate statistics	LN	1	0.05
X _{str}	Stress evaluation	LN	1	0.03
X _{sim}	Simulation statistics	N	1	0.05
X _R	Model uncertainty for material strength	LN	1	0.05
Camp	Amplification factor	–	1.35	–
h	Hub height	–	70 m	–
F _{y, ss}	Yield strength for structural steel	LN	240 MPa	0.05
E	Young's modulus	LN	2.1 × 10 ⁵ MPa	0.02
X _{y, ss}	Yield strength for structural steel	LN	1	0.05
X _{E, ss}	Young's modulus	LN	1	0.02
X _{cr}	Critical load capacity	LN	1	0.10
η	Ratio of mean response to the expected extreme response	–	0.5	–
ξ	Ratio of the gravity dominated response to the expected extreme response	–	0.75 for flapwise bending moment	–
$\bar{\Sigma}$	Material strength	LN	1	0.10
\bar{T}	Extrapolated response	G	1	0.05
\bar{G}	Self-weight	N	1	0.05

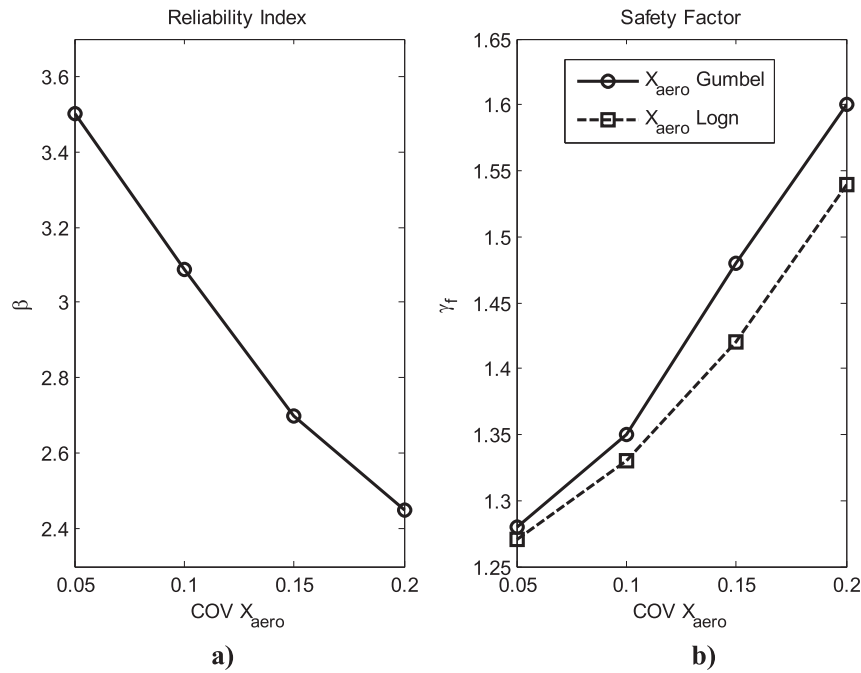


Fig. 18. a) Variation of reliability index with aerodynamic COV for fixed safety factors $\gamma_m = 1.25$ and $\gamma_f = 1.35$ b) Variation of the load safety factors as a function of COV when X_{aero} is assumed Gumbel distributed and Lognormal distributed and reliability index set to 3.09.

$$M_{cr} = \frac{1}{6} \left(1 - 0.84 \frac{D}{t} \frac{X_{y,ss} \cdot F_y}{X_{E,ss} \cdot E} \right) (D^3 - (D - 2t)^3) \cdot X_{y,ss} \cdot X_{cr} \cdot F_{y,ss} \quad (5)$$

Load – bending moment (thrust x hub height):

$$L = Qh = PC_T A \left(1 + 2K_p IC_{amp} X_{dyn} \right) \cdot X_{aero} \cdot X_{exp} \cdot X_{st} \cdot X_{str} \cdot X_{sim} \cdot h \quad (6)$$

The stochastic variables in the limit state function are described in Table 12. The target probability of failure in Equation (3) is set to $5 \cdot 10^{-4}$ corresponding to a reliability index $\beta = 3.3$. The design variables to be optimized are chosen to be the tower bottom diameter D and sheet thickness t . The initial cost C_I is modeled by the following expression [37]:

$$\frac{C_I}{C_0} = \frac{1}{6} \frac{R}{R_0} + \frac{1}{6} \frac{Dt}{A_0} + \frac{1}{3} \quad (7)$$

where C_0 is the reference cost corresponding to the reference onshore foundation radius $R_0 = 8.5$ m and area $A_0 = 3/26$ m². The failure costs are assumed to be $C_F/C_0 = 1/36$. The benefits per year are $b/C_0 = 1/8$ and the real rate of interest is assumed to be $r = 5\%$ and finally R is set to a constant $R = 4.0$ m. Using the simple but representative ultimate limit state function and cost models, the optimum values of the design variables can be calculated for the target probability of failure. The results are shown in Table 11.

A typical value of 10% COV for X_{aero} is reported in the literature [8]. However it was shown earlier that lower values (between 2 and 4% in stand-still) can be used for a tower (see Fig. 16). The benefits of reducing the tower bottom diameter D and sheet thickness t are however limited compared to $COV = 10\%$. This is a general feature of structural reliability based optimization due to the fact that the optimum is rather flat. Other design factors such as stiffness, frequencies, buckling and fatigue strength, geometric standardization, and transportation should be taken into consideration before the reduction in tower diameter materializes as a real benefit.

8.2. Application 2: safety factors

In light of the new COV of the aerodynamic uncertainty presented above, it is now of interest to see the effect on the loads safety factor. The probability of failure is estimated based on a failure mode defined by an ultimate limit state function of a wind turbine blade in normal production [8]:

$$\Phi(\beta) = \Pr \left\{ \gamma_m \gamma_f \tilde{\Sigma} X_R \geq \xi \left[\eta + (1 - \eta) \tilde{T} X_{dyn} X_{st} X_{ext} X_{sim} \right] X_{exp} X_{aero} X_{str} + (1 - \xi) \tilde{G} \right\} \quad (8)$$

where γ_m , γ_f are the material and loads safety factor respectively. The remaining stochastic variables in Equation (8) are described in Table 12.

The material safety factor γ_m is set to a constant value of 1.25. Equation (8) is then solved with respect to the loads safety factor γ_f for $\beta = 3.09$, $\eta = 0.5$, $\xi = 0.75$ and varying the COV of airfoil data uncertainty X_{aero} between 5% and 20%. The result is shown in Fig. 18. The two lines in Fig. 18(b) correspond to the safety factors as a function of COV when X_{aero} is assumed Gumbel distributed [8] and Lognormal distributed. The effect on the safety factors from the choice of distribution becomes apparent for large COV. From Table 10 a COV value of the order of 7.0% is appropriate for the blade root (flapwise), resulting in a loads safety factor of the order of 1.30. Fig. 18 (a) shows the variation of the reliability index β with aerodynamic COV for fixed safety factors $\gamma_m = 1.25$ and $\gamma_f = 1.35$. For $X_{aero} = 7\%$, β corresponds to a value of the order of 3.3 which is higher than the currently accepted value of 3.09 in the IEC61400-1 design standard. The large variation of the reliability index in Fig. 18 (a) reflects the large influence of aerodynamics on the blade flapwise design ($\xi = 0.75$).

9. Conclusion

In the IEC61400-1 design standard for wind turbines, a value of 10% for the coefficient of variation (COV) on the uncertainty related

to the assessment of the aerodynamic lift and drag coefficients is used. The findings in this article indicate that while this value is appropriate for certain structural components, it is conservative for others. An overall assessment of uncertainties in the aerodynamic static lift and drag coefficients in this article shows a tangible reduction in both the extreme load safety factors and the dimension of structural components when exposed to extreme loading conditions. Generally, uncertainties in airfoil aerodynamics have a larger impact on extreme loads during power production compared to stand-still. The assessment of aerodynamic uncertainties is done through a heuristic based stochastic model which replicates the uncertainties in airfoil characteristics by parameterizing the lift and drag coefficient polar curves. The parameters are assigned distributions and coefficient of variations based on field measurements, aerolastic simulations and engineering judgment. Large wind turbine manufactures can further update the stochastic model by integrating their own data to assess the impact of the aerodynamic uncertainty on their specific wind turbine design. In addition to possible reduction in the levelized cost of energy, the stochastic model is a tool for risk mitigation in the early stages of the aerodynamic design of a wind turbine rotor. One limitation to the stochastic model is that it does not include model uncertainties (such as dynamic stall and dynamic wake models). The aero-servo-elastic simulations were performed with a basic controller. Advanced load alleviation features were not included. Hence, the COV values are judged to be on the conservative side. Future research could integrate advanced load alleviation features in the assessment of the COV. Furthermore, the assessment of aerodynamic uncertainties in this article is done towards extreme loading, it can be envisaged that a similar assessment can be made towards fatigue loading in the future.

Acknowledgments

The work presented herein is a part of the Danish Energy Technology Development and Demonstration (EUDP) project titled, “Demonstration of a basis for tall wind turbine design”, Project no 64011 -0352. The financial support is greatly appreciated. The Danish Ministry of Science, Innovation and Higher Education are also gratefully acknowledged for their financial support. MiTa-Teknik are acknowledged for their technical and financial support.

Appendix A. Geometric distortions of the blade during manufacturing and handling

This appendix presents a description of a model that generates stochastic airfoil data (lift, drag and moment coefficients) based on geometric distortions of airfoils sections during manufacturing and handling. The stochastic model is implemented in Matlab[®].

A series of measurements in a blade factory were performed and primary geometric distortions incurred to airfoil sections during manufacturing and handling have been categorized and quantified. In order to simplify the analysis, the observed distortions are consolidated into four categories as shown in Fig. 19, namely change in chord length, change in TE thickness, change in the absolute thickness of the airfoil near the spar cap region and depression of the shell behind the shear web either on the pressure or the suction side or both. It was observed that a combination of these distortions can occur at any given section along the span of the blade. Based on the collected data, each distortion category is assigned a probability distribution with an expected value and a COV as shown in Table 13. The four categories of geometric distortions are assumed to be fully uncorrelated.

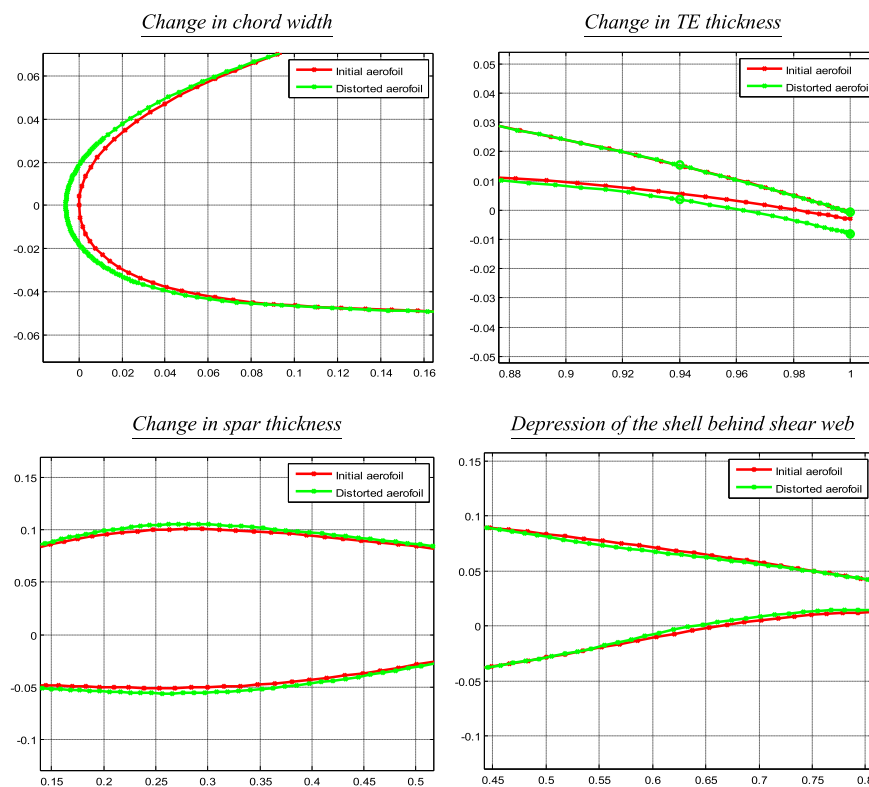


Fig. 19. Categories of the geometric distortions in manufacturing and handling.

First a set of control points are selected from the original airfoil geometry. The control points are chosen appropriately to correspond to the LE, TE, spar cap region and shell regions behind the shear web. The control points are then distorted based on the stochastic model in Table 13. Finally a spline is fitted to the distorted control points. An example of a possible geometric distortion based on this methodology is shown in Fig. 22 for a NACA 63418 profile. A Monte Carlo simulation is then used to generate such samples of

geometric distortions for a NACA 63418 and Risø B15 profiles. The distorted airfoil geometry is then passed to XFOIL [32] to compute the lift, drag and moment coefficients. As an example the effect of geometric distortions on the lift and drag coefficients is shown in Fig. 20 for a NACA 63418 profile. In addition, as an example, the effect of geometric distortion on max lift and the slope of the lift coefficient curve in the form of empirical cumulative distribution functions (CDF) are shown in Fig. 21 for a NACA 63418 profile.

Table 13
Stochastic variables for airfoil geometry distortion.

Geometric distortion category	Distribution	Expected value	COV ^a [as a % of chord length]	Bias [as a % of chord length]
Change in chord width	Normal	initial undistorted airfoil geometry	0.0004	-0.52
Change in TE thickness	Lognormal	initial undistorted airfoil geometry	0.001	-
Change in profile thickness in the main spar region	Lognormal	initial undistorted airfoil geometry	0.002	0.15
Depression in the shells behind the shear web	Lognormal	Initial undistorted airfoil geometry	0.005	-

^a Say a chord length is 1000 mm, then the COV for the change in TE thickness is: $0.001 \cdot 1000 = 1\%$, where 0.001 is the COV as a percent of chord length.

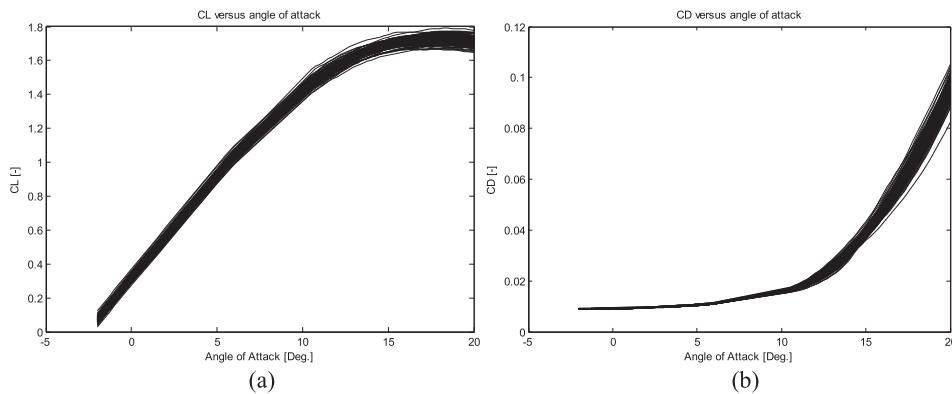


Fig. 20. Variation in a) lift coefficient and b) drag coefficient due to geometric distortions for a NACA 63418 profile computed in XFOIL [32].

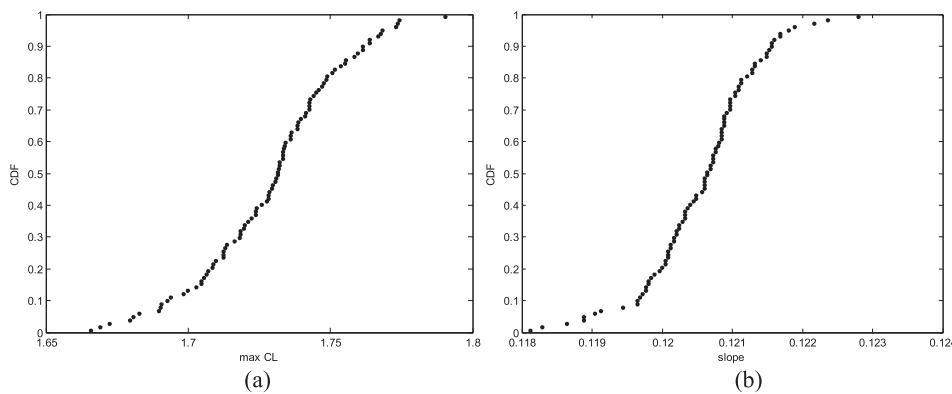


Fig. 21. CDF of a) max lift coefficient and b) the slope of the lift coefficient curve for a NACA 63418 profile.

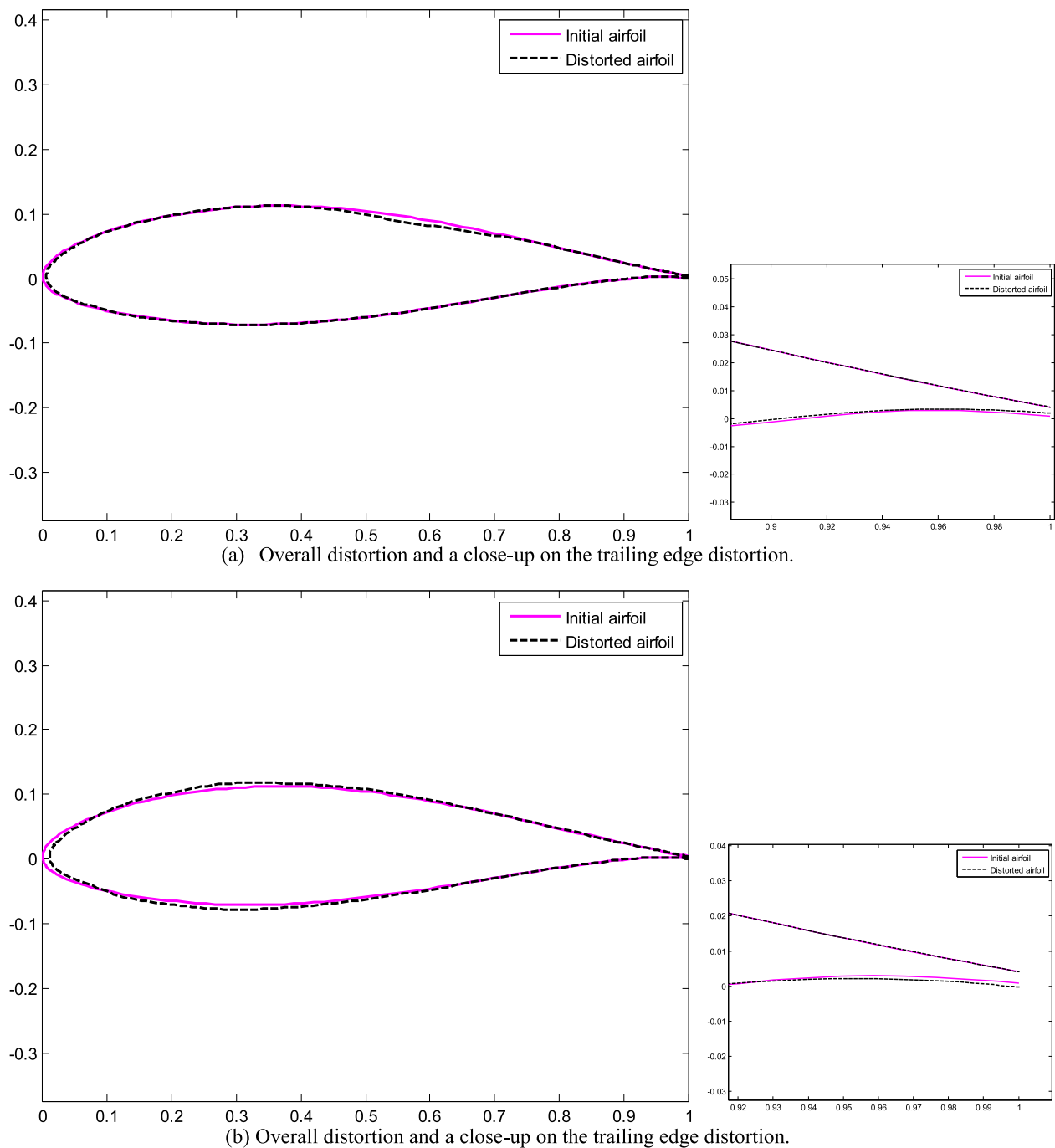


Fig. 22. Synthetic samples of possible geometric distortions for a NACA 63,418 profile based on the stochastic model.

References

- [1] McCroskey WJ. A critical assessment of wind tunnel results for the NACA 0012 airfoil. 1987. NASA Tech. Memo. 100019 USAAVSCOM Tech. Rep. 87-A-5.
- [2] Simms D, Schreck S, Hand M, Fingersh LJ. NREL unsteady aerodynamics experiment in the NASA-Ames wind tunnel: a comparison of predictions to measurements. 2001. NREL/TP-500-29494.
- [3] Loeven GJA, Bijl H. Airfoil analysis with uncertain geometry using the probabilistic collocation method. In: 49th AIAA/ASME/ASCE/AHS/ASC structures, structural dynamics, and materials conference, AIAA 2008-2070; 2008.
- [4] Witteveen JAS, Doostan A, Pecnik R, Iaccarino G. Uncertainty quantification of the transonic flow around the RAE 2822 airfoil. In: Center for turbulence research, annual research briefs. Stanford University; 2009.
- [5] Bak C, Madsen H, Gaunaa M, Paulsen U, Fuglsang P, Romblad J, et al. DAN-AERO MW: comparisons of airfoil characteristics for two airfoils tested in three different wind tunnels. In: The science of making torque from wind; 2010. p. 59–70.
- [6] Petrone G, de Nicola C, Quagliarella D, Witteveen JAS, Iaccarino G. Wind turbine performance analysis under uncertainty. In: 49th AIAA aerospace sciences meeting including the new horizons forum and aerospace exposition, AIAA 2011-544; 2011 [no. January].
- [7] Bak C, Troldborg N, Madsen H. DAN-AERO MW: measured airfoil characteristics for a MW rotor in atmospheric conditions. In: Scientific proceedings: european wind energy association; 2011. p. 171–5.
- [8] Tarp-johansen NJ, Madsen P, Frandsen S. Partial safety factors for extreme load effects – proposal for the 3rd Ed. of IEC 61400: wind turbine generator

- systems – part 1: safety requirements. 2002. Risø-R-1319(EN), Roskilde, Denmark.
- [9] Madsen H, Bak C, Paulsen U, Gaunaa M, Fuglsang P, Romblad J, et al. The DAN-aero MW experiments – final report. 2010. Risø-R-1726(EN), Roskilde, Denmark.
- [10] Schepers JG, Snel H. Model experiments in controlled conditions – final report. ECN-E-07-042. 2007.
- [11] Timmer WA. An overview of NACA 6-digit airfoil series characteristics with reference to airfoils for large wind turbine blades. In: 47th AIAA aerospace sciences meeting including the new horizons forum and aerospace exposition; 2009 [no. January].
- [12] Timmer WA. Aerodynamic characteristics of wind turbine blade airfoils at high angles-of-attack. In: The science of making torque from wind; 2010. p. 71–8. no. 1.
- [13] Yoshida K, Noguchi M. Adverse reynolds number effect on maximum lift of two dimensional airfoils. In: ICAS 2000 Congress, 22nd congress of international council of the aeronautical sciences; 2000. 295.1–295.10.
- [14] Timmer WA, Schaffarczyk AP. The effect of roughness at high reynolds numbers on the performance of DU 97-W-300Mod. *Wind Energy J* 2004;7(4): 295–307.
- [15] Schneemann J, Knebel P, Milan P, Peinke J. Lift measurements in unsteady flow conditions. In: European wind energy conference & exhibition (EWEC); 2010.
- [16] Bak C, Johansen J, Andersen PB. Three-dimensional corrections of airfoil characteristics based on pressure distributions. In: European wind energy conference & exhibition (EWEC); 2006.
- [17] Laino DJ, Hansen a C, Minnema JE. Validation of the AeroDyn subroutines using NREL unsteady aerodynamics experiment data. *Wind Energy Apr.* 2002;5(2–3):227–44.
- [18] Fuglsang P, Antoniou I, Bak C, Madsen H. Wind tunnel test of the RISØ-1 airfoil. 1998. Risø-R-999(EN), Roskilde, Denmark.
- [19] Fuglsang P, Dahl KS, Antoniou I. Wind tunnel tests of the Risø-A1-18, Risø-A1-21 and Risø-A1-24 airfoils. 1999. Risø-R-1112(EN), Roskilde, Denmark.
- [20] Broeren A, Lee S, LaMarre C, Bragg M. Effect of airfoil geometry on performance with simulated ice accretions volume 2: numerical investigation. DOT/FAA/AR-03/64. Washington, D.C. 20591: Office of Aviation Research; 2003.
- [21] Broeren A, Lee S, LaMarre C, Bragg M. Effect of airfoil geometry on performance with simulated ice accretions Volume 1: experimental investigation. DOT/FAA/AR-03/64. Washington, D.C. 20591: Office of Aviation Research; 2003.
- [22] Ward K. The effect of small variation in profile of airfoils. National Advisory Committee for Aeronautics; 1931. Technical Note No. 361.
- [23] Yamauchi W, Johnson G. Trends of reynolds number effects on two-dimensional airfoil characteristics for helicopter rotor analyses. 1983. NASA Technical Memorandum 84363, NASA-TM-84363.
- [24] Ceyhan O. High reynolds number effects on 20 MW wind turbine rotor design. In: The science of making torque from wind; 2012 [no. October].
- [25] Tangler J, Kocurek D. Wind turbine Post-Stall airfoil performance characteristics guidelines for blade-element momentum methods. In: 43rd AIAA aerospace sciences meeting and exhibit; 2005.
- [26] Ostowari C, Naik D. Post stall studies of untwisted varying aspect ratio blades with NACA 44xx series airfoil sections-PartII. *Wind Eng* 1985;9(3):149–64.
- [27] Ostowari C, Naik D. Post stall studies of untwisted varying aspect ratio blade with NACA 4415 airfoil section - Part I. *Wind Engineering* 1984;8(3):176–94.
- [28] Petrilli J, Paul R, Gopalathnam A, Frink N. A CFD database for airfoils and wings at Post-Stall angles of attack. In: Proc. of the 31st AIAA applied aerodynamics conference, San Diego, CA; 2013. no. 919.
- [29] Montgomerie B. Methods for root effects, tip effects and extending the angle of attack range to ± 180 deg., with application to aerodynamics for blades on wind turbines and propellers. 2004. FOI-R-1305-SE.
- [30] Breton S-P, Cotton FN, Moe G. A study on rotational effects and different stall delay models using a prescribed wake vortex scheme and NREL phase VI experiment data. *Wind Energy Sep.* 2008;11(5):459–82.
- [31] Gumbert C, Newman P, Hou G. Effect of random geometric uncertainty on the computational design of a 3-D flexible wing. In: Proceedings of the 20th AIAA applied aerodynamics conference, AIAA paper 2002–2806; 2002.
- [32] Drela M. XFOIL: an analysis and design system for low Reynolds number airfoils. In: Low reynolds number aerodynamics; 1989.
- [33] Viterna D, Janetzke L. Theoretical and experimental power from large horizontal-axis wind turbines. 1982. NASA Technical Memorandum 82944, NASA-TM-82944.
- [34] Jonkman J, Buhl M. FAST user's guide. 2005. NREL/EL-500-38320.
- [35] IEC61400-1. Wind turbines – part 1: design requirements. ed. 3 2005.
- [36] Shen WZ, Mikkelsen R, Sørensen JN, Bak C. Tip loss corrections for wind turbine computations. *Wind Energy* 2005;8:457–75.
- [37] Sørensen JD, Tarp-johansen NJ. Reliability-based optimization and optimal reliability level of offshore wind turbines. *Int J Offshore Polar Eng* 2005;15(2).

6 *Publication:* Influence of the control system on wind turbine loads in power production in extreme turbulence: structural reliability

Influence of the control system on wind turbine loads in power production in extreme turbulence: structural reliability

I. Abdallah^{a,*}, A. Natarajan^a, J.D. Sørensen^{a,b}

^aTechnical University of Denmark, Department of Wind Energy, Roskilde, Denmark

^bAalborg University, Department of Civil Engineering, Aalborg, Denmark

Abstract

The wind energy industry is continuously researching better computational models of wind inflow and turbulence to predict extreme loading (the nature of randomness) and their corresponding probability of occurrence. Sophisticated load alleviation control systems are increasingly being designed and deployed to specifically reduce the adverse effects of extreme load events resulting in lighter structures. The main objective herein is to show that despite large uncertainty in the extreme turbulence models, advanced load alleviation control systems yield both a reduction in magnitude and scatter of the extreme loads which in turn translates in a change in the shape of the annual maximum load distribution function resulting in improved structural reliability. Using a probabilistic loads extrapolation approach and the first order reliability method, a large multi-megawatt wind turbine blade and tower structural reliability are assessed when the extreme turbulence model is uncertain. The structural reliability is assessed for the wind turbine when three configurations of an industrial grade load alleviation control system of increasing complexity and performance are used. The load alleviation features include a cyclic pitch, individual pitch, static thrust limiter, condition based thrust limiter and an active tower vibration damper. We show that large uncertainties in the extreme turbulence model can be mitigated and significantly reduced while maintaining an acceptable structural reliability level when advanced load alleviation control systems are used. We end by providing a rational comparison between the long term loads extrapolation method and the environmental contour method for the three control configurations.

Keywords: wind turbines, probabilistic modelling, extreme turbulence, load alleviation control systems, structural reliability, environmental contours

Nomenclature

AEP Annual Energy Production
BEM Blade Element Momentum theory
CDF Cumulative Distribution Function
COV Coefficient of Variation
EC Environmental Contours
ETM Extreme Turbulence Model
FORM First Order Reliability Method
IFORM Inverse First Order Reliability Method
LSF Limit State Function
PDF Probability Density Function

*Principal corresponding author

Email address: imad.abdallah.81@gmail.com (I. Abdallah)

1. Introduction

This is the first of a set of papers dealing with the influence of advanced load alleviation control systems on structural reliability and safety factors of wind turbines. Over the past decade, significant advances have been achieved in smart load alleviation control systems and algorithms resulting in impressive reduction in the magnitude and scatter of extreme and fatigue loads. Today, advanced load alleviation control systems are an integral part of the design of large wind turbines. Power production in extreme turbulence (DLC1.3ETM [1]) ranks as one of the top design driving load cases on various components such as blades and towers. In the IEC61400-1 wind turbine design standard [1] the extreme turbulence model is calibrated to a 50 year return period. It has recently come under scrutiny with regard to its accuracy in flat terrain versus complex terrain versus offshore versus wake operation in large wind farms. Consequently, an analysis of the effect of smart load alleviation control systems on structural reliability of a wind turbine is warranted especially in the presence of large uncertainty in the extreme turbulence model.

Various aspects related to load control of a wind turbine during power production in extreme turbulence have not been so far studied, specifically: how does the structural reliability of the wind turbine change if the turbulence model is uncertain? How can the uncertainty in the turbulence model be represented? In the presence of such uncertainty how does the structural reliability change with/without smart load alleviation control systems? The aim of this work is thus to assess the structural reliability of a large multi-megawatt wind turbine blade and tower when the turbulence model is uncertain given that various load alleviation control features are used.

[2] have examined the effect of varying turbulence levels and wind speeds on long term extrapolation techniques using a joint probability density function of both mean wind speed and turbulence for loads calculations on a constant speed active-stall regulated wind turbine. [3] have demonstrated through a probabilistic based method that a reduction in half of the probability of failure of the control system reduces the structural probability of failure of a wind turbine by approximately 2 times assuming the dominant contribution to the overall reliability is a storm situation in stand-still. [4] have used a cost and reliability based optimization of a wind turbine using various objective function formulations including no reconstruction of the wind turbine in case of structural failure when the control system fails. The authors show that given a target reliability level, the optimal turbine geometry (tower bottom diameter and sheet thickness) is independent of the initial cost of the control system and its failure rate. [5] and [6] have used a classical system reliability approach to assess the overall probability of failure of an actively controlled structure, including the case where the structure is in full reliance on the control system (i.e. series system).

The novelty in this paper is based on the fact that load alleviation control systems not only affect the magnitude of the extreme load level but also the scatter and the shape of the probability distribution function of the extreme loads. The shape and magnitude of the probability distribution is dependent on the sophistication and performance of the load alleviation control systems to limit the excursion of extreme loads. A probabilistic loads extrapolation approach is used to derive the annual maximum load distribution when various configurations of the load alleviation control systems are employed. The extreme load probabilistic model is then used in a First Order Reliability Model (*FORM*) to calculate the structural reliability level of a wind turbine blade and tower under various uncertainty scenarios. Each scenario describes a possible alteration to the reference design turbulence model as defined in the IEC61400-1 ed. 3 design standard. It is generally observed that load alleviation control systems reduce the extreme load and limit their excursion resulting in lower scatter. The rationale behind the implementation of probabilistic methodologies is today's larger variations of climates where wind turbines are installed, as well as smart features in modern controllers which makes it difficult to establish and abide by a relevant deterministic standard for design of wind turbines. In this paper a large commercial multi-megawatt offshore wind turbine is considered with nominal power $> 5MW$ and rotor diameter $> 130m$. An industrial grade control system is used which includes a cyclic pitch, individual pitch, static thrust limiter, condition based thrust limiter and an active tower vibration damper.

2. The control system

Manufacturers are increasingly deploying sophisticated control systems on wind turbines with the ultimate objective of removing blade, nacelle main frame and tower/foundation load variations due to turbulence and oblique inflow while maintaining maximum power production. In order to reach this goal, a variable speed pitch controlled wind turbine control system is supplemented with load alleviating features capable of: (1) limiting the peak thrust on the rotor, (2) nullifying the effect of asymmetric aerodynamic rotor loading and (3) reducing tower vibrations. The load control features used in this study (Fig. 1) are gain-scheduled PID controllers which have a simple structure and can be easily tuned. The load alleviation control features include a *thrust limiter*, *cyclic pitch*, *individual pitch* and *tower vibration damper*. These features are fairly representative of what can be found on modern wind turbines operating in the field today. The input/output parameters of these load alleviation control features are described in Table 3.

2.1. Description of the load control features

An industrial grade control system¹ equipped with four load alleviation control features is considered:

Thrust limiter. The Thrust limiter affects thrust driven loads such as blade flap, blade out-of-plane deflection and tower fore-aft. This is a control feature that induces thrust limiting capabilities obtained by prescribing a pitch level to the blades based on an estimated rotor averaged wind speed. Thus the prescribed pitch determines a maximum level that the peak thrust can reach. A static thrust limiter is a feature where the peak thrust allowed is constant regardless of external inflow conditions and loading conditions. Conversely the condition based thrust limiter sets the peak thrust as a function of on the estimated external inflow, estimated wind speed and turbulence and measured turbine load effects such as blade flapwise bending moment.

Cyclic pitch. The cyclic pitch control limits the asymmetric loads such as tilt and yaw caused by aerodynamic wind shear, tower shadow, skew inflow and yaw misalignment. Hence the cyclic pitch effects are limited to around the 1P frequency. The cyclic pitch scheduling and enabling depends mainly on the generator power and rotor speed (which should also be relatively representative for the asymmetric loads affecting the tilt and yaw bending moments on the main shaft and tower top), collective pitch value and rotor azimuth position. The cyclic pitch control handles tilt/yaw loading via a sine offset to the pitch reference. To a large extent this will also reduce the blade bending moments and out-of-plane deflection.

Individual pitch. On top of the cyclic pitch controller the individual pitch control (IPC) limits the individual blade loading in addition to asymmetric loads such as tilt and yaw bending moments on the main shaft due to stochastic disturbances caused by turbulence. For increasing rotor size the turbulence driven wind gusts shift from causing thrust variations toward giving rise to asymmetric loading. The IPC algorithm calculates a pitch demand which is augmented to the cyclic tilt/yaw pitch demand. Individual blade load measurements are used to compute a demand pitch for each blade, the algorithm then uses the resulting pitch demand from the preceding blade variably delayed to match rotor azimuth position and pitch actuator dynamics. The IPC effects are limited to around the 3P frequency range.

Active tower vibration damper. This is not a physical damper. The tower vibration damper controller is based on pitch control algorithms that limit the tower vibrations (tower top accelerations) rising to the shut-down level. Tower vibrations during power production are largest in two cases: (1) when a gust or a step in wind magnitude (turbulence) hits the rotor plane or counter-intuitively (2) when coherence of the wind turbulence across the rotor is high and turbulence intensity is low, while all blades have similar angles of attack in a region in which aerodynamic damping is negative.

2.2. The control system configurations

Three configurations of the control system are considered in this paper; The complexity and load reduction performance of the controllers to limit the excursion of extreme loads above a certain threshold increase from configuration 1 to configuration 3:

Configuration 1 This is a basic control system that ensures that the wind turbine runs at optimal collective pitch and tip speed below rated wind speed and constant rotor speed (RPM) above rated wind speed. No load alleviation features are included.

Configuration 2 In addition to the control configuration 1 functionalities, a cyclic pitch control and a static thrust limiter control are included. This configuration is the reference configuration.

Configuration 3 In addition to the control configuration 2 functionalities, individual pitch control and condition based thrust limiter are included, which set the control parameters based on the estimated external inflow and turbine loading conditions.

3. The IEC61400-1 ed. 3 extreme turbulence model

The background for the turbulence model in [1] is described below based on environmental contours (EC) derived through the Inverse First Order Reliability Method (IFORM).

The annual distribution of the 10-minute mean wind speed, denoted by random variable V , is given by a Rayleigh density function:

$$f_V(v) = \frac{2v}{(2\mu_V/\sqrt{\pi})^2} \exp \left[- \left(\frac{v}{2\mu_V/\sqrt{\pi}} \right)^2 \right] \quad (1)$$

¹Developed at MiTa-Teknik A/S

where v is the hub wind speed and μ_V is the mean wind speed. This function describes how many times each 10-minute interval with a certain average wind speed occurs in 20 -25 years (typical design lifetime of a wind turbine) [7]. According to [1] the distributions to be used have long term mean wind speeds $\mu_V = 10m/s$ (class I), $\mu_V = 8.5m/s$ (class II) or $\mu_V = 7.5m/s$ (class III). The Rayleigh distribution can be generalized to a Weibull distribution where corrections for the local siting can be modelled a scaling factor A and form factor k :

$$f_V(v) = \frac{k}{A} \left(\frac{v}{A}\right)^{k-1} \exp\left[-\left(\frac{v}{A}\right)^k\right] \quad (2)$$

The standard deviation of the 10-minute wind speed is taken as the measure of turbulence, whose longitudinal component is denoted by σ_1 . The long term distribution of turbulence σ_1 conditional on the 10-minute mean wind speed V is assumed to follow a lognormal distribution:

$$f_{\sigma_1|V}(\sigma_1 | v) = \frac{1}{\sqrt{2\pi}\xi\sigma_1} \exp\left[-\frac{1}{2}\left(\frac{\ln(\sigma_1) - \lambda}{\xi}\right)^2\right] \quad (3)$$

where the parameters λ and ξ are defined as:

$$\xi = \sqrt{\ln\left(\delta_{\sigma_1|V}^2 + 1\right)} \quad (4)$$

$$\lambda = \ln\left(\mu_{\sigma_1|V}\right) - \frac{1}{2}\xi^2 \quad (5)$$

with the coefficient of variation $\delta_{\sigma_1|V} = \frac{\sigma_{\sigma_1|V}}{\mu_{\sigma_1|V}}$. The conditional mean and standard deviation of turbulence are cast as [1]:

$$\mu_{\sigma_1|V} = I_{ref} (0.75v + c) \quad (6)$$

$$\sigma_{\sigma_1|V} = 1.44I_{ref} \quad (7)$$

The parameters I_{ref} and c are found in Table 1 for turbulence class A through C.

Table 1: I_{ref} and c for turbulence classes A-C.

Turbulence Class	I_{ref}	c [m/s]*
A	0.16	3.8
B	0.14	3.8
C	0.12	3.8

* $c = 5.6$ for 90% quantile

3.1. 50-year Environmental Contour Using IFORM

The joint Probability Density Function (PDF) of the environmental variables wind speed and turbulence is obtained by multiplying Equations 1 and 2:

$$f_{\sigma_1,V}(\sigma_1, v) = f_{\sigma_1|V}(\sigma_1 | v)f_V(v) \quad (8)$$

The resulting joint PDF for IEC turbine class I and turbulence level B (IECIB) is shown in Fig. 2a. Furthermore, assuming a probability of failure, p_f , defined in terms of the return period, r , an environmental contour can be constructed in the standard Normal u-space which represents all points on a circle such that:

$$\sqrt{u_1^2 + u_2^2} = \beta_r \quad (9)$$

where the reliability index β_r and the probability of failure p_f are defined as follows $\Phi(-\beta_r) = p_f$ with $\Phi(\cdot)$ being the distribution function for the standardized Normal distribution. The independent standard Normal random variables U_1 and U_2 can be transformed into contours in the physical space utilizing the above equations and the Rosenblatt transformations:

$$\Phi(u_1) = F_V(v) \Rightarrow v = F_V^{-1}(\Phi(u_1)) \quad (10)$$

$$\Phi(u_2) = F_{\sigma_1|V}(\sigma_1 | v) \Rightarrow \sigma_1 = F_{\sigma_1|V}^{-1}(\Phi(u_2)) \quad (11)$$

where F_V is the Cumulative Distribution Function (CDF) of the random variable V , $F_{\sigma_1|V}$ is the CDF of the random variable σ_1 conditional on the mean wind speed V . It must be noted here that the extreme turbulence model in [1] is simply an approximation

of the 50-year environmental contour of the normal turbulence model. Taking a 10-minute reference period and assuming subsequent 10-minute periods are statistically independent, the probability of failure p_f corresponding to the 50-year return period is $10/(50 \cdot 365 \cdot 24 \cdot 60) = 3.8 \cdot 10^{-7}$. Hence, $\beta_{50} = \Phi^{-1}(p_f) = 4.95$. Fig. 2b compares the 50-year environmental contour line for *IECIB* with the empirical extreme turbulence model (DLC1.3ETM) from [1] given by:

$$\sigma_1 = c \cdot I_{ref} \left[0.072 \left(\frac{\mu_V}{c} + 3 \right) \left(\frac{v}{c} - 4 \right) + 10 \right]; c = 2m/s \quad (12)$$

where parameter c is used to calibrate the extreme turbulence loads to the long-term extrapolated normal production load (DLC1.1 NTM [1]).

We have now established that the extreme turbulence model described in the IEC61400-1 ed.3 [1] corresponds to the 50-year return period contour line of the normal turbulence model. Hence, the normal turbulence model and the extreme turbulence model are consistent with respect to each other. One can then ask the following pertinent questions: what is the uncertainty associated with this formulation of the extreme turbulence model? Is the assumption of lognormally distributed turbulence always correct? Is it correct to assume that turbulence level varies linearly with mean wind speed and is deterministic for a given wind speed [2]? How would the extreme turbulence model vary on a single turbine versus wind farm operation? How would the extreme turbulence model vary between onshore and offshore? How would the extreme turbulence model vary under various atmospheric stability conditions? One way to examine these questions is to perform long term multiple site-specific measurements and extract the extreme values of the turbulence to which a stochastic model would be fitted. The wind turbine structural reliability could then be examined against the site specific extreme turbulence models. Another, more general, approach is to formulate various alterations of the turbulence model (i.e. Equations 3,6,7) and examine the effect of turbulence variations along with variations in wind speed through long term extreme loads extrapolations. This second approach is adopted in this paper.

4. Probabilistic framework

In this section we describe how the probability density function of the annual maximum load can be obtained using a probabilistic loads extrapolations approach when the aero-servo-elastic simulations are performed using the three control configurations. The annual maximum load distribution is then used in the subsequent structural reliability analysis.

4.1. Simulations of extreme loads

The simulated wind turbine is erected on a 110 meters tower, has a rotor diameter larger than 130 meters and rated power larger than 5MW. The aero-servo-elastic simulations of the wind turbine are performed using FAST [8].

Table 2: Design of experiments for the FAST simulations. The variables are wind speed [m/s] and turbulence [m/s].

Wind Speed [m/s]	Turbulence [m/s]
4, 5, \dots , 25	1, 2, \dots , 8

FAST is a time-domain aero-servo-elastic simulator that employs a combined modal and multibody dynamics formulation. FAST models the turbine using 24 Degrees of Freedom (DOFs). These DOFs include two blade-flap modes and one blade-edge mode per blade. It has two fore-aft and two side-to-side tower bending modes in addition to nacelle yaw. The other DOFs represent the generator azimuth angle and the compliance in the drive train between the generator and hub/rotor. The aerodynamic model is based on the Blade Element Momentum theory [9]. A design of experiments (Table 2) is produced in order to examine the effects of wind speed and turbulence on the predicted extreme loads. The wind speed is varied over a range from 4 to 25 m/s in 1 [m/s] increments and turbulence is varied from 1 to 8 in 1 [m/s] increments. For each combination of wind speed and turbulence level we generate realizations of wind time series with 48 stochastic seeds, resulting in a total of 8448 10-minute time series simulations. One 10-minute wind time series simulation in FAST takes approximately three CPU-minutes. The FAST aero-servo-elastic simulations were performed with the control systems in the form of an external DLL. The output used from the simulations are the blade out-of-plane deflection in front of the tower (within +/-10 degrees azimuth), and the tower bottom fore-aft bending moment (Fig. 3).

The global maxima of the blade deflection and tower bending moment are extracted for each of the 8448 10-minute time series. The maxima are further used as the basis for the probabilistic loads extrapolation. An example of the FAST simulations output is presented in Fig. 4a which shows how the extreme blade out-of-plane deflection in front of the tower varies as a function of wind speed and turbulence. Fig. 4b shows a comparison of the extreme blade out-of-plane deflection in front of the tower when load alleviation control features are active and when not active.

4.2. Loads extrapolation

For a given wind speed and turbulence level, the short-term load response is modelled as a stationary random process. Assuming that the extreme load values are statistically independent, the probability that the extreme load l_{max} exceeds a given load l in the observation time T_{10min} is given by:

$$F_{shortterm}(l_{max} \geq l | T_{10min}, v, \sigma_1) = F_{local}(T_{10min}, v, \sigma_1)^{n(\sigma_1, v)} \quad (13)$$

where $n(\sigma_1, V) = 1$ is the expected number of uncorrelated maxima extracted from each 10 min simulation. F_{local} is the local probability distribution for the load process. F_{local} is chosen to be a 3-parameter Weibull distribution function² [2, 10]. The long term probability distribution for the extreme 10-minute load l_{max} conditional on mean wind speed v and turbulence σ_1 is computed by integrating all of the short-term loads distributions with the joint PDF of wind speed and turbulence:

$$F_{longterm}(l_{max} \geq l | T_{10min}) = \int_{V_{in}}^{V_{out}} \int_0^{\infty} F_{shortterm} f_{\sigma_1, V}(\sigma_1, v) d\sigma_1 dv \quad (14)$$

Since we are interested in the yearly probability of failure, the probability distribution of the extreme load with a yearly reference period (annual maximum load probability distribution) is derived as follows³

$$F_{longterm}(l_{max} | T_{1year}) = F_{longterm}(l_{max} | T_{10min})^N \quad (15)$$

where N is the number of 10min periods in one year ($= 365 \cdot 24 \cdot 60min/10min$).

It is important to note that both $F_{longterm}(l_{max} | T_{1year})$ and $F_{longterm}(l_{max} | T_{10min})$ distributions are equivalent. However, only the yearly distributions is used in the structural reliability analysis in order derive the yearly probability of failure.

4.3. The probabilistic model

Structural failure occurs in the tail of the extreme load distribution, hence the loads probabilistic model is derived by fitting a 3-parameter Weibull distribution to the tail of the empirical annual extreme load distribution [11]. The parameters of the fitted distributions are estimated through the Maximum Likelihood Estimation method using the data points between the 80th and the 90th percentiles of the empirical annual maximum load distribution $F_{longterm}(l_{max} | T_{1year})$. The annual maximum load distributions are plotted in Fig. 5-6 the blade out-of-plane deflection in front of the tower and for the tower bottom fore-aft bending moment, respectively. The plots indicate that the resulting long term distributions with/without load alleviation control features differ significantly. At the fifty year return period, the observed reduction in the extreme blade out-of-plane deflection in front of the tower is approximately 12% while the observed reduction in the tower bottom fore-aft extreme bending moment is approximately 23%.

A conclusion can be drawn at this point: load alleviation control features not only affect the magnitude and scatter of the extreme load level but also the shape of the annual maximum load distribution. Consequently, a turbine designer should assess the impact of the controller on structural reliability of the wind turbine. Should an augmented failure in the load alleviation control systems takes place, the extreme load exceedance probability increases significantly as shown in Fig. 5-6.

5. Structural reliability

Structural reliability is expected to differ significantly depending on the performance of the load alleviation control systems. Prior reliability analyses were performed in normal turbulence or in stand-still in extreme wind conditions (see [3] and [12]). In this study the reliability analysis is done during power production in extreme turbulence under the influence of an industrial grade control systems equipped with load alleviation features. The model, numerical and parameters' uncertainties of the control systems and failure rates are not considered here, in other words the control system always performs as expected given there is a demand.

²Gumbel, Lognormal, 2-parameter Weibull, 3-parameter Weibull and normal distributions were tested. The normalized mean absolute error, Bayesian information criterion (BIC), the Akaike information criterion (AIC) and visual inspections consistently showed that the 3-parameter Weibull distribution fits best the local extrema for all three control configurations, followed closely by the Lognormal distribution. This result is supported by findings in [10]. No tail fitting was performed. All outliers were retained.

³Say $L = \max(X_1, X_2, \dots, X_N)$ where X is a random variable with distribution F_X . Using the accumulation of probability in independent repeated trials, the distribution of L can be written as: $F_L(x) = P(\max X_i \leq x \{i = 1, \dots, N\}) = P(X_1 \leq x \cap X_2 \leq x \cap \dots \cap X_N \leq x) \Rightarrow F_L(x) = \prod_{i=1}^N P(X_i \leq x) = F_X(x)^N$. If F_L is the distribution (non-exceedance probability) of extreme load in a reference period t_r and F_X is the distribution of extreme load occurring in much shorter period τ , the exponent N is then equal to $\frac{t_r}{\tau}$. Example: the 50year non-exceedance probability with a reference period of 10min corresponds to 0.98 non-exceedance probability with a reference period of 1year.

5.1. Limit state function

For the structural reliability analysis an ultimate Limit State Function (LSF) g is defined in order to include the load and resistance uncertainties:

$$g = RX_R - L_{ULT}(\sigma_1, v)X_{dyn}X_{st}X_{ext}X_{sim}X_{exp}X_{aero}X_{str} \quad (16)$$

where R is the resistance, X_R represents the model and statistical uncertainties of the resistance, $L_{ULT}(\sigma_1, v)$ is the random variable for the extreme load defined in terms of the turbulence and mean wind speed. $L_{ULT,c}$ is the characteristic value of the ultimate load. $L_{ULT}(\sigma_1, v)$ is represented by the annual maximum distribution function derived through the extrapolation process. $L_{ULT}(\sigma_1, v)$ for the blade extreme out-of-plane deflection in front of the tower is shown in Fig. 5 for each of the three control configurations. $L_{ULT}(\sigma_1, v)$ for the tower extreme bottom fore-aft bending moment is shown in Fig. 6 for each of the three control configurations. Additional stochastic variables are defined as multiplicative factors to the load to take into account the model and statistical sources of uncertainties. X_{dyn} accounts for model uncertainty due to the modelling of the wind turbine dynamic response. X_{st} accounts for the statistical uncertainty of wind climate assessment. X_{ext} is associated with the extrapolated load model. X_{sim} accounts for statistical uncertainties caused by the limited number of loads simulations. X_{exp} accounts for the model uncertainties related to modelling the terrain and roughness. X_{aero} accounts for the model uncertainties related to the assessment of aerodynamic lift and drag coefficients. Finally the uncertainties related to the computation of the stresses on components from the loads is considered through X_{str} . Uncertainties related the control parameters are not directly included here. The stochastic variables of the LSF are described in Table 4. The structural reliability is assessed by solving the LSF using FORM⁴. The outcome is defined by the reliability index β .

For the tower, the resistance is cast as the ultimate bending capacity[13]:

$$M_{cr}X_R = \frac{1}{6} \left(1 - 0.84 \frac{D}{t} \frac{X_{y,ss}F_{y,ss}}{X_{E,ss}E} \right) (D^3 - (D - 2t)^3) X_{y,ss}X_{cr}F_{y,ss} \quad (17)$$

where D is the tower bottom diameter and t is the sheet thickness. $X_{y,ss}$ is the yield strength model uncertainty, $X_{E,ss}$ is the Youngs modulus model uncertainty, $F_{y,ss}$ is the yield strength for structural steel, E is the Youngs modulus and X_{cr} is the critical load capacity. D and t of the reference wind turbine tower are specified to $6.34m$ and $0.041m$, respectively. For the blade, the resistance is cast as the maximum allowed blade deflection δl_{cr} in front of the tower corresponding to $2/3$ of the distance from the tower to the undeflected blade δl_{undfl} :

$$\delta l_{cr}X_R = \frac{2}{3}\delta l_{undfl}X_{\delta l} \quad (18)$$

5.2. Reliability assessment

The structural reliability is assessed for eight uncertainty scenarios. Each scenario describes a possible alteration of the reference design turbulence model as defined in the IEC61400-1 design standard (see section 3).

Scenario 1. This is the reference scenario where the turbulence model is as defined in the IEC61400-1 design standard [1] with an $I_{ref} = 0.14$ and annual average wind speed of $10m/s$. The turbulence is:

$$\begin{aligned} \mu_{\sigma_1|V} &= I_{ref} (0.75v + c) \\ Var_{\sigma_1|V} &= 1.44I_{ref} \end{aligned}$$

Scenario 2. This scenario is similar to scenario 1 except the distribution of the turbulence (Equ. 3) is assumed to follow an extreme value distribution instead of the lognormal distribution. The objective here is to study the effect on structural reliability if the turbulence σ_1 is not lognormally distributed.

Scenario 3. This scenario is similar to scenario 1 except the annual average wind speed is set to $11m/s$ instead of $10m/s$ and follows a Rayleigh distribution. The objective here is to study the effect on structural reliability if the mean wind speed is higher than the reference design. This could be the case if the mean wind speed from certain wind sectors is higher than expected.

⁴A custom First Order Reliability Method is written in Matlab®.

Scenario 4. In this scenario the turbulence is assumed to follow a lognormal distribution with $I_{ref} = 0.16$ instead of 0.14 and the annual average wind speed is set to $10m/s$ and follows a Rayleigh distribution. The objective here is to study the effect on structural reliability if I_{ref} is higher than the reference design. This could be the case if the turbulence from certain wind sectors is higher than expected, or when the turbine is in half of full wake operation.

Scenario 5. This scenario is similar to scenario 1 except the distribution of the turbulence (Equ. 3) is assumed to follow a normal distribution instead of the lognormal distribution. The objective here is to study the effect on structural reliability if the turbulence σ_1 is not lognormally distributed.

Scenario 6. In this scenario the turbulence model is redefined according to [14]:

$$\begin{aligned}\mu_{\sigma_1|V} &= I_{ref} (0.64v + 3) \\ Var_{\sigma_1|V} &= (I_{ref} (0.089v + 2))^2\end{aligned}$$

with $I_{ref} = 0.14$. σ_1 follows a normal distribution, $\sigma_1 \sim N(\mu_{(\sigma_1|v)}, \sigma_{\sigma_1|v})$. Note that $Var_{\sigma_1|v}$ varies as a function of wind speed and not a constant. The annual average wind speed is set to $10m/s$ and follows a Rayleigh distribution. The turbulence model is derived based on 6-years of wind measurements from Høvsøre. The objective here is to study the effect on structural reliability if the definition of the turbulence model (including mean and standard deviation of turbulence) are modified compared to the reference design.

Scenario 7. This scenario is similar to scenario 1 except for $I_{ref} = 0.20$ instead of 0.14 and the annual average wind speed is set to $10m/s$ and follows a Rayleigh distribution. The objective here is to study the effect on structural reliability if I_{ref} is significantly higher than the reference design. This could be the case in operation in complex terrain or under specific atmospheric conditions resulting in severe turbulence.

Scenario 8. This scenario is similar to scenario 6 with slight modification in $\mu_{(\sigma_1|v)}$:

$$\begin{aligned}\mu_{\sigma_1|v} &= I_{ref} (v - 1) \\ Var_{\sigma_1|v} &= (I_{ref} (0.089v + 2))^2\end{aligned}$$

with $I_{ref} = 0.16$ instead of 0.14. σ_1 follows a lognormal distribution, $\sigma_1 \sim LOGN(\mu_{\sigma_1|v}, Var_{\sigma_1|v})$. This could be the case in operation in near-shore complex terrain locations with large variations in atmospheric conditions (from sea and/or land) resulting in severe turbulence from all or specific wind sectors.

The annual maximum load distribution is derived through extrapolation for each of the uncertainty scenarios as described in section 4. The structural reliability of the blade (extreme out-of-plane deflection in front of the tower) and tower (tower bottom extreme fore-aft bending moment) are assessed for each of the eight uncertainty scenarios for the three control system configurations. The blade out-of-plane deflection and tower fore-aft bending moments are chosen because they are more influenced by turbulent wind variations. An acceptable (target) value for the nominal failure probability for structural design for extreme limit states for a reference period of 1 year is $p_f \leq 5 \cdot 10^{-4}$. The corresponding target value for the reliability index is $\beta \geq 3.3$. Application of this target value assumes that the risk to human lives is negligible in case of failure of a structural element. The target reliability level is assumed to correspond to component class 2 (moderate consequences of failure). The results of the reliability analysis are shown in tables 5 and 6 for the blade and tower respectively⁵. The absolute value of the reliability index is not necessarily of interest here but the relative change in the reliability index amongst control configurations and uncertainty scenarios.

5.3. Discussion

Quantification of structural reliability based on analysis. The reference control configuration 2 in Tables 5 and 6 delivers an acceptable structural reliability index $\beta \geq 3.3$ for both blade and tower for scenarios 1-6 except when the turbulence level increases significantly and starts to dominate the loading conditions as in scenarios 7 and 8. This shows that in control configuration 2, some alterations to the turbulence model such as the distribution of the turbulence, or slight increase in the mean wind speed or I_{ref} or redefinition of the turbulence mean and variance as in scenario 6 do not impact the structural reliability. On the other hand, the structural reliability index exceeds 3.3 in control configuration 3 (advanced load alleviation) in all uncertainty scenarios for both

⁵The annual reliability index assumes failure at one critical location.

blade and tower. The structural reliability index drops significantly below 3.3 in all scenarios when no load alleviation features are included in the control system (configuration 1). This is not unexpected as the load alleviation features are an integral part of the reference turbine loads calculations in configuration 2.

This indicates that when a turbine design relies heavily on control features to achieve structural load reductions (lighter turbine design), control architecture and failure mode analysis should be studied very closely beyond the load cases recommended in the IEC6400-1 due to the severe drop in reliability.

Does the control system performance affect the structural reliability when the turbulence model is uncertain? Advanced load control features which include individual pitch and condition based thrust limiter (configuration 3 in tables 5-6) displays an improved performance of the control system reflected in the increased structural reliability as showcased in scenario 7 and 8 corresponding to a large increase in the turbulence compared to the design turbulence. For instance, the reliability index increases from 2.90 to 3.53 for the blade in uncertainty scenario 7 and from 2.85 to 3.79 for the tower⁶. The reliability index increases from 2.82 to 3.45 for the blade in uncertainty scenario 8 and from 2.73 to 3.70 for the tower. In both cases, the advanced load alleviation control features moved the reliability index from a value below the acceptable target to a value just above an acceptable target level of 3.3. This indicates that large uncertainty in the turbulence model can be mitigated and significantly lowered through the use of advanced load control features.

The load alleviation control features affect the shape of the exceedance probability distribution function as shown in Figures 5 and 6 (in these figures only scenario 1 is depicted). The shape of the probability distribution is dependent on the sophistication and performance of the load alleviation control features to limit the excursion of extreme loads. This load limiting effect of advanced load alleviation control systems on a wind turbine, such as control configuration 3, yield both a reduction in the mean of the annual maximum load distribution and its scatter (COV). In Fig. 5, the 50-year blade deflection drops by approximately 12% when using the advanced control configuration 3 compared to the reference control configuration 2, while the COV of the probability density function remains unchanged (0.027 versus 0.025). In Fig. 6, the 50-year tower bottom fore-aft bending moment drops by approximately 23% when using the advanced control configuration 3 compared to the reference control configuration 2, while the COV of the probability density function drops from 0.07 to 0.023. Similarly, in uncertainty scenario 7 the reliability index increases from 2.90 to 3.53 for the blade and from 2.85 to 3.79 for the tower. The corresponding 50-year blade deflection drops by approximately 14% when using the advanced control configuration 3 compared to the reference control configuration 2, while the COV of the probability density function remains largely unchanged (0.034 versus 0.031). The 50-year tower bottom fore-aft bending moment drops by approximately 20% when using the advanced control configuration 3 compared to the reference control configuration 2, while the COV of the probability density function drops from 0.056 to 0.037.

However, the cost and complexity of the control system increases which warrants additional failure modes analysis of the controller and its architecture and probably additional maintenance provisions.

Effect of load control on annual energy production? Increased structural reliability under uncertainty of the turbulence model is achieved with increased performance of the load alleviation control features to reduce the extreme loads and scatter. The next logical step is to verify the impact of the load control on the Annual Energy Production (AEP). Load reduction is achieved by reducing the aerodynamic thrust on the rotor. The power coefficient C_P and thrust coefficient C_T are related through the axial induction factor a (2D actuator disk: $C_P = 4a(1 - a)^2$ and $C_T = 4a(1 - a)$). Hence any reduction in thrust is accompanied with a reduction in power and vice-versa. Fig. 7 shows a comparison of the power curves when no load control features are included, when load control features are included and when advanced load control features are included (configurations 1-3). In the reference control configuration 2 a 3.1% loss in AEP is incurred relative to configuration 1. However, this value drops to 1.8% AEP loss when advanced load reduction features are included (control configuration 3) mostly due to the condition based thrust limiter. The AEP are calculated for an average wind speed of 10m/s and turbulence intensity of 10%. The loss in AEP is generally accepted in light of the improved structural reliability or equivalently maintaining the same reliability for lighter wind turbines.

The above discrete uncertainty scenarios give an intuitive and clear understanding of the effect of uncertainty in the mean wind speed or the turbulence or turbulence distribution or the definition of the extreme turbulence model on the structural reliability. One can easily generalize the above discrete uncertainty scenarios and assume inter-annual variations in the mean wind speed and the turbulence intensity or add any other environmental variables and generate a surrogate model of the extreme annual loads which can then be used in the reliability analysis (for instance using Kriging and/or Polynomial Chaos as shown in [15] and [16]).

⁶The larger increase in reliability for the tower compared to the blade is due to the design of the algorithms and tuning of the advanced load alleviation control features

6. Comparison of the 50-year Loads from the Environmental Contours Method with those from Extrapolation

A loads extrapolation approach is chosen herein to estimate the annual maximum loads distribution which is then used in the structural reliability analysis in FORM. A question that may arise is how does the 50-year extreme loads predicted through long term extrapolation (DLC1.1NTM) compare to the extreme loads derived through the environmental contours approach (i.e. DLC1.3 ETM)? We will tackle this question now.

In principle, the extrapolated 50-year extreme load from DLC1.1 NTM (power production in normal turbulence) and the extreme load corresponding to the 50-year environmental contour (DLC1.3 ETM power production in extreme turbulence) model the same extreme events. In order to derive the extreme load corresponding to the 50-year environmental contour, we first compute a Kriging meta-model through the 8448 design of experiments points. UQLab [17] is used to compute the Kriging meta-model. We then project the 50-year environmental contour onto the Kriging meta-model and compute the corresponding maximum load response. The 50-year environmental contour lines for the various uncertainty scenarios are shown in Fig. 8a, and the extreme loads corresponding to the 50-year environmental contours are shown projected onto the Kriging meta-model in Fig. 8b. The extreme loads corresponding to the 50-year environmental contour are then compared to the extrapolated 50-year extreme loads in Table 7 (for blade deflection in front of the tower) and Table 8 (for the tower bottom fore-aft bending moment) for the various uncertainty scenarios. What is evident from this comparison is that the 50-year extrapolated load is consistently higher compared to the 50-year extreme load from the environmental contour method. The difference between the extrapolated blade deflection and the deflection computed directly through the environmental contour is on the order to 20 – 40% with the largest difference being when the control configuration 3 is used (advanced load alleviation). The difference between the extrapolated extreme tower bottom bending moment and the one computed directly through the environmental contour is on the order to 10 – 40% with the largest difference being when the control configuration 2 is used. Similar differences have been observed in [18]. There could be two reasons for this (or a combination thereof):

- The extrapolation method has difficulty in modeling the short-term extreme loads for the variable speed pitch-regulated wind turbine because of the load limiting effects introduced by the load alleviation control features [18], resulting in over-prediction of the 50-year load level.
- The 50-year environmental contour parameters (i.e. turbulence and wind speed) are input to the aero-servo-elastic simulator with an expected output load response corresponding to the 50-year extreme load level. However, given the load limiting effect of the load alleviation control features and the non linear nature of the wind turbine response the output response does not necessarily correspond to the 50-year return period, resulting in under-prediction of the 50-year load level.

Furthermore, we evaluate how the extrapolated load and the load computed directly through the environmental contour compare when the return period is varied between 50-years to 1-month. Fig. 9a and 9b show how the ratio of extrapolated to EC vary for the extreme blade deflection and tower bottom bending moment, respectively. The trend indicate a clear drop in the difference. This can be explained by a combination of factors: (1) the smaller error incurred on the extrapolated load for shorter return periods, (2) the less extreme environmental variables for shorter return periods indicate less interference from the control system and (3) better loads predictions by the aero-servo-elastic (BEM) model in more "normal" environmental conditions (shorter return periods). Note that in Fig. 9a (extreme blade deflection) the difference is consistently largest when the advanced load alleviations features are used in the aero-servo-elastic simulations. This, however, is not the case in Fig. 9b (tower bottom bending moment); the lowest difference is observed when the control configuration 3 (advanced control) is used.

Advantages of the long term loads extrapolation.

- Despite well reported difficulties in fitting probability distribution to local maxima, It is still possible to quantify the statistical uncertainty associated with such fits, and consequently with the long term extrapolated loads.
- Various techniques and approaches associated with the long term loads extrapolation have been suggested, e.g. [2, 19, 20, 10, 21, 22, 23, 24, 25].
- Normal production loads (i.e. DLC1.1NTM), upon which the long term loads extrapolation is based, can be verified through a full scale prototype measurement. It is very unlikely to be the case for the 50-year environmental contours (i.e. DLC1.3ETM) during the prototype measurement period.
- The BEM models are more likely to provide correct aero-servo-elastic predictions around more "normal" environmental conditions upon which long term loads extrapolation is based, especially for larger multi-megawatt wind turbines under the influence of a control system.

Advantages of the EC.

- Predicting extreme loads through the EC method (i.e. DLC 1.3 ETM) requires far fewer aero-servo-elastic simulations compared to the extrapolation method (is this still relevant given the advent of high speed and distributed computing?).

- Most interestingly, unlike the extrapolation method, the environmental contours method yields contemporaneous extreme loads [10].

It is reasonable to conclude that deriving extreme loads through the extrapolation method and EC method are both required, for a mix of reasons:

- The EC method (DLC 1.3ETM) yields contemporaneous extreme loads which the extrapolation method does not. Contemporaneous extreme loads are necessary for realistic stress analysis on structural components such as the blades. Designers should keep in mind that the EC method might under-predict the long term extreme loads due to the load limiting effects of advanced load alleviation features in the wind turbine control system [20, 18, 10]. It could also be the case that less severe environmental parameters combinations (those associated with a smaller return period than say 50-years) might cause larger loads than are found from combinations on the 50-year contour itself [18] due to, for instance, tuning issues in the control system or due to resonance or low aerodynamic damping issues generated by specific combinations of the less severe environmental variables.
- Normal production loads (upon which long term extrapolations are based) are "verifiable" through full scale prototype measurements.
- The extrapolation method can deliver an estimate of the annual maximum load distribution which can then be used in a reliability analysis such as FORM (as demonstrated above). EC does not perform such a feat.

7. Conclusion

A probabilistic loads extrapolation approach was used to assess the structural reliability of a large multi-megawatt wind turbine blade and tower during power production when the extreme turbulence model is uncertain and when three configurations of the load alleviation control systems of increasing complexity and performance are used. The structural reliability was assessed for eight uncertainty scenarios including variation to the definition of the turbulence model in the IEC61400-1 design standard. The first controller configuration is a basic control system that ensures that the wind turbine runs at optimal collective pitch and tip speed below rated wind speed and constant rotor speed above rated wind speed. No load alleviation control features were included in this configuration. The second controller configuration includes a cyclic pitch control and a static rotor thrust limiter control. The third and most advanced controller configuration includes individual pitch control and condition based thrust limiter which sets the control parameters based on the estimated external inflow and turbine loading conditions.

The structural reliability index dropped significantly below an acceptable level of $\beta = 3.3$ when the load alleviation features were not included in the control system (control configuration 1). Additionally, it was found that when the turbulence level increased due to uncertainty in the extreme turbulence model, the structural reliability index of the reference blade and tower designs in control configuration 2 dropped in the worst case to 2.82 and 2.73, respectively. However, advanced load control features (configuration 3) displayed a satisfactory performance in improving the structural reliability: the reliability index increased from 2.90 to 3.53 for the blade in uncertainty scenario 7 and from 2.85 to 3.79 for the tower. The reliability index increased from 2.82 to 3.45 for the blade in uncertainty scenario 8 and from 2.73 to 3.70 for the tower. This indicates that large uncertainty in the extreme turbulence model can be significantly mitigated through the use of advanced load control features. However, the complexity of the control features increases which warrants additional failure modes analysis of the controller and its architecture. Furthermore, the improvement in the structural reliability comes at a cost of 1.8% loss in annual energy production. The load alleviation control features affect the shape of the exceedance probability distribution function. The shape of the probability distribution is dependent on the sophistication and performance of the load alleviation control features to limit the excursion of extreme loads. This load limiting effect of advanced load alleviation control systems on a wind turbine, such as individual pitch control and condition based thrust limiter, yield both a reduction in the mean of the annual maximum load distribution and its scatter (COV) which in turn translates into higher structural reliability level in the face of uncertainty in the extreme turbulence model. However, the extreme load distribution is very difficult to determine due to the limiting effects of the advanced load control features on the peak loads. A poorly determined distribution tail would invariably result in a highly sensitive reliability analysis in FORM.

We also provided a rational comparison between the long term loads extrapolation method (i.e. DLC1.1NTM) and the environmental contour (EC) method (i.e. DLC1.3ETM) for the three control configurations. We concluded that deriving extreme loads through the extrapolation method and EC method are both required, for a mix of reasons, namely (1) the EC method (DLC 1.3ETM) yields contemporaneous extreme loads which the extrapolation method does not and (2) normal production loads (upon which long term extrapolations are based) are "verifiable" through full scale prototype measurements, while the BEM models are more likely to provide correct aero-servo-elastic predictions around more "normal" environmental conditions.

Few shortcomings were identified; the first being that the model, numerical and parameters' uncertainties of the control systems and failure rates were not considered here. Furthermore, the use of extrapolation where uncertainties associated with fitting a probability

distributions to the extreme loads are widely reported in the literature. Another limitation is the uncertainty models used in the structural reliability calculations; any improvement in the uncertainty models will have a notable effect on the conclusions reported in this paper. Since the uncertainty models themselves are uncertain, future work can consider the sensitivity of the structural reliability analysis to the uncertainty models. Future studies could also explore various controller redundancy configurations (i.e. in sensors, actuators, algorithms and safety system) and their impact on the overall structural reliability of the wind turbine. More advanced limit state function and design equations for the blade and tower could be considered in the future. Another important aspect not considered here is the probability of failure of the load alleviation control features and the consequence on the overall structure-control reliability.

Given the tangible increase in structural reliability under large extreme inflow and turbulence uncertainty it is recommended to increase the effort in research and development of advanced load alleviation control features for wind turbines, both in terms of algorithms and failure rate of the control components. The objective should not only be a reduction in the extreme operating loads but also the shape of the resulting extreme loads distribution given its significant impact on the overall wind turbine reliability.

8. Acknowledgements

The work presented herein is a part of the Danish Energy Technology Development and Demonstration (EUDP) project titled, Demonstration of a basis for tall wind turbine design, Project no 64011 -0352. The financial support is greatly appreciated. The Danish Ministry of Science, Innovation and Higher Education are also gratefully acknowledged for their financial support. MiTa-Teknik are acknowledged for their generous financial and technical support and for providing the control systems for the FAST aero-servo-elastic simulations.

References

- [1] International Electrotechnical Commission, IEC61400-1:2005 (ed. 3): Wind turbines - Part 1: Design Requirements., Tech. rep., International Electrotechnical Commission (2005).
- [2] P. J. Moriarty, W. E. Holley, S. Butterfield, Effect of Turbulence Variation on Extreme Loads Prediction for Wind Turbines, *Journal of Solar Energy Engineering* 124 (4) (2002) 387.
- [3] N. J. Tarp-johansen, I. Kozine, L. Radermakers, J. D. Sørensen, K. Ronold, Optimised and Balanced Structural and System Reliability of Offshore Wind Turbines An account, Tech. Rep. April, Risø, Risø-R-1420(EN), Roskilde, Denmark (2005).
- [4] J. D. Sørensen, N. J. Tarp-johansen, Reliability-based Optimization and Optimal Reliability Level of Offshore Wind Turbines, *International Journal of Offshore and Polar Engineering* 15.
- [5] M. Battaini, F. Casciati, L. Faravelli, Reliability Analysis of Controlled Structures, in: *Intelligent Information Systems*, 1997, pp. 589–593.
- [6] M. Battaini, F. Casciati, L. Faravelli, Some reliability aspects in structural control, *Probabilistic Engineering Mechanics* 15 (1) (2000) 101–107.
- [7] H. Veldkamp, Chances in Wind energy: a Probabilistic Approach to Wind Turbine Fatigue Design, Ph.D. thesis, Delft Technical University, Delft (2006).
- [8] J. Jonkman, M. Buhl, FAST User's Guide, Tech. rep., National Renewable Energy Laboratory, NREL/EL-500-38320 (2005).
- [9] M. Hansen, Aerodynamics of wind turbines : rotors, loads and structure, James & James (Science Publishers) Ltd. pp. 152. ISBN 1902916069, 2001.
- [10] K. Freudenreich, K. Argyriadis, The Load Level of Modern Wind Turbines according to IEC 61400-1, *Journal of Physics: Conference Series* 75.
- [11] M. Florian, G. Danciu, Title : Assessment of uncertainties in wind turbine design loads, Tech. rep., Aalborg University, Master Thesis, M.S.c. Structural and Civil Engineering, Aalborg University (2013).
- [12] N. Tarp-johansen, P. Madsen, S. Frandsen, Partial Safety Factors for Extreme Load Effects - Proposal for the 3rd Ed. of IEC 61400: Wind Turbine Generator Systems - Part 1: Safety Requirements, Tech. Rep. March, Risø, Risø-R-1319(EN), Roskilde, Denmark (2002).
- [13] N. Tarp-johansen, J. Sørensen, P. Madsen, Experience with Acceptance Criteria for Offshore Wind Turbines in Extreme Loading, in: *JCSS Workshop on Reliability based code calibration*, Zurich, 2002, p. .
- [14] K. Dimitrov, A. Natarajan, J. Mann, Effects of Normal and Extreme turbulence spectral parameters on wind turbine loads, *Journal of Wind Engineering and Industrial Aerodynamics* (submitted).
- [15] R. Schöbi, B. Sudret, Polynomial-chaos-based kriging, *Int. J. Uncertainty Quantification*, Submitted.
- [16] B. Sudret, Uncertainty propagation and sensitivity analysis in mechanical models – Contributions to structural reliability and stochastic spectral methods, Université Blaise Pascal, Clermont-Ferrand, France, habilitation à diriger des recherches, 173 pages (2007).
- [17] S. Marelli, B. Sudret, UQLab: a framework for uncertainty quantification in MATLAB, in: *Proc. 2nd Int. Conf. on Vulnerability, Risk Analysis and Management (ICVRAM2014)*, Liverpool, United Kingdom, 2014.
- [18] K. Saranyasoontorn, L. Manuel, Design Loads for Wind Turbines Using the Environmental Contour Method, *Journal of Solar Energy Engineering* 128 (4) (2006) 554.
- [19] P. W. Cheng, A reliability based design methodology for extreme response of offshore wind turbines, Ph.D. thesis, Delft University (2002).
- [20] J. M. Peeringa, Extrapolation of extreme responses of a multi megawatt wind turbine, Tech. rep., ECN (2003).
- [21] P. Ragan, L. Manuel, Statistical Extrapolation Methods for Estimating Wind Turbine Extreme Loads, in: *45th AIAA Aerospace Sciences Meeting and Exhibit, AIAA 2007-1221*, 2007.
- [22] A. Natarajan, W. E. Holley, Statistical Extreme Load Extrapolation With Quadratic Distortions for Wind Turbines, *Journal of Solar Energy Engineering* 130.
- [23] J. Peeringa, Comparison of extreme load extrapolations using measured and calculated loads of a MW wind turbine, in: *European Wind Energy Conference*, Marseille, France, 2009.
- [24] H. S. Toft, Assessment of Load Extrapolation Methods for Wind Turbines, in: *48th AIAA Aerospace Sciences Meeting Including the New Horizon Forum and Aerospace Exposition, AIAA 2010-1581*, 2010.
- [25] H. S. Toft, J. D. Sørensen, D. Veldkamp, Assessment of Load Extrapolation Methods for Wind Turbines, *Journal of Solar Energy Engineering* 133 (2) (2011) 021001.

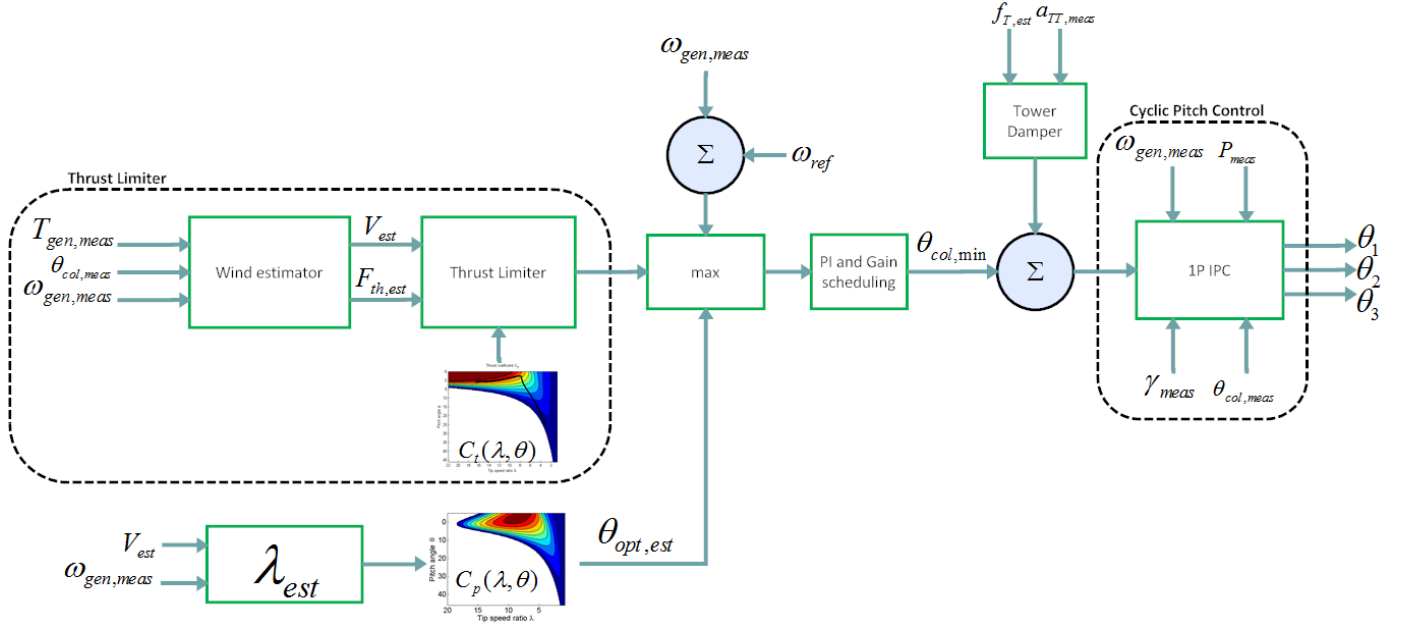
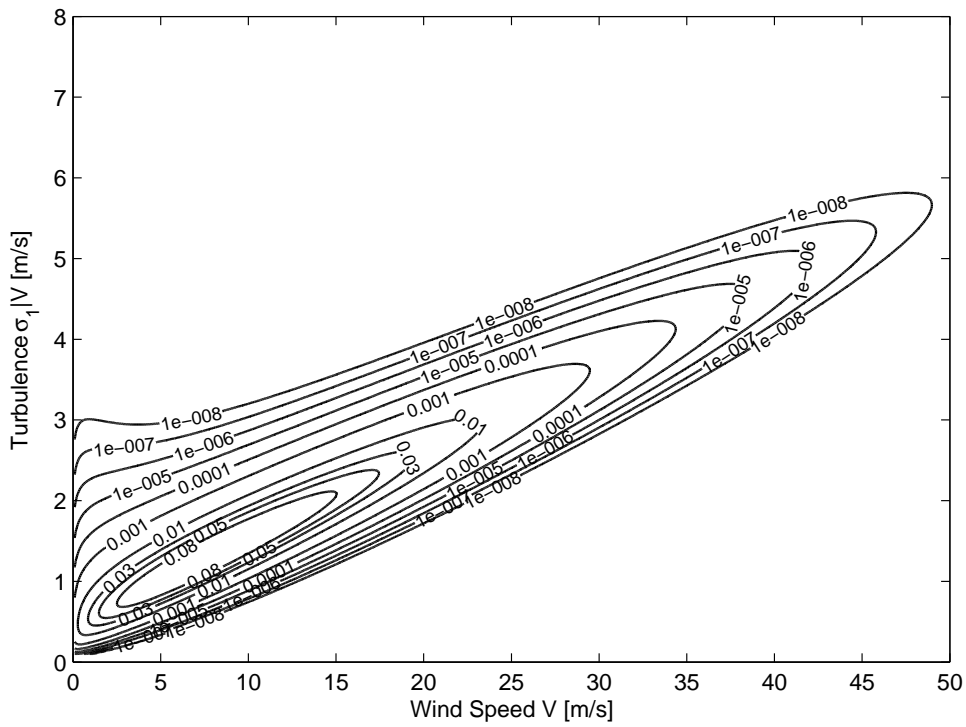


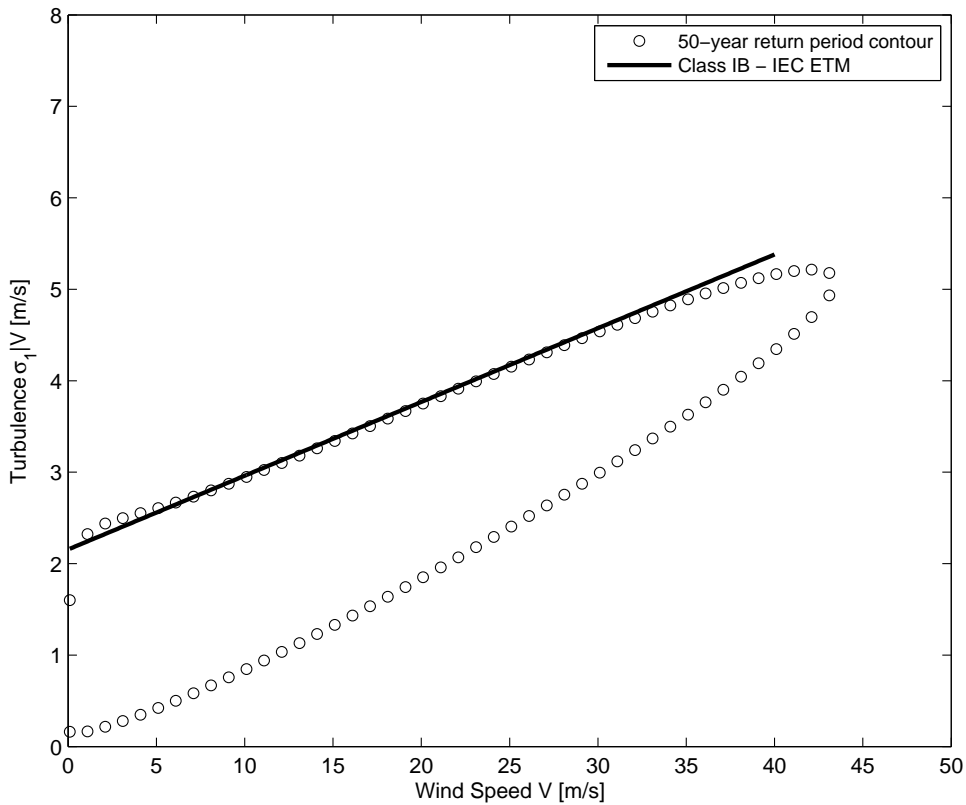
Fig. 1: Simplified block diagram of the load control features including the thrust limiter, tower vibration damper and individual pitch control. The square boxes in the block diagram represent computational algorithms while the arrows represent the control system input/output.

Table 3: Definition of the parameters of the control system.

Parameter	Description
$T_{gen,meas}$	generator torque
$\omega_{gen,meas}$	generator angular velocity
$\omega_{col,meas}$	inter-blade mean (collective) pitch angle
P_{meas}	generator electrical power
γ_{meas}	rotor azimuth position
$a_{TT,meas}$	tower top fore-aft acceleration
$f_{T,est}$	tower first eigen-frequency
$\theta_{col,min}$	minimum pitch for operation below a safe thrust level
$\theta_{opt,est}$	pitch angle for optimal power production
γ_{est}	tip speed ratio
$F_{th,est}$	rotor thrust force based on C_t table lookup
V_{est}	rotor averaged wind speed
ω_{ref}	Reference generator speed
C_p, C_t	power and thrust coefficients tables
$\theta_1, \theta_2, \theta_3$	Pitch signal to blade 1, 2 and 3



(a) Joint probability density function.



(b) The 50-year return period contour.

Fig. 2: (2a) Joint probability density function of wind speed and turbulence for class IEC-IB and (2b) A comparison between the 50-year return period environmental contour and the IEC-IB extreme turbulence model as defined in [1].

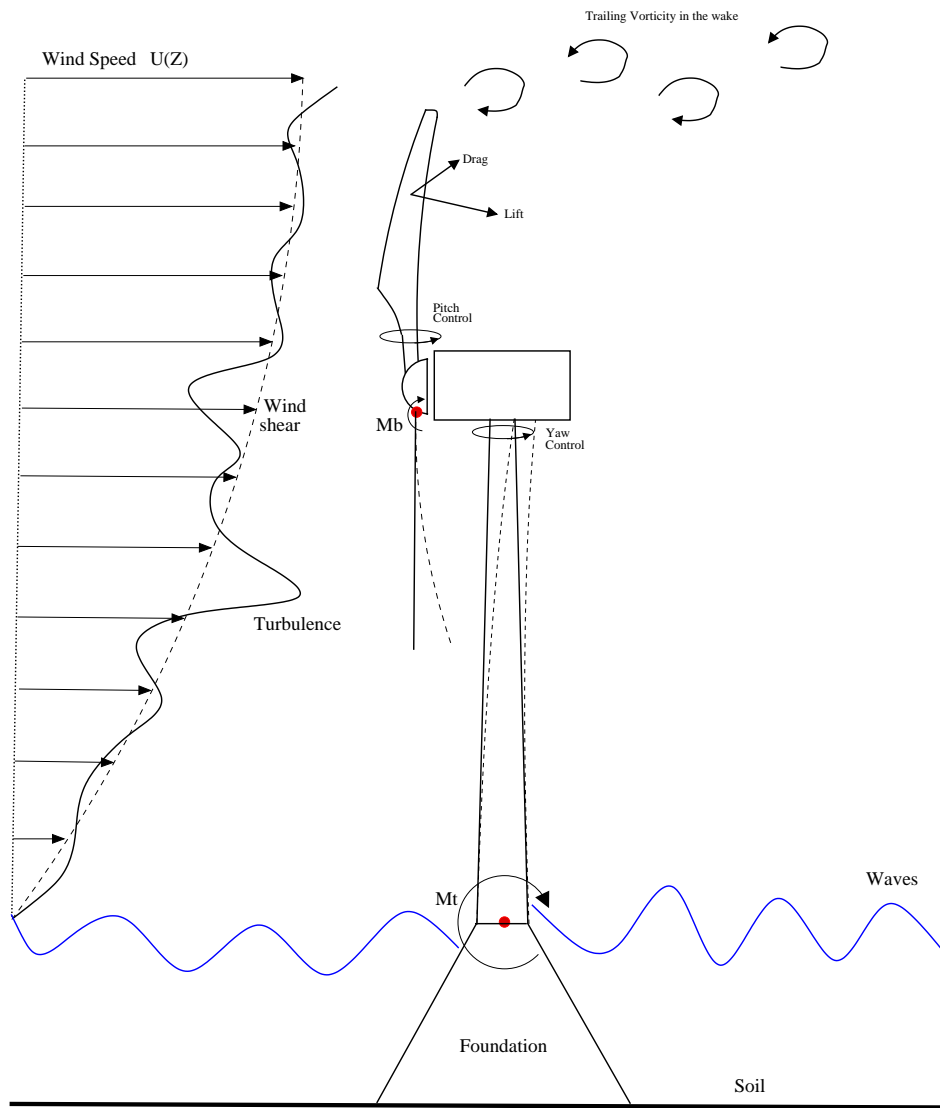
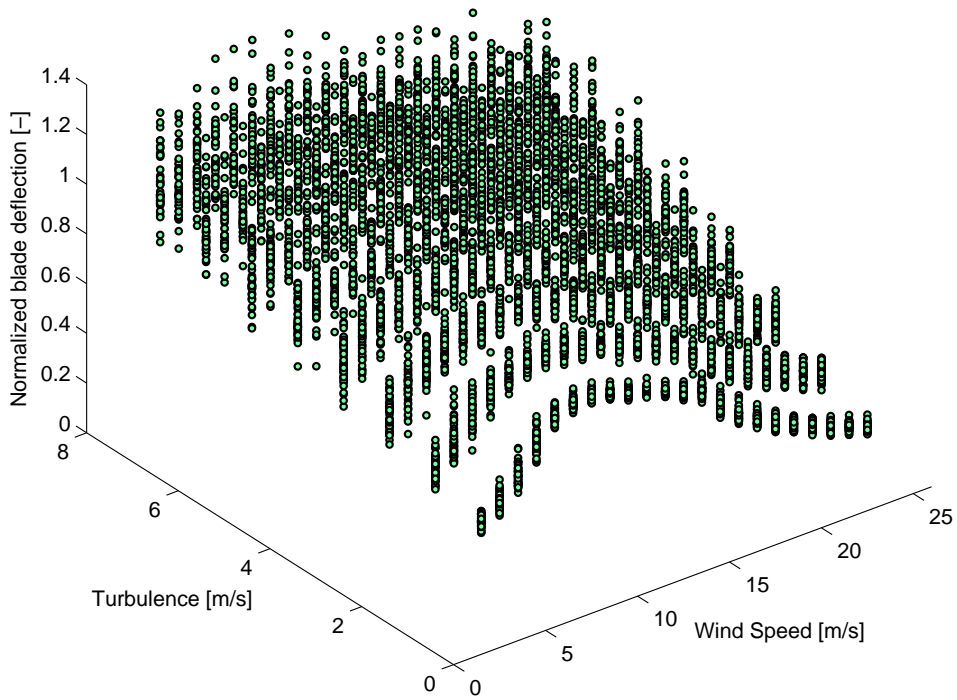
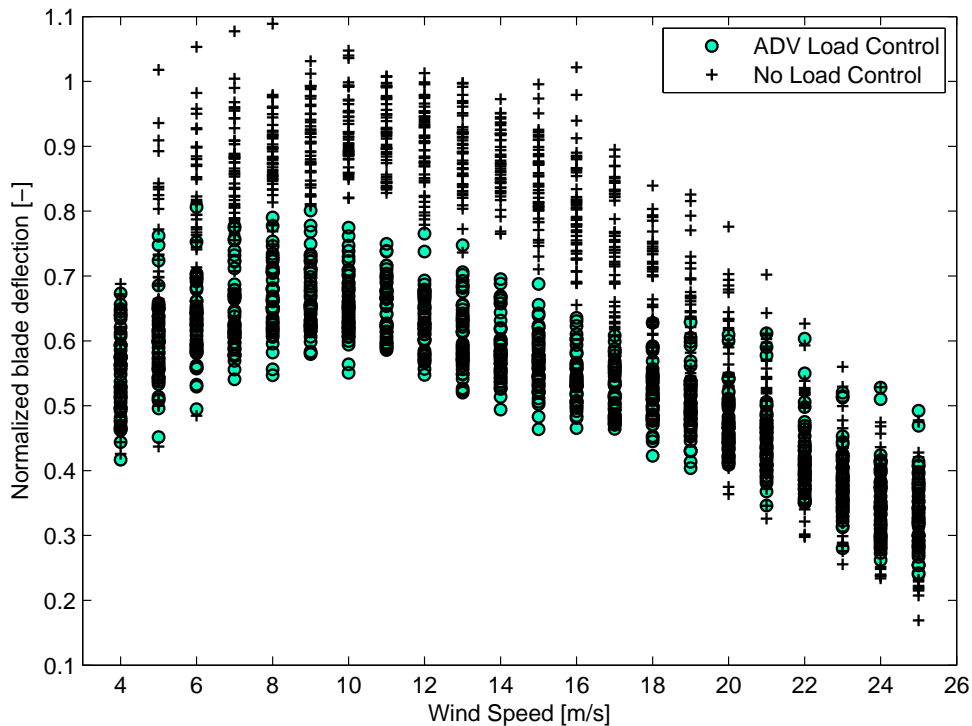


Fig. 3: A wind turbine. M_b is the flapwise bending moment at the blade root. $U(Z)$ is the mean wind speed at height Z . Vertical wind shear (dotted grey line) and turbulence (thick black line).

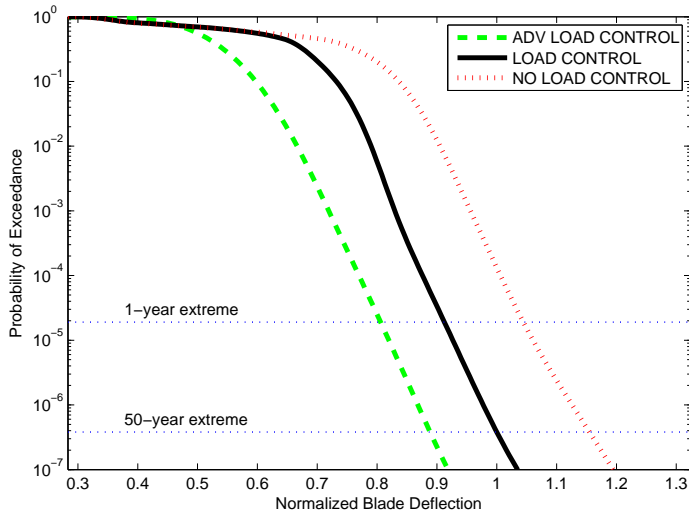


(a) Scatter plot of the normalized extreme blade out-of-plane deflection in front of the tower.

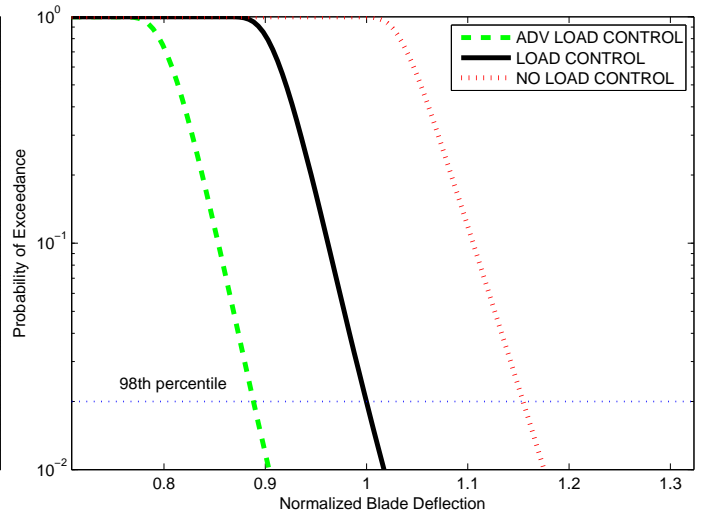


(b) Effect of load alleviation control features on the extreme blade out-of-plane deflection in front of the tower.

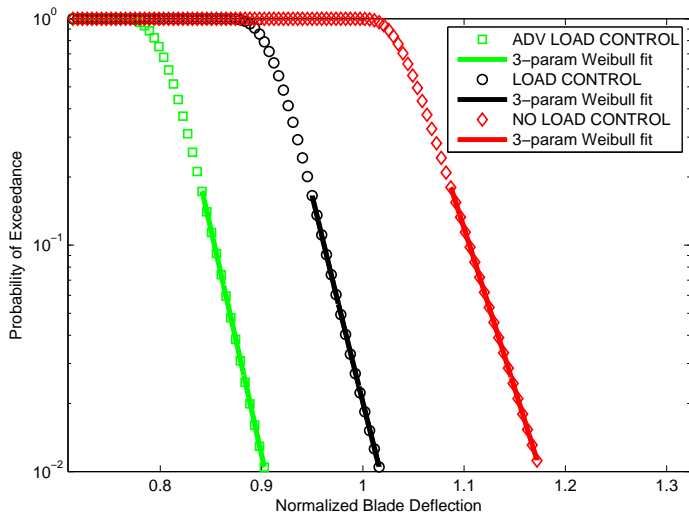
Fig. 4: 4a Scatter plot of the normalized extreme blade out-of-plane deflection in front of the tower as a function of wind speed and turbulence. Normalized with the 50-year blade deflection of control configuration 2. 4b Scatter plot of the normalized blade out-of-plane deflection in front of the tower as a function of wind speed when the load alleviation features are active (control configuration 2) and when not active (control configuration 1) for Turbulence $\sigma_1 = 3m/s$. The normalization is done with the 50-year blade deflection of control configuration 2. 48 maxima for the Load control case and 48 maxima for the no load control case are plotted at each wind speed.



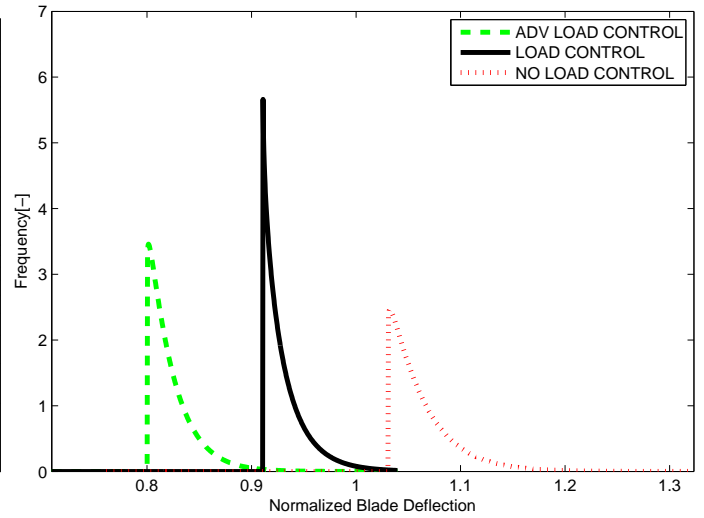
(a) exceedance probability (10min reference period).



(b) exceedance probability (1 year reference period).

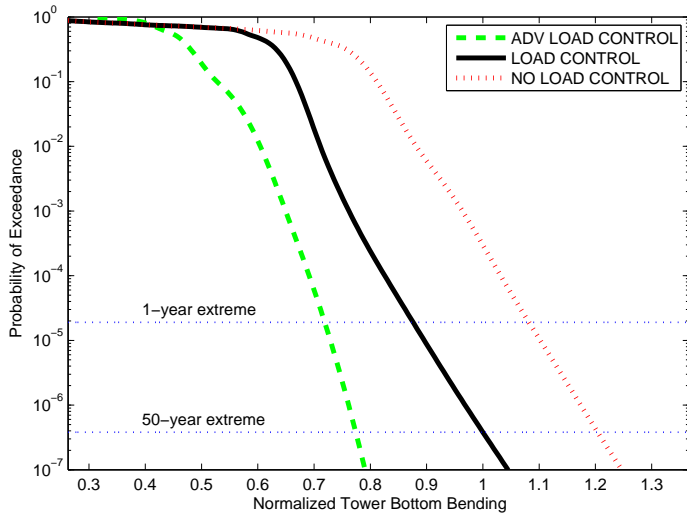


(c) 3-parameter Weibull distribution fit.

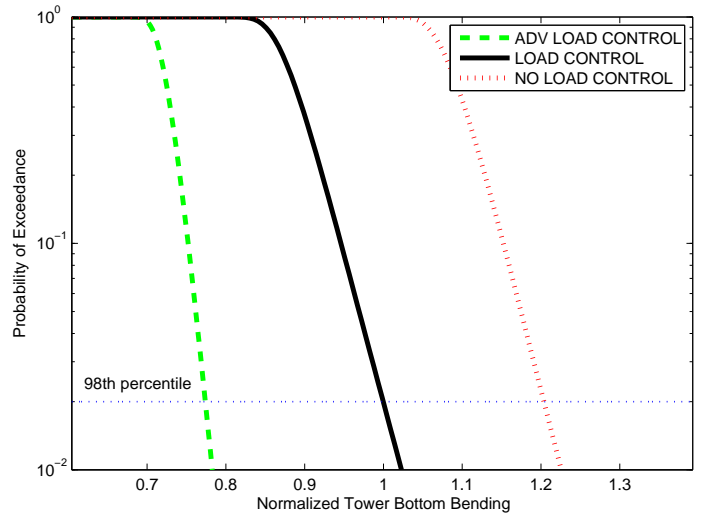


(d) PDF (1 year reference period).

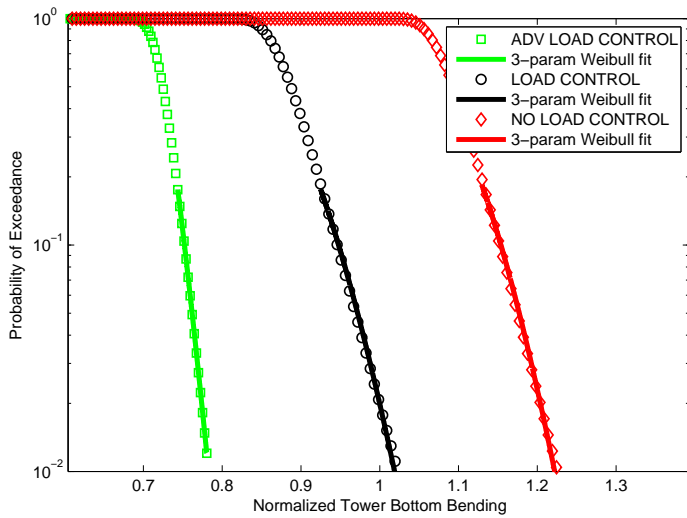
Fig. 5: Long term exceedance probability for the blade out-of-plane deflection in front of the tower in uncertainty scenario 1 for control configuration 1 (no load control), configuration 2 (load control) and configuration 3 (advanced load control). (a) 10-min reference period, (b) 1-year reference period, (c) 3-parameter Weibull distribution fit to the annual maximum load distribution and (d) the corresponding density function for the blade out-of-plane deflection in front of the tower. The extrapolated loads are normalized with the 50-year extrapolated load level derived from the simulations with control configuration 2. The COV of the probability density function with advanced load control is 0.027, $COV = 0.025$ with load control, and $COV = 0.029$ when no load control is used.



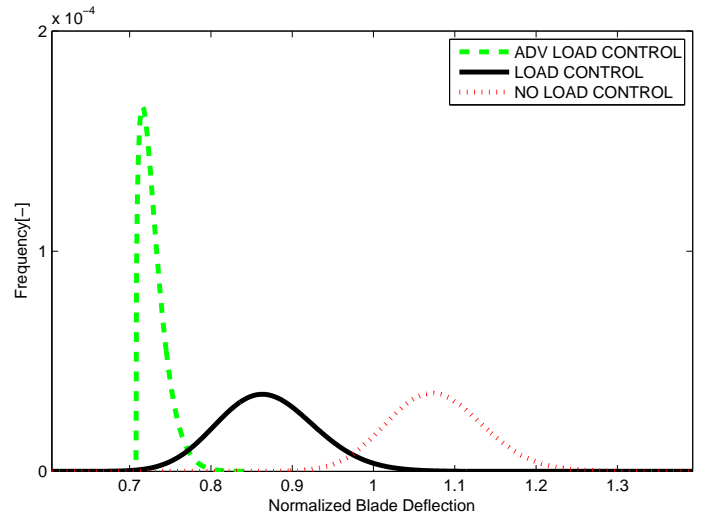
(a) exceedance probability (10min reference period).



(b) exceedance probability (1 year reference period).



(c) 3-parameter Weibull distribution fit.



(d) PDF (1 year reference period).

Fig. 6: Long term exceedance probability for the tower bottom fore-aft bending moment in uncertainty scenario 1 for control configuration 1 (no load control), configuration 2 (load control) and configuration 3 (advanced load control). (a) 10-min reference period and (b) 1-year reference period. (c) 3-parameter Weibull distribution fit to the annual maximum load distribution and (d) the corresponding density function for the tower bottom fore-aft bending moment. The extrapolated loads are normalized with the 50-year extrapolated load level derived from the simulations with control configuration 2. The COV of the probability density function with advanced load control is 0.023, COV = 0.07 with load control, and COV = 0.056 when no load control is used.

Table 4: The stochastic variables of the Limit State Function.

Variable	Description	Distribution	Expected value	COV
X_{dyn}	Structural dynamics	LN	1	0.05
X_{aero}	Airfoil data uncertainty	G	1	0.07
X_{sim}	Simulation statistics	N	1	0.05
X_{exp}	Exposure (terrain)	LN	1	0.10
X_{ext}	Extrapolation	LN	1	0.05
X_{st}	Climate statistics	LN	1	0.05
X_{str}	Stress evaluation	LN	1	0.03
$X_{\delta l}$	Blade deflection model uncertainty	LN	1	0.05
X_{cr}	Critical load capacity	LN	1	0.10
$F_{y,ss}$	Yield strength for structural steel [MPa]	LN	240	0.05
E	Young's modulus [MPa]	LN	$2.1 \cdot 10^5$	0.02
$X_{y,ss}$	Model uncertainty for yield strength	LN	1	0.05
$X_{E,ss}$	Model uncertainty for Young's modulus	LN	1	0.02

Table 5: Annual structural reliability index β of the blade (extreme out-of-plane deflection in front of the tower).

Uncertainty Scenario	Control Configuration 1: No load alleviation features, simple controller	Control Configuration 2: with load alleviation features (Reference)	Control Configuration 3: with advanced load alleviation features
1	2.66	3.31	3.88
2	2.63	3.30	3.87
3	2.65	3.31	3.88
4	2.42	3.10	3.79
5	2.66	3.30	3.87
6	2.62	3.33	3.90
7	2.16	2.90	3.53
8	2.11	2.82	3.45

Table 6: Annual structural reliability index β of the tower (tower bottom extreme fore-aft bending moment). The tower bottom diameter and thickness are $6.34m$ and $0.041m$, respectively.

Uncertainty Scenario	Control Configuration 1: No load alleviation features, simple controller	Control Configuration 2: with load alleviation features (Reference)	Control Configuration 3: with advanced load alleviation features
1	2.35	3.33	4.30
2	2.38	3.33	4.31
3	2.36	3.28	4.24
4	2.37	3.10	4.13
5	2.38	3.32	4.31
6	2.41	3.34	4.31
7	1.97	2.85	3.79
8	1.92	2.73	3.70

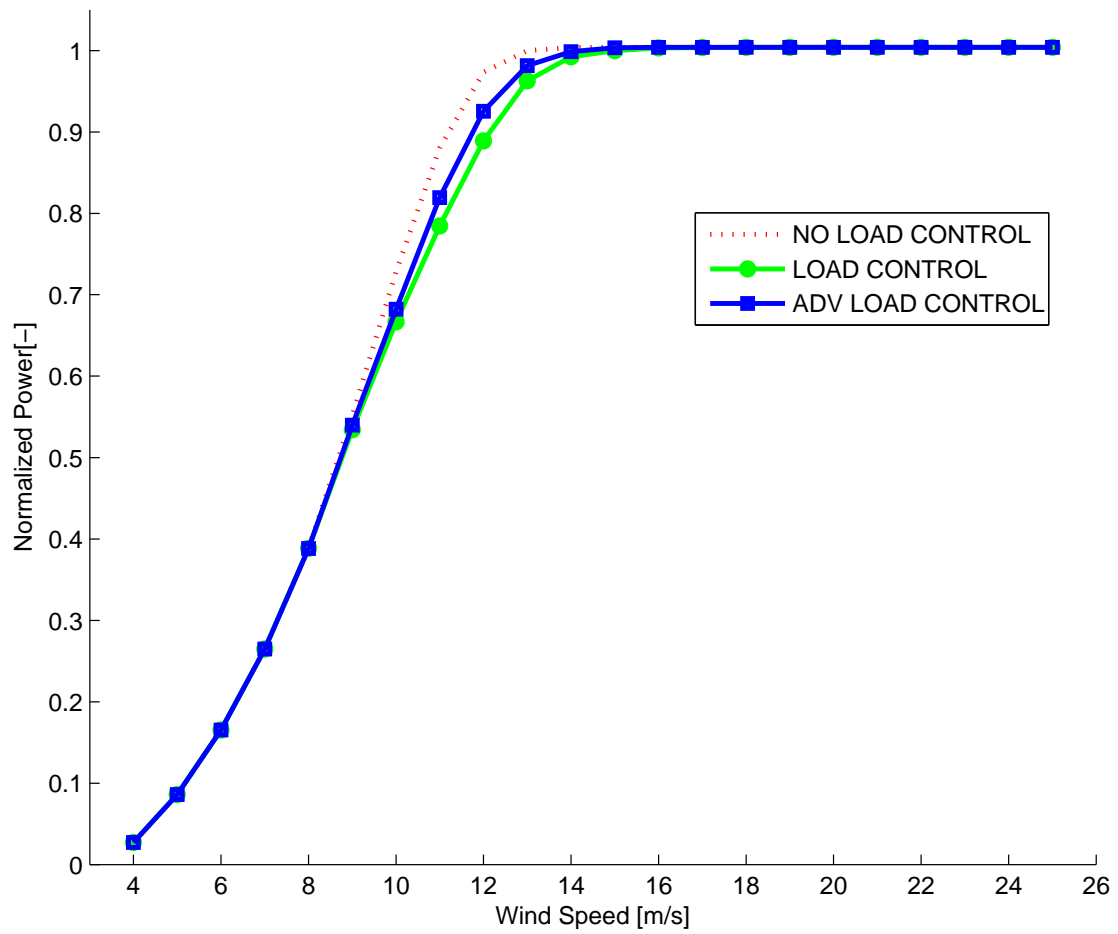
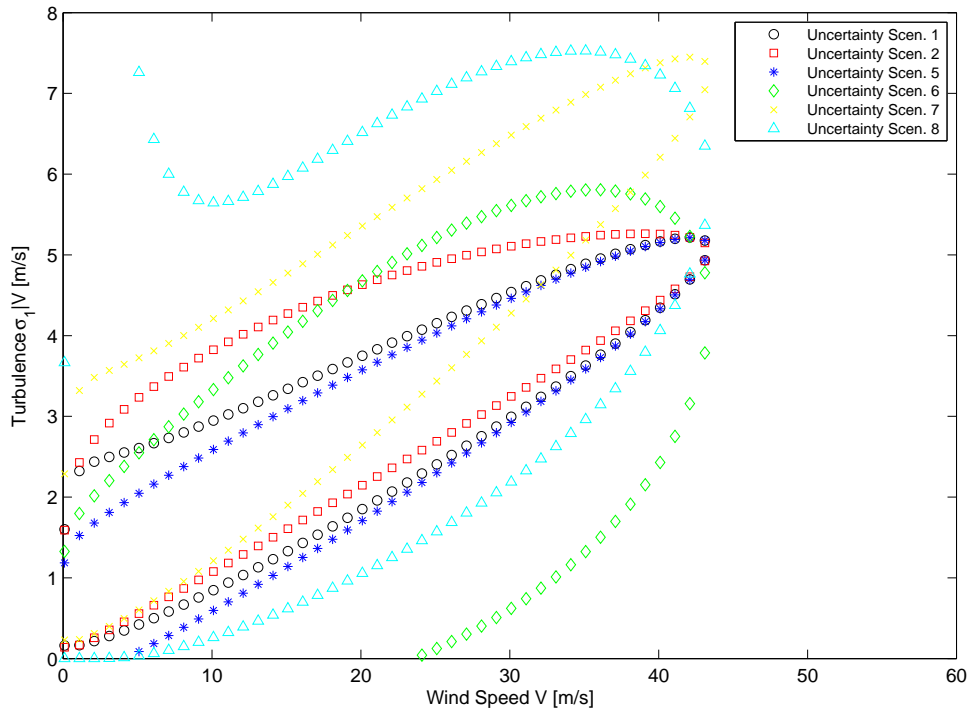
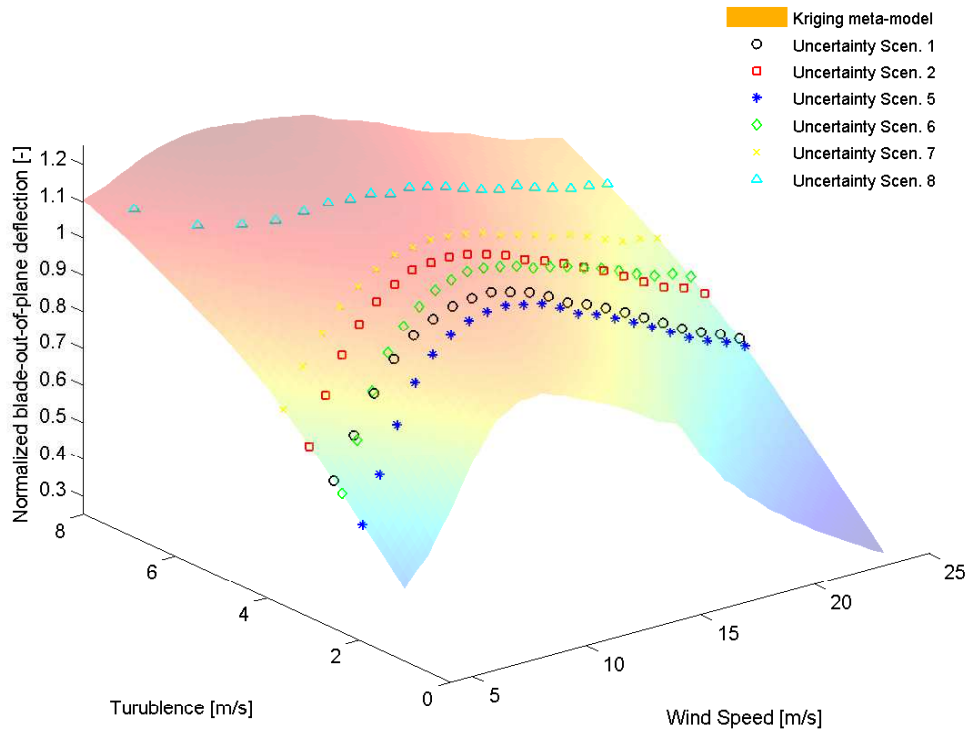


Fig. 7: Power curves (normalized by rated power) when (1) no structural load control features are included - control configuration 1, when (2) structural load control features are included - control configuration 2, and when (3) advanced structural load control features are included - control configuration 3.



(a) 50-year environmental contour lines of the turbulence models.



(b) Projection of the 50 year environmental contours on the Kriging surface response of the normalized extreme blade deflection in front of the tower as a function of wind speed and turbulence.

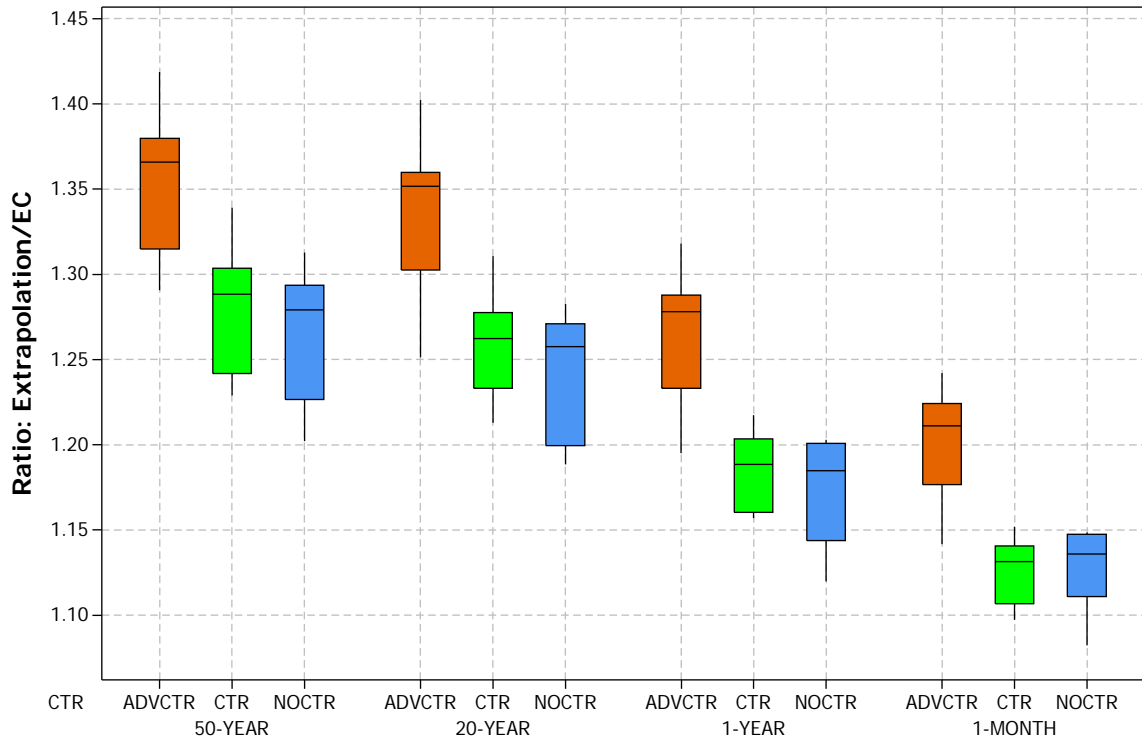
Fig. 8: 8a 50-year environmental contour lines of the turbulence models. Each contour line describes a possible alteration to the reference design extreme turbulence model as defined in the IEC61400-1 design standard. 8b Projection of the 50 year environmental contours on the Kriging surface response of the normalized extreme blade deflection in front of the tower as a function of wind speed and turbulence.

Table 7: Comparison of the extreme blade deflection from direct aero-servo-elastic simulations of the 50-year environmental contour line and the 50-year extrapolated extreme blade deflection in front of the tower.

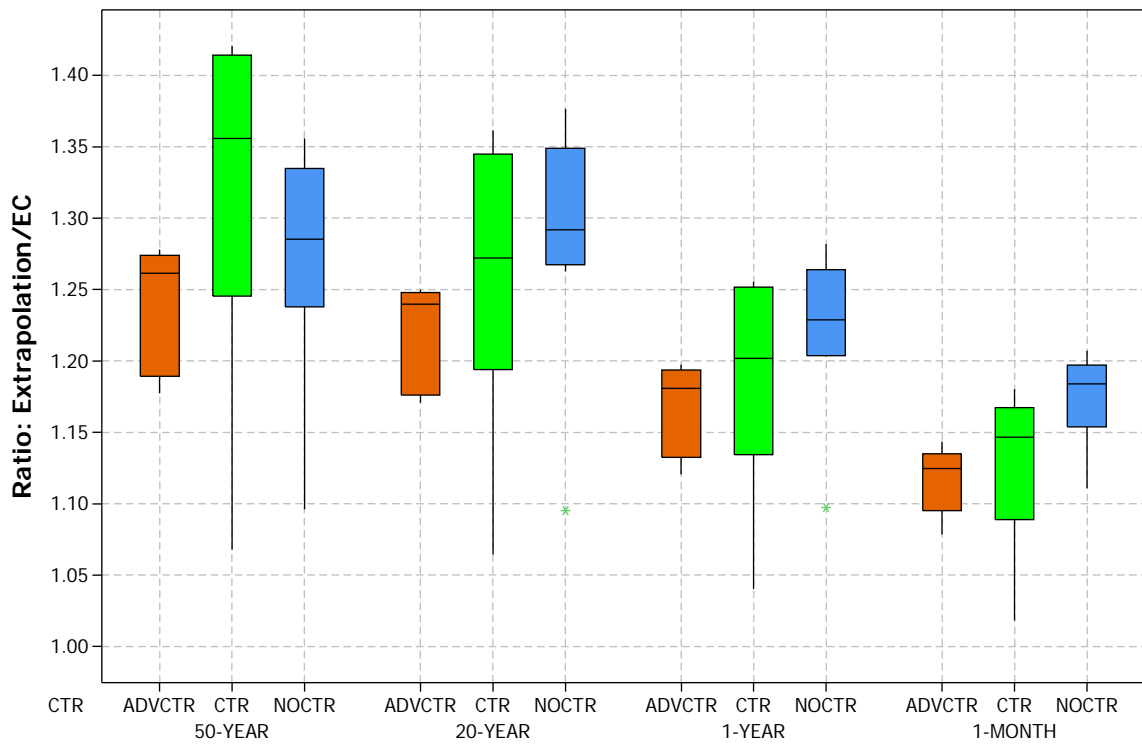
Scenario	Turbulence Model	Ratio: 50-year Extrapolation/EC		
		NO CTR	CTR	ADV CTR
1	IEC, LOGN	1.28	1.29	1.37
2	IEC, EV	1.20	1.23	1.31
3	IEC, LOGN, Vmean=11	1.28	1.29	1.37
4	IEC, LOGN, Iref=0.16	1.30	1.29	1.36
5	IEC, NORM	1.31	1.31	1.42
6	NATARAJAN, NORM	1.24	1.25	1.34
7	IEC, LOGN, Iref=0.20	1.28	1.34	1.38
8	NATARAJAN, Mod., Iref=0.16	1.22	1.24	1.29

Table 8: Comparison of the extreme tower bottom bending moment from direct aero-servo-elastic simulations of the 50-year environmental contour line and the 50-year extrapolated extreme tower bottom bending moment.

Scenario	Turbulence Model	Ratio: 50-year Extrapolation/EC		
		NO CTR	CTR	ADV CTR
1	IEC, LOGN, Iref=0.14	1.33	1.41	1.26
2	IEC, EV	1.24	1.31	1.19
3	IEC, LOGN, Vmean=11	1.34	1.42	1.28
4	IEC, LOGN, Iref=0.16	1.27	1.40	1.26
5	IEC, NORM	1.36	1.42	1.28
6	NATARAJAN, NORM	1.24	1.27	1.18
7	IEC, LOGN, Iref=0.20	1.30	1.24	1.26
8	NATARAJAN, Mod., Iref=0.16	1.10	1.07	1.19



(a) Ratio of extrapolated to EC for blade deflection.



(b) Ratio of extrapolated to EC for tower bottom bending moment.

Fig. 9: (9a) Ratio of extrapolated to EC for blade deflection as a function of control configuration and long term extrapolation period. and (9b) Ratio of extrapolated to EC for tower bottom bending moment as a function of control configuration and long term extrapolation period.

7 *Publication:* Influence of the control system on wind turbine loads in power production in extreme turbulence: Cost and reliability-based optimization of partial safety factors

Influence of the control system on wind turbine loads in power production in extreme turbulence: Cost and reliability-based optimization of partial safety factors

I. Abdallah^{a,*}, A. Natarajan^a, J.D. Sørensen^{a,b}

^aTechnical University of Denmark, Department of Wind Energy, Roskilde, Denmark

^bAalborg University, Department of Civil Engineering, Aalborg, Denmark

Abstract

Sophisticated load alleviation control systems are increasingly being designed and deployed to reduce the adverse effects of extreme load events, such as extreme turbulence, resulting in lighter structural design of wind turbines. The load alleviation features and algorithms in wind turbine control systems affect the magnitude, scatter and shape of the probability distribution of the extreme loads. Few studies have prospectively delved into the subject of optimizing the loads partial safety factors in wind turbines under the influence of advanced load alleviation control features. The objective here is to optimize the loads partial safety factor for a wind turbine in power production in extreme turbulence when three configurations of load alleviation control features of varying performance and complexity are employed. A cost and reliability-based optimization is used to optimize the loads partial safety factor, turbine geometry, controller failure rate and structural reliability metrics of a large multi-megawatt wind turbine. The load alleviation features considered in this study are cyclic pitch, individual pitch, static thrust limiter, condition based thrust limiter and tower damping. We demonstrate how tangible reduction in the loads partial safety factor can be achieved when advanced load alleviation control features are deployed on a wind turbine. We also show that, from a cost and reliability perspective, the overall probability of failure of the structure-control system is dominated by the failure rate of the control system. This means that decreasing the failure rate of the control system would have a larger impact on the overall probability of failure than solely improving the reliability of the structure. We also give an insight into the range of optimal annual failure rate of advanced load alleviation control features.

Keywords: wind turbines, loads partial safety factor, probabilistic modelling, load alleviation control systems, structural reliability, control failure rate

Nomenclature

COV Coefficient of Variation: ratio of the standard deviation to the mean

CTR Control System

ETM Extreme Turbulence Model

FORM First Order Reliability Method

LSF Limit State Function

PDF Probability Density Function

*Principal corresponding author

Email address: imad.abdallah.81@gmail.com (I. Abdallah)

1. Introduction

This paper should be considered as a direct continuation of [1] in which a probabilistic loads extrapolation approach is used to assess the structural reliability of a wind turbine blade and tower during power production when the extreme turbulence model is uncertain and when three load alleviation control systems of increasing complexity and performance are used. The load alleviation control features, which are an integral part of the structural design of large wind turbines, not only affect the magnitude of the extreme load level but also the scatter and the shape of the probability distribution function of the extreme loads. The magnitude, scatter and shape¹ of the probability distribution is dependent on the performance of the load alleviation control features to limit the excursion of extreme loads above a certain threshold. This means that in the presence of advanced load alleviation control features, the extreme loads become less dependent on the site parameters [2] and increasingly dependent on the performance and tuning of the controller and its load alleviation features (algorithms). The central question to be answered in this paper is: how can engineers leverage the load limiting effects of the advanced load alleviation control features to optimize the loads partial safety factor, turbine geometry, controller failure rate and structural reliability metrics?

[3] have demonstrated how to derive cost optimal safety factors while neglecting the cost of the wind turbine control/safety systems; they showed a drop of upto 10% in the initial building cost of the cost optimal turbine but was accompanied with an increase in the probability of failure by a factor of 4 to 8 times. Assuming the control system perform as expected on demand (or not) [3] observe small improvements in gain of the optimal turbine relative to a present-day designed reference wind turbine. This is due to the fact that the optima is rather flat which is a general feature of reliability based structural optimization problems. [4] studied the acceptance criteria of an offshore wind turbine tower and foundation in a cost and reliability based optimization. The discussed the idea of reducing structural reliability in extreme limit state function. It is not clear if the effects of the control/safety systems were considered or not. The main conclusion was that the economic optimal level of structural reliability could be lowered compared to reference wind turbine designed following current standards. It was also found that the cost and reliability based optimization is sensitive to operation and maintenance costs. [5] have used a cost and reliability based optimization of a wind turbine using various objective function formulations including no reconstruction of the wind turbine in case of structural failure when the control system fails. The authors showed that given a target reliability level, the optimal turbine geometry (tower bottom diameter and sheet thickness) is independent of the initial cost of the control system and its failure rate. [2] have derived cost optimal safety factors for a target probability of failure assuming the wind turbine components are designed by fatigue considerations; the optimal safety factors for the blades are smaller than the standard [6], while the values for hub, nacelle and tower are higher. The loads simulations in [2] assume a basic power and speed control system with no load alleviation control features.

The novelty in this paper is that loads partial safety factor, turbine geometry, controller failure rate and structural reliability metrics are derived and compared using a cost and reliability based optimization method for a large wind turbine when three configurations of load alleviation control features of varying performance and complexity are used. A large commercial multi-megawatt offshore wind turbine is considered with nominal power $> 5MW$ and rotor diameter $> 130m$. An industrial grade control system is used. The method is demonstrated through five design scenarios.

2. The structural reliability framework with load alleviation control

2.1. Load alleviation control features

The load control features used in this study are gain-scheduled PID controllers which have a simple structure and can be easily tuned. The load alleviation control features include a *thrust limiter*, *cyclic pitch*, *individual pitch* and *tower vibration damper*. These features are fairly representative of what can be found on modern wind turbines operating in the field today. Three configurations of the control system are considered in this paper; The complexity and load reduction performance of the controllers to limit the excursion of extreme loads above a certain threshold increase from configuration 1 to configuration 3:

Configuration 1: This is a basic control system that ensures that the wind turbine runs at optimal collective pitch and tip speed below rated wind speed and constant rotor speed (RPM) above rated wind speed. No load alleviation features are included.

Configuration 2: In addition to the control configuration 1 functionalities, a cyclic pitch control and a static thrust limiter control are included. This configuration is the reference configuration.

Configuration 3: In addition to the control configuration 2 functionalities, individual pitch control and condition based thrust limiter are included, which sets the control parameters based on the estimated external inflow and turbine loading conditions.

¹shape of distribution \equiv type of distribution (e.g. Lognormal or Weibull,etc.). Magnitude and scatter \equiv mean and coefficient of variation.

2.2. Influence of load alleviation control features on extreme loads

The simulated wind turbine is erected on a 110 meters tower, has a rotor diameter larger than 130 meters and rated power larger than 5MW. The aero-servo-elastic simulations of the wind turbine are performed using FAST [7]. A design of experiments is made in order to examine the effects of wind speed and turbulence variations on the predicted extreme loads. The mean wind speed is varied over a range from 4 to 25 m/s in 1 [m/s] increments and turbulence is varied from 1 to 8 in 1 [m/s] increments. For each combination of wind speed and turbulence level we generate realizations of wind time series with 48 stochastic seeds, resulting in a total of 8448 10-minute time series simulations. The FAST aero-servo-elastic simulations [7] were performed with the three control system configurations in the form of an external DLL. The output used from the simulations are the blade out-of-plane deflection in front of the tower (within +/-10 degrees azimuth) and the tower bottom fore-aft bending moment. A probabilistic loads extrapolation approach is then used to derive the annual maximum probability density function of the extreme loads [1]. The annual maximum load distributions are plotted in Fig. 1-2 for the blade extreme out-of-plane deflection in front of the tower and the tower extreme bottom fore-aft bending moment, respectively. The shape of the probability distribution is dependent on the sophistication and performance of the load alleviation control features to limit the excursion of extreme loads. In Fig. 1, the 50-year blade deflection drops by approximately 12% when using the advanced control configuration 3 compared to the reference control configuration 2, while the COV of the probability density function remains unchanged (0.027 versus 0.025). In Fig. 2, the 50-year tower bottom fore-aft bending moment drops by approximately 23% when using the advanced control configuration 3 compared to the reference control configuration 2, while the COV of the probability density function drops from 0.07 to 0.023. A conclusion can be drawn at this point: load alleviation control features not only affect the magnitude and scatter of the extreme load level but also the shape of the annual maximum load distribution. Should an augmented failure in the load alleviation control systems takes place, the extreme load exceedance probability increases significantly as shown in Fig. 1-2.

2.3. Structural reliability framework

Structural reliability is expected to differ significantly depending on the performance of the load alleviation control systems. For the structural reliability analysis an ultimate Limit State Function (LSF) g is defined in order to include the load and resistance uncertainties:

$$g = R X_R - L_{ULT}(\sigma_1, v) X_{dyn} X_{st} X_{ext} X_{sim} X_{exp} X_{aero} X_{str} \quad (1)$$

and the corresponding design equation is:

$$G = \frac{1}{\gamma_m} R_c - \gamma_l L_{ULT,c}(\sigma_1, v) \quad (2)$$

where G is the design equation corresponding to the limit state function (Equation 1), R_c is the characteristic value of the resistance R , X_R represents the model and statistical uncertainties of the resistance, γ_m is the partial material factor, γ_l is the partial load safety factor. $L_{ULT}(\sigma_1, v)$ is the random variable for the extreme load defined in terms of the turbulence and mean wind speed. $L_{ULT,c}$ is the characteristic value of the ultimate load. $L_{ULT}(\sigma_1, v)$ is represented by the annual maximum distribution function derived through the extrapolation process. $L_{ULT}(\sigma_1, v)$ for the blade extreme out-of-plane deflection in front of the tower is shown in Fig. 1 for each of the three control configurations. $L_{ULT}(\sigma_1, v)$ for the the tower extreme bottom fore-aft bending moment is shown in Fig. 2 for each of the three control configurations. Additional stochastic variables are defined as multiplicative factors to the load to take into account the model and statistical sources of uncertainties. X_{dyn} accounts for model uncertainty due to the modelling of the wind turbine dynamic response. X_{st} accounts for the statistical uncertainty of wind climate assessment. X_{ext} is associated with the extrapolated load model. X_{sim} accounts for statistical uncertainties caused by the limited number of loads simulations. X_{exp} accounts for the model uncertainties related to modelling the terrain and roughness. X_{aero} accounts for the model uncertainties related to the assessment of aerodynamic lift and drag coefficients. Finally the uncertainties related to the computation of the stresses on components from the loads is considered through X_{str} . Uncertainties related the control parameters are not directly included here. The stochastic variables of the LSF are described in Table 1. The structural reliability is assessed by solving the LSF using FORM². The outcome is defined by the reliability index β .

For the tower, the resistance is cast as as the ultimate bending capacity[4]:

$$M_{cr} X_R = \frac{1}{6} \left(1 - 0.84 \frac{D}{t} \frac{X_{y,ss} F_{y,ss}}{X_{E,ss} E} \right) \left(D^3 - (D - 2t)^3 \right) X_{y,ss} X_{cr} F_{y,ss} \quad (3)$$

where D is the tower bottom diameter and t is the sheet thickness. $X_{y,ss}$ is the yield strength model uncertainty, $X_{E,ss}$ is the Youngs modulus model uncertainty, $F_{y,ss}$ is the yield strength for structural steel, E is the Youngs modulus and X_{cr} is the critical

²A custom First Order Reliability Method is written in Matlab®.

load capacity. D and t of the reference wind turbine tower are specified to $6.34m$ and $0.041m$, respectively. For the blade, the resistance is cast as the maximum allowed blade deflection δl_{cr} in front of the tower corresponding to $2/3$ of the distance from the tower to the undeflected blade δl_{undfl} :

$$\delta l_{cr} X_R = \frac{2}{3} \delta l_{undfl} X_{\delta l} \quad (4)$$

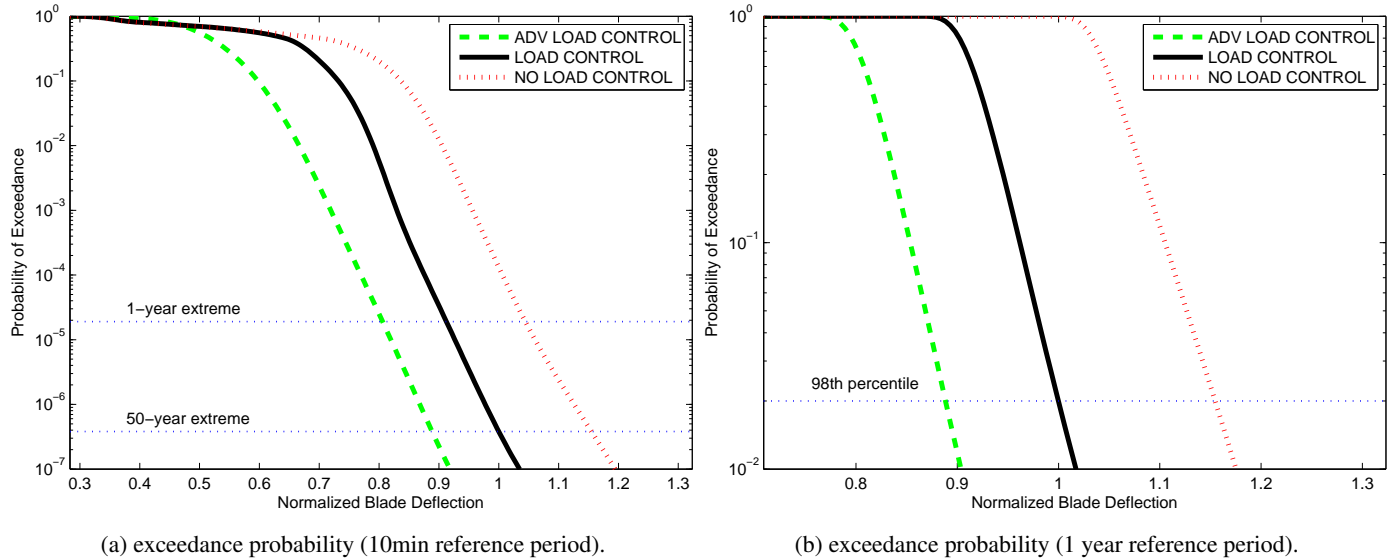


Fig. 1: Long term exceedance probability for the blade out-of-plane deflection in front of the tower in uncertainty scenario 1 for control configuration 1 (no load control), configuration 2 (load control) and configuration 3 (advanced load control). (a) 10-min reference period, (b) 1-year reference period. The extrapolated loads are normalized with the 50-year extrapolated load level derived from the simulations with control configuration 2. The COV of the probability density function with advanced load control is 0.027, COV = 0.025 with load control, and COV = 0.029 when no load control is used.

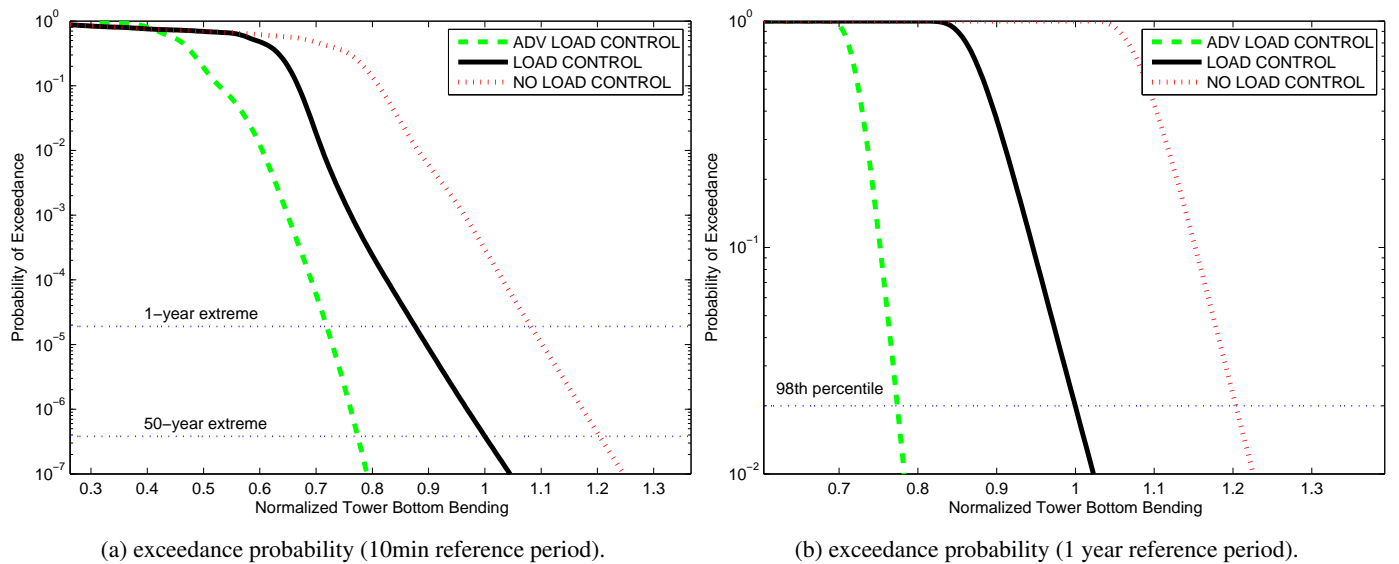


Fig. 2: Long term exceedance probability for the tower bottom fore-aft bending moment in uncertainty scenario 1 for control configuration 1 (no load control), configuration 2 (load control) and configuration 3 (advanced load control). (a) 10-min reference period and (b) 1-year reference period. The extrapolated loads are normalized with the 50-year extrapolated load level derived from the simulations with control configuration 2. The COV of the probability density function with advanced load control is 0.023, COV = 0.07 with load control, and COV = 0.056 when no load control is used.

Table 1: The stochastic variables of the Limit State Function.

Variable	Description	Distribution	Expected value	COV
X_{dyn}	Structural dynamics	LN	1	0.05
X_{aero}	Airfoil data uncertainty	G	1	0.07
X_{sim}	Simulation statistics	N	1	0.05
X_{exp}	Exposure (terrain)	LN	1	0.10
X_{ext}	Extrapolation	LN	1	0.05
X_{st}	Climate statistics	LN	1	0.05
X_{str}	Stress evaluation	LN	1	0.03
$X_{\delta l}$	Blade deflection model uncertainty	LN	1	0.05
X_{cr}	Critical load capacity	LN	1	0.10
$F_{y,ss}$	Yield strength for structural steel [MPa]	LN	240	0.05
E	Young's modulus [MPa]	LN	$2.1 \cdot 10^5$	0.02
$X_{y,ss}$	Model uncertainty for yield strength	LN	1	0.05
$X_{E,ss}$	Model uncertainty for Young's modulus	LN	1	0.02

3. Cost and reliability based optimizations in the presence of load alleviation control features

[1] established that advanced load alleviation control features increase the structural reliability of a wind turbine and reduce the effect of extreme inflow and turbulence uncertainty. In the following we will attempt to resolve the following question: can wind turbine designers leverage the load limiting effects of the advanced load alleviation control features to optimize the loads partial safety factor, and other structural, control and reliability metrics? and how?

3.1. Why cost and reliability based optimizations in the presence of load alleviation control features?

In one scenario, turbines designed with control configuration 2 could exceed the design loads due to site specific severe conditions in certain wind sectors. The turbines can thus be retrofitted and operated with advanced load alleviation control features (control configuration 3) to reduce the operating loads in those specific wind sectors in order to safeguard the structural integrity of the wind turbine; the wind turbine operates under the reference control system otherwise. This means that in Fig. 3a the reference controller (dashed green box) and the advanced controller are in parallel as represented by the fault tree in Fig. 3c, whereby additional/new sensors might be required for the advanced controller. The objective is thus to optimize the failure rate of the advanced controller within a cost and reliability framework. In another scenario, it is a common practice in the wind turbine industry to "upscale" existing wind turbine models; this often involves keeping the hub-drivetrain-nacelle structure-yaw systems as little changed as possible while modifying the rated power, the IEC design climate, the rotor size, the rotor speed, etc. or a combination thereof. This "upscaling" is mostly made possible³ by advances in the load alleviation control features as demonstrated in [1]. This means that in Fig. 3a the reference controller (dashed green box) is fully replaced by the advanced controller (as represented by the fault tree in Fig. 3b).

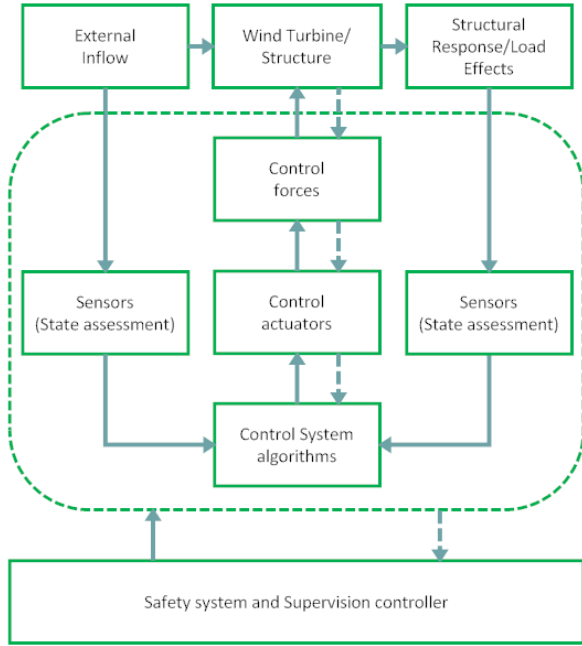
Thus it becomes essential to optimize the loads partial safety factor and other structural, control and reliability metrics in order to achieve the integration of advanced load control features and make the "upscaling" possible within a cost and reliability framework.

3.2. Annual failure rate of the load alleviation features in the control system

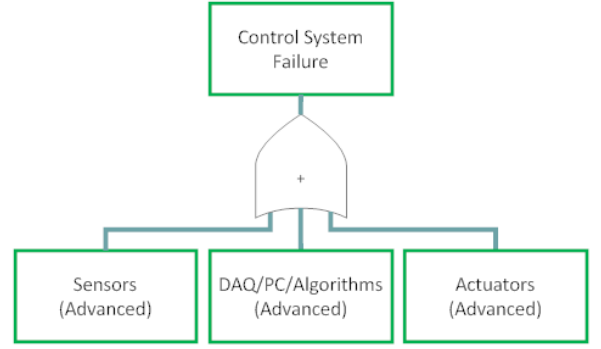
In the structural reliability analysis [1] it was tacitly assumed that the load alleviation control features always work (i.e. never fail). The probability that the extreme load l_{max} exceeds a given load l in an observation time T_{10min} given that the load alleviation control features work and perform as expected reads:

$$P(L \geq l_{max}) = P(L \geq l_{max} | CTR) P(CTR) \quad (5)$$

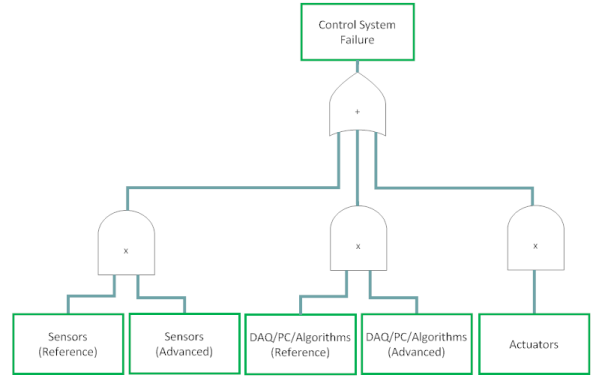
³and to a certain extent by the availability of additional stress reserve factors in the design of the various mechanical and structural components



(a) A simplified block diagram of the structural load control of a wind turbine.



(b) Simple fault tree of advanced controller.



(c) Simple fault tree of when reference and advanced controller are in parallel.

Fig. 3: (a) a simplified block diagram of the structural load control of a wind turbine whereby the reference controller (dashed green box) can be fully replaced by an advanced load alleviation controller as shown in fault tree (b) or retrofitted and ran in parallel with the reference controller as shown in the fault tree (c).

Expanding and generalizing Equation 5 we get:

$$P(L \geq l_{max}) = P(L \geq l_{max} | CTR) P(CTR) + \sum_{i=1}^N P(L \geq l_{max} | \overline{CTR}_i) P(\overline{CTR}_i) \quad (6)$$

where N is the total number of the controller failure modes. The first term in Equation 6 relates to the probability that the extreme load l_{max} exceeds a load l given that the control system works, and the second term relates to the probability that the extreme load l_{max} exceeds a load l given a failure in the load alleviation control features^{4, 5}.

Designating $f_{\overline{CTR}_i}$ the probability density function of controller failure mode i occurring, and assuming that the controller failure events follow a Poisson process, then the probability of controller failure i occurring in time interval $[t, t + dt]$ reads:

$$P(\overline{CTR}_i) = f_{\overline{CTR}_i}(t) dt \quad (7)$$

Failure modes are however assumed to be independent and exclusive from each other, meaning that no other failure event k have occurred before failure event i until time $t + dt$:

$$P(\overline{CTR}_k) = 1 - F_{\overline{CTR}_k}(t) \quad (8)$$

Given the independence of the failure events, we can write:

$$P(\overline{CTR}_i) = \int_0^T f_{\overline{CTR}_i}(t) \prod_{k=1}^N (1 - F_{\overline{CTR}_k}(t)) dt \quad (9)$$

⁴Faults are a sequence of accidental events that manifest themselves as failures.

⁵Further expansion can be made: conditioning the probability of failure of the control system on inflow conditions(i.e. storms, shear, extreme turbulence, etc.). This can further be expanded in such a way to include no structural failure given controller failure. It can still be further expanded to included safety system, etc.

where T is the time interval over which failure event i occurs. Since the failure events are assumed Poisson distributed, then:

$$f_{\overline{CTR}_i}(t) = \lambda_i e^{-\lambda_i t} \quad (10)$$

$$F_{\overline{CTR}_k}(t) = 1 - e^{-\lambda_k t} \quad (11)$$

where λ_i and λ_k are the failure rate. Inserting the expressions in 10 and 11 into 9 gives:

$$P(\overline{CTR}_i) = \int_0^T \lambda_i e^{-\lambda_i t} \prod_{k=1}^N e^{-\lambda_k t} dt \quad (12)$$

Which evaluates to⁶:

$$P(\overline{CTR}_i) = \frac{\lambda_i}{\lambda_i + \sum_{k=1}^N \lambda_k} \left[1 - e^{-T(\lambda_i + \sum_{k=1}^N \lambda_k)} \right] \quad (13)$$

One can then interpret $P(L > l_{max} | \overline{CTR}_i) P(\overline{CTR}_i)$ as the probability of the load L exceeding a certain maximum value l_{max} over the time interval where the control system is not functioning due to failure mode i and until the wind turbine can be out in a 'safe' operating mode.

3.3. Formulation of the cost and reliability based optimization

It can be argued⁷ that the acceptable reliability level of a wind turbine can be chosen based on a cost optimization with an objective function that includes the benefits (i.e. money made on selling energy production), the investment cost (money spent on research and development, design, testing, manufacturing and installation) and the failure cost (removal and replacement of failed component) in case of failure. The objective is thus to maximize the benefits relative to the incurred costs [2, 9, 10]:

$$W = B - [C_I + C_F] \quad (14)$$

where B are the benefits such as the annual energy production of a wind turbine, C_I are the initial investments costs including the costs of research, development, manufacturing and installation, C_F are the costs related to replacement and the cost of lost energy due to failure of components. In case where one wind turbine is considered and assuming systematic rebuild in case of failure, Equation 14 becomes [4, 5]:

$$W = \frac{B}{rC_0} - \left[\frac{C_I}{C_0} + \left(\frac{C_I}{C_0} + \frac{C_F}{C_0} \right) \frac{p_f}{r + p_f} \right] \quad (15)$$

where r is the real rate of interest, p_f is the annual probability of failure and C_0 are the initial costs of a reference wind turbine design. The cost and reliability based optimization can thus be cast as follows:

$$\begin{aligned} & \underset{z, \gamma}{\text{maximize}} && W(z, \gamma) \\ & \text{subject to} && z^l \leq z \leq z^u, \\ & && p_f \leq p_f^{max}, \\ & && \gamma^l \leq \gamma \leq \gamma^u, \\ & && G = \frac{M_{cr,c}(z)}{\gamma_m} - \gamma_l L_{ULT,c} = 0 \end{aligned} \quad (16)$$

where $z = \{D, t\}$, p_f^{max} is the maximum allowable probability of failure of the structure, and superscripts u and l correspond to upper and lower bounds, respectively. In equation 15, the control system is not taken into account. In order to take the control system into account, Equation 15 is modified⁸ to:

⁶Keld Hammerum, Vestas Wind Systems A/S

⁷Since human involvement in the operation of a wind turbine is marginal, the risk to human injury is minor in case of structural failure

⁸referring to equation 6 and setting $N = 1$, the structural probability of failure can be written as $P(L > l_{max}) = P(L > l_{max} | CTR) P(CTR) + P(L > l_{max} | \overline{CTR}) P(\overline{CTR})$. $P(CTR)$ and $P(\overline{CTR})$ are implicitly conditioned on an extreme demand being present. $P(\overline{CTR})$ is to be optimized. $P(CTR) = 1 - P(\overline{CTR}) \approx 1$. $P(L > l_{max} | CTR)$ is calculated using the structural reliability analysis in FORM presented in section 2.3. The wind turbine is assumed to suffer a structural failure with surety if the control system fails, meaning $P(L > l_{max} | \overline{CTR}) = 1$. Putting it all together $P(L > l_{max}) \approx P(L > l_{max} | CTR) + P(\overline{CTR}) = p_f + P(\overline{CTR})$.

$$W = \left[\frac{B}{rC_0} - \nu_{CTR} \frac{B}{rC_0} \right] - \left[\left(\frac{C_I}{C_0} + \frac{C_{cs}}{C_0} \right) + \left(\frac{C_I}{C_0} + \frac{C_F}{C_0} \right) \left(\frac{p_f + \nu_{CTR}}{r + p_f + \nu_{CTR}} \right) \right] \quad (17)$$

where ν_{CTR} is the annual failure rate of the advanced load alleviation control features. The expression in Equation 17 is intuitive; the benefits B decrease with increased control system failure, the initial investment costs C_I increase with additional load alleviation control features costs C_{cs} (advanced load alleviation control features might require additional research and development, additional sensors, algorithms, larger requirements for computing power, additional quality control, etc.), and finally the discounted lifetime failure and replacement costs increases with increasing failure rate of the advanced load alleviation control features. The cost and reliability based optimization formulation becomes:

$$\begin{aligned} & \underset{z, \gamma, \nu_{CTR}}{\text{maximize}} && W(z, \gamma, \nu_{CTR}) \\ & \text{subject to} && z^l \leq z \leq z^u, \\ & && \gamma^l \leq \gamma \leq \gamma^u, \\ & && p_f + \nu_{CTR} \leq p_f^{max}, \\ & && G = \frac{M_{cr,c}(z)}{\gamma_m} - \gamma_l L_{ULT,c} = 0 \end{aligned} \quad (18)$$

The structural probability of failure p_f is derived when solving the LSF (Equation 1) in FORM. The superscripts l and u denote lower and upper bounds respectively. The computed safety factors reflect the possible savings resulting from the cost optimal reliability level computed in the optimization problem cast in Equations 16 and 18. Following [3], the initial investment costs are:

$$\frac{C_I}{C_0} = \frac{2}{3} + \frac{1}{3} \frac{Dt - t^2}{D_0 t_0 - t_0^2} \quad (19)$$

The annual benefits are set to:

$$\frac{B}{C_0} = \frac{1}{8} \quad (20)$$

and the failure and replacement costs:

$$\frac{C_F}{C_0} = \frac{1}{36} \quad (21)$$

Finally the cost related to the marginal improvements in the control system is inversely proportional to the annual failure rate of the advanced load alleviation control features:

$$\frac{C_s}{C_0} = 0.001 \frac{1}{\nu_{CTR}} \quad (22)$$

4. Applications

What follows is a set of applications showing how the cost and reliability based optimization can be used to optimize the loads partial safety factor, wind turbine geometry, controller failure rate and reliability metrics.

4.1. Application 1: upscaling of existing wind turbine geometry

A wind turbine operating with the reference controller (configuration 2) is to be "upscaled" (extract more power through the rotor) while keeping the rotor-hub-drivetrain-nacelle structure-yaw systems and tower as little modified as possible. The specifications indicate that the "upscaling" should involve either modifying rated power (e.g. increase), modify pitch settings, IEC design climate conditions (e.g. higher mean wind speed or turbulence), or the rotor speed (e.g. increase RPM around the upper knee of the power curve), etc. or a combination thereof. The design scenario specifies that the rotor thrust is to be increased while maintaining the reference extreme blade deflection in front of the tower unchanged. The reference turbine is designed using control configuration 2 which yields a normalized extreme blade deflection in front of the tower of 1, see Fig. 4a, corresponding to an annual probability of failure of $p_f = 5.0 \cdot 10^{-4}$. The objective is thus to investigate how much could the extreme blade deflection in front of the tower be increased (due to upscaling) while maintaining the same target annual failure probability⁹ $p_f^{max} = 5 \cdot 10^{-4}$. This is

⁹The value $p_f = 5 \cdot 10^{-4}$ assumes that the risk to human lives is negligible in case of failure of a structural element. The target reliability level is assumed to correspond to component class 2 (Moderate consequences of failure).

done by examining how far can the blade deflection annual maximum distribution derived with load controller configuration 3 be shifted (corresponding to higher characteristic extreme load level) until the annual probability of failure derived in FORM reaches p_f^{max} , see Fig. 4a and 4b. By examining Fig. 4a we see that control configuration 3 yields an 11.13% drop in the 98th percentile of the annual extreme blade deflection in front of the tower relative to control configuration 2. In a deterministic context we are contended in "upscaling" so that we make full usage of the 11.13% of reserves, regardless of the full distribution. However, upon further inspection of the tail of both annual maximum distributions in Fig. 4c, we observe that the tail of control configuration 3 is "thinner" compared to control configuration 2. We take advantage of this fact by introducing the full annual maximum distribution of configuration 3 in FORM and examine the probability of failure using the LSF (Equation 1), we find out that we can shift the distribution by a value of 13% while keeping the annual probability of failure to $p_f = p_f^{max} = 5 \cdot 10^{-4}$. Indeed this assumes that the annual maximum distribution of the blade deflection of the "upscaled" turbine maintains the same shape and same tail which may or may not be true.

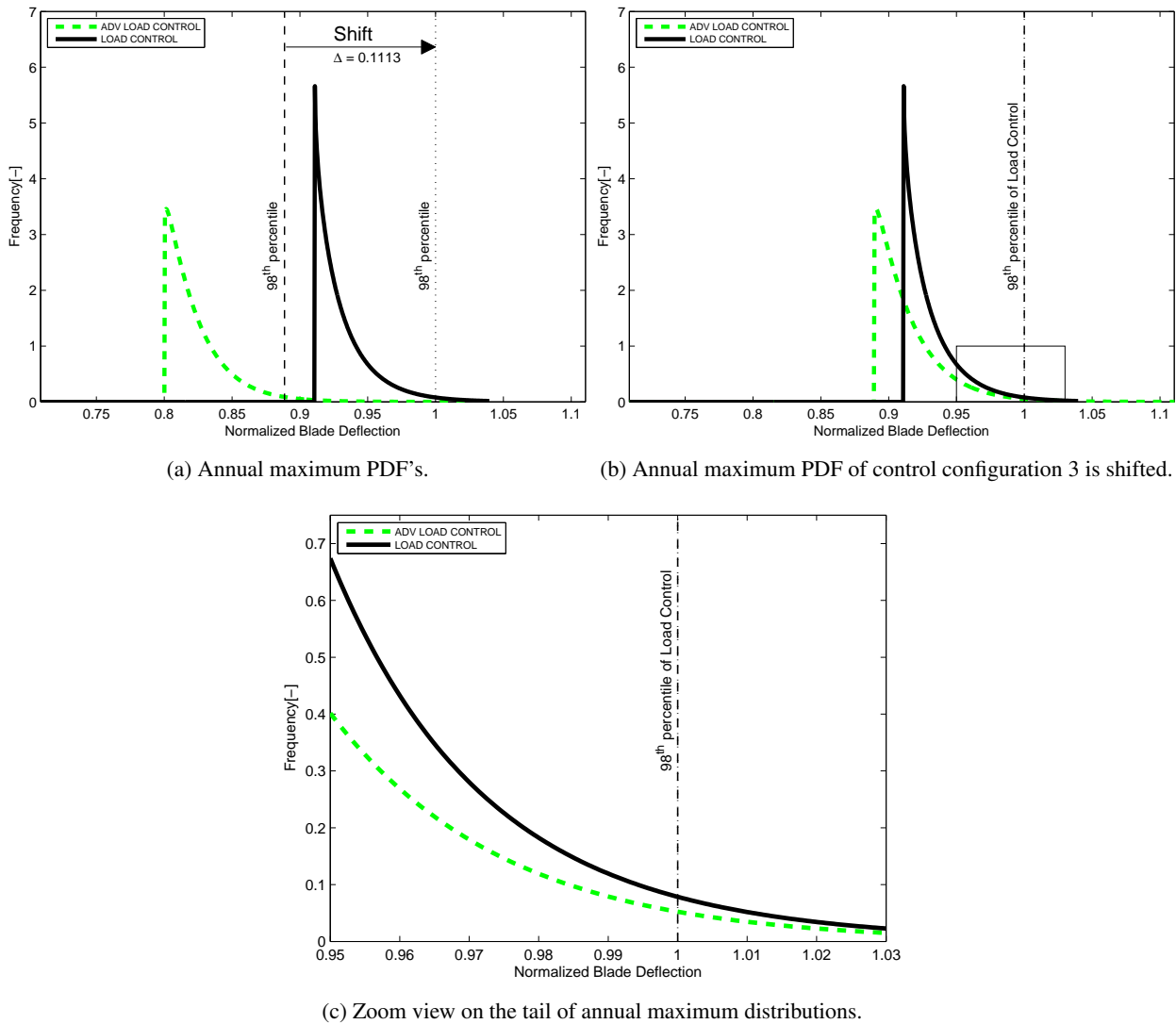


Fig. 4: Comparison between the annual maximum PDF of the blade deflection in front of the tower when the turbine is operated with control configuration 2 (Load control) and configuration 3 (Advanced load control). Advanced load alleviation control features in configuration 3 drops the 50-year extreme blade deflection by 11.13% relative to configuration 2. Comparison of the tail of both distributions is done by shifting the annual maximum PDF of configuration 3 so that the 98th percentile overlaps with that of configuration 2.

The advanced load alleviation control features (configuration 3) made it possible to reduce the extreme blade deflection in front of the tower, but knowing the full annual maximum distribution of the blade deflection made it possible to assess the probability of failure and further improve the design of the upscaled wind turbine. Given that the control configuration 3 yields a "thinner" tale meant that under configuration 3 the same blade can be deflected even further while maintaining the same annual probability of failure. A designer can now translate the 13.0% increase in extreme blade deflection into a higher rated output power, higher rotor

speed, higher operating extreme turbulence or a combination thereof.

4.2. Application 2: Deterministic versus Probabilistic approach

In this application we determine the tower bottom characteristic yield bending strength $M_{cr,c}$ using a deterministic approach and compare the outcome to a probabilistic approach.

The starting point is a wind turbine operating with a control configuration 1 for which the tower bottom characteristic yield bending strength $M_{cr,c} = 386517$ corresponding to a probability of failure of $p_f = 3.6 \cdot 10^{-4}$, partial load safety factor $\gamma_l = 1.35$ and partial material factor $\gamma_m = 1.25$. The same turbine operating with control configuration 2 would result in a $\sim 17\%$ drop in the 50-year load level relative to control configuration 1 as shown in Table. 2. A simple deterministic approach would suggest that the tower bottom characteristic yield bending strength becomes $0.8306 \cdot M_{cr,c}^{NOCTR} = 321043$. Similarly, when using the advanced control configuration 3 the tower bottom characteristic yield bending strength becomes $0.6430 \cdot M_{cr,c}^{NOCTR} = 248540$. Following a deterministic approach for the design of the tower strength in control configuration 2 and 3, where the loads partial safety factor is maintained to $\gamma_l = 1.35$ and the material partial safety factor is maintained to $\gamma_m = 1.25$, we are indirectly assuming that the following remains true: $p_f \leq 3.6 \cdot 10^{-4}$ and $W \geq 1.073$. An advantage of a deterministic approach is its simplicity and the speed with which the tower bottom characteristic yield bending strength can be computed. However, we don't get a clear insight into the probability of failure of the structure p_f nor do we get a full understanding of the real benefits W when advanced load alleviation control features are used. Furthermore, if we maintain the partial load safety factor equal to 1.35 we might end up in over-estimating (over-designing) the tower bottom characteristic yield bending strength.

Table 2: Cost and reliability based optimization of tower base geometry and load partial safety factor when stiffness and frequency constraints are not included. The control system failure rate is not included in this optimization. The material safety factor is set to a constant $\gamma_m = 1.25$. The target probability of failure is set to $p_f^{max} = 5 \cdot 10^{-4}$. $0.8306 \cdot M_{cr,c}^{NOCTR} = 321043$, $0.6430 \cdot M_{cr,c}^{NOCTR} = 248540$

Control Configuration	50-year load	Deterministic Approach			
		γ_l, γ_m	$M_{cr,c} [kNm]$	W	p_f
Control Config. 1	1	1.35,1.25	386517	1.073	$3.6 \cdot 10^{-4}$
Control Config. 2	0.8306	1.35,1.25	321043	≥ 1.073	$\leq 3.6 \cdot 10^{-4}$
Control Config. 3	0.6430	1.35,1.25	248540	≥ 1.073	$\leq 3.6 \cdot 10^{-4}$

Next we perform the probabilistic optimization as described in Equation 16, again with the starting point being the wind turbine operating with a control configuration 1 for which the tower bottom characteristic yield bending strength $M_{cr,c} = 386517$ corresponding to a probability of failure of $p_f = 3.6 \cdot 10^{-4}$, load partial safety factor $\gamma_l = 1.35$ and partial material factor $\gamma_m = 1.25$. In the probabilistic optimization the target probability of failure is set to $p_f^{max} = 5 \cdot 10^{-4}$. The objective is to maximize the benefits W . The results are shown in Table 3. The optimization of the same turbine operating with control configuration 2 would suggest that the tower bottom characteristic yield bending strength becomes 308574 kNm, an approximately 4% drop compared to the deterministic approach. A 4% that would have remained "hidden" was it not for the probabilistic approach. This indeed could simply be due to the higher probability of failure $p_f^{max} = 5 \cdot 10^{-4}$ vs $3.6 \cdot 10^{-4}$. The corresponding load partial safety factor is now 1.30 instead of 1.35, and $W = 1.12$ instead of 1.073 (i.e. W is now quantifiable instead of being "hidden" or assumed).

Given the very low coefficient of variation of the load distribution in control configuration 3 ($COV = 0.023$), we checked the sensitivity of the probabilistic optimization to the type of distribution of the load model and statistical sources of uncertainties X [11]. In FORM, X are assumed to follow Lognormal distributions as shown in Table 1. Now we assume that those random variables follow Gumbel distribution while maintaining the same mean and coefficient of variation; the probabilistic optimization suggests that for the same target probability of failure $M_{cr,c}$ becomes 249281kNm versus a value of 249813kNm (shown in Table 3) while the load partial safety factor γ_l and W hardly change.

Table 3: Cost and reliability based optimization of tower base geometry and load partial safety factor when stiffness and frequency constraints are not included. The control system failure rate is not included in this optimization. The material safety factor is set to a constant $\gamma_m = 1.25$. The target probability of failure is set to $p_f^{max} = 5 \cdot 10^{-4}$.

Control Configuration	50-year load	Probabilistic Approach			
		γ_l, γ_m	$M_{cr,c} [kNm]$	W	p_f
Control Config. 1	1	1.35,1.25	386517	1.073	$3.6 \cdot 10^{-4}$
Control Config. 2	0.8306	1.30,1.25	308574	1.12	$5.0 \cdot 10^{-4}$
Control Config. 3	0.6430	1.36,1.25	249813	1.16	$5.0 \cdot 10^{-4}$

4.3. Application 3: cost and reliability optimization of tower bottom geometry and loads partial safety factor. No constraints on tower geometry.

The reference tower, designed using control configuration 2, has $D_o = 6.34m$ and $t_o = 0.041m$, corresponding to a reliability index of 3.326 ($p_f = 4.41 \cdot 10^{-4}$). The tower base is designed to the limit with a partial load and material factors of 1.35 and 1.25 respectively. It is clear that the probability of failure for this reference tower design is indeed lower than the target of $5 \cdot 10^{-4}$. The normalized direct cost for the reference tower is by definition $C_I/C_0 = 1.0$ (Equation 19) and the benefit-cost equation $W = 1.08$ for a real rate of interest $r = 0.06$. We will apply the cost and reliability optimization described in equation 16 with $p_f^{max} = 5 \cdot 10^{-4}$ in order to derive a cost optimal tower geometry and loads partial safety factor. The optimization is done using the Matlab function *fmincon*. The cost and reliability optimization of the tower base is done without any constraints on tower geometry, stiffness or frequency. Table 4 shows the results assuming the tower is designed with control configuration 2 (basic reference controller) and control configuration 3 where advanced load alleviation control features are used.

The cost optimal turbine, with control configuration 2, has $D = 8.91m$, $t = 0.026m$, a load partial safety factor $\gamma_l = 1.30$ and a corresponding cost optimal probability of failure of $p_f = 5 \cdot 10^{-4}$. The partial materials factor is set to a constant $\gamma_m = 1.25$. The normalized direct cost $C_I/C_0 = 0.96$ and the benefit-cost equation $W = 1.11$. The drop in load partial safety factor from 1.35 to 1.30 is largely attributed to the increase in probability of failure from $p_f = 4.41 \cdot 10^{-4}$ to the cost optimal probability of failure $p_f = 5.0 \cdot 10^{-4}$.

The cost optimal turbine, with control configuration 3 (with advanced load alleviation control features) has $D = 8.31m$, $t = 0.024m$, a load partial safety factor $\gamma_l = 1.36$ and a corresponding cost optimal probability of failure $p_f = 5 \cdot 10^{-4}$. The partial material factor is set to a constant $\gamma_m = 1.25$. The normalized direct cost $C_I/C_0 = 0.93$ and the benefit-cost equation $W = 1.15$. The drop in the C_I/C_0 from 0.96 to 0.93 (a drop of 3.2%) and the increase in benefits from 1.11 to 1.15 (an increase of 3.6%) is largely attributed to the drop in the extreme load level due to the introduction of the advanced load alleviation control features.

The above optimization is repeated while setting the target probability of failure to $p_f^{max} = 1 \cdot 10^{-3}$. We optimize for the load partial safety factor while keeping the partial material factor constant ($\gamma_m = 1.25$). The results are shown in Table 5. A tangible reduction in safety factor is achieved because of the lower target probability of failure ($p_f = 5 \cdot 10^{-4}$ versus $p_f = 1.0 \cdot 10^{-3}$). However we observe that the benefits W and the direct costs C_I/C_0 are unchanged compared to previously. This is typical behaviour of cost and reliability based structural optimization problems where the optimal benefit-cost is rather flat [3]. This is an interesting result that indicates that we are able to significantly reduce the structural probability of failure for no or marginal change in benefits and costs. This result confirms the findings in [3].

In Table 5 the cost optimal probability of failure is $p_f = 6.95 \cdot 10^{-4}$ ($\leq 1.0 \cdot 10^{-3}$), yielding a load partial safety factor $\gamma_l = 1.32$ for control configuration 3. Now if instead of constraining the probability of failure to be $\leq 1.0 \cdot 10^{-3}$, we force the probability of failure to be equal to $1.0 \cdot 10^{-3}$. We find that the corresponding load partial safety factor drops to $\gamma_l = 1.30$ with no change in the benefit-cost function ($W = 1.15$) nor in the initial investment cost ($C_I/C_0 = 0.92$). This is typical behaviour of cost and reliability based structural optimization problems where the optimal benefit-cost is rather flat [3, 2].

The advanced load alleviation control features in control configuration 3 result in a lower extreme characteristic load level and tighter spread (i.e. lower COV) compared to control configuration 2 ; in Fig. 2, the 50-year tower bottom fore-aft bending moment drops by approximately 23% when using the advanced control configuration 3 compared to the reference control configuration 2, while the COV of the probability density function drops from 0.07 to 0.023. However, in the optimization scheme we see that this does not necessarily translate into lower load partial safety factor as one would expect That could be due to several reasons:

- The low COV of the extreme load distribution in control configuration 3 forces the characteristic load level (98 percentile) to be close to the mean of the distribution (i.e. tight extreme load distribution). Hence a larger safety factor would be required to reach the design load level.
- The low COV of the extreme load distribution in control configuration 3 means that model uncertainties in the limit state function (Equation 1) start to dominate the reliability analysis in FORM. Hence, any reduction in the load partial safety factor would require a reduction in model uncertainties, if possible.
- The tail of the extreme load distribution in control configuration 3 is very difficult to determine due to the limiting effects of the advanced load control features on the peak loads. A poorly determined distribution tail would inevitably result in a highly sensitive reliability analysis and hence loads partial safety factor.

Note however that even though the load partial safety factor increase in control configuration 3 is on the order of 4% – 5% (Table 4 and 5), the drop in the 50-year load level is approximately 23%, resulting in an overall lower design load level in configuration 3 compared to configuration 2 which is reflected in the higher benefit-cost W .

4.4. Application 4: cost and reliability optimization of tower bottom geometry and loads partial safety factor. Constrained tower stiffness.

We now repeat the above cost and reliability based optimization but we impose constraints on the tower stiffness and frequency by forcing the plastic section modulus¹⁰ of the cost optimal tower to be equal to that of the reference tower. The target probability of failure is set to $p_f^{max} = 5 \cdot 10^{-4}$ and the partial material factor is kept constant ($\gamma_m = 1.25$). The results are shown in Table 6. For control configuration 3, the optimal loads partial safety factor, reliability index, benefits W and direct cost C_I/C_0 are unchanged compared to the non-stiffness constrained optimization presented in the Section 4.3. For control configuration 2, we observe that the benefits W drop from 1.11 to 1.08 and the direct cost C_I/C_0 increase from 0.96 to 0.99. The reason for this is when imposing the stiffness constrain in control configuration 2, the tower geometry will tend to the reference geometry for which $W = 1.08$ and $C_I/C_0 = 1$. The optimization is repeated while setting the target probability of failure to $p_f^{max} = 1 \cdot 10^{-3}$. We optimize for the load partial safety factor while keeping the partial material factor constant ($\gamma_m = 1.25$). The results are shown in Table 7. The cost optimal probability of failure is $p_f = 1.0 \cdot 10^{-3}$ ($\leq 6.7 \cdot 10^{-4}$), yielding a load partial safety factor $\gamma_l = 1.23$ and $\gamma_l = 1.33$ for control configuration 2 and 3, respectively. Now instead of constraining the probability of failure to $\leq 1.0 \cdot 10^{-3}$, we force the probability of failure to be equal to $1.0 \cdot 10^{-3}$. We find that the corresponding load partial safety factor drops to $\gamma_l = 1.30$ for control configuration 3 with no change in the benefit-cost function $W = 1.15$ nor the initial investment cost remains unchanged $C_I/C_0 = 0.92$. As in the previous example, this is typical behaviour of cost and reliability based structural optimization problems where the optimal benefit-cost is rather flat [2, 3].

Thus it can be concluded that tangible reduction in the load partial safety factor can be achieved when advanced load alleviation control features are used, but the magnitude of reduction will depend not only on the constraints put in place during the optimization and on the target probability of failure but also on the shape of the long term probability density function of the extreme loads.

4.5. Application 5: cost and reliability optimization of tower bottom geometry and loads partial safety factor. The controller cost C_{cs} and controller failure rate ν_{CTR} are INCLUDED:

We now include the annual failure rate ν_{CTR} of the load alleviation control features in the cost and reliability based optimization.

First, we perform the cost and reliability optimization while fixing ν_{CTR} to a constant values $10^{-2}, 5 \cdot 10^{-3}, 10^{-3}, 5 \cdot 10^{-4}$ and 10^{-4} . The structural probability of failure p_f is unconstrained. The results are shown in Table 8. Even though ν_{CTR} is varied over a significant range between 10^{-2} to 10^{-4} , the structural probability of failure p_f of the tower varies over a narrow range between $2.2 \cdot 10^{-3}$ to $1.6 \cdot 10^{-3}$ for control configuration 2, and between $9.8 \cdot 10^{-4}$ to $6.7 \cdot 10^{-4}$ for control configuration 3. This indicates that the overall annual probability of failure of the tower $\nu_{CTR} + p_f$ is dominated by the controller failure rate. This means that decreasing the failure rate of the control system (increase its reliability) would have a larger impact than improving the reliability of the structure. This however comes with an increased initial investment cost. For instance, decreasing the annual failure rate of the control system by a decade (from $1.0 \cdot 10^{-2}$ to $1.0 \cdot 10^{-3}$) would increase the initial investment cost C_I/C_0 by approximately 5%. Further decrease in the controller annual failure rate would accelerate the costs. We also observe that a peak value of W is reached for ν_{CTR} around 10^{-3} .

Next, we perform the cost and reliability optimization without imposing any constraints on both the annual failure rate of the controller ν_{CTR} nor the tower probability of failure p_f . The results are shown in Table 9. The difference in the load partial

¹⁰The plastic section modulus of a circular tube: $\frac{1}{6} (D^3 - (D - 2t)^3)$

safety factor between the two control configurations is significantly larger than the difference between the loads partial safety factor presented in Table 6. This is due to the inclusion of the failure rate of the control system which dominates the overall failure of the structure. Furthermore, the difference in the benefits-cost function W between the two control configurations is 6.5% in Table 6 and drops to 4.8% in Table 9 when the failure rate of the control system is included in the optimization. However, the difference in the initial investment cost C_I/C_0 between the two control configurations is approximately 6.5% in Table 6 but drops to 4.2% in Table 9 when the cost of the control system is included in the optimization.

Finally, we perform the cost and reliability optimization while constraining the the tower structural reliability to $p_f \leq 5 \cdot 10^{-4}$ and the overall annual probability of failure of the tower to $\nu_{CTR} + p_f \leq 5 \cdot 10^{-4}$. The results are shown in Table 10. Here again we observe that the overall probability of failure is dominated by the annual failure rate of the controller, especially in the case of control configuration 3 where advanced load alleviation control features are used. The probability of failure p_f drops by 60% when advanced load alleviation control features are used (configuration 3), the benefits W increase by approximately 15% and the initial investment costs C_I/C_0 drops by approximately 11% relative to control configuration 2.

In Table 9 the benefits W increase by 5% when control configuration 3 is used relative to configuration 2; this value increases to 15% in Table 10. This points that larger benefits are to be had when advanced load alleviation control features are used under strict requirements for structural probability of failure. However, under strict requirements for structural probability of failure (Table 10), the controller failure rate by far dominates the overall structure-control probability of failure compared to when no constraints are imposed on the structural probability of failure (Table 9).

Table 4: Cost and reliability based optimization of tower base geometry and load partial safety factor when stiffness and frequency constraints are not included. The control system failure rate is not included in this optimization. The material safety factor is set to a constant $\gamma_m = 1.25$. The target probability of failure is set to $p_f^{max} = 5 \cdot 10^{-4}$.

Control Configuration	D	t	γ_l	γ_m	β	p_f	W	C_I/C_0
Control Configuration 2	8.91	0.026	1.30	1.25	3.3	$5 \cdot 10^{-4}$	1.11	0.96
Control Configuration 3	8.31	0.024	1.36	1.25	3.3	$5 \cdot 10^{-4}$	1.15	0.93

Table 5: Cost and reliability based optimization of tower base geometry and loads partial safety factor when no stiffness and frequency constraints are not included. The control system failure rate is not included in this optimization. The material safety factor is set to a constant $\gamma_m = 1.25$. The target probability of failure is set to $p_f^{max} = 1 \cdot 10^{-3}$.

Control Configuration	D	t	γ_l	γ_m	β	p_f	W	C_I/C_0
Control Configuration 2	8.82	0.026	1.27	1.25	3.17	$7.69 \cdot 10^{-4}$	1.11	0.96
Control Configuration 3	7.62	0.026	1.32	1.25	3.19	$6.95 \cdot 10^{-4}$	1.15	0.92

Table 6: Cost and reliability based optimization of tower base geometry and load partial safety factor when section modulus constraints are included. The control system failure rate is not included in this optimization. The target probability of failure is set to $p_f^{max} = 5 \cdot 10^{-4}$. The material safety factor is set to a constant $\gamma_m = 1.25$.

Control Configuration	D	t	γ_l	γ_m	β	p_f	W	C_I/C_0
Control Configuration 2	6.43	0.040	1.29	1.25	3.3	$5.0 \cdot 10^{-4}$	1.08	0.99
Control Configuration 3	8.14	0.025	1.36	1.25	3.3	$5.0 \cdot 10^{-4}$	1.15	0.93

Table 7: Cost and reliability based optimization of tower base geometry and load partial safety factor when section modulus constraints are included. The control system failure rate is not included in this optimization. The material safety factor is set to a constant $\gamma_m = 1.25$. The target probability of failure is set to $p_f^{max} = 1 \cdot 10^{-3}$.

Control Configuration	D	t	γ_l	γ_m	β	p_f	W	C_I/C_0
Control Configuration 2	6.89	0.035	1.23	1.25	3.09	$1.0 \cdot 10^{-3}$	1.10	0.97
Control Configuration 3	8.23	0.024	1.33	1.25	3.20	$6.7 \cdot 10^{-4}$	1.15	0.92

Table 8: Cost and reliability based optimization of tower base geometry and load partial safety factor when section modulus constraints are included. The control system cost and failure rate are included in this optimization. The annual failure rate ν_{CTR} of the load alleviation control features is fixed to the following values $10^{-2}, 5 \cdot 10^{-3}, 10^{-3}, 5 \cdot 10^{-4}$ and 10^{-4} . No constraint is set on the tower structural probability of failure p_f .

Control Configuration	D	t	γ_l	γ_m	p_f	ν_{CTR}	W	C_I/C_0
Control Configuration 2	7.36	0.030	1.17	1.25	$2.2 \cdot 10^{-3}$	$1.0 \cdot 10^{-2}$	0.94	0.96
Control Configuration 2	7.27	0.031	1.18	1.25	$1.9 \cdot 10^{-3}$	$5.0 \cdot 10^{-3}$	1.00	0.97
Control Configuration 2	7.18	0.032	1.19	1.25	$1.6 \cdot 10^{-3}$	$1.0 \cdot 10^{-3}$	1.03	1.00
Control Configuration 2	7.18	0.032	1.20	1.25	$1.6 \cdot 10^{-3}$	$5.0 \cdot 10^{-4}$	0.99	1.06
Control Configuration 2	7.17	0.032	1.20	1.25	$1.6 \cdot 10^{-3}$	$1.0 \cdot 10^{-4}$	0.59	1.46
Control Configuration 3	8.36	0.024	1.30	1.25	$9.8 \cdot 10^{-4}$	$1.0 \cdot 10^{-2}$	0.99	0.92
Control Configuration 3	8.30	0.024	1.32	1.25	$8.2 \cdot 10^{-4}$	$5.0 \cdot 10^{-3}$	1.06	0.93
Control Configuration 3	8.24	0.024	1.33	1.25	$6.9 \cdot 10^{-4}$	$1.0 \cdot 10^{-3}$	1.08	0.97
Control Configuration 3	8.24	0.024	1.33	1.25	$6.8 \cdot 10^{-4}$	$5.0 \cdot 10^{-4}$	1.04	1.02
Control Configuration 3	8.24	0.024	1.33	1.25	$6.7 \cdot 10^{-4}$	$1.0 \cdot 10^{-4}$	0.65	1.42

Table 9: Cost and reliability based optimization of tower base geometry and load partial safety factor when section modulus constraints are included. The control system cost and failure rate are included in this optimization. No constraints on both the annual failure rate of the controller ν_{CTR} and the tower structural reliability p_f .

Control Configuration	D	t	γ_l	γ_m	p_f	ν_{CTR}	W	C_I/C_0
Control Configuration 2	7.2	0.031	1.19	1.25	$1.7 \cdot 10^{-3}$	$1.7 \cdot 10^{-3}$	1.04	0.99
Control Configuration 3	8.26	0.024	1.32	1.25	$7.17 \cdot 10^{-4}$	$1.7 \cdot 10^{-3}$	1.09	0.95

Table 10: Cost and reliability based optimization of tower base geometry and load partial safety factor when section modulus constraints are included. The control system cost and failure rate are included in this optimization. The annual failure rate of the structure-control is constrained to $\nu_{CTR} + p_f \leq 5 \cdot 10^{-4}$ and the tower structural reliability $p_f \leq 5 \cdot 10^{-4}$.

Control Configuration	D	t	γ_l	γ_m	p_f	ν_{CTR}	W	C_I/C_0
Control Configuration 2	5.49	0.055	1.37	1.25	$1.65 \cdot 10^{-4}$	$3.34 \cdot 10^{-4}$	0.87	1.20
Control Configuration 3	7.36	0.030	1.51	1.25	$6.5 \cdot 10^{-5}$	$4.35 \cdot 10^{-4}$	1.00	1.07

5. Conclusion

The magnitude, scatter and shape of the probability distribution is dependent on the performance of the load alleviation control features to limit the excursion of extreme loads above a certain threshold. This means that in the presence of advanced load alleviation control features, the extreme loads become less dependent on the site parameters and increasingly dependent on the performance and tuning of the controller. This paper presented a probabilistic cost and reliability based optimization methodology to optimize the loads partial safety factor (load safety factors), turbine geometry, controller failure rate and structural reliability metrics for a multi-megawatt wind turbine in power production in extreme turbulence when three advanced load alleviation control features of varying performance are used.

In a first application we showed how a reference wind turbine can be "upscaled" for extreme blade deflection in front of the tower while maintaining an acceptable target probability of failure ($p_f = 5 \cdot 10^{-4}$) when advanced load alleviation control features are used. In another application we determine the tower bottom characteristic yield bending strength using a deterministic approach and compared the outcome to a probabilistic approach when three control configurations of varying performance to limit extreme loads excursions are used. In a further applications the cost and reliability-based optimization was used to optimize the tower geometry and the extreme loads partial safety factor with/without any geometry constraints and for a target probability of failure of $p_f = 5 \cdot 10^{-4}$ and $p_f = 1 \cdot 10^{-3}$. We observed a tangible reduction in the loads partial safety factor when advanced load alleviation control features are used while maximizing the benefits versus costs and while maintaining acceptable target probability of failure. The cost and reliability based optimization resulted in tangible reduction in the extreme loads partial safety factor but the magnitude of the reduction is not only dependent on the constraints put in place during the optimization and on the target probability

of failure but also on the shape of the long term probability density function of the extreme loads, which in turn is dependent on the performance and tuning of the load alleviation controller features. It was observed that if the load alleviation control features yield very low scatter in the extreme loads distribution, then model and statistical uncertainties dominated the optimization of the loads partial safety factor. In a final application we included the controller cost and controller failure rate in the cost and reliability-based optimization of the tower geometry and the loads partial safety factor. In this application we observed that the benefits are maximized when the advanced load alleviation control features failure rate is around $\nu_{CTR} = \lambda_1 0^{-3}$. A key finding is that the overall probability of failure of the structure-control system is dominated by the failure rate of the control system. This means that decreasing the failure rate of the control system would have a larger impact than improving the reliability of the structure. This however comes with an increased initial investment cost. For instance, we showed that decreasing the annual failure rate of the control system by a decade (from $1.0 \cdot 10^{-2}$ to $1.0 \cdot 10^{-3}$) would increase the initial investment cost by approximately 5%. Further decrease would accelerate the costs.

Few shortcomings are identified. The first being the uncertainty models used in the structural reliability calculations in FORM; any improvement in the uncertainty models will have an effect on the conclusions reported in this paper. Since the uncertainty models themselves are uncertain, future work can consider the sensitivity of the optimization to the uncertainty models. More advanced limit state function and design equations for the tower can be considered. The applications presented here were concerned with the blade extreme deflection and tower bottom bending moment, future work can include further components such as blades, drive train and main frame. The extreme load distributions for blade deflection and tower bending moment were determined using long term probabilistic extrapolation. The extreme load distributions are very difficult to determine due to the limiting effects of the advanced load control features on the peak loads. A poorly determined distribution tail would invariably result in a highly sensitive reliability analysis in FORM. Finally, a correlation structure should be implemented amongst the random variables as correlations will influence the optimization of the loads partial safety factor.

Given the tangible decrease in partial loads factors advanced load alleviation control features are used in power production in turbulence uncertainty it is recommended to increase the effort in research and development of advanced load alleviation control features for wind turbines, both in terms of algorithms and components reliability. The objective should not only be a reduction in the magnitude of the extreme operating loads but also the shape and scatter of the resulting extreme loads distribution given its significant impact on the overall wind turbine benefits, initial investment costs and reliability.

6. Acknowledgements

The work presented herein is a part of the Danish Energy Technology Development and Demonstration (EUDP) project titled, Demonstration of a basis for tall wind turbine design, Project no 64011-0352. The financial support is greatly appreciated. The Danish Ministry of Science, Innovation and Higher Education are also gratefully acknowledged for their financial support. MiTa-Teknik are acknowledged for their generous financial and technical support and for providing the control systems for the FAST aero-servo-elastic simulations.

References

- [1] I. Abdallah, A. Natarajan, J. Sørensen, Influence of the control system on wind turbine loads in power production in extreme turbulence: structural reliability, Submitted to: Renewable Energy, 2015.
- [2] H. Veldkamp, Chances in Wind energy: a Probabilistic Approach to Wind Turbine Fatigue Design, Ph.D. thesis, Delft Technical University, Delft (2006).
- [3] N. J. Tarp-johansen, I. Kozine, L. Radermakers, J. D. Sørensen, K. Ronold, Optimised and Balanced Structural and System Reliability of Offshore Wind Turbines An account, Tech. Rep. April, Risø, Risø-R-1420(EN), Roskilde, Denmark (2005).
- [4] N. Tarp-johansen, J. Sørensen, P. Madsen, Experience with Acceptance Criteria for Offshore Wind Turbines in Extreme Loading, in: JCSS Workshop on Reliability based code calibration, Zurich, 2002, p. .
- [5] J. D. Sørensen, N. J. Tarp-johansen, Reliability-based Optimization and Optimal Reliability Level of Offshore Wind Turbines, International Journal of Offshore and Polar Engineering 15 (2).
- [6] International Electrotechnical Commission, IEC61400-1:2005 (ed. 3): Wind turbines - Part 1: Design Requirements., Tech. rep., International Electrotechnical Commission (2005).
- [7] J. Jonkman, M. Buhl, FAST User's Guide, Tech. rep., National Renewable Energy Laboratory, NREL/EL-500-38320 (2005).
- [8] N. Tarp-johansen, P. Madsen, S. Frandsen, Partial Safety Factors for Extreme Load Effects - Proposal for the 3rd Ed. of IEC 61400: Wind Turbine Generator Systems - Part 1: Safety Requirements, Tech. Rep. March, Risø, Risø-R-1319(EN), Roskilde, Denmark (2002).
- [9] R. Rackwitz, Risk control and optimization for structural facilities, System Modelling and Optimization (2003) 143–167.
- [10] J. Sørensen, Optimal reliability based design of offshore wind turbine parks, in: Second IFED Forum, Lake Louise, Canada, 2006, pp. 1–12.
- [11] J. Sørensen, I. Enevoldsen, Sensitivity weaknesses in application of some statistical distributions in First order reliability methods, Structural Safety 12 (4) (1993) 315–325. doi:10.1016/0167-4730(93)90060-E.

8 *Publication: Co-Kriging: fusing simulation results from multifidelity aero-servo-elastic simulators - Application to extreme loads on wind turbines*

Fusing Simulation Results From Multifidelity Aero-servo-elastic Simulators - Application To Extreme Loads On Wind Turbines

Imad Abdallah

Technical University of Denmark, Department of Wind Energy, Roskilde, Denmark

Bruno Sudret

ETH Zürich, Chair of Risk, Safety and Uncertainty Quantification, Zürich, Switzerland

Christos Lataniotis

ETH Zürich, Chair of Risk, Safety and Uncertainty Quantification, Zürich, Switzerland

John D. Sørensen

Aalborg University, Department of Civil Engineering, Aalborg, Denmark

Anand Natarajan

Technical University of Denmark, Department of Wind Energy, Roskilde, Denmark

ABSTRACT: Fusing predictions from multiple simulators in the early stages of the conceptual design of a wind turbine results in reduction in model uncertainty and risk mitigation. Aero-servo-elastic is a term that refers to the coupling of wind inflow, aerodynamics, structural dynamics and controls. Fusing the response data from multiple aero-servo-elastic simulators could provide better predictive ability than using any single simulator. The co-Kriging approach to fuse information from multifidelity aero-servo-elastic simulators is presented. We illustrate the co-Kriging approach to fuse the extreme flapwise bending moment at the blade root of a large wind turbine as a function of wind speed, turbulence and shear exponent in the presence of model uncertainty and non-stationary noise in the output. The extreme responses are obtained by two widely accepted numerical aero-servo-elastic simulators, FAST and BLADED. With limited high-fidelity response samples, the co-Kriging model produced notably accurate prediction of validation data.

1. INTRODUCTION

Analysts and designers increasingly use multiple commercial and research-based aero-servo-elastic simulators to compare the prediction of wind turbines' structural response. The aero-servo-elastic simulators are of varying fidelity and have different underlying assumptions. As a result, the aero-servo-elastic response may vary amongst simulators even if the external inflow condition is the same. The sub-models with the largest impact on the aero-servo-elastic response variability are aerodynamic, structural, control systems and wind inflow. The aero-servo-elastic simulators are validated using test measurements from prototype wind turbines. The current practice is to cover the

discrepancy amongst the simulators by imposing safety factors resulting in a safe design. It is reasonable to assume that model uncertainty is of the epistemic type and can be estimated at the design stage with (usually) decreasing uncertainty when more simulations from multiple sources are available.

The objective in this paper is to fuse the extreme response from multiple aero-servo-elastic simulators of various fidelity and complexity to predict "the most likely" extreme response of a wind turbine. Forrester et al. (2007) used the co-Kriging technique in the optimization of a generic aircraft wing using one "cheap" and one "expensive" flow solver. The Co-Kriging approach was also used by

Han and Görtz (2012) to predict the mean aerodynamic lift and drag coefficients on a two dimensional airfoil and a three dimensional aircraft using a low-fidelity Euler flow solver and a high-fidelity Navier-Stokes solver.

The novelty in this paper is the implementation of the co-Kriging technique to predict the extreme (not the mean) response in the presence of non-stationary noise in the output (i.e. the magnitude of noise varies as a function of the input variables) in the case when the low and high-fidelity aero-servo-elastic simulators of the same wind turbine are implemented by two independent engineers (i.e. human error and uncertainty in the modelling and input assumptions are implicitly included). In this paper, we demonstrate the co-Kriging methodology to fuse the extreme blade root flapwise bending moment of a large multi-megawatt wind turbine by using two aero-servo-elastic simulators, FAST (Jonkman and Buhl, 2005) and BLADED (Bossanyi (2003a), Bossanyi (2003b)).

2. THE CASE FOR DATA FUSION

Wind turbine aero-servo-elastic simulators of varying fidelities exhibit similarities and dependence in terms of the input variables and the underlying physical models (aerodynamic, structural, control systems and wind inflow). The dependence amongst various simulators may not be quantified by a single scalar number; it may well be that the dependence varies as a function of the design and input space (Christensen, 2012). Thus, we ask the fundamental question: Does it make any sense to fuse information from multifidelity aero-servo-elastic simulators \mathcal{M}_i ?

- To a great extent, simulators $\{\mathcal{M}_i, i=1, \dots, n\}$ share similar (often identical) inputs and describe similar (often identical) underlying modelling and physics assumptions.
- The various simulators may have been calibrated using the same test measurements.
- The higher fidelity simulators may simply be an expansion of the lower fidelity simulation model by inclusion of additional physics.
- Let us assume that for a given set of inputs $\mathcal{X} = [\mathbf{x}^{(1)}, \dots, \mathbf{x}^{(N)}]$, simulators \mathcal{M}_i predict responses $\mathcal{Y}_i = [\mathcal{M}_1(\mathbf{x}^{(1)}), \dots, \mathcal{M}_i(\mathbf{x}^{(N)})]^T$. Then,

\mathcal{Y}_i generally share the same trend and do not differ significantly from each other. In addition, the simulators \mathcal{M}_i do not exhibit clear bias in the predicted response \mathcal{Y}_i .

- The various aero-servo-elastic simulators may have been coded by the same or cooperating engineers, scientists and research institutes, and the same experts may have given their inputs/reviews/recommendations during the development and validation of the various simulators \mathcal{M}_i resulting in similar assumptions, biases and even possibly gross errors being used.
- The various simulators \mathcal{M}_i are certified by accredited institutes for use in the industry to design wind turbines. The certification process involves a lengthy validation and verification against measurements. Hence, no particular simulator \mathcal{M}_i is deemed better than the other.

The implication of the argumentation above is that rather than treating the aero-servo-elastic numerical simulators as parts of a hierarchy, they are considered as individual (but correlated) information sources. Furthermore, the simulators are assumed to be black boxes and we focus on the output quantity of interest (response) \mathcal{Y}_i .

3. METHODOLOGY

3.1. Co-Kriging

In this section we present a brief theoretical description of Kriging and Co-Kriging based on work by Sacks et al. (1989), Kennedy and O'Hagan (2000), Jones (2001), Forrester et al. (2007), Dubourg (2011), Han et al. (2012), Picheny et al. (2012), Sudret (2012) and Schöbi and Sudret (2014). Kriging is a stochastic interpolation technique which assumes that the "true" model output is a realization of a Gaussian process:

$$Y(x) = \mu(x) + Z(x) \quad (1)$$

where $\mu(x)$ is the mean value of the Gaussian process (trend) and $Z(x)$ is a zero-mean stationary Gaussian process with variance σ_Y^2 and a Covariance of the form:

$$C(\mathbf{x}, \mathbf{x}') = \sigma_Y^2 R(\mathbf{x} - \mathbf{x}' \mid \boldsymbol{\theta}) \quad (2)$$

where $\boldsymbol{\theta}$ gathers the hyperparameters of the autocorrelation function R . From a design of experiments \mathcal{X} , one can build the correlation matrix with terms $\mathbf{R}_{ij} = R(\mathbf{x}^{(i)}, \mathbf{x}^{(j)} | \boldsymbol{\theta})$ representing the correlation between the sampled (observed) points. In the case of simple Kriging $\mu(x)$ is assumed to be a known constant. In the case of ordinary Kriging $\mu(x)$ is assumed to be an unknown constant. In the case of universal Kriging $\mu(x)$ is cast as $\sum_{j=1}^m \beta_j f_j(x)$, i.e. a linear combination of unknown (to be determined) linear regression coefficients $\beta_j, j = 1, \dots, m$ and a set of preselected basis functions $f_j(x), j = 1, \dots, m$ (usually predefined polynomial functions). The autocorrelation function R may be a generalized exponential kernel:

$$R(\mathbf{x}, \mathbf{x}') = \exp\left(-\sum_{i=1}^M \theta_i (\mathbf{x}_i - \mathbf{x}'_i)^{p_i}\right), \theta_i \geq 0, p_i \in (0, 2] \quad (3)$$

where M is the number of dimensions of the input space and θ_i and p_i are unknown parameters to be determined. Other choices for R is a Gaussian kernel, or a Matérn kernel, etc. In order to establish a Kriging surrogate model, a design of experiments is formed $\mathcal{X} = [\mathbf{x}^{(1)}, \dots, \mathbf{x}^{(N)}]$ and a corresponding set of computer simulations are performed. The output is gathered in a vector $\mathcal{Y} = [\mathcal{M}(\mathbf{x}^{(1)}), \dots, \mathcal{M}(\mathbf{x}^{(N)})]^T$. The Kriging estimator (predicted response given the design of experiments) at a new point $\mathbf{x}^* \in \mathcal{D}_X$ is a Gaussian variable $\hat{Y}(\mathbf{x}^*)$ with mean $\mu_{\hat{Y}}$ and variance $\sigma_{\hat{Y}}^2$ defined as (Best Linear Unbiased Estimator):

$$\begin{aligned} \mu_{\hat{Y}}(\mathbf{x}^*) &= \mathbb{E} \left[\hat{Y}(\mathbf{x}^*) | \mathcal{M}(\mathbf{x}^{(i)}) \right] \\ &= \mathbf{f}^T \hat{\boldsymbol{\beta}} + \mathbf{r}^T \mathbf{R}^{-1} (\mathcal{Y} - \mathbf{F} \hat{\boldsymbol{\beta}}) \end{aligned} \quad (4)$$

$$\begin{aligned} \sigma_{\hat{Y}}^2(\mathbf{x}^*) &= \text{Var} \left[\hat{Y}(\mathbf{x}^*) | \mathcal{M}(\mathbf{x}^{(i)}) \right] \\ &= \hat{\sigma}_Y^2 \left[1 - \mathbf{r}^T \mathbf{R}^{-1} \mathbf{r} + \mathbf{u}^T (\mathbf{F}^T \mathbf{R}^{-1} \mathbf{F})^{-1} \mathbf{u} \right] \end{aligned} \quad (5)$$

where the optimal Kriging variance $\hat{\sigma}_Y^2$ and optimal Kriging trend coefficients $\hat{\boldsymbol{\beta}}(\boldsymbol{\theta})$ are given by:

$$\hat{\sigma}_Y^2 = \frac{(\mathcal{Y} - \mathbf{F} \hat{\boldsymbol{\beta}})^T \mathbf{R}^{-1} (\mathcal{Y} - \mathbf{F} \hat{\boldsymbol{\beta}})}{N} \quad (6)$$

$$\hat{\boldsymbol{\beta}} = (\mathbf{F}^T \mathbf{R}^{-1} \mathbf{F})^{-1} \mathbf{F}^T \mathbf{R}^{-1} \mathcal{Y} \quad (7)$$

and \mathbf{u}, \mathbf{r} and \mathbf{F} are given by:

$$\mathbf{u} = \mathbf{F}^T \mathbf{R}^{-1} \mathbf{r} - \mathbf{f} \quad (8)$$

$$\mathbf{r} = \begin{bmatrix} R(\mathbf{x}^* - \mathbf{x}^{(1)}; \hat{\boldsymbol{\theta}}) \\ \vdots \\ R(\mathbf{x}^* - \mathbf{x}^{(N)}; \hat{\boldsymbol{\theta}}) \end{bmatrix} \quad (9)$$

$$\mathbf{F} = \begin{bmatrix} f_j(\mathbf{x}^{(i)}) \end{bmatrix} = \begin{bmatrix} f_0(\mathbf{x}^{(1)}) & \dots & f_m(\mathbf{x}^{(1)}) \\ \vdots \\ f_0(\mathbf{x}^{(N)}) & \dots & f_m(\mathbf{x}^{(N)}) \end{bmatrix} \quad (10)$$

Note that \mathbf{r} is the correlation matrix between the sampled points and the point where a prediction is to be made. In the general case of a-priori unknown correlation parameters $\hat{\boldsymbol{\theta}}$, the optimal values can be estimated through Bayesian inference, maximum likelihood estimate or a leave-one-out cross-validation (Bachoc, 2013).

In case the outputs of the computer experiments contain "noise", the Kriging model should regress the data in order to generate a smooth trend. The Kriging thus amounts to conditioning $\hat{Y}(\mathbf{x}^*)$ on noisy observations $\mathcal{M}(\mathbf{x}^{(i)}) + \varepsilon_i$. The Kriging estimator mean $\mu_{\hat{Y}}(\mathbf{x}^*)$ and variance $\sigma_{\hat{Y}}^2(\mathbf{x}^*)$ are given by Equations 4 and 5, respectively by replacing the correlation matrix \mathbf{R} with $\mathbf{R} + \lambda^2 \mathbf{I}$, where λ^2 is the estimated variance of the noise term ε_i . We now consider how to build a surrogate model of a highly complex and expensive-to-run aero-servo-elastic response that is enhanced with data from cheaper and approximate analyses. This approach is traditionally known as co-Kriging (Kennedy and O'Hagan, 2000). Co-Kriging has been proposed under various names such as "hierarchical Kriging", "multifidelity surrogate modelling", "variable fidelity surrogate modelling", "data fusion", "multi-stage surrogate modelling", "recursive co-Kriging", etc. The formulation of co-Kriging presented here is based on Han and Görtz (2012): we consider l sets of response data obtained by running l aero-servo-elastic numerical simulators of varying fidelity and computational expense. We denote by level s the response data of the highest level of fidelity. For any given level $1 \leq l \leq s$, co-Kriging can

be written as:

$$\mu_{\hat{Y}}^{(l)} = \hat{\beta} \mu_{\hat{Y}}^{(l-1)} + \mathbf{r}^T \mathbf{R}^{-1} (\mathcal{Y} - \mathbf{F} \hat{\beta}) \quad (11)$$

where $\hat{\beta}$ is a scaling factor with a similar expression as in Equation 7, indicating how much the low- and high-fidelity responses are correlated to each other. $\mu_{\hat{Y}}^{(l-1)}$ is the trend in the kriging of the data at level l and the expression $\mathbf{R}^{-1} (\mathcal{Y} - \mathbf{F} \hat{\beta})$ depends only on the sampled data at level l . An appealing feature of the above formulation is that it entails very little modifications to an existing Kriging code if the latter is sufficiently modular.

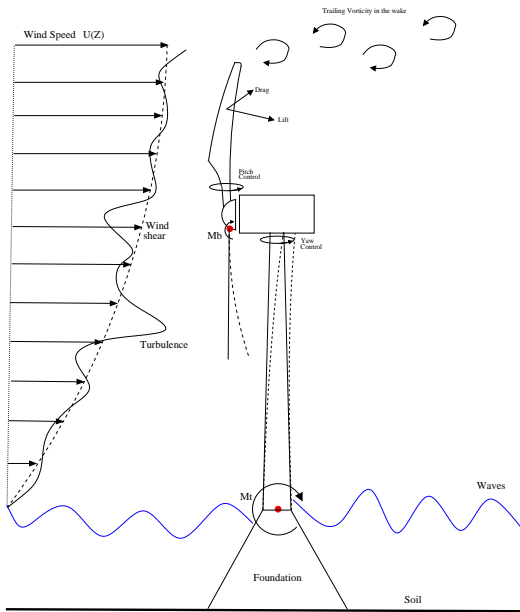


Figure 1: A wind turbine. M_b is the flapwise bending moment at the blade root. $U(Z)$ is the mean wind speed at height Z . Vertical wind shear (dotted grey line) and turbulence (thick black line).

4. APPLICATION TO EXTREME LOADS ON WIND TURBINE

We illustrate co-Kriging in fusing the extreme flapwise bending moment at the blade root of a wind turbine (Figure 1) by using two numerical aero-servo-elastic simulators, FAST and BLADED.

4.1. Aero-servo-elastic simulations

FAST is a time-domain aero-servo-elastic simulator that employs a combined modal and multibody dynamics formulation. FAST models the turbine using 24 Degrees of Freedom (DOFs). These DOFs

include two blade-flap modes and one blade-edge mode per blade. It has two fore-aft and two side-to-side tower bending modes in addition to nacelle yaw. The other DOFs represent the generator azimuth angle and the compliance in the drive train between the generator and hub/rotor. The aerodynamic model is based on the Blade Element Momentum theory (Hansen, 2001). A design of experiments (Table 1) is produced in order to examine the effects of wind speed, inflow turbulence and shear variations on the predicted extreme loads. For each combination of wind speed, turbulence level and shear exponent we generate realizations of wind time series with 24 stochastic seeds. Some of the wind speed, turbulence and shear exponent combinations are excluded because they are unphysical, resulting in a total of 33,480 10-minute time series simulations. One 10-minute wind time series simulation in FAST takes approximately three minutes in real time. The output used from the simulations are the blade root flapwise bending moment. The global maxima of the bending moment data are extracted for each of the 33,480 10-minute time series.

Table 1: Design of experiments for the FAST simulations. The variables are wind speed [m/s], turbulence [m/s] and the wind shear exponent.

Wind Speed [m/s]	Turbulence [m/s]	Shear exponent [-]
4, 5, ..., 25	0.1, 1, 2, 3, 4, 5, 6	+/-1.0, +/-0.6, +/-0.1, 0, 1.5

BLADED is a time domain aero-servo-elastic simulator that is used to conduct the high-fidelity aero-servo-elastic simulations of the same turbine geometry. The structural dynamics within BLADED are based on a modal model. The blade is modelled using up to 12 modes, six blade-flap and six blade-edge per blade. It also has three fore-aft and three side-to-side tower bending modes. Sophisticated power train dynamics are included. The aerodynamic model is based on the Blade Element Momentum theory. A design of experiments is produced as shown in Table 2. For each combina-

tion of wind speed, turbulence level and shear exponent we generate realizations of wind time series with 12 stochastic seeds. Some of the wind speed, turbulence and shear exponent combinations are excluded because they are unphysical, resulting in a total of 4344 10-minute simulations. One 10-minute wind time series simulation in BLADED takes approximately 25 minutes in real time. The output used from the simulations are the blade root flapwise bending moment. The global maxima of the bending moment data are extracted for each of the 4344 10-minute time series. The simulations in BLADED and FAST consider a wind turbine that has a 110 meters rotor diameter and 2 MW rated power. The wind turbine is erected on a 90 meters tower. Both the FAST and BLADED aero-servo-elastic simulations were performed with exactly the same control systems in the form of an external DLL. The FAST and BLADED simulation models do not use exactly the same input parameters in the structural and aerodynamic sub-models.

Table 2: Design of experiments for the BLADED simulations. The variables are wind speed [m/s], turbulence [m/s] and the wind shear exponent.

Wind Speed [m/s]	Turbulence [m/s]	Shear exponent [-]
4, 8, 10, 12, 15, 20, 25	0.1, 1, 2, 3, 4, 5, 6	+/-1.0,+/-0.6,+/-0.2,+/-0.1,0,1.5

5. RESULTS AND DISCUSSIONS

We start with a simple generic example to demonstrate Kriging and co-Kriging. In Figure 2, the noisy response of the low-fidelity simulator is plotted as a function of wind speed. A Universal Kriging model is fitted to the noisy response using a Gaussian correlation function R and a 3rd-order polynomial basis. The low-fidelity Kriging model is then used as the trend to fit a co-Kriging model to the noisy high-fidelity response.

In Figure 3, we compare the co-Kriging model to a universal Kriging model (Gaussian correlation function R and a 2nd-order polynomial basis).

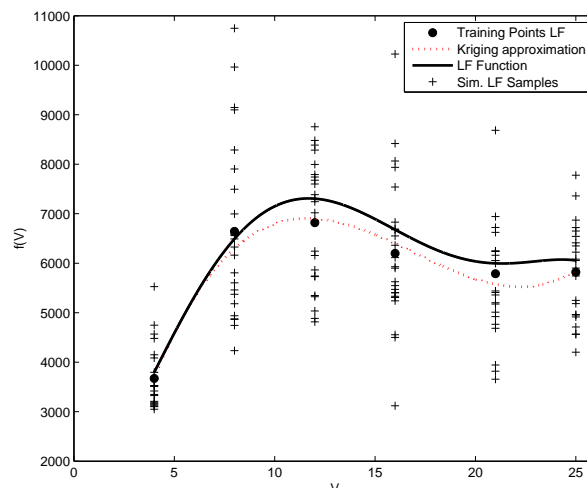


Figure 2: Response of the low-fidelity simulator at 6 wind speeds with 24 stochastic repetitions each (black crosses). The mean of the 24 samples is calculated and represented by the black dots. The Kriging model with noisy observations is the dotted red line. The low-fidelity (LF) function is the response if a large number of stochastic simulations are performed.

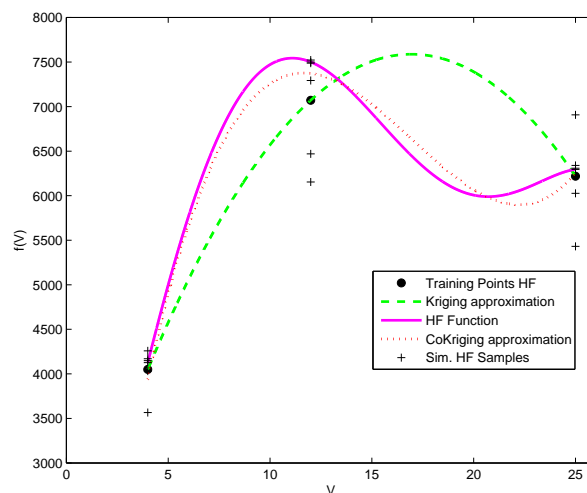


Figure 3: Response of the high-fidelity simulator at 3 wind speeds with 6 stochastic repetitions each (black crosses). The mean of the 6 samples is calculated and represented by the black dots. The Kriging model with noisy observations is the dashed green line. The Co-Kriging model with noisy observations is the dotted red line. The high-fidelity (HF) function is the response if a large number of stochastic simulations are performed.

Note that the high-fidelity responses are placed at only three wind speeds (4 m/s: turbine starts, 25 m/s: turbine shuts-down and 12 m/s: peak ro-

tor aerodynamic thrust). The co-Kriging predictions of the noisy high-fidelity response are notably better than the Kriging prediction based only on the high-fidelity samples. UQLab (Marelli and Sudret, 2014) is used to compute the Kriging and co-Kriging meta-models.

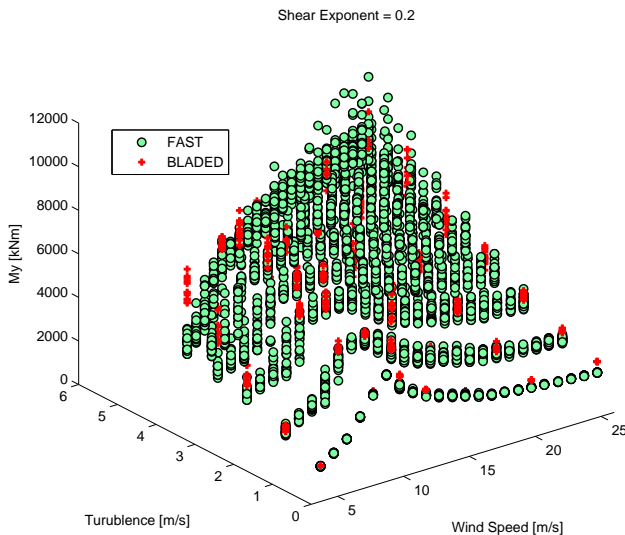


Figure 4: Scatter plot of the blade root extreme flapwise bending moment M_y as a function of wind speed and turbulence for shear exponent $\alpha = 0.2$. Note the variability (noise) of M_y for a given turbulence and wind speed.

A common practice during the design and optimization of a wind turbine is to generate a significant number of stochastic simulations, typically using two or more aero-servo-elastic simulators. Next, we show an example where the entirety of the loads simulations (as described in Section 4) are used to demonstrate a "real world" engineering application of data fusion using co-Kriging in high dimensions. The FAST and BLADED simulators were prepared by two independent engineers (one of whom is the first author of this paper). The simulations output are shown in Figure 4; even though the magnitude of the extreme flapwise bending moment at the blade root for low and high-fidelity simulators are not the same, they yield a similar trend. In Figure 4, for the same pair of turbulence and wind speed the output of the simulations is noisy due to the stochastic nature of the simulated wind speed time series. In addition, the magnitude of scatter (noise) increases with increasing turbulence

level. Note that the low and high-fidelity simulators are not sampled at exactly the same input variables.

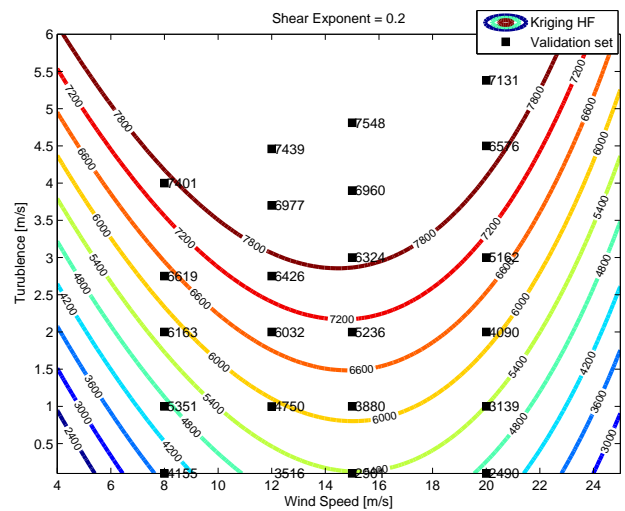


Figure 5: Projection of the Kriging model of the noisy high-fidelity (Bladed) extreme flapwise bending moment M_y compared to a validation set at wind speeds $V = 8, 12, 15, 20$ m/s and shear $\alpha = 0.2$.

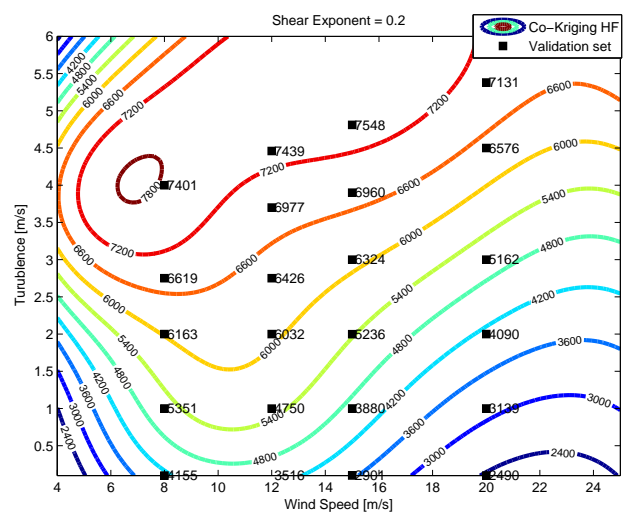


Figure 6: Projection of the Co-Kriging model of the noisy high-fidelity (Bladed) extreme flapwise bending moment M_y compared to a validation set at wind speeds $V = 8, 12, 15, 20$ m/s and shear $\alpha = 0.2$.

A Universal Kriging model is first fitted to all the noisy load response of the low-fidelity simulator (FAST) using a Gaussian correlation function R and 3rd-order polynomial basis. The low-fidelity Kriging model is then used as a model trend to fit a co-Kriging model to the noisy high-fidelity (Bladed)

load response. A subset of the high-fidelity data is used to build the co-Kriging model while the remaining data is used as validation points. This subset corresponds to the load response at wind speeds $V = [4, 10, 25] m/s$ as depicted in Figure 4. A universal Kriging model is also fitted to the same subset of the noisy high-fidelity load response using a Gaussian correlation function R and 2^{nd} -order polynomial basis. A projection of the Kriging and co-Kriging models of the noisy high-fidelity load response together with validation points are shown in Figures 5 and 6, respectively. To allow visualization of the meta-models predictions we set the shear exponent to $\alpha = 0.2$. Qualitatively, one can see that the co-Kriging model predictions are close to the validation points, while the Kriging model generally over-predicts the extreme load response. Using the low-fidelity Kriging model as a trend improves the predictive accuracy of the co-Kriging model of the high-fidelity load response, even in the presence of noise and by using very few high-fidelity sample points.

This is shown more clearly in Figures 7–9 where the accuracy of the Kriging and co-Kriging models of the high-fidelity extreme load response are compared. In those figures the validation points are shown with the corresponding scatter. The Kriging model from the high-fidelity response points gives a poor approximation of the validation points, while the co-Kriging model performs notably better in high dimensions. Hence, despite the difference between the output of the low and high-fidelity simulators, we were able to fuse both data sets so that the prediction error of the high-fidelity load response is reduced. The 95% confidence interval of the co-Kriging predictions is also shown in Figures 7, 8 and 9. The confidence interval of the co-Kriging predictions reflects a mix of epistemic (statistical) uncertainty due to the number of sampled points and due to the noise in the simulations output.

6. CONCLUSIONS

We have shown a co-Kriging based methodology to fuse the "noisy" extreme flapwise bending moment at the blade root of a large wind turbine from a low-fidelity and a high-fidelity aero-servo-elastic simulator. With limited high-fidelity response samples,

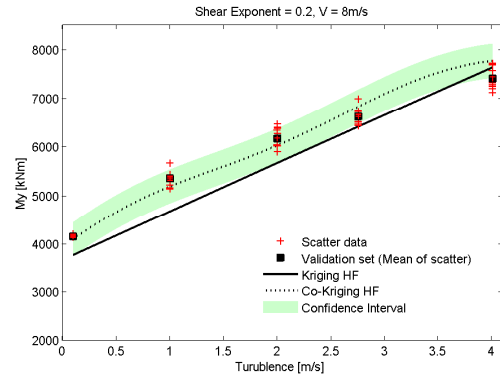


Figure 7: Comparison of the Kriging and co-Kriging models of the high-fidelity (HF) extreme flapwise bending moment M_y as a function of turbulence for $\alpha = 0.2$ and $V = 8m/s$.

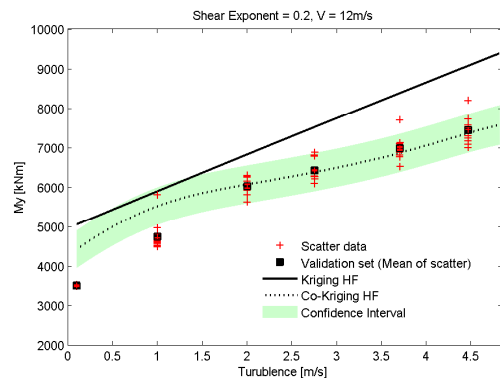


Figure 8: Comparison of the Kriging and co-Kriging models of the high-fidelity (HF) extreme flapwise bending moment M_y as a function of turbulence for $\alpha = 0.2$ and $V = 12m/s$.

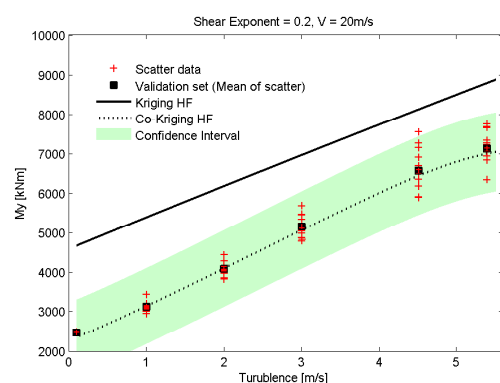


Figure 9: Comparison of the Kriging and co-Kriging models of the high-fidelity (HF) extreme flapwise bending moment M_y as a function of turbulence for $\alpha = 0.2$ and $V = 20m/s$.

the co-Kriging predictions compared well with val-

ication data. The notably accurate prediction performance is due to using the low-fidelity Kriging model as a model trend for the co-Kriging model. It is straight forward to extend this method to multiple fidelity levels. The confidence interval on the predictions of the co-Kriging model reflects a mix of epistemic (statistical) uncertainty due to the number of sampled points and due to the noise in the simulations output. A future study could attempt to quantify these two sources of uncertainties separately. In this paper, the main assumption is that the high and low-fidelity aero-servo-elastic simulations follow similar trends, which makes the fusion of results feasible. If the trend were not present then fusing data using co-Kriging would become hard to perform and less reliable. Finally, extreme loads response of a wind turbine are known not to follow a Gaussian process; a future study could attempt to modify the co-Kriging methodology to include non-Gaussian processes.

7. REFERENCES

- Bachoc, F. (2013). "Cross validation and maximum likelihood estimations of hyper-parameters of Gaussian processes with model misspecifications." *Comput. Stat. Data Anal.*, 66, 55–69.
- Bossanyi, E. (2003a). "GH Bladed theory manual." *Report No. 282-BR-009*, DNV GL.
- Bossanyi, E. (2003b). "GH Bladed user manual." *Report No. 282-BR-010*, DNV GL.
- Christensen, D. E. (2012). "Multifidelity methods for multidisciplinary design under uncertainty." M.S. thesis, Massachusetts Institute of Technology, Department of aeronautics and astronautics.
- Dubourg, V. (2011). "Adaptive surrogate models for reliability analysis and reliability-based design optimization." Ph.D. thesis, Université Blaise Pascal - Clermont II, LaMI.
- Forrester, A. I., Sóbester, A., and Keane, A. J. (2007). "Multi-fidelity optimization via surrogate modelling." *Proceedings of the Royal Society A: Mathematical, Physical and Engineering Sciences*, 463(2088), 3251–3269.
- Han, Z., Zimmerman, R., and Görtz, S. (2012). "Alternative cokriging method for variable-fidelity surrogate modeling." *AIAA Journal*, 50(5), 1205–1210.
- Han, Z.-H. and Görtz, S. (2012). "Hierarchical Kriging model for variable-fidelity surrogate modeling." *AIAA Journal*, 50(9), 1885–1896.
- Hansen, M. (2001). *Aerodynamics of wind turbines : rotors, loads and structure*. James & James (Science Publishers) Ltd. pp. 152. ISBN 1902916069.
- Jones, D. R. (2001). "A Taxonomy of global optimization methods Based on response surfaces." *Journal of Global Optimization*, 345–383.
- Jonkman, J. and Buhl, M. (2005). "FAST user's guide." *Report No. NREL/EL-500-38230*, National Renewable Energy Laboratory.
- Kennedy, M. and O'Hagan, A. (2000). "Predicting the output from a complex computer code when fast approximations are available." *Biometrika*, 87(1), 1–13.
- Marelli, S. and Sudret, B. (2014). "UQLab: a framework for uncertainty quantification in MATLAB." *Proc. 2nd Int. Conf. on Vulnerability, Risk Analysis and Management (ICVRAM2014)*, Liverpool, United Kingdom.
- Picheny, V., Wagner, T., and Ginsbourger, D. (2012). "A benchmark of kriging-based infill criteria for noisy optimization.
- Sacks, J., Welch, W., Mitchell, T., and Wynn, H. (1989). "Design and analysis of computer experiments." *Stat. Sci.*, 4, 409–435.
- Schöbi, R. and Sudret, B. (2014). "Polynomial-chaos-based kriging." *Int. J. Uncertainty Quantification*, submitted.
- Sudret, B. (2012). "Meta-models for structural reliability and uncertainty quantification." *Fifth Asian-Pacific Symposium on Structural Reliability and its Applications*, <<http://arxiv.org/abs/1203.2062>>.

In this chapter we look back at the aims and research questions stated in section 1.2 and synthesize the main findings and their implications. We also stress the limitations of the current work and provide guidance for further research.

9.1 Uncertainty in aerodynamic lift and drag

We systematically identified all sources of uncertainty affecting the aerodynamic lift and drag coefficients, from which we established a stochastic model by tapping into publicly available aerodynamic tests, measurements and simulations on various aspects of aerodynamic uncertainties. Some of the sources of uncertainty include variations among wind tunnel measurements, geometric distortions of the blade, effect of Reynolds number and 3-dimensional corrections. The stochastic model is developed by (1) replicating the physical variations in aerofoil characteristics by parameterizing the lift and drag coefficients curves, (2) allowing selected points on the lift and drag curves to be distributed randomly around the measured values and (3) simulating their impact on extreme loads using a Monte Carlo scheme with varying degree of correlation among the aerodynamic properties along the span of the blade. A commercial multi-megawatt offshore wind turbine is considered in the calculations of the extreme loads effects (nominal power $\geq 5MW$ and rotor diameter $\geq 130m$). We assessed the effect of the net aerodynamic uncertainty on the prediction of extreme loads and structural reliability of the wind turbine using the First Order Reliability Method (FORM). We also assessed the effect on the load partial safety factor in extreme operating conditions. We established that there is sufficient evidence for a tangible

reduction in the load partial safety factor for the blade and the tower given a lower coefficient of variation of the extreme loads distribution due to the aerodynamic uncertainties than previously believed. Such is not the case for load partial safety factor for tilt and yaw moments on the main shaft and tower top. We also established that the uncertainties in the aerodynamic lift and drag coefficients generally have a larger impact on extreme loads during power production compared to stand-still.

9.2 Effect of advanced load alleviation control features on structural reliability

A probabilistic loads extrapolation approach was used to assess the structural reliability of a large multi-megawatt wind turbine blade and tower during power production when the extreme turbulence model is uncertain and when three configurations of the load alleviation control systems of increasing performance and complexity are used. The first controller configuration is a basic control system that ensures that the wind turbine runs at optimal collective pitch and tip speed below rated wind speed and constant rotor speed above rated wind speed. No load alleviation control features were included in this configuration. The second controller configuration includes a cyclic pitch control and a static rotor thrust limiter control. The third and most advanced controller configuration includes individual pitch control and condition based thrust limiter which sets the control parameters based on the estimated external inflow and turbine loading conditions. The structural reliability was assessed for eight uncertainty scenarios including variation to the definition of the turbulence model in the IEC61400-1 design standard. Some of the uncertainty scenarios of the turbulence model are based on long term field measurements of site specific wind conditions. We showed that large uncertainty in the extreme turbulence model can be significantly mitigated through the use of advanced load control features. The improvement in the structural reliability is due to the reduction in the mean and coefficient of variation of the annual maximum distribution of the extreme loads when a turbine is operated by advanced load alleviation control features. However, the complexity of the control features increases which warrants additional failure modes analysis of the controller and its architecture. The improvement in the structural reliability also comes at a cost of loss in annual energy production.

Furthermore, we leveraged the load limiting effects of the advanced load alleviation control features in order to optimize the partial load factors in a cost and reliability based optimization scheme. Three take-aways here: (a) The overall structure-control series system is by far dominated by the annual failure rate of the control system given that it is an integral part of the structural design of modern wind turbines, (b) an optimal annual failure rate of the load alleviation control feature is on the order of 10^{-3} and (c) advanced load alleviation control features could yield a tangible reduction in the load partial safety factor but not always; the low coefficient of variation of the extreme load distribution in advanced load control configurations forces the characteristic load level (98 percentile) to be close to the mean of the distribution (i.e. tight extreme load distribution). A larger safety factor would then be required to reach the design load level. The low COV of the extreme load distribution due to the load limiting effect of advanced load control configurations means that model uncertainties in the limit state function start to dominate the reliability analysis in FORM. Hence, any further reduction in the load partial safety factor would

9.3. Fusing the output of multi-fidelity aero-servo-elastic simulators

require a reduction in model uncertainties, if possible. The tail of the extreme load distribution when advanced load control configurations are employed is very difficult to determine due to the aggressive limiting effects on the peak loads. A poorly determined distribution tail would inevitably result in a highly sensitive reliability analysis. Note, however, that even though the load partial safety factor might increase in advanced load control configurations, the drop in the 50-year load level is generally much higher compared to the increase in partial load factor, resulting in an overall lower design load level compared to more standard control configurations.

The way forward is for engineers and researchers to design controllers that not only reduce the extreme operating loads but also affect the shape of the resulting extreme loads distribution given its significant impact on the overall structural reliability of the wind turbine.

9.3 Fusing the output of multi-fidelity aero-servo-elastic simulators

Here we elucidated some of the arguments behind fusing output from multiple aero-servo-elastic simulations; as a result we argued that rather than treating the aero-servo-elastic numerical simulators as parts of a hierarchy, they are considered as individual (but correlated) information sources. Hence, it is reasonable to assume that model uncertainty is of the epistemic type and can be estimated at the design stage with (usually) decreasing uncertainty when more simulations from multiple sources are available. We then reviewed, implemented and demonstrated five analytical methods for fusing simulations output including coKriging, multivariate normal aggregation approach, adjustment factor approach, Copula models for information aggregation, Bayesian model averaging. One difficulty not fully addressed in this research is the assumption of Gaussianity in the first three analytical methods; extreme loads are not Gaussian. Another difficulty is establishing a correlation structure amongst the outputs of the various multi-fidelity aero-servo-elastic simulators. Correlations amongst the simulators does have a large impact on the aggregated (fused) response and the corresponding model uncertainty. Despite the assumption of Gaussianity, the aggregated (fused) coKriging model of the flapwise extreme bending moment of a multi-megawatt wind turbine compared well with the validation data; the low fidelity output were simulations from the FAST aero-servo-elastic simulator and the high fidelity output were simulations from the BLADED aero-servo-elastic simulator.

9.4 Recommendations for further research

There are a number of aspects that the author considers as deserving further attention.

- The parameters of the stochastic model of the uncertainties of aerodynamic lift and drag are assumed to be normally distributed. Non-Gaussian distributions could be implemented in order to check the sensitivity of the results to the parameters' distributions. Same goes for the correlation matrix of the parameters. More wind tunnel and full scale measurements on multiple aerofoil families could be used to further update the stochastic model.
- The annual maximum distribution of the extreme loads were derived based on long term extrapolation methodologies. The annual maximum distribution of the extreme loads is then used in FORM to compute the structural reliability and probability of failure. Reliability analysis are highly sensitive to the tail of distributions (rare events). However,

long term loads extrapolations methods are known to be ineffective in determining the tails. Better approaches should be explored.

- In this research the structural reliability analysis is largely based on a formulation of the limit state function that looks like:

$$g = zM_{cr}X_R - L_{ULT}(\sigma_1, v)X_{dyn}X_{st}X_{ext}X_{sim}X_{exp}X_{aero}X_{str} \quad (9.1)$$

where X' s are additional multiplicative stochastic variables to take into account the model and statistical sources of uncertainties on the load and resistance. The research in this thesis addressed and refined the definition of X_{aero} . [Veldkamp, 2006] looked into the various sources of model and statistical uncertainties. However, further laser focused insight into X' s should be performed if we want to have better confidence in the reliability and probabilistic analysis going forward.

- The various aero-servo-elastic simulators \mathcal{M}_i (such as FLEX, FAST, BLADED, HAWC2, Cp-Lambda, etc.) are certified by accredited certification institutes for use in the industry to design wind turbines. The certification process involves a lengthy validation and verification against measurements. Hence, no particular simulator \mathcal{M}_i is deemed necessarily better than the other. It is thus the belief of the author that further work on the topic of model fusion should be carried out in order to refine the model uncertainties of the predicted wind turbine response.
- The coKriging model fusion methodology assumes Gaussian process of the input variables. The formulation of the coKriging methodology could be modified to accept non-Gaussian processes, for instance through copulas to generalize the concept of covariance functions.
- A better understanding of the correlation and dependence structure amongst multi-fidelity aero-servo-elastic simulators would help improve the aggregated model (fused model) and the corresponding model uncertainties

A Appendix - Iso-probabilistic transformations for FORM

The first step when using FORM is to transform the original random variables $\mathbf{X} = \{x_1, x_2, \dots, x_n\}$ to the independent standard normal variables $\mathbf{U} = \{u_1, u_2, \dots, u_n\}$. We denote the transformation by \mathcal{T} , i.e. $\mathbf{X} \rightarrow \mathbf{U} = \mathcal{T}(\mathbf{X})$. We will briefly look at some aspects of those transformations. We will explore a basic case when all random variables have Gaussian marginal distributions and are independent. Then we will look at the general case when the random variables are non-Gaussian and are dependent.

Case for independent random variables: For independent random variables \mathbf{X} , the joint probability density function is simply the product of all marginals. The transformation to the standard normal space is then applied to each random variable at a time. In this case, the cumulative distribution function at x_i should equal the cumulative distribution function at u_i :

$$F_{X_i}(x_i) = F_{U_i}(u_i) \quad (\text{A.1})$$

But since the standard normal space is sought, the above equation becomes:

$$F_{X_i}(x_i) = \Phi(u_i) \quad (\text{A.2})$$

from which we deduce:

$$u_i = \Phi^{-1}[F_{X_i}(x_i)] \quad (\text{A.3})$$

where Φ is the standard normal cumulative distribution function.

Case for correlated Gaussian random variables: In this case the joint probability density function is a multivariate normal distribution. The Cholesky triangulation is used to facilitate the transformation. The random variables \mathbf{X} in the physical space are first transformed to a correlated standard normal Z-space \mathbf{Z} and finally to the uncorrelated standard normal space \mathbf{U} : $\mathbf{X} \rightarrow \mathbf{Z} \rightarrow \mathbf{U}$. Given a correlation matrix R_X , the Cholesky matrix is defined as $LL^T = R_X$. The subsequent transformations become:

$$x_i \rightarrow z_i : z_i = \Phi^{-1}[F_{X_i}(x_i)] \quad (\text{A.4})$$

where Φ is a standard multivariate normal distribution and the variables z_i are normally distributed with zero means and unit variances. However, they are correlated. Finally, the independent

Appendix A. Appendix - Iso-probabilistic transformations for FORM

random variables in standard normal space are derived as:

$$\mathbf{Z} \rightarrow \mathbf{U} : \mathbf{U} = \mathbf{L}^{-1}\mathbf{Z} \quad (\text{A.5})$$

Case for correlated non-Gaussian random variables: When the random variables are not normally (or lognormally) distributed, then the dependency cannot be described in terms of correlation matrix \mathbf{R}_X and the transformation described above can no longer be applied. In such cases, three iso-probabilistic transformations should be considered: the Rosenblatt transformation, the Nataf transformation, and transformations using Copulas.

If random variables $\mathbf{X} = \{x_1, x_2, \dots, x_n\}$ are correlated and their joint probability density function can be expressed as a sequence of conditional probability density functions:

$$f_{\mathbf{X}}(\mathbf{x}) = f_1(x_1)f_2(x_2 | x_1)f_3(x_3 | x_1, x_2) \cdots f_n(x_n | x_1, x_2, \dots, x_{n-1}) \quad (\text{A.6})$$

As a result of this sequential conditioning in the PDF the conditional CDFs are written:

$$\begin{aligned} F_{x_1}(x_1) &= \int_{-\infty}^{x_1} f_1(x_1)dx_1 \\ F_{x_2}(x_2 | x_1) &= \int_{-\infty}^{x_2} f_2(x_2 | x_1)dx_2 \\ F_{x_3}(x_3 | x_1, x_2) &= \int_{-\infty}^{x_3} f_3(x_3 | x_1, x_2)dx_3 \\ &\vdots \\ F_{x_n}(x_n | x_1, x_2, \dots, x_{n-1}) &= \int_{-\infty}^{x_n} f_n(x_n | x_1, x_2, \dots, x_{n-1})dx_n \end{aligned} \quad (\text{A.7})$$

and as in Equation A.2, we can equate:

$$\begin{aligned} \Phi(u_1) &= F_{x_1}(x_1) \\ \Phi(u_2) &= F_{x_2}(x_2 | x_1) \\ \Phi(u_3) &= F_{x_3}(x_3 | x_1, x_2) \\ &\vdots \\ \Phi(u_n) &= F_{x_n}(x_n | x_1, x_2, \dots, x_{n-1}) \end{aligned} \quad (\text{A.8})$$

Having these CDFs facilitates the transformation to standard normal space (Rosenblatt transformation [Rosenblatt, 1952]):

$$\begin{aligned} u_1 &= \Phi^{-1}[F_{x_1}(x_1)] \\ u_2 &= \Phi^{-1}[F_{x_2}(x_2 | x_1)] \\ u_3 &= \Phi^{-1}[F_{x_3}(x_3 | x_1, x_2)] \\ &\vdots \\ u_n &= \Phi^{-1}[F_{x_n}(x_n | x_1, x_2, \dots, x_{n-1})] \end{aligned} \quad (\text{A.9})$$

Generally the Rosenblatt transformation can only be used for low dimension, analytically known

probability density functions. The Rosenblatt transformations rely on having known conditional probability density functions of the random variables, which is not always possible. Even though Rosenblatt transformation has advantages (such as being an exact transformation), it may not be widely applicable to practical engineering problems due to following reasons. First, the joint PDF or conditional CDFs should be available for all variables to estimate the probability of failure, which is often too expensive or difficult or impossible to obtain in industrial applications where the marginal CDF and covariance are more commonly available. Also, when the distribution types of input variables are mixed, i.e., some of the variables are lognormal and others are Weibull, it is not possible to explicitly express the joint PDF in a mathematical formulation [Noh et al., 2007].

Nataf transformation originates from the need to include dependency when the available information (e.g. from sample sets of data) is limited to the marginal distributions $\{F_{X_i}, i = 1, \dots, n\}$ and the linear correlation matrix \mathbf{R} , but full joint distributions are not known. The Nataf transformation uses the Gaussian Copula to transform correlated input variables into correlated standard normal variables and linear transformation to transform correlated standard normal variables into independent standard normal variables. As in the case of correlated Gaussian random variables, the first step is to transform the variables from the physical space of the standard normal Z-space, where z_i variables are correlated:

$$x_i \rightarrow z_i : z_i = \Phi^{-1} [F_{X_i}(x_i)] \quad (\text{A.10})$$

a general expression of a bivariate standard normal density function:

$$\phi(x_i, x_j) = \frac{1}{2\pi\sqrt{1-\rho_{i,j}^2}} \exp \left\{ -\frac{1}{2(1-\rho_{i,j}^2)} [z_i^2 - 2\rho_{i,j}z_i z_j + z_j^2] \right\} \quad (\text{A.11})$$

A linear correlation coefficient expressed in terms of expectations:

$$\rho_{i,j} = \frac{COV [Z_i, Z_j]}{\sqrt{\sigma_i^2 \sigma_j^2}} \quad (\text{A.12})$$

In terms of expectations, the $COV [Z_i, Z_j], \sigma_i^2, \sigma_j^2$:

$$\begin{aligned} COV [Z_i, Z_j] &= \mathbb{E} [(Z_i - \mathbb{E} [Z_i]) (Z_j - \mathbb{E} [Z_j])] \\ &= \mathbb{E} [Z_i Z_j] - \mathbb{E} [Z_i] \mathbb{E} [Z_j] \end{aligned} \quad (\text{A.13})$$

$$\begin{aligned} \sigma_i^2 &= \mathbb{E} [(Z_i - \mathbb{E} [Z_i])^2] \\ &= \mathbb{E} [Z_i^2] - \mathbb{E} [Z_i]^2 \end{aligned} \quad (\text{A.14})$$

$$\begin{aligned} \sigma_j^2 &= \mathbb{E} [(Z_j - \mathbb{E} [Z_j])^2] \\ &= \mathbb{E} [Z_j^2] - \mathbb{E} [Z_j]^2 \end{aligned} \quad (\text{A.15})$$

Appendix A. Appendix - Iso-probabilistic transformations for FORM

substituting A.14 and A.15 into A.13:

$$\rho_{i,j} = \frac{\mathbb{E}[Z_i Z_j] - \mathbb{E}[Z_i] \mathbb{E}[Z_j]}{\sqrt{\mathbb{E}[Z_i^2] - \mathbb{E}[Z_i]^2} \sqrt{\mathbb{E}[Z_j^2] - \mathbb{E}[Z_j]^2}} \quad (\text{A.16})$$

Or Z_i and Z_j are standard normal random variables with zero mean ($\mathbb{E}[Z_i] = 0$ and $\mathbb{E}[Z_j] = 0$) and unit variance ($\sqrt{\mathbb{E}[Z_i^2] - \mathbb{E}[Z_i]^2} = 1$ and $\sqrt{\mathbb{E}[Z_j^2] - \mathbb{E}[Z_j]^2} = 1$), hence Equation A.16 becomes:

$$\rho_{i,j} = \mathbb{E}[Z_i Z_j] \quad (\text{A.17})$$

The Nataf assumption is that the random variables z_i and z_j are jointly normally distributed (Gaussian Copula) with correlation matrix \mathbf{R}_0 . In general $\mathbf{R}_0 \neq \mathbf{R}$ and they are related as follows:

$$\begin{aligned} \rho_{i,j} &= \mathbb{E}[Z_i Z_j] \\ &= \int_{-\infty}^{+\infty} \int_{-\infty}^{+\infty} z_i z_j \phi(z_i, z_j, \rho_{0,i,j}) dz_i dz_j \end{aligned} \quad (\text{A.18})$$

where $\phi(z_i, z_j, \rho_{0,i,j})$ defined in equation A.12.

Finally, \mathbf{Z} are transformed to \mathbf{U} :

$$\mathbf{Z} \rightarrow \mathbf{U} : \mathbf{U} = \mathbf{L}_0^{-1} \mathbf{Z} \quad (\text{A.19})$$

where \mathbf{L}_0 is the Cholesky decomposition of \mathbf{R}_0^{-1} . An advantage (and a disadvantage) of Nataf transformation is that it involves a Gaussian Copula that can generate a joint CDF for various types of correlated input variables based on limited information. However, it cannot be used for input variables with non-Gaussian joint distribution. One limitation of the Nataf transformation is the need to compute the elements of \mathbf{R}_0 which is difficult because it involves the resolution of a double integral in Equation A.18, and the second limitation is that there is no guarantee the resulting \mathbf{R}_0 will be symmetric and positive definite [Noh et al., 2007]. [Lebrun and Dutfoy, 2009a] indicates that for certain choices of the marginal distributions - following the *Frechet-Hoeffding* theorem - Equation A.18 might not have a solution. However, since the iterative process is very tedious and unknowns are within the double integral, an approximation to Equation A.18 has been proposed:

$$\rho_{0,i,j} = B_{i,j} \rho_{i,j} \quad (\text{A.20})$$

where $B_{i,j}$ is approximated by a polynomial:

$$B_{i,j} = a + bV_i + cV_i^2 + d\rho_{i,j} + e\rho_{i,j}^2 + f\rho_{i,j}V_i + gV_j + hV_j^2 + k\rho_{i,j}V_j + lV_iV_j \quad (\text{A.21})$$

where V_i and V_j are the coefficients of variation of z_i and z_j , and the coefficients are constants dependent on the type of the marginal distributions of the input random variables and are given in references such as [Liu and Der Kiureghian, 1986], [Der Kiureghian and Liu, 1986] and [Ditlevsen and Madsen, 2007].

Nataf transformation transforms the original variables into the correlated standard normal variables using Gaussian Copula, and then transforms correlated standard normal variables to independent standard normal variables using linear transformation that is the same as Rosenblatt

transformation for correlated normal variables. [Noh et al., 2009] proposes that for non-Gaussian joint distributions, once a Copula which captures the data is selected, the Rosenblatt transformation can be used to transform to the standard normal joint distribution. Also [Lebrun and Dutfoy, 2009b] proposed to extend the Nataf transformation to cover non-Gaussian jointly distributed random variables. That said, a non-Gaussian Copula which provides best fit to the data needs to be selected. proposes a generalization of the Nataf transformation to any random vector \mathbf{X} which Copula is elliptical and not necessarily Gaussian.

B Truncating probability density functions

Informally, the truncated normal probability density function is defined in two steps. We choose a general normal PDF by specifying parameters μ and σ^2 , and then a truncation range (a, b). The PDF associated with the general normal distribution is modified by setting values outside the range to zero, and uniformly scaling the values inside the range so that the total integral is 1.

A truncated distribution represents the distribution obtained by truncating the values of dist to lie between and. Let X be a discrete (continuous) random variable and denote its probability function and probability mass (density) function by $F(x)$ and $f(x)$, respectively. If the distribution is truncated so that only the values in X are observed, then the probability mass (density) function of the truncated random variable is given by:

$$f(x | X \in \mathcal{X}) = \frac{1 \{x \in \mathcal{X}\} f(x)}{F(x \in \mathcal{X})} \quad (\text{B.1})$$

We can have four cases:

- The non-truncated case – $\text{inf} = a, b = \text{inf}$
- The lower truncated case – $\text{inf} < a, b = \text{inf}$
- The upper truncated case – $\text{inf} = a, b < \text{inf}$
- The doubly truncated case – $\text{inf} < a, b < \text{inf}$

There are several ways to sample from a truncated distribution:

The inverse of the truncated distribution is known: If the the inverse of the truncated distribution has a closed form or can be computed numerically, then we can sample from a truncated distribution by $x = F^{-1}(u)$ where F is the cumulative function of the truncated distribution and $u | \text{Uniform}(0, 1)$.

The truncation range is wide (i.e. $\pm 5\sigma$): If the inverse of the truncated distribution F^{-1} is expensive to evaluate or cannot be determined, and the truncation range is wide (i.e. on the order of $\pm 5\sigma$), an alternative approach is to sample from the original (un-truncated distribution), and impose the truncation interval by rejection. The wide truncation range would ensure a large acceptance rate of the samples. The pseudo-code reads:

Appendix B. Truncating probability density functions

```
while true do  
  sample  $u = \text{Uniform}[0, 1]$   
   $x = F^{-1}(u)$   
  if  $x \in [a, b]$  then  
    accept  
  else  
    reject  
  end if  
end while  
return  $x$ 
```

Further methods are expanded in [Arul and Iyer, 2013] where importance sampling and Markov chain Monte Carlo methods are described to sample truncated distributions, an inverse transform sampling method is described in [Olver and Townsend, 2013] and Gibbs sampling of truncated distributions are described in [Robert, 1995, Wilhelm and Manjunath, 2010].

C FORM iterative scheme

A simple iterative scheme is hereby described to search for u^* provided that the limit state function is differentiable and is not highly non-linear [Haukaas, 2014]

1. set $i = 1$
2. Select a starting point in the standard normal space, \mathbf{u}_i
3. Transform \mathbf{u}_i into the original physical space \mathbf{x}_i $\mathbf{u}_i \rightarrow \mathbf{x}_i = \mathcal{T}(\mathbf{u}_i)^{-1}$
4. evaluate the limit state function $g(\mathbf{x}_i)$
5. evaluate the gradient of the limit state function $\nabla g(\mathbf{u}_i) = [\mathbf{J}(\mathbf{x}_i, \mathbf{u}_i)^{-1}]^T \nabla g(\mathbf{x}_i)$, where $\mathbf{J}(\mathbf{x}_i, \mathbf{u}_i)^{-1}$ is the inverse of the Jacobian matrix.
6. calculate an improved guess of the closest point on the hyperplane to the origin:

$$\mathbf{u}_{i+1} = \nabla g(\mathbf{u}_i) \frac{\nabla g(\mathbf{u}_i)^T \mathbf{u}_i - g(\mathbf{u}_i)}{\nabla g(\mathbf{u}_i)^T \nabla g(\mathbf{u}_i)} \quad (\text{C.1})$$

7. calculate the reliability index β_{i+1} (distance from trial point to origin): $\beta_{i+1} = \sqrt{\mathbf{u}_{i+1}^T \mathbf{u}_{i+1}}$
8. check for convergence according to $|\beta_{i+1} - \beta_i| < e$.
9. if convergence is reached, then stop. Else $i = i + 1$ and restart at step 3.

Finally, the probability of failure in Equation 3.18 is approximated as:

$$p_f \approx \Phi(-\beta) \quad (\text{C.2})$$

Several algorithms (with tweaks and corrections to the β value) have been suggested to perform this optimization process including the Hassofer-Lind-Rackwitz-Fiessler (HLRF) algorithm which is a simple algorithm but could run into convergence and stability problems [Rackwitz and Fiessler, 1978], later expanded by [Ditlevsen, 1981] to cover dependent variables. An improved version of the same algorithm has been suggested by [Liu and Der Kiureghian, 1991], [Zhang and Der Kiureghian, 1995] where a merit function is introduced to adjust the search direction.

Appendix C. FORM iterative scheme

Further optimization algorithms have been proposed by [Abdo and Rackwitz, 1991], [Lee et al., 2002] and [Haukaas and Der Kiureghian, 2006], and [Jiang et al., 2014].

D A simple example of load and resistance uncertainty

In this chapter the derivation of partial safety factors corresponding to a target reliability index is presented. In this simple example, the load and resistance are both assumed to follow the normal distribution:

Load: $L \sim N(\mu_L, \sigma_L)$

Resistance: $R \sim N(\mu_R, \sigma_R)$

The safety margin or Limit State Function (LSF) is given as $G = R - L$. The reliability index of the system defined by M should thus have a reliability index $\beta \geq \beta^*$, where β^* is the target reliability index.

Since L and R are normally distributed, then G is also normally distributed with $G \sim N(\mu_R - \mu_L, \sqrt{\sigma_L^2 + \sigma_R^2})$. Hence, by definition:

$$\beta = \frac{\mu_R - \mu_L}{\sqrt{\sigma_L^2 + \sigma_R^2}} \quad (\text{D.1})$$

Furthermore, we strive to have the reliability of the system higher or equal to the target reliability, $\beta \geq \beta^*$, then

$$\beta = \frac{\mu_R - \mu_L}{\sqrt{\sigma_R^2 + \sigma_L^2}} \geq \beta^* \quad (\text{D.2})$$

This is reformulated as:

$$\mu_R - \mu_L \geq \beta^* \sqrt{\sigma_R^2 + \sigma_L^2} \quad (\text{D.3})$$

Through a substitution, one can write:

$$\begin{aligned} \mu_R - \mu_L &\geq \frac{\sqrt{\sigma_R^2 + \sigma_L^2}}{\sqrt{\sigma_R^2 + \sigma_L^2}} \beta^* \sqrt{\sigma_R^2 + \sigma_L^2} \\ &= \left(\frac{\sigma_R^2 + \sigma_L^2}{\sqrt{\sigma_R^2 + \sigma_L^2}} \right) \beta^* \\ &= \left(\frac{\sigma_R}{\sqrt{\sigma_R^2 + \sigma_L^2}} \sigma_R + \frac{\sigma_L}{\sqrt{\sigma_R^2 + \sigma_L^2}} \sigma_L \right) \beta^* \\ &= (\alpha_R \sigma_R + \alpha_L \sigma_L) \beta^* \end{aligned} \quad (\text{D.4})$$

Appendix D. A simple example of load and resistance uncertainty

where $\alpha_R = \frac{\sigma_R}{\sqrt{\sigma_R^2 + \sigma_L^2}}$ and $\alpha_L = \frac{\sigma_L}{\sqrt{\sigma_R^2 + \sigma_L^2}}$ are known as the sensitivity factors. Furthermore, we substitute the coefficients of variation $COV_R = \frac{\sigma_R}{\mu_R}$ and $COV_L = \frac{\sigma_L}{\mu_L}$ in Equation D.4:

$$\mu_R - \mu_L \geq (\alpha_R \mu_R COV_R + \alpha_L \mu_L COV_L) \beta^* \quad (D.5)$$

By separating the terms related to the load and resistance, Equation D.5 can be written as:

$$\mu_R (1 - \alpha_R COV_R \beta^*) \geq \mu_L (1 + \alpha_L COV_L \beta^*) \quad (D.6)$$

Let R_c and L_c be the characteristic resistance and load levels respectively. Since the resistance R and the load L are normally distributed, then R_c and L_c can be written as:

$$\begin{aligned} R_c &= \mu_R - k_R \sigma_R \equiv R_c = \mu_R (1 - k_R COV_R) \\ L_c &= \mu_L + k_L \sigma_L \equiv L_c = \mu_L (1 + k_L COV_L) \end{aligned} \quad (D.7)$$

Where for instance¹ $k_R = \Phi^{-1}(0.05)$ and $k_L = \Phi^{-1}(0.98)$. Φ is the standard normal cumulative distribution. Substituting Equation D.7 into D.6, we obtain:

$$R_c \frac{(1 - \alpha_R COV_R \beta^*)}{(1 - k_R COV_R)} \geq L_c \frac{(1 + \alpha_L COV_L \beta^*)}{(1 + k_L COV_L)} \quad (D.8)$$

Consequently, the resistance and load partial safety factors (γ_R and γ_L) consistent with the target reliability index β^* are:

$$\begin{aligned} \gamma_R &= \frac{(1 - \alpha_R COV_R \beta^*)}{(1 - k_R COV_R)} \\ \gamma_L &= \frac{(1 + \alpha_L COV_L \beta^*)}{(1 + k_L COV_L)} \end{aligned} \quad (D.9)$$

The method described above is the so called Load and Resistance Factor Design or LRFD for short. The following example illustrates how the partial loads factor varies as a function of the loads coefficient of variation and target reliability index β^* , based on the derivations presented above. In this example both the resistance and load are assumed to follow the normal distribution and the following values are used:

- $COV_R = 0.10$ (assumed to remain constant in this example)
- COV_L is varied between 0.01 to 0.36 in 0.05 steps
- The target reliability index β^* is varied between 2.5 and 5
- $k_R = \Phi^{-1}(0.05)$ and $k_L = \Phi^{-1}(0.98)$

Fig. D.1 shows how the loads safety factor γ_L varies as a function of the loads coefficient of variation. One can intuitively observe how the loads safety factor increases for increasing coefficient of variation for a given reliability index β ; an increasing coefficient of variation reflect an increased level of uncertainty. Furthermore, the safety factor increases for increasing target reliability index, however the rate of change in the safety factor as a function of COV_L is significantly higher for high β compared to low β values.

The above derivation can be easily extended to log-normal distributions for the load and resistance random variables. However, in case a additional random variables are used in the limit state

¹0.05 is the 5% quantile of the uncertain resistance level and 0.98 corresponds to the 98% quantile of the uncertain load level. The quantile levels are arbitrary; however they are chosen in such a way that the reliability is less sensitive to the assumed distributions. 5% quantile for resistance and 98% quantile for load and generally used.

function, then no easy derivations are to be had and new methods are required as will be shown below.

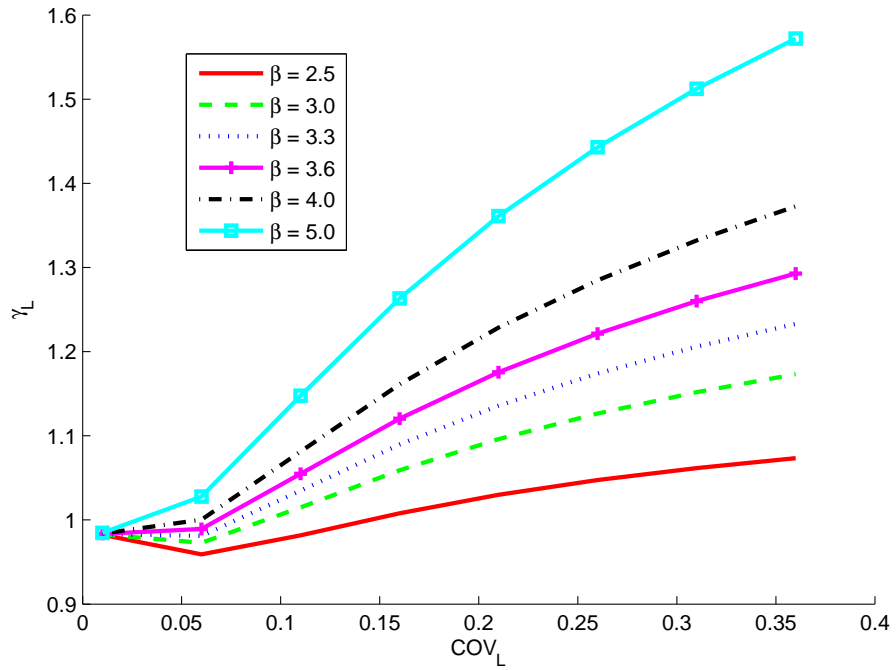


Figure D.1: Plot of the partial load factor as a function of the coefficient of variation of the load random variable, while the coefficient of variation of the resistance is maintained constant $COV_R = 0.10$.

E Background of the partial load factors in the IEC61400-1 ed. 3 design standard

Here we discuss the background and derivation of the safety factors in the IEC61400-1 design standard edition 3. We also discuss some of the new developments in edition 4. The background of the current IEC61400-1 ed. 3 partial safety factors for extreme loads is described by Tarp-Johansen in ref [11]. A brief summary of [11] is hereby presented.

Stand-still loads on tower and foundation The general limit state function for a wind turbine component is:

$$g = X_R R(X) - X_S Q(P_w, I) \quad (\text{E.1})$$

where $R(X)$ is the load-bearing capacity model and $S(P_w, I)$ is the load model dependent on the mean wind pressure and the turbulence intensity. The load-bearing capacity and the load model and statistical uncertainties are explicitly expressed in the limit state function by X_R and X_S respectively. For the load the model and statistical uncertainties are divided into their respective components. X_{dyn} is the uncertainty related to modelling of the dynamic response for the wind turbine, such as damping ratios and eigenfrequencies. X_{exp} is the uncertainty related to the modelling of the exposure such as the terrain roughness and the landscape topography. X_{st} is taking the statistical uncertainty related to the limited amount of wind data into account and X_{aero} is related to the uncertainty in assessment of the lift and drag coefficients. X_{str} accounts for the uncertainty related to the computation of stresses from the wind load. The uncertainty X_{sim} accounts for the statistical uncertainty related to the limited number of simulations in order to estimate the extreme load effect. The general limit state function becomes:

$$g = X_R R(X) - X_{dyn} X_{exp} X_{st} X_{aero} X_{str} X_{sim} S(P_w, I) \quad (\text{E.2})$$

Where, R is the load bearing capacity model, S is the load model, P_w is the mean wind pressure model and I is the turbulence intensity model. The above approach is general for all limit states; it can thus be developed to express ultimate stand-still loading as well as ultimate operational loading conditions on steel towers, steel and reinforced concrete foundations and fibre reinforced polymers blades. Tarp-Johansen writes the design equation for a tower in stand-still load as:

$$\frac{\sigma_c}{\gamma_m} = \gamma_f C_{inf} q_c = \gamma_f C_{inf} p_{w,c} (1 + 2k_p I_c C_{amp}) \quad (\text{E.3})$$

Appendix E. Background of the partial load factors in the IEC61400-1 ed. 3 design standard

Where σ_c is the characteristic material strength, C_{inf} is the influence factor and $p_{w,c}$ is the characteristic mean wind pressure. Based on the design equation, the limit state function of the tower in ultimate stand still load is:

$$g = X_R \Sigma - C_{inf} P_w (1 + 2k_p I C_{amp}) X_S \quad (E.4)$$

The reliability is the conjugate of the probability of failure:

$$\begin{aligned} P_f &= P(g < 0) \\ &= P\{X_R \Sigma < C_{inf} X_S Q\} \\ &= P\{X_R \Sigma < C_{inf} P_w (1 + 2k_p I C_{amp} X_{dyn}) X_{exp} X_{st} X_{aero} X_{str} X_{sim}\} \end{aligned} \quad (E.5)$$

At this stage the value of C_{inf} from Equ. (14) is substituted in Equ. (16) giving:

$$P_f = P\left\{\gamma_m \gamma_f X_R \frac{\Sigma}{\sigma_c} < \frac{P_w}{p_{w,c}} \frac{(1 + 2k_p I C_{amp} X_{dyn})}{1 + 2k_p I_c C_{amp}} X_{exp} X_{st} X_{aero} X_{str} X_{sim}\right\}$$

Now all is needed is to assess the product $2k_p C_{amp}$ in order to evaluate the probability of failure (or reliability) for a given total safety factor $\gamma_m \gamma_f$. It turns out that the product $2k_p C_{amp}$ can be assessed as follows:

$$\eta = \frac{\text{mean response}}{\text{extreme response}} = \frac{p_{w,c}}{p_{w,c} (1 + 2k_p I_c C_{amp})} = \frac{1}{1 + 2k_p I_c C_{amp}}$$

$$2k_p C_{amp} = \frac{1/\eta - 1}{I_c}$$

Substituting Equ. (18) into Equ. (17) yields

$$P_f = P\{\gamma_m \gamma_f X_R \Sigma < P_w (\eta + (1 - \eta) I X_{dyn}) X_{exp} X_{st} X_{aero} X_{str} X_{sim}\}$$

Stand-still loads on the blades Tarp-Johansen writes the design equation for a blade in stand-still load as:

$$\begin{aligned} \frac{\sigma_c}{\gamma_m} &= \gamma_f (C_{inf,q} q_c + C_{inf,g} g_c) \\ &= \gamma_f (C_{inf,q} p_{w,c} (1 + 2k_p I_c C_{amp}) + C_{inf,g} g_c) \end{aligned}$$

Based on the design equation the limit state function of the tower in ultimate stand still load is:

$$M = X_R \Sigma - (C_{inf,q} P_w (1 + 2k_p I C_{amp}) X_S + C_{inf,g} G)$$

Unlike a tower, the blade load safety factor γ_f depends on both gravity and aerodynamic loading. Therefore a ratio of aerodynamic load to the total extreme load (including gravity) is defined as:

$$\xi = \frac{\text{extreme response} - \text{gravity response}}{\text{extreme response}} = \frac{C_{inf,q} q_c}{C_{inf,q} q_c + C_{inf,g} g_c}$$

As in the case of the tower, Equ.(21) and (22) are expanded in the probability of failure equation to yield

$$P_f = P\{\gamma_m \gamma_f X_R \Sigma < \xi P_w (\eta + (1 - \eta) I X_{dyn}) X_{exp} X_{st} X_{aero} X_{str} X_{sim} + (1 - \xi) G\}$$

Normal operation on the tower, foundation and blades According to Tarp-Johansen, the extreme load in normal production is composed of a mean wind pressure component, period load (mainly gravitational component) and a stochastic load component (mainly due to turbulence). During operation there are many repeated 10-min periods with the same mean wind speed; as a result, the extreme load in normal operation is obtained by extrapolation. However, it is only the stochastic load component which is extrapolated because the mean wind pressure component is assumed to be deterministic because the mean wind speed over a 10-min period is well defined with no uncertainty. Tarp-Johansen writes the design equation in normal operation as:

$$\frac{\sigma_c}{\gamma_m} = \gamma_f (C_{inf,p}p + C_{inf,t}\sigma_q t_c + C_{inf,g}g_c)$$

Based on the design equation, the limit state function in normal operation is:

$$M = X_R \Sigma - ((C_{inf,p}p + C_{inf,t}\sigma_q T X_{dyn} X_{ext} X_{st} X_{sim}) X_{exp} X_{aero} X_{str} + C_{inf,g}G)$$

After some manipulations, the probability of failure becomes:

$$P_f = P\{\gamma_m \gamma_f X_R \Sigma < \xi (\eta + (1 - \eta) T X_{dyn} X_{ext} X_{st} X_{sim}) X_{exp} X_{aero} X_{str} + (1 - \xi)G\}$$

The nominal failure probability for structural design for extreme limit states for a reference period of 1 year is $p_f \leq 1.0 \cdot 10^{-3}$. The corresponding target value for the reliability index is $\beta \geq 3.09$. Application of this target value assumes that the risk to human lives is negligible in case of failure of a structural element. Given this derivation, Tarp-Johansen recommends a loads safety factor not less than 1.35 satisfying a probability of failure of $1.0 \cdot 10^{-3}$.

IEC61400-1 ed.4 chapter 7.6.6 Special partial safety factors Lower partial safety factors for loads may be used where the magnitudes of loads have been established by measurement or by analysis confirmed by measurement to a higher than normal degree of confidence. The values of all partial safety factors used shall be stated in the design documentation.



Bibliography

- Extremes of Nonlinear Vibration : Comparing Models Based on Moments , L-Moments , and. *Journal of offshore mechanics and arctic engineering*, 135(2013):1–7, 2015.
- K. Aas, C. Czado, A. Frigessi, and H. Bakken. Pair-copula constructions of multiple dependence. *Insurance: Mathematics and Economics*, 44(2):182–198, 2009. ISSN 01676687. doi: 10.1016/j.insmatheco.2007.02.001. URL <http://dx.doi.org/10.1016/j.insmatheco.2007.02.001>.
- I. Abdallah, A. Natarajan, and J.D. Sørensen. Impact of uncertainty in airfoil characteristics on wind turbine extreme loads. *Renewable Energy*, 75:283–300, 2015. ISSN 0960-1481. doi: 10.1016/j.renene.2014.10.009.
- T. Abdo and R. Rackwitz. New beta-point algorithm for large time-invariant and time-variant reliability problems. *Lecture Notes in Engineering, Proceedings of the 3rd IFIP WG 7.5 Conference on Reliability and Optimization of Structural Systems*, 61(4):1–12, 1991.
- T. Ahooyi, M. Soroush, J. Arbogast, W. Seider, and U. Oktem. Maximum-Likelihood Maximum-Entropy Constrained Probability Density Function Estimation for Prediction of Rare Events. *AIChE*, 60(3):1013–1026, 2014.
- H. Akaike. A new look at the statistical model identification. *IEEE Transactions on Automatic Control*, 19(6), 1974. ISSN 0018-9286. doi: 10.1109/TAC.1974.1100705.
- S. Akpinar and E. Akpinar. Wind energy analysis based on maximum entropy principle (MEP) -type distribution function. *Energy conversion and management*, 48:1140–1149, 2007.
- D. Allaire and K. Willcox. A mathematical and computational framework for multifidelity design and analysis with computer models. *International Journal for Uncertainty Quantification*, 4(1):1–20, 2014.
- D. Allaire, K. Willcox, and O. Toupet. A Bayesian-Based Approach to Multifidelity Multidisciplinary Design Optimization. In *13th AIAA/ISSMO Multidisciplinary Analysis Optimization Conference*, Fort Worth, Texas, 2010. doi: AIAA2010-9183.
- K. Alvin, W. Oberkamp, K. Diegert, and B. Rutherford. Uncertainty quantification in computational structural dynamics: a new paradigm for model validation. In *16th International Modal Analysis Conference*, pages 1191–1198, 1998.
- A. Arul and K. Iyer. A method for importance sampling through Markov chain Monte Carlo with post sampling variational estimate. 2013.

Bibliography

- F. Bachoc. Cross validation and maximum likelihood estimations of hyper-parameters of Gaussian processes with model misspecifications. *Comput. Stat. Data Anal.*, 66:55–69, 2013.
- T. Bedford and R.M. Cooke. Vines—a new graphical model for dependent random variables. *The Annals of Statistics*, 30:1031–1068, 2002. ISSN 2168-8966. doi: 10.1214/aos/1031689016.
- E.A Bossanyi. GH Bladed User Manual. Technical Report June, 2003a.
- E.A Bossanyi. GH Bladed Theory Manual. Technical Report July, 2003b.
- E. Brechmann, K. Hendrich, and C. Czado. Conditional copula simulation for systemic risk stress testing. *Insurance: Mathematics and Economics*, 53(3):722–732, 2013.
- C. Bucher. Asymptotic sampling for high-dimensional reliability analysis. *Probabilistic Engineering Mechanics*, 24(4):504–510, 2009.
- M. Buhl and A. Manjock. A Comparison of Wind Turbine Aeroelastic Codes Used for Certification. In *44th AIAA Aerospace Sciences Meeting and Exhibit*, Reno, Nevada, 2006. doi: NREL/CP-500-39113. URL <http://www.nrel.gov/docs/fy06osti/39113.pdf>.
- M. Buhl, A. Wright, and K. Pierce. Wind turbine design codes: A comparison of the structural response. In *19th American Society of Mechanical Engineers (ASME) Wind Energy Symposium*, 2000. doi: NREL/CP-500-27470. URL <http://arc.aiaa.org/doi/pdf/10.2514/6.2000-22>.
- M. Buhl, A. Wright, and K. Pierce. FAST _ AD Code Verification : A Comparison to ADAMS. In *20th American Society of Mechanical Engineers (ASME) Wind Energy Symposium*, Reno, Nevada, 2001. doi: NREL/CP-500-28848. URL <http://www.nrel.gov/docs/fy01osti/28848.pdf>.
- J.A. Carta, P. Ramirez, and S. Velazquez. A review of wind speed probability distributions used in wind energy analysis Case studies in the Canary Islands. *Renewable and sustainable energy reviews*, 13:933–955, 2009.
- D.E Christensen. *Multifidelity Methods for Multidisciplinary Design Under Uncertainty*. PhD thesis, Massachusetts Institute of Technology, 2012.
- CleanEnergyPipeline. Offshore wind project cost outlook. Technical report, Clean Energy Pipeline, a division of VB/Research, 2014. URL <http://www.cleanenergypipeline.com/Resources/CE/ResearchReports/OffshoreWindProjectCostOutlook.pdf>.
- R. Clemen and R. Winkler. Aggregation point estimates: a flexible modelling approach. *management Science*, 39(4):501–515, 1993.
- R. Clemen and R. Winkler. Combining Probability Distributions From Experts in Risk Analysis. *Risk Analysis*, 19(2):187–203, 1999.
- C. Czado. Pair-Copula Constructions of Multivariate Copulas BT - Copula Theory and Its Applications. *Copula Theory and Its Applications*, 198:93–109, 2010. doi: 10.1007/978-3-642-12465-5. URL [http://www.springerlink.com/index/10.1007/978-3-642-12465-5_4\\$delimiter"067A848\\$npapers2://publication/doi/10.1007/978-3-642-12465-5_4](http://www.springerlink.com/index/10.1007/978-3-642-12465-5_4$delimiter).
- A. Der Kiureghian and P. Liu. Structural reliability under incomplete probability information. *Journal of Engineering Mechanis*, (112):85–104, 1986.

- O. Ditlevsen. Principle of normal tail approximation. *Journal of the engineering mechanics division ASCE*, 107(6):1191–1208, 1981.
- O. Ditlevsen and H.O. Madsen. *Structural Reliability Methods*. Internet edition 2.3.7, 2007. DNV/Risø. *Guidelines for Design of Wind Turbines*. 2002. ISBN 87-550-2870-5.
- D. Draper. Assessment and propagation of model uncertainty. *J. R. Statist. Soc.*, 57(1):45–97, 1995.
- Q. Duan, Newsha K. Ajami, X. Gao, and S. Sorooshian. Multi-model ensemble hydrologic prediction using Bayesian model averaging. *Advances in Water Resources*, 30(5):1371–1386, May 2007. ISSN 03091708. doi: 10.1016/j.advwatres.2006.11.014. URL <http://linkinghub.elsevier.com/retrieve/pii/S030917080600220X>.
- V. Dubourg. *Adaptive surrogate models for reliability analysis and reliability-based design optimization*. PhD thesis, Université Blaise Pascal - Clermont II, LaMI, 2011.
- V. Dubourg, B. Sudret, and J.-M. Bourinet. Reliability-based design optimization using kriging and subset simulation. *Struct. Multidisc. Optim.*, 44(5):673–690, 2011.
- P. Embrechts, A. McNeil, and D. Straumann. Correlation and dependence in risk management: Properties and pitfalls. In *Risk management: value at risk and beyond*, pages 176–223. Cambridge University Press, 1999.
- A. Evren and E. Tuna. on Some Properties of Goodness of Fit Measures Based. 13(1):192–205, 2012.
- A. Forrester, A. Sobester, and A. Keane. Multi-fidelity optimization via surrogate modelling. *Proceedings of the Royal Society*, (463):3251–3269, 2007.
- P. Fris Hansen and J.D. Sørensen. Reliability-based code calibration of partial safety factors. *Workshop on Reliability Based Code Calibration*, 2002.
- J. Gibbons, G.M. Cox, A. Wood, J. Craigon, S. Ramsden, D. Tarsitano, and N. Crout. Applying Bayesian Model Averaging to mechanistic models: An example and comparison of methods. *Environmental Modelling & Software*, 23(8):973–985, August 2008. ISSN 13648152. doi: 10.1016/j.envsoft.2007.11.008. URL <http://linkinghub.elsevier.com/retrieve/pii/S1364815207002241>.
- S. Han, Z. and Görtz. Hierarchical kriging model for variable-fidelity surrogate modeling. *AIAA Journal*, 50(9):1885–1896, 2012.
- Z. Han, R. Zimmerman, and S. Görtz. Alternative cokriging method for variable-fidelity surrogate modeling. *AIAA Journal*, 50(5):1205–1210, 2012.
- M. Hansen. *Aerodynamics of Wind Turbines*. James&James, 2000. ISBN 1-902916-06-9.
- E. Hau and H. von Renouard. *Wind Turbines: Fundamentals, Technologies, Application, Economics*. Springer, 2005. ISBN 978-3540242406.
- T. Haukaas. The First-order Reliability Method (FORM), 2014. URL www.inrisk.ubc.ca.

Bibliography

- T. Haukaas and A. Der Kiureghian. Strategies for Finding the Design Point in Nonlinear Finite Element Reliability Analysis. *Probabilistic Engineering Mechanics*, 21(2):133–147, 2006.
- J. C. Helton and F. J. Davis. Latin hypercube sampling and the propagation of uncertainty in analyses of complex systems. *Reliability Engineering and System Safety*, 81:23–69, 2003.
- I. Hobæk, K. Aas, and A. Frigessi. On the simplified pair-copula construction - Simply useful or too simplistic? *Journal of Multivariate Analysis*, 101:1296–1310, 2010. ISSN 0047259X. doi: 10.1016/j.jmva.2009.12.001.
- J. Hoeting, D. Madigan, A. Raftery, and C. Volinsky. Bayesian model averaging: A tutorial. *Statistical Science*, 14(4):382–417, 1999.
- IRENA. renewable energy technology: cost analysis series. Technical report, 2012.
- E. T. Jaynes. On the rationale of maximum entropy methods. *IEEE*, 1982.
- C. Jiang, S. Han, M. Ji, and X. Han. A new method to solve the structural reliability index based on homotopy analysis. *Acta Mechanica*, pages 1–17, 2014.
- H. Joe. Families of m -variate distributions with given margins and $m(m-1)/2$ bivariate dependence parameters. *Distributions with fixed marginals and related topics*, 28:120–141, 1996. doi: 10.1214/lnms/1215452614.
- H. Joe. *Multivariate Models and Dependence Concepts*. Chapman and Hall, 1997.
- D. Jones. A taxonomy of global optimization methods based on response surfaces. *Journal of Global Optimization*, 21:345–383, 2001.
- J. Jonkman and M. Buhl. FAST User’s Guide. Technical report, National Renewable Energy Laboratory, NREL/EL-500-38320, 2005.
- J. Jonkman and W. Musial. Offshore code comparison collaboration (OC3) for IEA task 23 offshore wind technology and deployment. Technical report, 2010. URL <http://www.nrel.gov/docs/fy11osti/48191.pdf>.
- J. Jonkman, S. Butterfield, T. Camp, J. Nichols, J. Azcona, and A. Martinez. Offshore Code Comparison Collaboration within IEA Wind Annex XXIII : Phase II Results Regarding Monopile Foundation Modeling. In *IEA European Offshore Wind Conference*, 2008. doi: NREL/CP-500-42471. URL <http://www.nrel.gov/docs/fy08osti/42471.pdf>.
- M. Jouini and R. Clemen. Copula models for aggregating expert opinions. *Operations Research*, 44(3):444–458, 1995.
- M. Kennedy and A. O’Hagan. Predicting the output from a complex computer code when fast approximations are available. *Biometrika*, 87(1):1–13, 2000.
- M. Kennedy and A. O’Hagan. Bayesian Calibration of Computer Models. *Journal of the royal statistical society, Series B*, 63(3):425–464, 2001.
- A. Kiureghian and O. Ditlevsen. Aleatory or epistemic? Does it matter? *Structural Safety*, 31(2): 105–112, 2009. ISSN 01674730. doi: 10.1016/j.strusafe.2008.06.020.

- R. Lebrun and A. Dutfoy. An innovating analysis of the Nataf transformation from the copula viewpoint. *Probabilistic Engineering Mechanics*, 24(3):312–320, 2009a.
- R. Lebrun and A. Dutfoy. A generalization of the Nataf transformation to distributions with elliptical copula. *Probabilistic Engineering Mechanics*, 24(2):172–178, 2009b.
- J. Lee, Y. Yang, and W. Ruy. A comparative study on reliability-index and target-performance-based probabilistic structural design optimization. *Computers and Structures*, 80:257–269, 2002.
- M. Lemaire, A. Chateauneuf, and J.C. Mitteau. *Structural Reliability*. Wiley, 2009. ISBN 978-1848210820.
- C. Li, W. Wang, and S. Wang. Maximum-Entropy Method for Evaluating the Slope Stability of Earth Dams. *Entropy*, (14):1864–1876, 2012.
- P. Liu and A. Der Kiureghian. Multivariate distribution models with prescribed marginals and covariances. *Probabilistic Engineering Mechanics*, 1(2):105–112, 1986.
- P.L. Liu and A. Der Kiureghian. Optimization algorithms for structural reliability. *Probabilistic Engineering Structural Safety*, 9:161–177, 1991.
- D. Madigan and A. Raftery. Model selection and accounting for model uncertainty in graphical models using Occam’s window. *Journal of the American Statistical Association*, 89(428):1534–1546, 1994.
- J.F. Manwell, J.G. McGowan, and A.L. Rogers. *Wind Energy Explained: Theory, Design and Application*. Wiley, 2010. ISBN 978-0-470-01500-1.
- S. Marelli and B. Sudret. UQLab: a framework for uncertainty quantification in MATLAB. In *Proc. 2nd Int. Conf. on Vulnerability, Risk Analysis and Management (ICVRAM2014)*, Liverpool, United Kingdom, 2014.
- R. Melchers. *Structural Reliability Analysis and Prediction, 2nd Edition*. Wiley, 1999. ISBN 978-0-471-98771-0.
- N. Metropolis and S. Ulam. The Monte Carlo Method. *Journal of the American Statistical Association*, 44(247):269–306, 1949.
- A. Mosleh and G. Apostolakis. The assessment of probability distributions from expert opinions with an application to seismic fragility curves. *Risk Analysis*, 6(4):447–461, 1986.
- A. Naess, B. J. Leira, and O. Batsevych. System reliability analysis by enhanced Monte Carlo simulation. *Structural Safety*, 31(5):349–355, 2009.
- R.B. Nelsen. *An Introduction to Copulas*. Springer, 2010. ISBN 9780387775005. doi: 10.1007/978-0-387-98135-2.
- Y. Noh, K.K. Choi, and L. Du. New Transformation of Dependent Input Variables Using Copula for RBDO. In *7th World Congresses of Structural and Multidisciplinary Optimization*, Seoul, 2007.

Bibliography

- Y. Noh, K.K. Choi, and L. Du. Reliability-based design optimization of problems with correlated input variables using a Gaussian Copula. *Structural and Multidisciplinary Optimization*, 38: 1–16, 2009.
- S. Olver and A. Townsend. Fast inverse transform sampling in one and two dimensions. 2013.
- M. D. Pandey and S. T. Ariaratnam. Crossing rate analysis of non-Gaussian response of linear systems. *Journal of engineering mechanics*, 507, 1996.
- I. Park, H.K. Amarchinta, and R.V. Grandhi. A Bayesian approach for quantification of model uncertainty. *Reliability Engineering & System Safety*, 95(7):777–785, July 2010. ISSN 09518320. doi: 10.1016/j.ress.2010.02.015. URL <http://linkinghub.elsevier.com/retrieve/pii/S095183201000058X>.
- V. Picheny, T. Wagner, and D. Ginsbourger. A benchmark of kriging-based infill criteria for noisy optimization. 2012.
- R. Rackwitz and B. Fiessler. Structural reliability under combined load sequencces. *Computers and Structures*, pages 489–494, 1978.
- A. Raftery. Bayesian model selection in structural equation models. Technical report, 1993.
- A. Raftery. Bayesian Model Selection in Social Research, 1995. ISSN 00811750. URL <https://www.stat.washington.edu/raftery/Research/PDF/socmeth1995.pdf>.
- A. Raftery, T. Gneiting, F. Balabdaoui, and M. Polakowski. Using Bayesian Model Averaging to Calibrate Forecast Ensembles. *American Meteorological Society*, pages 1155–1174, 2005.
- P. Ramirez and J.A. Carta. The use of wind probability distributions derived from the maximum entropy principle in the analysis of wind energy . A case study. *Penelope Ramirez Jose Antonio Carta*, 47:2564–2577, 2006.
- F. Rasmussen, M.H. Hansen, K. Thomsen, T. Juul Larsen, F. Bertagnolio, J. Johansen, H.A. Madsen, C. Bak, and A.M. Hansen. Present status of aeroelasticity of wind turbines. *Wind Energy*, 6(3):213–228, 2003. ISSN 10954244. doi: 10.1002/we.98.
- M. Riley. Quantification of model-form, predictive, and parametric uncertainties in simulation-based design. *Doctoral thesis*, 2007.
- M.E. Riley and R.V. Grandhi. Quantification of model-form and predictive uncertainty for multi-physics simulation. *Computers & Structures*, 89(11-12):1206–1213, June 2011. ISSN 00457949. doi: 10.1016/j.compstruc.2010.10.004. URL <http://linkinghub.elsevier.com/retrieve/pii/S0045794910002245>.
- A. Ristig. Hierarchical Archimedean Copulae : The HAC Package. *Journal of Statistical Software*, 58, 2014.
- C.P. Robert. Simulation of truncated normal variables. 5:121–125, 1995. ISSN 09603174. doi: 10.1007/BF00143942.
- M. Rosenblatt. Remarks on a multivariate transformation. *Annals of Mathematical Statistics*, 23 (3):470–472, 1952.

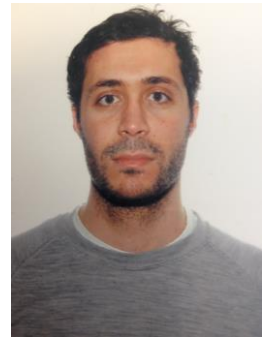
- J. Sacks, W. Welch, T. Mitchell, and H. Wynn. Design and analysis of computer experiments. *Statist. Sci.*, 4:409–435, 1989.
- J G Schepers, J Heijdra, D Foussekis, S Oye, and R R Smith et. al. Verification of European Wind Turbine Design Codes , VEWTDC ; Final report. Technical report, 2002. URL <http://www.ecn.nl/docs/library/report/2002/c01055.pdf>.
- D. Schirmacher and E. Schirmacher. Multivariate Dependence Modeling Using Pair-Copulas. In *Enterprise Risk Management Symposium Monograph*, pages 1–52, Chicago, 2008.
- R. Schöbi and B. Sudret. Pc-kriging: A new metamodelling method combining polynomial chaos expansions and kriging. *Proceedings of the 2nd International Symposium on Uncertainty Quantification and Stochastic Modeling*, 2014.
- R. Schöbi and B. Sudret. Polynomial-chaos-based kriging. *Int. J. Uncertainty Quantification*, 2014. submitted.
- M. Schwabe, P., Lensink, S., Hand. Multi-national case study of the financial cost of wind energy - work package 1. Technical report, 2011.
- M. T. Sichani, S. R K Nielsen, and C. Bucher. Applications of asymptotic sampling on high dimensional structural dynamic problems. *Structural Safety*, 33(4-5):305–316, 2011.
- D. Simms, S. Schreck, M. Hand, and L.J. Fingersh. NREL Unsteady Aerodynamics Experiment in the NASA-Ames Wind Tunnel : A Comparison of Predictions to Measurements NREL Unsteady Aerodynamics Experiment in the NASA-Ames Wind Tunnel : A Comparison of Predictions to Measurements. Technical Report June, NREL, 2001.
- A. Sklar. Fonctions de répartition à n dimensions et leurs marges. *Publications de l'Institut de Statistique de l'Université de Paris*, 8:229–231, 1959.
- M.S. Smith. Bayesian Approaches to Copula Modelling. *Hierarchical Models and MCMC: A Tribute to Adrian Smith.*, 2011. doi: 10.2139/ssrn.1974297. URL <http://arxiv.org/abs/1112.4204>.
- J.D. Sørensen. *Notes in Structural Reliability Theory and Risk Analysis.* , Aalborg, 2004.
- B. Sudret. *Uncertainty propagation and sensitivity analysis in mechanical models - Contributions to structural reliability and stochastic spectral methods.* PhD thesis, Habilitation a diriger des recherches, Universite Blaise Pascal, Clermont-Ferrand, 2007a.
- B. Sudret. *Uncertainty propagation and sensitivity analysis in mechanical models – Contributions to structural reliability and stochastic spectral methods.* Université Blaise Pascal, Clermont-Ferrand, France, 2007b. Habilitation à diriger des recherches, 173 pages.
- B. Sudret. Meta-models for structural reliability and uncertainty quantification. *Asian-Pacific symposium on structural reliability and its applications*, 2012.
- H.F. Veldkamp. *Chances in Wind energy: a Probabilistic Approach to Wind Turbine Fatigue Design.* PhD thesis, Delft Technical University, Delft, 2006.

Bibliography

- C.T. Volinsky, D. Madigan, A. Raftery, and R. Kronmal. Bayesian Model Averaging in Proportional Hazard Models : Assessing the Risk of a Stroke. *Appl. Statist.*, 46(4):433–448, 1997.
- E. von Collani, A. Binder, W. Sans, A. Heitmann, and K. Al-ghazali. Design Load Definition by LEXPOL. *Wind Energy*, (11):637–653, 2008.
- T. Vrouwenvelder. Reliability Based Code calibration The use of the JCSS Probabilistic Model Code. In *JCSS Workshop on code calibration*, Zurich, 2002.
- S. Wilhelm and B.G. Manjunath. tmvtnorm : A Package for the Truncated Multivariate Normal Distribution Generation of random numbers computation of marginal densities. *The R Journal*, 2(June):25–29, 2010.
- R. Winkler. Combining probability distribution from dependent information sources. *Management Science*, 27(4):479–488, 1981.
- Y. Zhang and A. Der Kiureghian. Two improved algorithms for reliability analysis. *Reliability and Optimization of Structural Systems, IFIP working group 7.5 The International Federation for Information Processing*, pages 297–304, 1995.
- E. Zio and G. Apostolakis. Two methods for the structured assessment of model uncertainty by experts in performance assessments of radioactive waste repositories. *Reliability Engineering & System Safety*, 54:225–241, 1996.

Imad Abdallah

Husumgade 44, sal.3, lejl. 5
2200 Copenhagen, Denmark
Tel: (+45) 22 83 30 05
Email: imad.abdallah.81@gmail.com



Education

Industrial PhD <i>Technical University of Denmark & Mita-Teknik A/S</i>	2012–present
Master of Science in Wind Energy <i>Technical University of Denmark</i>	2006
Baccalaureate in Applied Science, Mechanical Engineering (Magna Cum Laude)	2004
Baccalaureate in Science, Computing Technology (Magna Cum Laude) <i>University of Ottawa (Canada)</i>	2004

Specialties

- Wind energy
- Uncertainty quantification & Probabilistic design
- Loads and aerodynamics of wind turbines
- Aeroelastic simulations of wind turbines

Work Experience

Mita-Teknik A/S

Senior Load Engineer/Industrial PhD Candidate at DTU 2013–present

- PhD Thesis: Assessment of extreme design loads for modern wind turbines using the probabilistic approach. Objective: Apply uncertainty quantification and probabilistic based methods to the design of extreme loads on wind turbines.

WindNordic A/S, Denmark

Senior Load Engineer/Industrial PhD Candidate at DTU 2012–2013

- Worked on loads evaluation and optimization on customers' turbines using GH-Bladed
- PhD Thesis: Assessment of extreme design loads for modern wind turbines using the probabilistic approach. Objective: Apply uncertainty quantification and probabilistic based methods to the design of extreme loads on wind turbines.

Vestas Wind Systems A/S, Denmark

Lead Loads Engineer in the LAC team 2008–2012

- Responsible for the aeroelastic loads simulations on the Vestas 2MW fleet of wind turbines:
 - Aeroelastic loads simulations and loads optimizations using Flex 5
 - Loads verification and turbines certification according to the IEC61400 standards
 - Feasibility studies for new 2MW variants and new control features for load reduction
 - Worked very closely with turbine components specialists
- Holder of multiple patents
- Taught technical courses on wind turbines loads and aerodynamics
- Certified DMAIC Six Sigma Green Belt

Vestas Wind Systems A/S, Denmark

Aerodynamics Engineer in the LAC team 2006 –2008

- Performed the aerodynamic design of the rotor of the V60-850kW wind turbine
- Performed field tests of rotor blade aerodynamics (3MW turbine)

- Developed software for rotor design (BEM and blade shape distortion tolerancing)
- Power curve calculations and verifications on the Vestas 2 and 3MW wind turbines
- Power performance sensitivity analysis on the Vestas 2 and 3MW wind turbines

Qingdao Aeromag Wind Energy Equipment Co. LTD, Qingdao, China

Student Intern

June - August 2005

- Developed data acquisition software for the Aeromag's small wind turbine program
- Designed and built a wing of 2.4 m span and 0.6 m chord

NRC Institute for Aerospace Research, Canada

Student Intern

May - August 2003/2004

- CFD validation and performance study of the ONARE M6 wing
- Data analysis and post processing of CFD results for the Very Large Optical Telescope project.

CANMET Energy Technology Centre, Canada

Student Intern

Jan. - Apr./ Sep. - Dec. 2002

Worked on the development of the *Ash Monitoring System* which is a control system to monitor and control the amount of ash accumulated in the boiler of a coal fired power generation station; I developed heat transfer and flow models, and did extensive code development (Visual Basic) and testing of the AMS software on a coal fired boiler of a power generation station in Ontario, Canada

i-STAT, Canada

Student Intern

May - August 2001

Carried out the mechanical design and production of two manual assembly jigs in the R&D department of i-STAT

Software and Programming

Software

Aeroelastic software Bladed, FAST, FLEX5 and HAWC2, MATLAB/SIMULINK, Minitab, Xfoil

Programming Languages

Matlab, Python, Delphi, Visual Basic, C/C++, JAVA

Additional Information

Personal

- Date of birth: 02-June-1981
- Nationality: Canadian and Lebanese
- Fluent in English, French and Arabic. Basic in Danish.

Publications

- Abdallah, I., Natarajan, A., Sørensen, J. D., "Influence of the control system on wind turbine loads in power production in extreme turbulence: structural reliability". In: Renewable Energy (submitted).
- Abdallah, I., Sudret, B., Lataniotis, C., Natarajan, A., Sørensen, J.D., "Fusing Simulation Results From Multifidelity Aero-servo-elastic Simulators - Application To Extreme Loads On Wind Turbine". In: ICASP12: Proceedings of the 12th International Conference on Applications of Statistics and Probability in Civil Engineering (ICASP12): Vancouver, Canada, 12 - 15 July 2015 (To Appear).

- Abdallah, I., Natarajan, A., Sørensen, J. D., “Impact of uncertainty in airfoil characteristics on wind turbine extreme loads”. In: Renewable Energy, Vol. 75, 2015, p. 283-300.
- Abdallah, I., Natarajan, A., Sørensen, J. D., “Influence of the control system on wind turbine reliability in extreme turbulence”. In: Journal of Physics: Conference Series (Online), Vol. 524, No. 1, 012069, 2014.
- Abdallah, I., Natarajan, A., Sørensen, J. D., “Predicting the Extreme Loads on a Wind Turbine Considering Uncertainty in Airfoil Data”. Safety, Reliability, Risk and Life-Cycle Performance of Structures & Infrastructures: Proceedings of the 11th international conference on structural safety and reliability. ed. / George Deodatis; Bruce R. Ellingwood; Dan M. Frangopol. C R C Press LLC, 2014. p. 215-222.
- Mamou, M., Tahi, A., Benmeddour, A., Cooper, K.R., Abdallah, I., Khalid, M., Fitzsimmons, J., “Computational fluid dynamics simulations and wind tunnel measurements of unsteady wind loads on a scaled model of a very large optical telescope: A comparative study”, Journal of Wind Engineering and Industrial Aerodynamics, Volume 96, Issue 2, February 2008, Pages 257-288
- Abdallah, I., “Advanced Load Alleviation for Wind Turbines Using Adaptive Trailing Edge Geometry: Sensing Techniques”, Master of Science at Risø National Laboratory, 2006.

Interests

- Adventure racing (multi-sports events over long distances and periods of up to 24 hours)
- Running (ran the Hamburg and Zurich marathons several times)
- Tennis
- Politics, history and geography
- Stocks and finance

DTU Wind Energy is a department of the Technical University of Denmark with a unique integration of research, education, innovation and public/private sector consulting in the field of wind energy. Our activities develop new opportunities and technology for the global and Danish exploitation of wind energy. Research focuses on key technical-scientific fields, which are central for the development, innovation and use of wind energy and provides the basis for advanced education at the education.

We have more than 240 staff members of which approximately 60 are PhD students. Research is conducted within nine research programmes organized into three main topics: Wind energy systems, Wind turbine technology and Basics for wind energy.

Technical University of Denmark

Department of Wind Energy
Frederiksborgvej 399
Building 118
4000 Roskilde
Denmark
Telephone 46 77 50 85

info@vindenergi.dtu.dk
www.vindenergi.dtu.dk